Spectrum and Pulse Profile Formation in Strong-Field X-ray Pulsars

by

Duncan K. Galloway, B.Sc.(Hons.)

Submitted in fulfilment of the requirements
for the degree of
Doctor of Philosophy
at the
University of Tasmania

August, 2001

Declaration

This thesis contains no material which has been accepted for the award of any other higher degree or graduate diploma in any tertiary institution. To the best of my knowledge and belief, this thesis contains no material previously published or written by another person, except where due reference has been made in the text of the thesis.

This thesis may be made available for loan and limited copying in accordance with the *Copyright Act 1968*.

Duncan K. Galloway

Contents

Acknowledgements **v**

Abstract **vii**

1 Introduction **1**

1.1 Early developments . . . 2
1.2 X-ray Binaries . . . 4
1.3 X-ray Pulsars . . . 6
1.3.1 The magnetic field-disk interaction . . . 6
1.3.2 The boundary region and accretion column . . . 8
1.3.3 The emission region . . . 10
1.4 GX 1+4 . . . 13
1.5 RX J0812.4-3114 . . . 14

2 Methodology **15**

2.1 X-ray observations: *RXTE* . . . 16
2.1.1 Screening and background subtraction . . . 16
2.1.2 Spectral analysis . . . 17
2.1.3 Timing analysis . . . 19
2.1.4 Pulse-phase spectroscopy . . . 20
2.2 X-ray observations: BATSE/*CGRO* . . . 21
2.3 Monte-Carlo simulation of pulsar emission . . . 22
2.3.1 Initial photon selection . . . 23
2.3.2 Photon transport and scattering . . . 25
2.3.3 Light bending and photon eclipse . . . 25
2.3.4 Photon binning . . . 26
2.3.5 Calibration . . . 27
2.3.6 Spectral analysis . . . 28

3 Mean X-ray spectra from GX 1+4 **33**

3.1 Observations . . . 34
3.1.1 A — 12–13 February 1996 . . . 37
3.1.2 R — 16 January 1997 . . . 41
3.1.3 V–Y — 26 February – 20 May 1997 . . . 43

3.2 Mean X-ray spectra . . . 48
3.3 Discussion . . . 57

4 Luminosity dependence of pulse profiles from GX 1+4 65
4.1 Pulse period determination . . . 66
4.2 *RXTE* pulse profiles . . . 69
4.3 Pulse profile asymmetry . . . 76
4.3.1 *RXTE* profiles . . . 76
4.3.2 BATSE profiles . . . 78
4.3.3 Previously published profiles . . . 82
4.4 Discussion . . . 82

5 Accretion column eclipses in GX 1+4 87
5.1 Pulse-phase spectroscopy . . . 88
5.2 Dip timing . . . 93
5.3 Discussion . . . 96

6 X-ray observations of RX J0812.4−3114 103
6.1 Observations . . . 104
6.2 Discussion . . . 109

7 Monte-Carlo simulation of the pulsar emission region 113
7.1 Comptonization in a spherically symmetric cloud . . . 114
7.2 Comptonization in an accretion column . . . 114
7.3 Influence of the source aspect . . . 122
7.4 Pulse profiles . . . 125
7.5 Pulse phase spectroscopy . . . 128
7.6 Pulse profile asymmetry . . . 131
7.7 Observational effects . . . 133
7.8 Discussion . . . 133

A Spectral fitting results from GX 1+4 139

B Publications and presentations 143

Bibliography 144

Acknowledgements

I have been fortunate to work with, and learn from, many knowledgeable people during this project.

My supervisors, Dr. John Greenhill and Dr. Kinwah Wu, have complemented each other well in their expertise on the observational and theoretical sides of astronomy respectively. The diversity of the research I have undertaken as part of this thesis — which is perhaps its greatest strength — is thanks to their tutelage.

Dr. Barry Giles and Dr. Michelle Storey have encouraged me immensely through their collaboration and friendship.

I undertook most of the research towards this thesis at the Physics departments of the University of Tasmania and the University of Sydney, whose combined support allowed me to travel almost constantly and attend several excellent overseas conferences. Shorter intervals were spent at James Cook University in Townsville and recently the Australia Telescope National Facility. I thank the staff at each of these institutions for their hospitality and generosity.

I thank the Astronomical Society of Australia for supporting my attendance at its annual meetings between 1997 and 1999, and also the Harley Wood Winter Schools which have been as educational as they were enjoyable. The ASA and the Science Foundation at the University of Sydney both contributed significantly to my conference travel costs, for which I am grateful.

The *RXTE* Guest Observer Facility provided timely and vital help and information throughout my struggle to learn the esoteric secrets of X-ray data reduction. This research has made extensive use of data obtained through the High Energy Astrophysics Science Archive Research Center Online Service, provided by the NASA/Goddard Space Flight Center. I would also like to thank Dr. Bob Wilson and Dr. Colleen Wilson-Hodge from Marshall Space Flight Center for their advice and re-analysis of BATSE data.

I thank my parents, for their advice; the Hammings, for their welcome; and Stephen Kane, for never losing his sense of humour.

And finally, thanks to Gretta for helping me begin; and Jasmina for making me finish.

Abstract

I present the results of an analytic and modelling study of X-ray pulsar emission. Satellite X-ray observations of the binary pulsars GX 1+4 and RX J0812.4−3114 made using the Rossi X-ray Timing Explorer (*RXTE*) and the Burst and Transient Source Experiment (BATSE) aboard the Compton Gamma Ray Observatory (*CGRO*) were analysed to quantify source variations with time and pulse phase. A numerical model simulating X-ray emission from pulsars in terms of Compton scattering of photons within a neutron star accretion column has been developed to test the consistency of the analysis results and to further investigate the spectral and pulse profile formation.

Mean Proportional Counter Array (PCA) spectra of both pulsars over the range 2–40 keV are adequately fitted with a Comptonization model, with blackbody source spectrum $T_0 \approx 1$–1.3 keV, plasma temperature $T_{\rm e} \approx 6$–10 keV, and optical depth $\tau \approx 2$–6. The source spectrum temperature is consistent with an origin at the neutron star polar cap, with Compton scattering taking place primarily in the hot plasma of the accretion column. Both the fitted optical depth and plasma temperature vary significantly with the source flux. The wide range of source luminosity spanned by archival observations of GX 1+4 offers evidence for two distinct spectral states above and below $L_{\rm X} \approx 1.4 \times 10^{37}\ {\rm erg\,s^{-1}}$ (2–20 keV, assuming a source distance of 10 kpc). GX 1+4 additionally exhibits dramatic hourly variations in neutral column density $n_{\rm H}$ indicative of density variations in the stellar wind from the giant companion.

Pulse profiles from GX 1+4 vary dramatically over timescales as short as 6 h. Low-order Fourier decomposition of pulse profiles in the 20–50 keV band from BATSE monitoring of the source, in addition to the pulse profiles observed by *RXTE* over a broader energy range have been used to investigate the relationship between source flux and profile asymmetry suggested on the basis of previously published profiles. The asymmetry of the pulse profiles (as measured by the asymmetry parameter α, Greenhill et al., 1998) exhibits large variation which decreases as the flux increases. No significant relationship is suggested by the recent data, although the span in flux is significantly narrower than from historical profiles which cover the 1970s during which the source was consistently very bright.

Pulse-phase spectroscopy of *RXTE* data from GX 1+4 and RX J0812.4−3114 support the interpretation of the sharp dips in the pulse profile as 'eclipses' of the emission region by the accretion column. The dip phase corresponds with the closest approach of the column axis to the line of sight, and the additional optical depth

experienced by photons escaping from the column in this direction gives rise to both the decrease in flux and increase in the fitted τ measured at this phase. Analysis of the arrival time of individual dips in GX 1+4 provides the first measurement of azimuthal wandering of a neutron star accretion column. The column longitude varies stochastically with standard deviation 2–6° depending on the source luminosity. Measurements of the phase width of the dip both from mean pulse profiles and individual eclipses demonstrates that the dip width is proportional to the flux. The variation is consistent with that expected if the azimuthal extent of the accretion column depends only upon the Keplerian velocity at the inner disc radius, which varies as a consequence of the accretion rate $\dot{M}$.

A numerical model using a Monte-Carlo approach has been developed to investigate the behaviour of the emission model suggested by the analysis results. The model simulates Comptonization of a source of blackbody photons emitted from the polar cap of a canonical neutron star in a semi-infinite cylindrical accretion column. The mean spectra vary with both inclination angle and magnetic colatitude (the source aspect). For certain ranges of aspect the pulse profiles exhibit dips similar to those observed in GX 1+4 and RX J0812.4−3114, although not as sharp. Pulse phase spectroscopy of the model data confirms the increase in fitted τ coincident with the dip. Latitudinal variations in density across the column, suggested as a possible source of profile asymmetry, result in significant asymmetry only if the brightness of the two poles is unequal.

Chapter 1

Introduction

1.1 Early developments

With X-rays from astronomical sources screened effectively by the upper atmosphere, the development of X-ray astronomy could not even begin until the commencement of space exploration (Hirsh, 1983). The first seeds were sown in the early studies of the ionosphere in the 1920s and 30s. Researchers realised at that time that the seasonal and diurnal variations in ionospheric conditions could only mean that the ionising radiation originated outside the atmosphere, in our own sun. As early as 1938 the suggestion was made that this radiation could be solar X-rays, as opposed to the mainstream view which held UV radiation as the likely source.

Whilst most civilian research efforts were significantly interrupted by World War two, captured German V-2 rockets provided the next generation of technology required to explore the upper reaches of the atmosphere. The same weapon used to bomb the south-east of Britain during the war was used from 1946 onwards as a platform for atmospheric research by the US Army. These vehicles could fly much higher than the balloons used to date, and the payload capability — originally intended for high explosives — was generous. Shielded photographic plates flown on a V-2 launch on 5 August 1948 showed significant X-ray radiation in the ionosphere. Photon counters developed by Herbert Friedman at the Naval Research Laboratories and launched later in the same year demonstrated that it was this X-ray rather than UV radiation responsible for the ionisation in the upper atmosphere. By 1952 it was clear that the sun was the source of the ionising radiation, and the study of solar X-rays began.

Although these early observations opened new vistas for the understanding of the structure of the sun, they had the side effect of discouraging searches for *extra*-solar X-rays. State of the art instruments could not hope to detect distant stars emitting X-rays at the same levels as the sun. Despite inconclusive observations during 1956, the detection of the first X-rays from outside the solar system did not come until 1962. Ricardo Giacconi and collaborators at American Science and Engineering, Inc., had developed a sophisticated (for the time) package consisting of paired scintillation detectors designed to reject the ever-present cosmic ray background by means of anticoincidence eletronics. An Aerobee rocket (which was designed specifically for scientific use and became the workhorse for early experiments following the V-2) carried this instrument in a flight on 18 June 1962. Intended to measure reflected solar X-rays from the moon, the experiment instead found evidence for two localised sources outside the solar system as well as a diffuse background (Giacconi et al., 1962). Friedman's followup flights later in 1962 and 1963 confirmed the result and the discovery of the first astronomical X-ray source — named Scorpius X-1.

Clearly, X-ray emission via some unexpected process was being observed. The X-ray flux of the newly discovered sources were many orders of magnitude greater than that observed from the sun, regardless of their exact distance. Theoretical understanding lagged behind the observations for almost ten years, as it turned out. The concept of 'neutron' stars had come from studies of the structure of white dwarves, but the expected cooling rates were simply too rapid to keep these exotic objects radiating brightly for any significant length of time. The diffuse X-ray background was just as important a discovery, and contributed to the demise of the steady-state universe model popular at the time. Rocket launches continued throughout the 1960s, and were augmented by much cheaper balloon experiments which were useful for high energy observations. These instruments led to the identification of the first optical counterpart of an X-ray source (Sandage et al., 1966) and the detection of X-ray pulsations from the source in the Crab nebula (Fritz et al., 1969) to match the prior detection in radio. While the emission in the latter source was understood relatively rapidly, the majority of X-ray sources were quite different and still lacked a viable emission mechanism. As early as 1964 it became clear that both rockets and balloons were extremely limited platforms for the new field of X-ray astronomy, and the idea for a small X-ray satellite was born.

The SAS-1 satellite, renamed *Uhuru* (Swahili for 'freedom') was launched from an oil rig off the Kenyan coast on 12 December 1970. The payload consisted of a pair of proportional counters, each 840 cm^2 in collecting area, with relatively advanced pulse shape discrimination in addition to anticoincidence electronics for cosmic ray rejection. But the greatest advantage was the ability to make pointed observations for almost an entire orbit — and repeated measurements over hours, days, or even weeks. The discovery of 4.8 s pulsations in Centaurus X-3 was soon matched with a secondary periodicity, clearly demonstrating the binary nature of the system (Schreier et al., 1972). Sources like Cen X-3 could not be more different than the Crab pulsar — there was no nebular emission, no detectable radio emission, and the pulse period was decreasing instead of increasing — the neutron star was being spun-up. With these new pieces of the puzzle, the modern theory of pulsars developed rapidly in a series of papers (Pringle and Rees, 1972, Davidson and Ostriker, 1973, Shakura and Sunyaev, 1973). Finally the broad theoretical understanding of these compact X-ray sources was in place.

X-ray astronomy has today reached a mature stage. Instrumental sensitivities have increased by many orders of magnitude, through the *Einstein* to the recently launched *Chandra* and *XMM* observatories. The development of imaging X-ray telescopes has further expanded our views of the universe. Locations of more than 60000 sources are known, most of these from the *ROSAT* survey undertaken in the six months following its launch in 1990. Launched in 1991, the Compton Gamma Ray Observatory (*CGRO*) was primarily intended for studies of gamma ray bursts, but the Burst and Transient Source Experiment (BATSE; Zhang et al., 1995) which also flew on this satellite generated the finest long-term X-ray pulsar period histories to date. Studies of rapid variability in both neutron star and black hole binaries reached a new level with the 1995 launch of the Rossi X-ray Timing Explorer (*RXTE*; Giles et al., 1995). Satellite observations of several hundred *thousand* seconds are now commonplace, contrasting dramatically with the several hundred seconds typical of early rocket and balloon launches. X-ray observations play an important complemetary role in studies of the universe on all scales of space and time.

And yet, like every scientific field, mysteries remain.

1.2 X-ray Binaries

Almost all binary X-ray sources are powered by accretion onto a compact object. The governing paradigm which describes these systems is deceptively simple and hides a truly bewildering range of behaviour. The nature of the compact object is thought to be determined by the initial masses of the main-sequence binary components. When the more massive star has $M_* \lesssim 10 M_\odot$ initially, the binary evolution will proceed through a common envelope phase to produce a white dwarf binary, normally referred to as a cataclysmic variable (Warner, 1995). For higher initial mass, the main sequence lifetime will instead terminate with a supernova explosion. So long as the kick velocity imparted by the supernova is insufficient to break up the binary it will persist as a compact object (neutron star or black hole) orbiting a (relatively) normal star. An excellent review of the properties and evolution of such sources can be found in Lewin et al. (1995).

Accretion can begin immediately if the companion's stellar wind is sufficient. For high-mass X-ray binaries (HMXBs) with companion masses > a few $M_\odot$ stellar winds can export up to $10^{-6}\, M_\odot\ \mathrm{yr}^{-1}$ into the binary environment. The accretion luminosity originates from gravitational potential energy liberated as the matter falls into the potential well of the compact object. If the compact star has mass M_*, radius R_*, and is accreting at $\dot{M}\ \mathrm{g\,s^{-1}}$ the accretion luminosity is

$$\begin{aligned} L_{\mathrm{acc}} &= GM_*\dot{M}/R_* \\ &= 1.33 \times 10^{36} \left(\frac{M_*}{M_\odot}\right) \left(\frac{\dot{M}}{10^{16}\ \mathrm{g\,s^{-1}}}\right) \left(\frac{R_*}{10\ \mathrm{km}}\right)^{-1} \mathrm{erg\,s^{-1}} \qquad (1.1) \end{aligned}$$

For a neutron star $M_* \approx 1.5 M_\odot$ and $R_* \approx 10$ km and so clearly only a tiny fraction of the stellar wind is sufficient to generate X-ray luminosities of the order of $L_\mathrm{X} \sim 10^{36}\ \mathrm{erg\,s^{-1}}$, which is fairly typical. Alternatively, accretion may be delayed until the low mass companion evolves to fill its Roche lobe. This is the approximately spherical region around the donor star where the combined gravitational potential of the two stars reaches an (unstable) equilibrium point. Once the Roche lobe is filled accretion can commence in these low-mass binaries (LMXBs) by overflow through the inner Lagrangian point. As with most branches of science, much effort to date has been directed at classifying objects based on one or more system parameters or types of behaviour. These classifications, while not actually contradictory, generate many exceptions and special cases which continue to challenge researchers. Various different types of behaviour can, for example, be found in both HMXBs and LMXBs.

Because of the binary nature of the system the accreting material will possess significant specific angular momentum with respect to the compact object. This momentum must be shed before the accreting gas can finally merge with the star. For Roche lobe accretors the inflowing gas stream circularizes at a radius dependent upon the orbital parameters, and then spreads out in the orbital plane to form an accretion disk. For stellar wind accretors the relative specific angular momentum is probably much lower, but disks are thought to arise in these systems also. The plasma circulates in the disk at approximately Keplerian velocities

$$v_{\mathrm{K}} = \left(\frac{GM_*}{r}\right)^{1/2} \tag{1.2}$$

and gradually spirals in towards the compact object. Angular momentum is transported outwards, and is eventually returned to the system through tidal interactions with the companion. The details of this process are not well understood, and remain one of the more long-standing and fundamental questions in accretion physics. The gas kinematic viscosity is many orders of magnitude too low to operate alone. Nevertheless, a great deal of theoretical work has been done on the physics of accretion disks with the assumption of convenient parametrisations of the disk viscosity (e.g. Shakura and Sunyaev, 1973).

As the accretion flow moves inwards it increasingly comes under the influence of the compact star at its destination. For unmagnetised white dwarves or neutron stars, the disk may extend to the star itself and decelerate in a boundary layer through viscous shearing before being absorbed into the star. General relativistic effects around a black hole prevent stable orbits within a certain radius dependent upon the mass of the central object. Once the disk material reaches this radius, it will cease orbiting and instead fall rapidly inwards through the event horizon. The most interesting case is for strongly magnetized neutron stars. The magnetic field is thought to arise as a by-product of the supernova explosion and subsequent collapse which generated the neutron star, possibly from amplification of an initial 'seed' field. If the field is sufficiently strong it will disrupt the disk flow at the boundary of a region called the magnetosphere, within which the accreting plasma can only flow along the magnetic field lines. Accretion can then only take place on those areas of the neutron star where the field lines make a large angle to the surface, i.e. the magnetic poles.

The gravitational potential energy liberated as the material flows towards the compact object heats it to temperatures of 10^6–$10^{7\circ}$ K. Deceleration onto the star may involve passage through a radiative or collisionless shock, which will further enhance the plasma temperature. Thus the effective blackbody temperature and the bulk of the accretion luminosity L_{acc} fall in the X-ray band. When the material accretes evenly over the surface of the neutron star, the radiation will be more or less isotropic and the X-ray luminosity L_{X} depends only upon $\dot{M}$. On the other hand, if the neutron star has a strong magnetic field accretion may only occur at the polar regions, which will radiate brightly compared to the rest of the neutron star surface. If the magnetic field is misaligned with respect to the rotation axis, these 'hot spots' will cause a periodic modulation of the X-ray emission from the star on the rotation period P_{spin}. These X-ray pulsars are the subject of this thesis.

1.3 X-ray Pulsars

Many neutron star binaries exhibit X-ray modulation on or close to P_{spin}. Sources which exhibit outbursts of varying duration and frequency where the X-ray flux changes by many orders of magnitude are generally classified as 'transients', and may show X-ray pulsations during outbursts (e.g. Negueruela et al., 2000, Santangelo et al., 1999). Type I bursts — with their characteristic fast rise and exponential decay — are observed from weak magnetic field neutron star binaries and result from runaway nuclear burning on the surface of the star (e.g. Swank, 2000). This burning appears to begin at a particular location and spread to the entire star, causing brief periods of atmospheric expansion. The dynamics of the burst are inferred from oscillations with frequency in the range 270–620 Hz observed in a handful of sources (van der Klis, 2000 ; Chakrabarty et al. 2001, in preparation). In some cases the oscillation frequency evolves asymptotically towards what is thought to be the neutron star spin frequency as the burst progresses. These two examples are somewhat distinct from the persistent, high magnetic field neutron star pulsars. Distinguishing between strictly 'transient' and 'persistent' sources is to some extent a matter of opinion. X-ray sources exhibit activity cycles on all sorts of timescales, some of which appear to depend upon system parameters and some of which do not (see e.g. Stella et al., 1986). But the restriction to 'high' field sources relates to more fundamental issues, namely the emission mechanism. If the magnetic field is sufficiently high, thermonuclear bursts are very effectively inhibited, and rather different emission processes dominate. A high magnetic field also seems to inhibit the production of jets and hence radio emission in pulsars. Radio detections coincident with other X-ray binaries are common, but no detections have been made to date for X-ray pulsars (Fender and Hendry, 2000).

1.3.1 The magnetic field-disk interaction

The neutron star magnetic field has important consequences for the accretion flow. The Ghosh and Lamb (1979a,b) model describes the broad-scale implications of their interaction. Far from the star the influence of the field is minimal, and the disk evolves according to the gravity of the central object and the gas dynamics alone. Between this region and the accretion column, the magnetic field must (more or less) completely penetrate the plasma, and it seems likely that this is achieved in stages. In the outermost region currents are generated within the disk to successfully expel the field. Moving radially inwards, the magnetic field will become strong enough to first thread the disk plasma at a radius r_{s}. This threading probably arises as a consequence of magnetic convection or turbulence within the disk; magnetohydrodynamic instabilities may also make a contribution. In this region the ram pressure due to the gas is still much greater than the magnetic pressure, and the flow is in the main unaffected by the field. Instead, the field lines are dragged by the flow, and may develop a significant poloidal component. This effect is moderated by reconnection which is a function of the conductivity of the disk. The stresses imparted to the field lines can be transmitted to the neutron star and give rise to significant 'magnetic torques' in addition to the torque applied directly by the matter accreting onto the stellar surface.

The flow continues inwards in this manner until the point where the magnetic pressure balances the ram pressure of the gas. At this radius (the Alfvén radius) the magnetic field takes over as the dominant influence on the flow. Given the magnetic moment of the star μ (related to the surface field strength B_* by $\mu = B_* R_*^3$), the Alfvén radius $r_{\rm A}$ for isotropic, spherical inflow at $\dot{M} = \dot{M}_{16} \times 10^{16}\ g\,s^{-1}$ can be estimated as

$$\begin{aligned} r_{\rm A} &\approx 2^{-3/7}\mu^{4/7}(GM_*)^{-1/7}\dot{M}^{-2/7} \\ &= 4.85 \times 10^8 B_{12}^{4/7}\dot{M}_{16}^{-2/7}\ {\rm cm} \end{aligned} \tag{1.3}$$

where $B_{12} = B_*/(10^{12}\ {\rm G})$. With the flow confined to a thin disk in the orbital plane, the ram pressure will clearly be greater (and hence $r_{\rm A}$ smaller) than for spherical inflow for the same $\dot{M}$. However, because the magnetic field pressure increases so rapidly as r decreases ($\propto B^2 \propto 1/r^6$) the discrepancy is probably small. Most authors generally adopt $r_{\rm A,disk} \approx 0.5 r_{\rm A}$.

The Ghosh and Lamb (1979a,b) model predicts a correlation between torque and $\dot{M}$ (inferred from $L_{\rm X}$) for accretion-driven X-ray sources. This correlation arises from the varying contributions of spin-up and spin-down torques as a function of the inner disk radius. At the corotation radius $r_{\rm co}$ the angular velocity corresponding to Keplerian orbits in the disk matches that of the neutron star. Disk material orbiting at $r_{\rm co}$ will thus contribute zero torque through the magnetic field to the neutron star; since the Keplerian velocity is higher closer to the star material within $r_{\rm co}$ will contribute a spin-up torque. This is balanced by spin-down torques contributed by material orbiting from $r_{\rm co}$ outwards to the where the last stellar field line threads the disk. Clearly as $\dot{M}$ increases, $r_{\rm A,disk}$ will decrease (equation 1.3) which will result in a greater range of disk radii contributing to spin-up torques. Conversely as $\dot{M}$ decreases, $r_{\rm A,disk}$ increases and the net spin-up contribution will decrease, possibly to the point where it is exceeded by the spin-down torque. Thus depending upon $\dot{M}$, X-ray pulsars can experience both net spin-up and spin-down, which is confirmed by long-term observations of accreting pulsars (Bildsten et al., 1997). In the extreme low-$\dot{M}$ case when $r_{\rm A,disk} > r_{\rm co}$ accretion may cease altogether since the disk material is centrifugally inhibited from entering the magnetosphere. For most sources it is difficult to test the relationship between $\dot{M}$ ($L_{\rm X}$) and the torque since the range of luminosities at which they are observed is small. However the correlation has been confirmed, at least approximately, for three transient sources using BATSE and *EXOSAT* data; EXO 2030+375 (Reynolds et al., 1996), A 0535+262 and GRO J1744-28 (Bildsten et al., 1997).

The situation for persistent pulsars is, however, less straightforward. The BATSE data have demonstrated that in general the torque is in fact *uncorrelated* with luminosity in these sources. The spin-up or spin-down rate can remain almost constant over intervals (referred to in this thesis as a 'constant torque state' or just 'torque state') which are long compared to other characteristic time-scales of the system, even when the luminosity varies by several orders of magnitude over that time. Transitions between these states of constant torque can be abrupt, with time-scales of < 1 d when the two torque values have the same sign; alternatively when switching from spin-up to spin-down (or vice-versa) the switch generally occurs smoothly over a period of 10–50 d. One recent suggestion is that the observed behaviour may be related to precession of the neutron star rotation axis as a consequence of accretion column torques (Jetzer et al., 1998). Despite the observational discrepancies, the Ghosh and Lamb (1979a,b) model is widely accepted and remains the basis for many studies of accreting sources.

1.3.2 The boundary region and accretion column

The boundary region in X-ray pulsars refers to that part of the accretion disk where the magnetic pressure initially dominates the flow. The plasma decelerates abruptly from Keplerian velocity to corotation with the neutron star magnetosphere, and enters the accretion column where it flows along the magnetic field lines to the neutron star poles (Figure 1.1). The deceleration region is thought to be relatively narrow radially, since the magnetic pressure increases so rapidly with decreasing distance to the star.

Much of what is known (or inferred) about accretion flow comes from observational studies of white dwarves, particularly polars and intermediate polars (Warner, 1995). In these sources the accretion column and polar cap radiate in the optical band. Polarimetry and spectroscopy resolved on the orbital period $P_{\rm orb}$ has provided a wealth of information about these regions. There is little doubt that these results can be equally well applied to neutron star binaries, taking into account the parametric differences between the two systems. In general the neutron star's magnetic field will be misaligned with the rotational axis (by the magnetic colatitude β). The accretion region on the surface of intermediate polars (which also accrete via a disk) have been shown to be narrow arcs through optical polarimetry. Projecting the field lines with footpoints within the accretion region back to the accretion disk traces out an arc-shaped region on the inner edge. Similarly, for neutron stars the boundary region is unlikely to cover the full azimuthal extent of the inner disk. Instead, it is thought to form an arc-shaped region over which the plasma deceleration and uptake to the accretion column occurs (see Chapter 5).

The detailed dynamics of this region are essentially a mystery. The confluence of highly sheared plasma flow with magnetic fields which vary in strength over the interaction region presents an astrophysical problem of nightmarish complexity. Unfortunately, this situation seems likely to persist indefinitely. Observations do not offer any real clues as to the detailed dynamics within this region, although pulse-phase spectroscopy using the recently launched *Chandra* (Weisskopf, 1999) or *XMM* (Jansen and Laine, 1998) observatories seems a promising approach. Analytically the situation is presently too complex for a solution. Numerical models are generally too coarse to provide any real predictive capability. Fortunately, this does not hinder

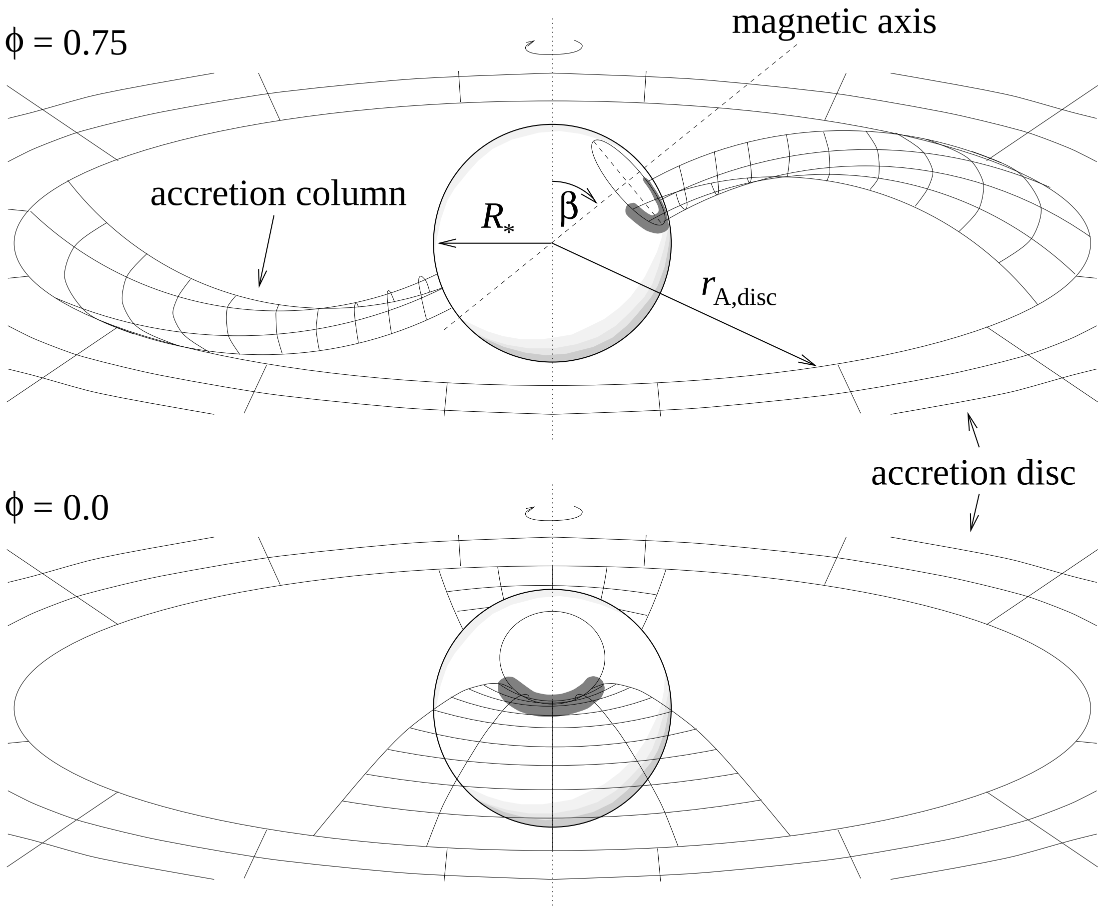

Figure 1.1 Schematic showing the accretion geometry of X-ray pulsars (not to scale) at two representative rotational phases. The accreting gas from the companion is thought to form an accretion disc far from the neutron star, which is disrupted at $r_{\mathrm{A,disc}}$ due to the strong (dipolar) magnetic field. Within this radius the accreting matter may only flow along the magnetic field lines, forming two accretion columns terminating at the magnetic poles. Thermal X-ray emission originates from the shaded region at each pole and may interact with the accretion column plasma above it. The magnetic axis is misaligned relative to the neutron star rotation axis by β (the magnetic colatitude).

the study of accreting sources overmuch. The accreting plasma is clearly able to enter the accretion column, and although the small-scale processes are not understood this does not prevent study of other aspects of these phenomena.

1.3.3 The emission region

A full understanding of the processes which shape spectra and pulse profiles in X-ray pulsars has been hampered to date by the extreme complexity of the problem. This complexity manifests both in the observational and theoretical approaches. Observed spectra generally feature a pseudo-thermal component (which in some cases is consistent with a blackbody) and a power law high-energy tail modified by an exponential cutoff around 20 keV. Such spectra cannot in general be fit with any single temperature model, and vary significantly as a function of time, source state and pulse phase. The geometry of the emission region is thought to depend on the accretion rate, magnetic field configuration at the neutron star surface and the detailed structure of the plasma entrainment region at the magnetospheric boundary. Mean pulse profiles vary dramatically between different sources, and also within the same source as a function of energy and time (see e.g. White et al., 1983, Bildsten et al., 1997).

It is important to distinguish between the processes operating in the emission region which conserve photon number and those that do not. Processes which fall into the latter category are responsible for producing the photons in the first place, while those in the former simply modify the initial distribution (perhaps drastically) to give the observed spectrum. Most studies in the literature fail to explicitly acknowledge this distinction, and complete understanding of the situation has suffered. In particular the origin of the initial photon distribution is uncertain. Some authors (e.g. Mészáros and Nagel, 1985a,b, Burnard et al., 1991) assume that the source photons orignate from electron-electron or electron-proton bremsstrahlung, while others suggest that these processes will be unimportant given the strong magnetic fields within the emission region (Kirk, 1986). In the absence of accreting material the spectra of neutron stars resemble a simple blackbody, although the apparent temperature is affected by the atmospheric structure (e.g. Rutledge et al., 1999). The magnetic field may play a critical role. Motion of the plasma perpendicular to the field lines is quantised into Landau energy levels, and due to very rapid rates of spontaneous de-excitation the great majority of electrons will be in the ground Landau state. A variety of resonant and nonresonant processes are possible which involve transitions through excited Landau states. In fact, spectral features resulting from these transitions are common in X-ray pulsars and are the best evidence for $\approx 10^{12}$ G surface magnetic field strengths. Most commonly a cyclotron scattering resonance feature (CSRF) is seen as a broad dip in the spectrum at an energy corrosponding to the cyclotron energy

$$\nu_{\rm cyc} \quad = \quad \frac{eB_*}{2\pi m_{\rm e} c}\ {\rm Hz} \qquad \text{or}$$

$$E_{\rm cyc} \approx 11.6 B_{12} \text{ keV} \tag{1.4}$$

and possibly its harmonics ($2E_{\rm cyc}$, $3E_{\rm cyc}$; e.g. Heindl et al., 2000). In particular, two-photon emission (resonant double Compton scattering) may be a significant source of soft photon generation (Kirk, 1986). This process involves an electron absorbing a photon with $E_\gamma \gtrsim E_{\rm cyc}$ which excites it to the first Landau level. De-excitation is rapid, but produces instead two photons which share the energy of the initial photon. The process favours a final energy distribution with one photon having $E_{\gamma 1} \approx E_{\rm cyc}$ as before and the other with $E_{\gamma 2} \ll E_{\rm cyc}$.

Once the source photons are generated, they may interact with the material surrounding the neutron star before escaping towards the observer. The accretion column plasma reaches the highest density immediately above the polar cap, and is generally fully ionised and at temperatures > 1 keV. Thus Compton scattering (e.g. Pozdnyakov et al., 1983) in the accretion column is likely to be the dominant process affecting the initial photon spectrum. This is equivalent to Thompson (electron) scattering generalised for cases where the scattering medium is not necessarily cool, and in fact may be so hot as to require relativistic corrections to the scattering cross section. The strong magnetic field of the neutron star further modifies the cross section (e.g. Daugherty and Harding, 1986), resulting in strongly anisotropic scattering which depends on the angle between the photon propagation direction and the local magnetic field vector. Hybrid processes involving transitions to excited Landau levels also become possible (as described above).

The power law tail generally observed in pulsar spectra is characteristic of Compton scattering where the source spectrum temperature T_0 is significantly *lower* than the scattering medium $T_{\rm e}$ (inverse Compton scattering or Comptonization). Photons with $E = h\nu$ interacting with hotter electrons will tend to gain energy at a rate of

$$(\Delta h\nu)_{\rm NR} \approx 4kT_{\rm e}\frac{h\nu}{m_{\rm e}c^2} \tag{1.5}$$

$$(\Delta h\nu)_{\rm R} \approx \frac{4}{3}\gamma^2 h\nu \tag{1.6}$$

(Rybicki and Lightman, 1979) per scatter. The subscripts 'NR' and 'R' refer to the nonrelativistic and relativistic regimes; the latter is appropriate when $kT_{\rm e} \gtrsim m_{\rm e}c^2$. The net effect of the scattering on the initial photon distribution is quantified by the Compton y-parameter, given by

$$y_{\rm NR} = 4\frac{kT_{\rm e}}{m_{\rm e}c^2}\,{\rm Max}(\tau,\tau^2) \tag{1.7}$$

$$y_{\rm R} = 16\left(\frac{kT_{\rm e}}{m_{\rm e}c^2}\right)^2 {\rm Max}(\tau,\tau^2) \tag{1.8}$$

where $\tau = \sigma_{\rm T} N_{\rm e} R$ is the characteristic optical depth of the scattering volume, and R, $N_{\rm e}$ are its radius and electron number density respectively. The y-parameter is effectively a product of the average photon energy increase per scattering and the mean number of scatters, and hence can be considered as a rough measure of the plasma cooling rate via Compton scattering. If $y \ll 1$ Comptonization will have little effect on the incident spectrum, whereas if $y \gg 1$ it will be modified significantly. Determining the resultant spectrum analytically involves solving the Kompaneets (1957) equation, which is impossible except for the simplest geometries. The analytical approximation of Titarchuk (1994) is applicable to a wide range of astrophysical sources. The form adopted for the shape the input spectum is a Wien law, which simplifies the required calculations considerably. For a finite, homogeneous cloud the effective τ for scattering depends on the cloud density but also on the distribution of photon escape times. The latter is a function of the geometry of the emitting region and the surrounding cloud, and approximations are derived relating the escape time distribution to τ for spherical and planar (disk) geometries separately. This formulation has been shown to be consistent with Monte-Carlo simulations over a wide range of input parameters (Hua and Titarchuk, 1995).

Detailed models of X-ray pulsar emission regions are generally limited to a particular accretion regime. For low accretion rates, radiation pressure will be negligible and the plasma will decelerate through Coulomb collisions or possibly a collisionless shock. Above some critical accretion rate, a radiative shock will form above the surface where the infalling plasma thermalises and then slowly settles to the surface. Within these regimes, a number of approaches have been used. Finite difference methods are generally applied by adopting a simplified, symmetric emission geometry ('slab', 'mound' or 'column') and solving the radiative transfer equations, possibly also taking into account the dynamical conditions above the shock (e.g. Mészáros and Nagel, 1985a,b, Burnard et al., 1991). Alternatively a particular 'beam pattern' (the variation of X-ray flux with viewing angle relative to the neutron star pole) can be adopted and the effect of various system geometries explored. With this approach it is possible to include the effects of gravitational light bending, which should be an important effect in the formation of pulsar profiles. Detailed fits utilising a misaligned, off-center magnetic axis have been performed by Leahy (1991).

Essentially all the approaches which have been used have serious limitations. The detailed radiative transfer calculations are necessarily restricted to rather simple geometries, where in reality the accretion column is thought to possibly form a hollow column or incomplete hollow column ('accretion curtain'; Basko and Sunyaev, 1975). The geometric fitting approach when applied to a range of pulsars require off-center magnetic axes to reproduce the observed asymmetry in pulse profiles, and in addition cannot reproduce sharper features observed in several sources. Monte-Carlo simulations (Pozdnyakov et al., 1983) offer a powerful technique to study emission in compact astrophysical sources. It is possible to include a diverse range of effects, including frame dragging and Doppler boosting in millisecond pulsars (Braje et al., 2000), gravitational light bending and inhomogeneous and arbitrarily complex scattering regions (see Chapter 7).

1.4 GX 1+4

At the time of its discovery (Lewin et al., 1971) GX 1+4 was one of the brightest objects in the X-ray sky. The optical counterpart is an M6 giant (Davidsen et al., 1977) which is readily classified as a symbiotic binary (Belczyński et al., 2000). Unusually this LMXB appears to be accreting from the companions stellar wind, which infrared observations suggest is at least an order of magnitude faster than typical red giant winds (Chakrabarty et al., 1998) and which presumably also gives rise to the optical emission line nebula. Optical spectroscopy suggests a source distance of 3–15 kpc (Chakrabarty and Roche, 1997).

Measurements of the average spin-up rate during the 1970s gave the largest value recorded for any pulsar (or in fact any astronomical object) at ≈ 2 per cent per year. Inexplicably, the average spin-up trend reversed around 1983, switching to spin-down at approximately the same rate. Since that reversal a number of changes in the sign of the torque (as inferred from the rate of change of the pulsar spin period) have been observed (Chakrabarty et al., 1997). In contrast to predictions of the Ghosh and Lamb (1979a,b) model BATSE measurements suggest that the torque measured for GX 1+4 is sometimes *anticorrelated* with luminosity (Chakrabarty et al., 1997). This behaviour has not been observed in other pulsars. The orbital period is not known, but secular torque variations suggest $P_{\rm orb} \approx 304$ d (Cutler et al., 1986, Pereira et al., 1999). Several estimates (Beurle et al., 1984, Dotani et al., 1989, Mony et al., 1991, Greenhill et al., 1993, Cui, 1997) indicate a neutron star surface magnetic field strength of 2–3×10^{13} G.

The X-ray flux from the source is extremely variable on time-scales of seconds to decades. Two principal flux states have been suggested, a 'high' state which persisted during the spin-up interval of the 1970s, and a 'low' state since. Although the mean flux has been increasing steadily during the current 'low' state it has not yet returned to the level of the 1970s. Superimposed on the long-term flux variations are smooth changes on time-scales of order hours to days. On the shortest time-scales the periodic variation due to the neutron star's rotation period at around 2 min is observed. Pulse profiles from the source exhibit a bewildering variety (see Chapter 4). Profiles are typically asymmetric, often with a sharp dip forming the primary minimum (Dotani et al., 1989, Greenhill et al., 1998, Kotani et al., 1999). During a low flux episode in July 1996, the pulse profiles were found to shift dramatically in the sense of asymmetry over an observation lasting just 34 hours made 10 days before a short-lived transition from rather constant spin-down to spin-up and back again (Giles et al., 2000, Galloway et al., 2000).

Compared to other accretion-powered X-ray pulsars, the phase-averaged spectrum of GX 1+4 is atypically hard (based on thermal bremsstrahlung fits at high energies; Frontera and Dalfiume, 1989). Historically the spectrum has been fitted with bremsstrahlung or power law models, however more recent observations with improved spectral resolution generally favour a power law model with exponential cutoff. Typical values for the cutoff power law model parameters are photon index $\alpha = 1.1-2.5$; cutoff energy $5-18$ keV; e-folding energy $11-26$ keV. For any spectral model covering the range 1-10 keV, it is also necessary to include a Gaussian component representing iron line emission at ≈ 6.4 keV, and a term to account for the effects of photoelectric absorption by cold gas along the line of sight with hydrogen column density in the range $n_H = (4 - 140) \times 10^{22}$ cm^{-2}. The source spectrum and in particular the column density n_H have previously exhibited significant variability on time-scales as short as a day (Becker et al., 1976). Measurements of spectral variation with phase are few; one example of pulse-phase spectroscopy was undertaken with data from the *Ginga* satellite from 1987 and 1988 (Dotani et al., 1989). Only the column density and the iron line centre energy were allowed to vary with phase in the spectral fits, and no significant variation was observed. Recent analysis of data obtained by the Rossi X-ray Timing Explorer undertaken as part of this thesis suggests that the spectrum is consistent with unsaturated Comptonization and that accretion column eclipses may be responsible for the sharp dips observed in the pulse profiles (Galloway et al., 2000 and Chapters 3, 5).

1.5 RX J0812.4-3114

The X-ray counterpart to the B0-1 III-IV star LS 992 was identified from cross-correlation of *ROSAT* galactic plane survey data with SIMBAD OB star catalogues (Motch et al., 1997). Pulsations in Be/X-ray binaries, as these systems are referred to, are common and they make up a significant subpopulation of the HMXBs. The optical companions are massive stars, which are thought to rotate so rapidly that the equatorial matter is expelled in a slow, dense wind — an 'excretion disk' (Negueruela, 1998). This equatorial wind provides the accreting material to the neutron star.

ROSAT observations revealed significant variability of the source over a timescale of hours, with flux variations on longer timescales of a factor ~ 100. Hourly flux variations, as well as X-ray pulsations at $P \approx 31.9$ s were discovered during an *RXTE* observation of the source in February 1998 (Reig and Roche, 1999). The X-ray behaviour of Be/X-ray binaries is strongly dependent upon the orbital parameters, and in fact the neutron star spin periods $P_{\rm spin}$ show a strong correlation with the orbital period $P_{\rm orb}$ (Corbet, 1986). The ≈ 81 d periodicity suggested by *RXTE* All-Sky Monitor (ASM) data obtained between 1998–99 (Corbet and Peele, 2000) is consistent with this correlation and probably represents the binary period. The distance estimated at 9 kpc based on the companion spectral type and interstellar reddening, with a likely uncertainty of 50% (Motch et al., 1997).

The pulse profile from the source is strongly asymmetric, with a sharp dip forming the primary minimum. As with GX 1+4, the profile dip has been suggested to arise from eclipses by the accretion column. The energy spectrum was fairly typical for X-ray pulsars, and could be adequately fit using a power law model with exponential cutoff. I explore the mean spectrum and origin of the dip further in Chapter 6.

Chapter 2

Methodology

2.1 X-ray observations: *RXTE*

In this section I describe analysis techniques for data from the Rossi X-ray Timing Explorer satellite (*RXTE*; Giles et al. 1995). These data were obtained both as a result of an observation proposal during the first announcement of opportunity (AO-1) for the satellite (GX 1+4, proposal ID 10103, July 1996) and from the High Energy Astrophysics Science Archive Research Centre (HEASARC) WWW site at `http://heasarc.gsfc.nasa.gov`.

RXTE consists of three instruments, the proportional counter array (PCA) sensitive to photons in the energy range 2–60 keV, the high-energy X-ray timing experiment (HEXTE) covering 16–250 keV, and the all-sky monitor (ASM) which spans 2–10 keV. The PCA consists of five identical (at launch) proportional counter units (PCUs), designated $0 \ldots 4$. Pointed observations are performed using the PCA and HEXTE instruments, while the ASM regularly scans the entire visible sky. During targeted observations, interruptions may be made for previously scheduled monitoring or target-of-opportunity (TOO) observations of other sources.

Six of the eight event analysers (EAs) aboard *RXTE* are available for processing of events measured by the PCA. Two EAs are dedicated to modes which are always present, 'Standard-1' and 'Standard-2'. The Standard-1 mode features 0.25 μs time resolution but only one spectral channel, while Standard-2 offers 128 spectral channels between 0–100 keV (the sensitivity above 60 keV is negligible) with binning on 16 s time resolution. The remaining four EAs may be used in a range of user-configurable modes, which are in general only necessary to obtain spectra on a finer time resolution. Because the data analysed in this thesis originate from proposals with a wide range of science objectives, the user-configurable modes also vary widely between observations. GoodXenon mode data were used for the pulse phase spectroscopy described in Chapter 5. This mode offers full 256-channel spectral resolution on $\approx 1\,\mu$s time resolution.

2.1.1 Screening and background subtraction

Analysis of *RXTE* data presented in this thesis was carried out using LHEASOFT version 5.0, released 23 February 2000 by the *RXTE* Guest Observer Facility (GOF). The data were first screened to ensure that the pointing offset was $< 0.02^\circ$ and the source was $> 10^\circ$ from the sun. This introduced additional gaps to the data. From mid-1996 onwards two of the five PCUs were regularly turned off to partially arrest a gradual sensitivity degradation measured by the *RXTE* team. Any given observation may thus be made with 3, 4 or 5 PCUs on, or a combination. If PCUs are switched off or on during the observation it is necessary to extract data from each interval with a constant number of PCU's on and analyse them separately.

The instrumental background count rate from cosmic rays and additional particle flux arising during satellite passages through the SAA are estimated using the PCABACKEST software which is included in the HEASOFT package. The background models used are from the 23 February 2000 release. Where the net source count rate is $\lesssim 60\,\mathrm{count\,s^{-1}}$ the 'faint' source models have been used, with the 'bright' models used otherwise. Due to the proximity of GX 1+4 to the galactic plane, an additional background component corresponding to diffuse 'galactic ridge' emission must be subtracted. For the purposes of spectral fitting, this component is modelled using a Raymond-Smith emission spectrum from hot, diffuse gas and a power law, both absorbed by a neutral column density of $n_{\rm H} = 2 \times 10^{21}\,\mathrm{cm^{-2}}$ (Table 2.1). Two additional power law components serve as a correction to the diffuse X-ray background assumed by PCABACKEST. The model is identical to that fitted to survey data from this region (Valinia and Marshall, 1998) with normalisations and metal abundance as fitted to spectra taken during slews to and from the source in July 1996 (observation H in Table 3.1). A constant background level of $6.95\,\mathrm{count\,s^{-1}}$ is subtracted from the full-range lightcurves to account for this additional background component; for the lightcurves in energy ranges 2–7, 7–20 and 20–60 keV the level is 4.31, 1.34 and $0.788\,\mathrm{count\,s^{-1}}$ respectively.

2.1.2 Spectral analysis

Candidate spectral models were tested by fitting to the count rate spectrum to minimise χ^2 using the XSPEC spectral fitting package version 11 (Arnaud, 1996). The goodness of fit is expressed by the reduced χ^2

$$\chi^2_\nu = \chi^2/\nu \tag{2.1}$$

where ν is the number of degrees of freedom, i.e the number of spectral channels in the fit minus the number of parameters in the model. A statistically acceptable fit is indicated by $\chi^2_\nu \approx 1$. Systematic errors, where present, will obviously affect the fit statistic. For *RXTE* observations of bright calibration sources such as the Crab nebula it is generally necessary to assume a systematic error of 1% in order to obtain statistically acceptable fits using the canonical power law spectral model. However, for fainter sources acceptable fits can often be obtained without assuming any systematic error; in some cases the adoption of a 1% systematic errors results in unrealistically small values of χ^2_ν. Thus for consistency no systematic error was assumed in the spectral fits undertaken in this thesis.

Each model takes the form of one (or more) continuum components and a multiplicative component to account for absorption by cold matter along the line of sight. Depending upon the source, it may be necessary to include a Gaussian component with energy 6.4–6.7 keV to account for fluorescent iron line emission, commonly detected in X-ray pulsars (e.g. Nagase, 1991).

Once the set of p parameter values giving the minimum $\chi^2_{\rm min}$ for a given model have been located, it is necessary to determine to what precision each parameter is known at some confidence level. A rigorous treatment of confidence intervals for a multiparameter model would require that we determine the p-dimensional hypersurface corresponding to the locus of parameter values for which $\chi^2 = \chi^2_{\rm min} + \Delta\chi^2$, with the value of $\Delta\chi^2$ dictated by the required confidence level and the number

Table 2.1 Spectral parameters used for the galactic ridge component in fits to GX 1+4 spectra using XSPEC. The component is modelled using a Raymond-Smith plasma and power law, both affected by absorbtion by neutral hydrogen in the plane of the galaxy. The component also includes a correction to account for additional absorbtion of the diffuse background spectrum assumed by PCABACKEST. The model can be expressed as `wabs(raymond+powerlaw`^{1}`+powerlaw`^{2}`)+powerlaw`^{3}, with the parameter values for each component given below. Confidence intervals, where shown, are 1σ. The Abundance describes metal abundances including C, N, O, Ne, Mg, Si, S, Ar, Ca, Fe, and Ni with He fixed at the cosmic level. The units for the Raymond-Smith component normalisation A_{raymond} are $10^{-14}/(4\pi/D^2)\int n_e n_H \mathrm{d}V$ where D is the distance to the source in cm and n_e and n_H are the electron and hydrogen densities respectively (cm^{-3}).

Parameter	Value
n_H ($\times 10^{22}\,\mathrm{cm}^{-2}$)	0.2
kT (keV)	3.4
Abundance	$0.140_{0.032}^{0.253}$
z	0.0
A_{raymond}	$(1.83_{1.67}^{1.99}) \times 10^{-2}$
α_1	1.7
A_1 (photons $\mathrm{cm}^{-2}\,\mathrm{s}^{-1}\,\mathrm{keV}^{-1}$)	$(2.43_{2.21}^{2.64}) \times 10^{-3}$
α_2, α_3	1.472
A_2 (photons $\mathrm{cm}^{-2}\,\mathrm{s}^{-1}\,\mathrm{keV}^{-1}$)	3.5977×10^{-3}
A_3	$-A_2$
χ^2_ν	0.72

of degrees of freedom (= the total number of parameters p; Lampton et al., 1976). (Note that this is distinct from the number of degrees of freedom when considering the model fit itself!) Clearly for $p > 2$ this becomes unfeasible. The usual method is to fix each parameter in turn at various trial values within a range around its best fit value, and then fit the remaining parameters to determine the maximal range of values for which $\chi^2 < \chi^2_{\mathrm{min}} + \Delta\chi^2$ for some value of $\Delta\chi^2$. This is achieved in XSPEC automatically using the `error` command. This approach will give the *projection* of the confidence hypersurface onto the axis corresponding to each parameter. In that case the confidence level achieved for a particular value of $\Delta\chi^2$ is calculated for only one degree of freedom. Thus for the parameter confidence limits calculated in this thesis I adopt $\Delta\chi^2 = 1.0$, appropriate for the 1σ confidence level for 1 degree of freedom. Note that such error limits may be of limited value particularly when two or more parameters are strongly correlated, such as the τ and T_e parameters for the `compTT` component used extensively throughout this thesis. For comparisons between fits based on correlated parameters it is much more valuable to consider the joint confidence interval of the two parameters, in which case the number of degrees of freedom is 2 and $\Delta\chi^2$ values should be chosen appropriately.

The number of spectral channels and the energy range for fitting typically varies between observations. Both the GX 1+4 and RX J0812.4−3114 observations span more than one PCA gain epoch, and the channel-to-energy conversion varies as a result. The maximal sensitivity of the PCA is between 2.2–40 keV, but for individual fits the range may be restricted further due to a number of factors. The background above 30 keV from the most recent 'bright' source models appears to be underestimated at low count rates, resulting in a hard excess at these energies. Spectral variation below 5 keV tends to result in significant residuals (particularly for GX 1+4) which cannot be accounted for by additional model components. Given the low sensitivity at these energies the reality of such variation is somewhat questionable. In general the channels at the extrema of the energy range can be excluded without significantly affecting the fit parameters. Note however that comparisons between different models for individual spectra are made over the same channel range for consistency.

To date, X-ray pulsar spectra have been typically modelled using power law, power law and blackbody, or modified power law components. In general each of these types of models is an approximation to a spectrum originating from a low-energy distribution of photons Comptonized by scattering within a hotter plasma. More detailed approximations to Comptonized spectra are an obvious choice for candidate models; I chose the Titarchuk (1994) formulation, implemented in XSPEC as '`compTT`'. The model parameters include the input spectrum temperature T_0 (approximated as a Wien law), the scattering plasma temperature T_e and normalisation A_C (in units of photons $\mathrm{cm^{-2}\,s^{-1}\,keV^{-1}}$). Additionally the redshift can be specified, fixed at 0.0 in the fits described here. The effective optical depth τ is determined from the spectrum assuming either a spherical or planar (disk) geometry. If the accretion column is, as I suggest, the primary region where Compton scattering takes place to shape the spectrum clearly neither of these assumptions are strictly appropriate. For the `compTT` model fits presented in this thesis I adopt the 'disk' geometry switch, noting that the calculated τ will thus be only an approximate measure of the true optical depth in the column. In fact for the disk geometry the fitted τ is the half-width optical depth of the slab, and thus the calculated τ for an assumed spherical geometry will be approximately twice as large. For comparisons between different spectra the absolute value of τ is not important.

2.1.3 Timing analysis

Pulsar timing was not the main focus of this thesis. Determination of pulsar periods was, however, necessary for generating pulse profiles (Chapter 4) and extracting spectra for pulse phase spectroscopy (Chapter 5). Pulse period determinations from the *RXTE* data were made in two ways.

Background-subtracted, barycentre corrected lightcurves on 1 s bins (extracted from Standard-1 data) were folded on a range of trial periods and a Gaussian fit applied to the χ^2-P curve. The vagaries of this technique are reasonably well known (e.g. Babu and Feigelson, 1996 page 162), however the calculation of pulse profiles and phase extraction from short-duration data does not require extremely accurate periods and period estimates using this method were found to be sufficient for these purposes. The error was estimated as the standard deviation of the period determined in the same manner from 100 simulated timeseries. Each simulated lightcurve was constructed with the mean pulse profile and count rate determined from the original lightcurve and a randomly determined error component appropriate for the count rate (including background) added to each bin.

The second method involved calculating the arrival times of the sharp primary minima. Due to the high count rate in most observations individual dips were prominent in lightcurves from GX 1+4 with sufficient time resolution; this method could not be used for RX J0812.4−3114. An initial period estimate P was chosen and the arrival time of each successive minimum $t_{\rm d} = t_0 + nP$ was calculated given the approximate time of the first minimum in the lightcurve t_0. The actual arrival time was estimated by fitting a parabolic profile to the lightcurve in a window surrounding the predicted arrival time

$$F(t_i) = w_{\rm q} \Delta t_i^2 + F_0 \qquad i \in \{1 \ldots 16\} \tag{2.2}$$

where $\Delta t_i = t_i - t_{\rm d}$ is the bin time offset from the fitted arrival time of the dip $t_{\rm d}$ and t_i, $F(t_i)$ are the times and count rates from the lightcurve. The period is then adjusted to minimize any net trend in the residuals between the predicted and estimated minima times. Results using this method are discussed in Chapter 5.

To evaluate the accuracy of these two methods the results were compared with interpolated periods from archival BATSE pulse timing data (see section 2.2), where available. The results of this comparison are presented in Chapter 4.

2.1.4 Pulse-phase spectroscopy

The 16 s time bin of Standard-2 data limits the temporal resolution for analysis of spectral variations. Where additional user-defined modes are present spectral extraction on much finer resolution is possible. The standard extraction tools, given the pulse period and an appropriate ephemeris, allow spectra to be extracted from GoodXenon data (for example) relative to pulse phase. The process becomes somewhat complicated because the extraction tools apply screening criteria based on times measured on the satellite, whereas the pulse period is generally determined from the data corrected to the solar system barycentre. Because of this it may be necessary to also calculate the pulse period as measured on the satellite and use this value for the phase selection. Additionally, the extraction tools cannot calculate the correct exposure for spectra which combine phase extraction and gaps due to screening criteria. To overcome these limitations I developed a perl script which located each interval of uninterrupted data within the observation, extracted required phase selected spectra from each interval, and finally combined all the spectra for the same phase range over all the intervals. The script determines the appropriate exposure and applies it to the resulting output file.

2.2 X-ray observations: BATSE/*CGRO*

The Burst and Transient Source Experiment (BATSE) consisted of eight identical detectors mounted on the corners of the Compton Gamma Ray Observatory (*CGRO*) satellite, launched by the space shuttle *Atlantis* in April 1991. Each unit held two scintillation detectors sensitive to photons in the energy range 20 keV to 1.8 MeV, and in concert were used primarily as an all-sky monitor for gamma ray bursts (Zhang et al., 1995). Sadly, the still-functioning *CGRO* satellite was commanded to undertake a re-entry and breakup in the atmosphere on 4 June 2000, bringing to an end an extremely successful mission which lasted 4 yr beyond its expected duration.

BATSE was also used in a program of regular monitoring of a number of persistent X-ray pulsars, including GX 1+4 (Bildsten et al., 1997). The standard timing analysis calculated pulse periods from data in the 20–60 keV energy range on 1.024 s time resolution. Typically pulse profiles were determined from 300–5000 s observations, and then the pulse period calculated from several observations over one or more days. The pulsed source flux was estimated assuming a spectral model of the form $\mathrm{d}N/\mathrm{d}E = (A/E)\exp(-E/kT)$, where the temperature T is held constant for each source. Public data now available (from the BATSE WWW site at `http://www.batse.msfc.nasa.gov/batse/pulsar/`) includes long-term timeseries with pulsed flux, spin frequency and rate of change, and coefficients and errors from low-order Fourier decompositions of mean pulse profiles. It is a straightforward matter to re-create the observed pulse profiles from the Fourier coefficients. The coefficients are $f_{i,j}$ where $i = 1, 2$, $j \in \{1 \ldots 6\}$. The flux at phase ϕ can then be calculated using

$$F(\phi) = \sum_{j=1}^{6} f_{1,j} \cos(2\pi j\phi) + f_{2,j} \sin(2\pi j\phi) \qquad (2.3)$$

and a profile can be generated by selecting a set of phases $\phi_k = k/n$, $k \in \{0 \ldots n-1\}$ and calculating $F(\phi_k)$ for each ϕ_k. The error on each bin can be calculated in terms of the errors on the coefficients $f_{i,j}$, which is also straightforward although tedious. The resulting pulse period and profile histories are unprecedented in terms of total duration and frequency.

2.3 Monte-Carlo simulation of pulsar emission

A Monte-Carlo code '`column5`' (version 3.3) was used to generate spectra and pulse profiles originating from a neutron star of radius $R_* = 10$ km with diametrically opposed, cylindrical accretion columns of radius R_C. The columns are centred on the magnetic axis of the star, which is misaligned with the rotational axis by an angle β. The aspect of the star with respect to the observer is characterised by the angle between the rotation axis and the line-of-sight i (Figure 2.1). Blackbody photons with temperature T_0 are emitted isotropically from each polar cap (the base of the accretion columns) and are then Compton scattered by electrons in the column (temperature T_e) before escaping towards the observer. The calculation neglects higher-order effects such as resonant scattering around ν_{cyc}, the cyclotron resonant frequency (equation 1.4). Deviation of photon trajectories due to gravitational effects is treated by numerical integration assuming a Schwarzchild metric (Riffert and Meszaros, 1988). The column plasma density can be set independently for two halves divided by the plane defined by the rotational and magnetic axes; within each zone the plasma is homogeneous. For a particular choice of i and β, only a small fraction of the photons emitted by the accretion column will actually reach the observer. The same set of photons can however be used to generate spectra and pulse profiles for multiple geometries. In the simulation this is implemented by checking if each photon is observed at any rotation phase for each choice of i and β considered. In a similar manner, only one accretion column is actually simulated but the photons which are emitted are translated appropriately to determine the contribution from both the 'north' and 'south' accretion columns.

The use of the unmagnetized cross section for Compton scattering limits application of the simulation results. Cyclotron absorbtion introduces additional features into continuum X-ray spectra (e.g. Santangelo et al., 1999, Heindl et al., 2000), and thus it is only possible to consider situations where ν_{cyc} and its low-order harmonics fall outside the energy band of interest. As the local magnetic field strength B approaches zero, the magnetic Compton scattering cross section approaches the nonmagnetic cross section. The simulation results are therefore directly applicable to situations where the cyclotron energy ν_{cyc} is much lower than the energy band of interest. If however ν_{cyc} is *higher* than the energy band the magnetic cross section increases with photon energy and also exhibits a strong dependence on the angle between the photon direction and the magnetic field vector (Daugherty and Harding, 1986). Magnetic effects on the mean spectrum, even neglecting cyclotron absorbtion, will thus be significant. The resulting spectrum may still be *consistent* with unmagnetised Comptonization spectra, but the calculated optical depth will be a biased measure of the actual scattering conditions in the accretion column.

The choice of cyclindrical geometry for the column is contrary to results from observations of white dwarves, which suggest an arc shaped emission region and accretion 'curtain' (Warner, 1995 page 329). Furthermore the curvature of the magnetic field lines (and hence the accretion column) is not considered. Neglecting radiation pressure on the infalling electrons, the model is limited to describing sources in the low accretion rate regime. At higher accretion rates the effects of radiation pressure on the column plasma become important, and the microscopic physics may be significantly different (e.g. Jernigan et al., 2000). The assumption of homogeneity, both horizontal and vertical, may break down in that case and a more complex simulation geometry may be necessary. Despite the extensive catalogue of simplifying assumptions, the model may yet qualitatively reproduce many features of X-ray pulsar emission. That observational spectra appear to be generally consistent with Comptonization continuum models (Chapters 3 and 6) is encouraging. The results presented in this thesis represent a pilot model study, and future investigations including these various additional influences are planned.

The code is based on the sample calculation described in Pozdnyakov, Sobel, and Syunyaev (1983), and uses their algorithms to draw the photon energy and direction, electron energies, and to calculate the fully relativistic (non-magnetic) cross-section for Compton scattering. Modifications related to the column geometry, light bending, and photon binning for profile and spectra are described as follows.

2.3.1 Initial photon selection

First the photon energy $E = h\nu$ is calculated. Photons are distributed according to a blackbody spectrum with radiation temperature T_0. The photons are emitted isotropically from the region of the neutron star (radius R_*) covered by the accretion column, which has radius $R_{\rm C}$. I choose a cartesian coordinate frame centred on the neutron star with the z-axis colinear with the column axis. The initial photon position $\underline{r} = (r_{\rm x}, r_{\rm y}, r_{\rm z})$ and propagation direction $\hat{\underline{\Omega}} = (\Omega_{\rm x}, \Omega_{\rm y}, \Omega_{\rm z})$ is calculated as follows:

1. Draw four random numbers $\xi_1, \ldots, \xi_4$, evenly distributed on [0,1). The random number generator used is the 'Mersenne Twister' of Matsumoto and Nishimura (1998).
2. Calculate

$$\begin{aligned} r_{\rm z} &= \xi_1(R_* - z_{\rm C}) + z_{\rm C} \\ r_{\rm x} &= \sqrt{R_*^2 - r_{\rm z}^2}\sin 2\pi\xi_2 \\ r_{\rm y} &= \sqrt{R_*^2 - r_{\rm z}^2}\cos 2\pi\xi_2 \end{aligned} \tag{2.4}$$

   where $z_{\rm C} = R_* \cos\delta$, and $\delta = \sin^{-1}(R_{\rm C}/R_*)$, i.e. the angular extent (opening angle) of the polar cap.
3. The photon direction is chosen to be isotropic as follows:

$$\begin{aligned} \Omega_3 &= 2\xi_3 - 1 \\ \Omega_1 &= \sqrt{1 - \Omega_3^2}\sin 2\pi\xi_4 \\ \Omega_2 &= \sqrt{1 - \Omega_3^2}\cos 2\pi\xi_4 \end{aligned} \tag{2.5}$$

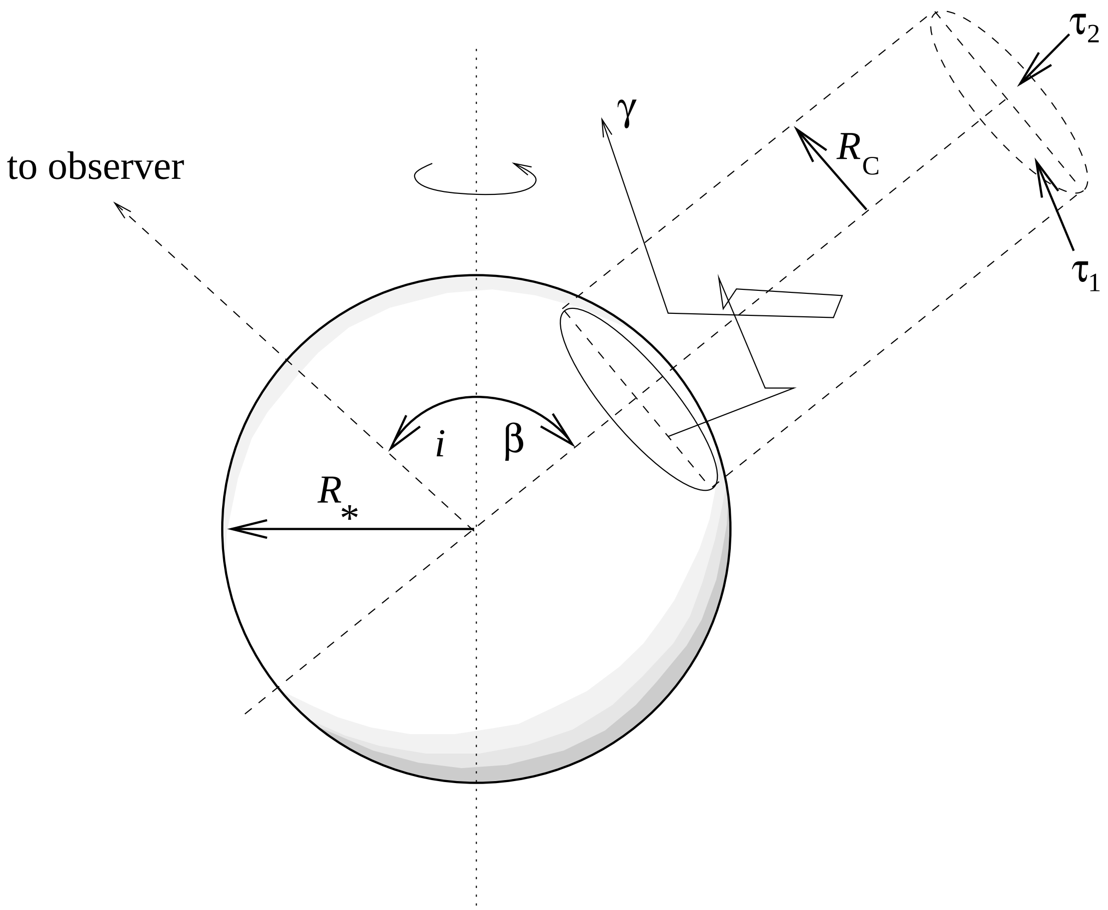

Figure 2.1 The model geometry (only one column shown for clarity). The neutron star radius R_* is 10 km, while the accretion column radius R_C may be varied; the nominal value is 1 km. The direction towards the observer forms an angle i with respect to the rotation axis, and the magnetic axis is inclined at an angle β (the magnetic colatitude). The accretion column plasma temperature T_e is constant within the column, however the density may be set independently within two zones separated by a plane parallel to the rotation axis, as shown. Each zone is characterised by a representative optical depth $\tau_j = \sigma_\mathrm{T} R_\mathrm{C} N_j$, with σ_T the Thompson cross section and N_j the (constant) plasma density within zone $j = 1, 2$. An example photon trajectory is shown.

Note that some photons will have directions which are into the star. If $\underline{\hat{\Omega}} \cdot \underline{r} < 0$ set $\underline{\hat{\Omega}}' = -\underline{\hat{\Omega}}$

2.3.2 Photon transport and scattering

Once the initial photon energy, position, and direction is chosen, proceed with multiple scattering steps. At each step a fraction of the photon escapes the column, and the scattering continues until the remaining weight of the photon drops below some threshold.

1. Calculate the mean free path $\bar{\lambda}$ (following Pozdnyakov et al., 1983).
2. Calculate the distance to the edge of the column

$$l = \frac{1}{\Omega_{\mathrm{x}}^2 + \Omega_{\mathrm{y}}^2} \left[\sqrt{(r_{\mathrm{x}}\Omega_{\mathrm{x}} + r_{\mathrm{y}}\Omega_{\mathrm{y}})^2 - (\Omega_{\mathrm{x}}^2 + \Omega_{\mathrm{y}}^2)(r_{\mathrm{x}}^2 + r_{\mathrm{y}}^2 - R_{\mathrm{C}}^2)} - (r_{\mathrm{x}}\Omega_{\mathrm{x}} + r_{\mathrm{y}}\Omega_{\mathrm{y}}) \right] \tag{2.6}$$

and the portion of the photon which escapes in this timestep

$$L_{\mathrm{esc}} = \exp\left(\frac{-l}{\bar{\lambda}}\right) \tag{2.7}$$

3. Draw a random number ξ on [0,1) and calculate the distance travelled by the photon in the next step

$$\lambda = -\bar{\lambda} \log[1 - \xi(1 - L_{\mathrm{esc}})] \tag{2.8}$$

4. In the case of an inhomogeneous column, the photon may cross the boundary between the two regions in this step. In this case the boundary is formed by the x-z plane; and so if $r_{\mathrm{y}}(r_{\mathrm{y}} + l\,\Omega_{\mathrm{y}}) < 0$ then place the photon on the boundary and set

$$\begin{aligned} l' &= -\frac{r_{\mathrm{y}}}{\Omega_{\mathrm{y}}} \\ \underline{r}' &= \underline{r} + l'\,\underline{\hat{\Omega}} \end{aligned} \tag{2.9}$$

The scattering step is then repeated using the plasma density for the new region. This treatment follows Hua (1997).

2.3.3 Light bending and photon eclipse

Gravitational effects are considered only for photons leaving the column. The redshift and deviation of photon trajectories is calculated assuming a Schwarzchild metric (Riffert and Meszaros, 1988). Initially the photon is at a distance

$$r_0 = \frac{|\underline{r}|}{R_{\mathrm{S}}} \tag{2.10}$$

from the centre of the neutron star (in units of the Schwarzchild radius; $R_{\mathrm{S}} =$ 4.135 km for a $1.5 M_{\odot}$ neutron star). The cosine of the angle between the radial vector $\underline{r}$ and the initial photon trajectory $\underline{\hat{\Omega}}$ is

$$\mu_0 = \underline{\hat{\Omega}} \cdot \frac{\underline{r}}{|\underline{r}|} \tag{2.11}$$

The relativistic impact parameter is

$$b = \frac{r_0}{A_0} \sqrt{1 - \mu_0^2} \tag{2.12}$$

where $A_0 = \sqrt{1 - \frac{1}{r_0}}$. Thus the redshifted photon energy for a sufficiently distant observer is

$$E' = A_0 h\nu \tag{2.13}$$

at which point the angle between the radial vector and the propagation direction is given by

$$K(\infty, r_0, \mu_0) = b \int_{r_0}^{\infty} \left[x^2 - b^2 \left(1 - \frac{1}{x} \right) \right]^{-1/2} \frac{dx}{x} + Q(r_0, \mu_0) \tag{2.14}$$

where

$$Q(r_0, \mu_0) = \begin{cases} 0 & \mu_0 \geq 0 \\ 2b \int_{r_{\mathrm{m}}}^{r_0} \left[x^2 - b^2 \left(1 - \frac{1}{x} \right) \right]^{-1/2} \frac{dx}{x} & \mu_0 < 0 \end{cases} \tag{2.15}$$

and r_{m} is the minimum distance from the neutron star reached by photons initially propogating towards it ($\mu_0 < 0$). The minimum distance determined by iterating

$$r_{j+1} = \sqrt[3]{b^2 (r_j - 1)} \tag{2.16}$$

beginning with r_0. This calculation converges rapidly and allows determination of r_{m} for arbitrary precision.

Equation 2.14 is integrated numerically using the Rhomberg method (Press et al., 1996) from the emission point to the observer at infinity. If the photon is initially propagating towards the star, the integration has two parts; from the starting point inwards to the minimum separation r_{m} and out again to the initial emission position ($= Q(r_0, \mu_0)$), in addition to the integration from this point out to infinity ($= K(\infty, r_0, \mu_0)$).

2.3.4 Photon binning

If the photon beam pattern (e.g. Figure 7.6) is required, then the photon is added to the spectrum in bin j where

$$(j-1)\pi/n \leq \cos^{-1} \Omega_{\mathrm{z}} < j\pi/n, \qquad j \in \{1 \ldots n\} \tag{2.17}$$

and in the case of an inhomogeneous column the beam pattern from each side of the x-z plane can be binned independently.

To calculate the pulse profile, it is necessary to determine the rotational phase of the neutron star at which the photon propagation may intersect the line of sight. For simplicity (and efficiency) I exploit the rotational symmetry of the column. In the case with a density differential between the leading and trailing parts of the column, each half will still exhibit symmetric emission with respect to rotation about the column axis. The angle between the column axis and the line of sight is θ where

$$\cos\theta = \cos i \cos\beta + \sin i \sin\beta \cos 2\pi\phi \tag{2.18}$$

where ϕ is the rotational phase of the star. The photon will be observed when

$$\cos\theta = \Omega_{\mathrm{z}} \tag{2.19}$$

or when

$$|\cos 2\pi\phi| = \left|\frac{\Omega_{\mathrm{z}} - \cos i \cos\beta}{\sin i \sin\beta}\right| \leq 1 \tag{2.20}$$

The full range of ϕ is recovered by examining Ω_{y}.

For phase bins equal in size the total solid emission angle subtended will vary substantially with phase. One solution is to scale each bin appropriately before generating the final profiles. I choose instead to use phase bins with equally spaced centres $\phi_j = (j-1)/n, j = \{1 \ldots n\}$ but varying width

$$\Delta\phi = \frac{1}{2\pi}[\arccos(\cos\phi_j - \delta_{\mathrm{B}}) - \arccos(\cos\phi_j + \delta_{\mathrm{B}})] \tag{2.21}$$

with δ_{B} chosen so that the largest bin (at $\phi = 0.0, 0.5$) does not overlap the adjacent bins

$$\delta_{\mathrm{B}} = 0.5\left(1 - \cos\frac{2\pi}{n}\right) \tag{2.22}$$

Note that extra care must be taken in defining the bin limits for $j = 1, \frac{n}{2}$ using equation 2.21.

2.3.5 Calibration

Run-time options allow simulations of isotropic photon emission from the centre of a spherical cloud undergoing Compton scattering with no light bending, i.e. exactly the situation described in Pozdnyakov et al. (1983). Testing has been undertaken to ensure consistency with the previous results obtained using this algorithm. Spectra were obtained from single and multiple scattering of monoenergetic input photon spectra in plasma having a wide range of temperatures, from sub- to highly-relativistic (Figure 2.2). Multiple scattering simulations with input blackbody spectra were made with the optical depth ranging from $\tau = 1$–10 (Figure 2.3). Power law fits to these spectra result in spectral indices generally consistent with those obtained previously (Pozdnyakov et al., 1983), although there are small variations which are a function of the range for fitting, the number of photons contributing to the spectrum, and even the random number generator used (Table 2.2). A notable exception is the $\tau = 7$ case which other equivalent codes have confirmed should be $\alpha \approx 0.29$ rather than 0.26 (K.Wu & J.Cullen, pers. comm.). The contribution of photons undergoing different numbers of scatters was assessed. All tests were consistent with the previous results.

Table 2.2 Power law photon slopes for Monte-Carlo simulations of Compton scattering in a homogeneous spherical cloud with optical depth τ. Fits are calculated for the spectra shown in Figure 2.3 over the energy range 0.01–10 keV. The second column shows the results from spectra calculated using the g77 '`rand`' random number generator, while the third column is from results made using the 'Mersenne Twister' of Matsumoto and Nishimura (1998). The results from Pozdnyakov et al. (1983) are listed for comparison in the fourth column.

	Power law slope		
τ	g77 '`rand`'	Mersenne Twister	Pozdnyakov et al. (1983)
3	1.01	0.93	1.00
4	0.69	0.68	0.68
5	0.51	0.50	0.5
7	0.30	0.29	0.26
10	0.13	0.13	0.13

2.3.6 Spectral analysis

In order to characterise the spectra generated by the model in an objective manner, I choose to fit to analytic models using the XSPEC software package (Arnaud, 1996) as used for observational spectra (see section 2.1.2). The output spectra are first converted to FITS format using the `flx2xsp` script, also written by Keith Arnaud. This script generates a response matrix based on the bin energy limits set for the simulation. The resulting spectra can be imported directly into XSPEC and fit using the full range of model spectra available within that package.

The response matrices created using `flx2xsp` describe an even, ideal response across the entire energy range. Instrumental responses however are generally far from ideal. Observational spectra will also have a background component, from diffuse galactic and extragalactic X-ray emission, cosmic rays, and other nearby

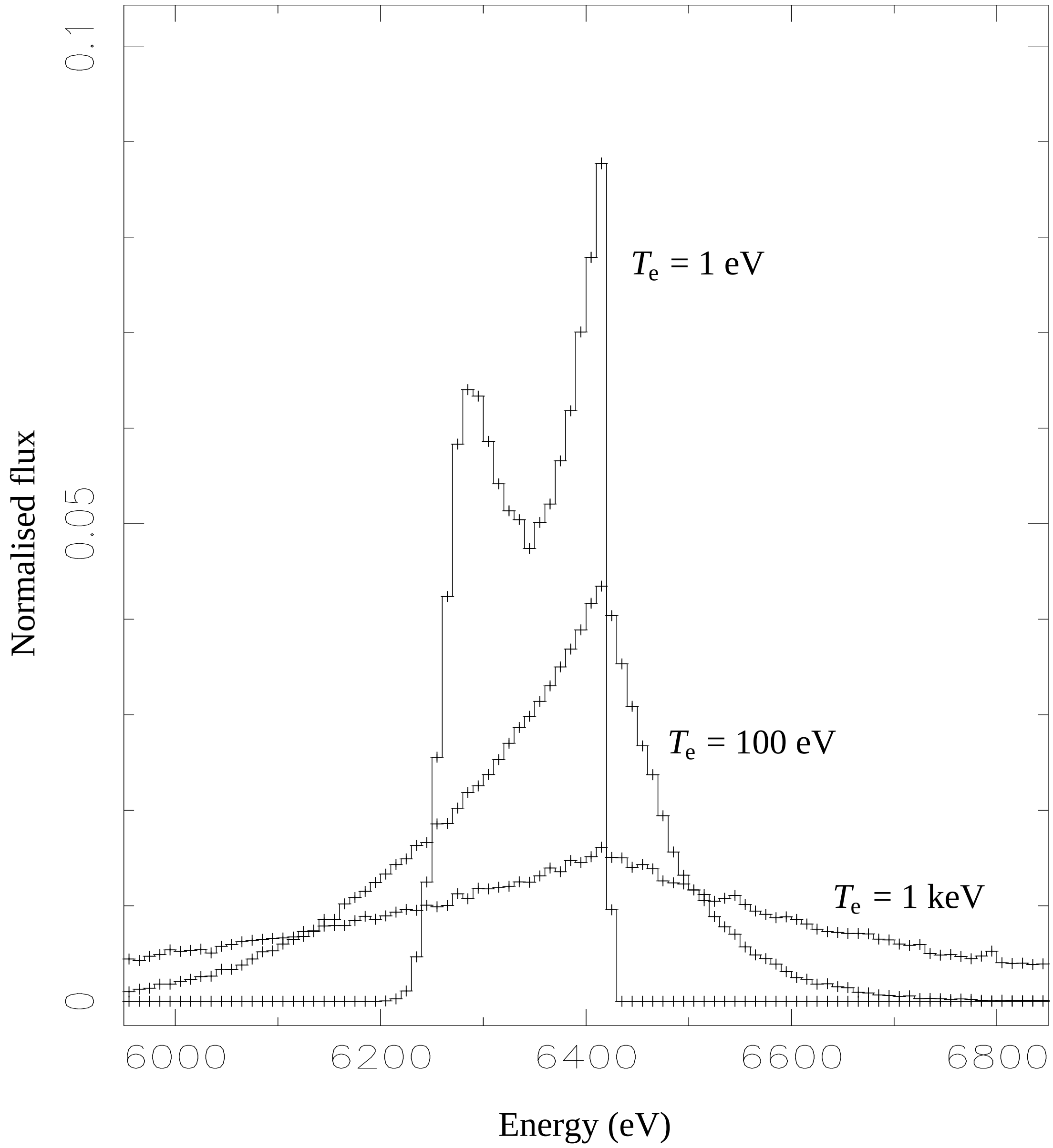

Figure 2.2 Monte-Carlo simulation results from single scattering of monoenergetic photons ($T_0 = 6.4$ keV) in a plasma cloud with temperature T_e.

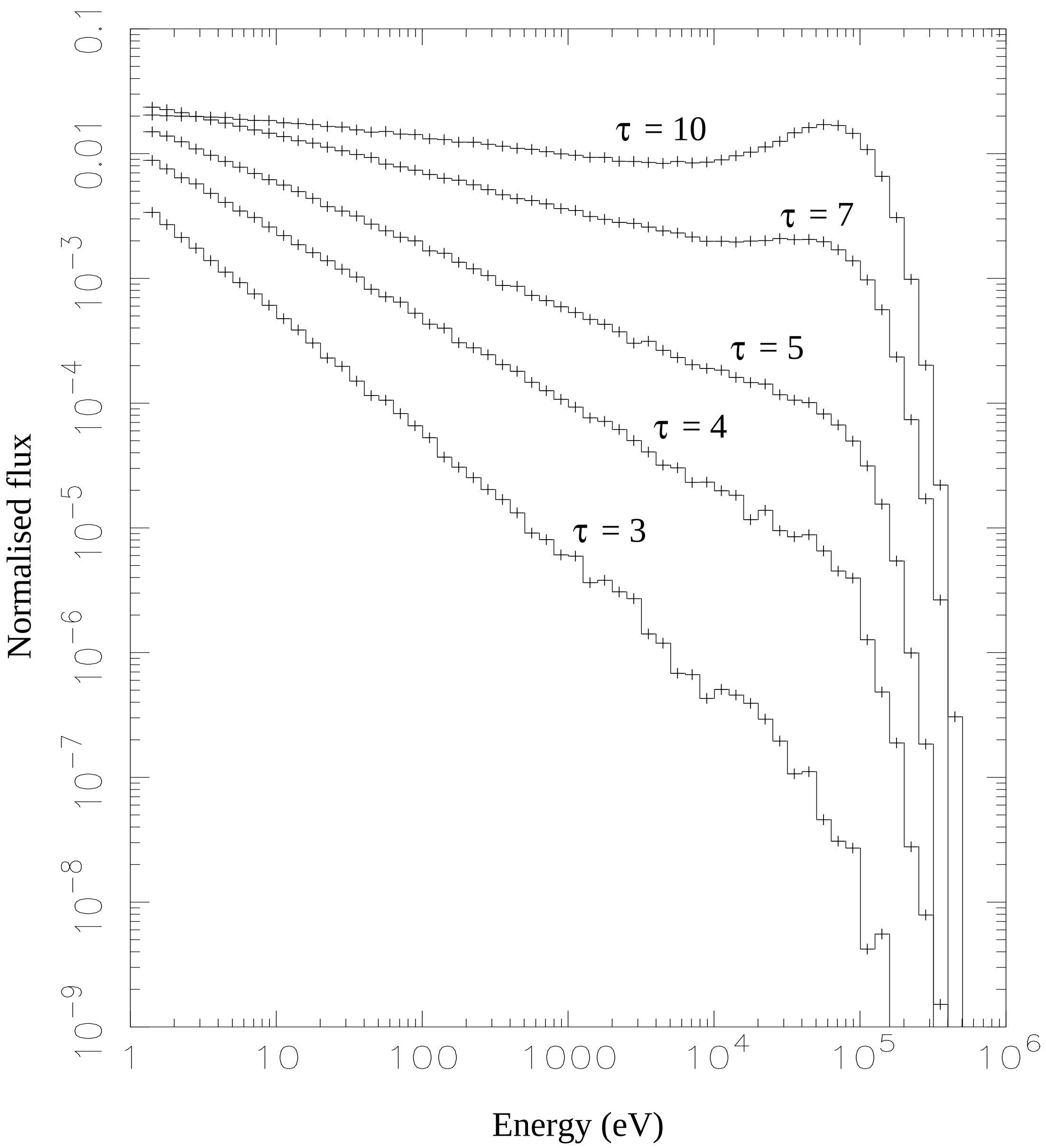

Figure 2.3 Monte-Carlo simulation results from multiple scattering of blackbody input spectra in a homogeneous spherical cloud with optical depth τ. The number of photons contributing to each spectrum is 10^5.

sources. Additionally, X-ray pulsars are generally observed at distances in the kpc range, and are thus subject to significant absorbtion by neutral hydrogen along the line of sight. For spectral fitting under more realistic conditions `txt2xspec` by Randall Smith (`rsmith@cfa.harvard.edu`) may be used to convert the model spectrum to a one-parameter XSPEC 'table' model. Simulated observational spectra can be generated using this model with a component describing the effects of absorbtion by neutral interstellar hydrogen (`wabs` in XSPEC), convolving with an instrumental response matrix (e.g. from *RXTE*) and adding appropriate background spectra.

Chapter 3

Mean X-ray spectra from GX 1+4

3.1 Observations

Between February 1996 and May 1997 GX 1+4 was observed by *RXTE* in 25 distinct intervals totalling ≈ 230 ks (Table 3.1). Since each of these observations was made as a result of proposals with a broad range of science objectives, the observing strategies varied markedly. This is illustrated by the range of duty cycles, i.e. the ratio between the on-source time and the total duration of the observation. For observation A the duty cycle was greater than 0.5 over almost 24 hours, in marked contrast to observation W with only 4768 s on-source over more than 5 days, resulting in a duty cycle of less than 0.011.

One or more user-defined data mode was generally present in addition to the standard modes; in most cases this was GoodXenon. This mode uses two EAs simultaneously to provide 256 spectral channels at 1 μs time resolution. For observation H a 'generic event' mode was chosen instead, with 250 μs time resolution and 128 spectral channels. Data from observation R includes instead a 'generic binned' mode, with 128 spectral channels binned on 250 ms.

The phase-averaged count rate from the source showed significant variability (Figure 3.1). All 5 PCUs were on for the majority of the observations. PCUs 3 and 4 were commanded off during observations D, N and P, and for part of observation H. PCU 4 alone was off for short intervals during observations H and R. The count rate for these observations was scaled appropriately to give the equivalent for all 5 PCUs on. The count rate spanned more than two orders of magnitude in less than two days on occasion (e.g. observation H). More typically the count rate varied by a factor of ~ 5 on hourly timescales when the count rate was 100 count s^{-1} or more, and a factor of ~ 10 otherwise. Increased variability at low flux levels was also noted by Greenhill et al. (1999) in analyses of archival hard X-ray observations. These variations in the *RXTE* data were superimposed on long-term trends with timescales of a year or more, which may be related to the orbital period (Pereira et al., 1999). The source flux appeared to be relatively high during the first half of 1996, after which it entered a ~ 50 d low state. The decrease in 20–60 keV flux was much more abrupt than that of the PCA count rate. At that time it was reported that pulsations from the source all but ceased, suggesting cessation of mass transfer from the companion or possibly centrifugal inhibition of accretion (Cui, 1997). A flare lasting about 30 days was observed by BATSE during August 1996, following the period of lowest flux during July. After the flare the source again entered a relatively low state, which persisted to June 1997. The PCA count rate generally traced the 20–60 keV flux as measured by BATSE reasonably well, but spectral variation in the source (in particular the degree of low-energy absorption; see section 3.2) resulted in a varying fractional contribution by high-energy photons.

Several of the observations listed in Table 3.1 have not before been the subject of publication. Consequently I now turn to a more detailed discussion of those results.

ID	Obs. ID	Start	End	Exposure (sec)	Ref.
		1996			
A	10133-02-01	Feb 12 14:11:11	Feb 13 13:35:11	46816	
B	10104-02-01	Feb 17 03:12:15	Feb 17 08:12:02	10400	[1,5]
C	10104-02-03	Apr 23 19:10:23	Apr 23 22:40:15	7680	[1]
D	10104-02-04	May 21 15:45:03	May 21 18:08:15	5568	[1]
E	10104-02-05	Jun 08 04:49:14	Jun 08 11:58:34	10112	[1,5]
F	10104-02-06-00/1	Jun 28 06:41:03	Jun 28 23:35:35	5392	[1]
G	10104-02-06-02/3	Jul 11 18:23:27	Jul 11 22:08:40	3552	[1]
H	10103-01-01	Jul 19 16:47:16	Jul 21 02:39:02	52832	[2,3]
I	10104-02-07	Sep 04 22:33:35	Sep 05 03:05:00	9232	[1]
J	10104-02-08-00/1	Sep 25 11:12:15	Sep 25 15:19:04	6672	[1]
K	10104-02-08-02	Oct 08 09:43:32	Oct 08 10:38:44	3280	[1]
L	10104-02-09	Oct 16 18:32:38	Oct 16 23:07:11	6016	[1]
M	10104-01-01	Oct 24 17:58:39	Oct 24 19:51:27	4528	[1]
N	10104-01-02	Nov 01 03:35:27	Nov 01 05:34:02	4720	[1]
O	10104-01-03	Nov 07 18:26:00	Nov 07 20:23:59	4592	[1]
P	10104-01-04	Nov 10 12:16:16	Nov 10 14:13:02	4688	[1]
		1997			
Q	10104-01-05	Jan 16 00:27:11	Jan 16 02:24:03	4592	[1]
R	10144-01-01	Jan 16 03:16:35	Jan 16 08:02:04	9760	
S	10104-01-06	Jan 21 19:13:51	Jan 21 21:32:31	5152	[1]
T	10104-01-07	Jan 26 22:57:03	Jan 27 00:54:15	4672	[1]
U	10104-01-08	Feb 02 14:35:11	Feb 02 16:50:02	4512	[1]
V	20170-04-01–04	Feb 26 00:41:15	Feb 27 18:48:31	2816	[4]
W	20170-04-05–10	Mar 20 16:39:00	Mar 25 18:56:02	4768	[4]
X	20170-04-11–15	Apr 18 12:34:28	Apr 22 23:45:02	4592	[4]
Y	20170-04-16–20	May 16 03:35:27	May 20 07:04:36	4080	[4]

Table 3.1 *RXTE* observations of GX 1+4. Start and end times and on-source durations are calculated from Standard-2 spectra taking into account screening (see section 2.1.1). Times are terrestrial time (TT). Publications describing particular observations are as follows: 1. Cui (1997), 2. Galloway et al. (2000), 3. Giles et al. (2000), 4. Galloway (2000) and 5. Galloway et al. (2001).

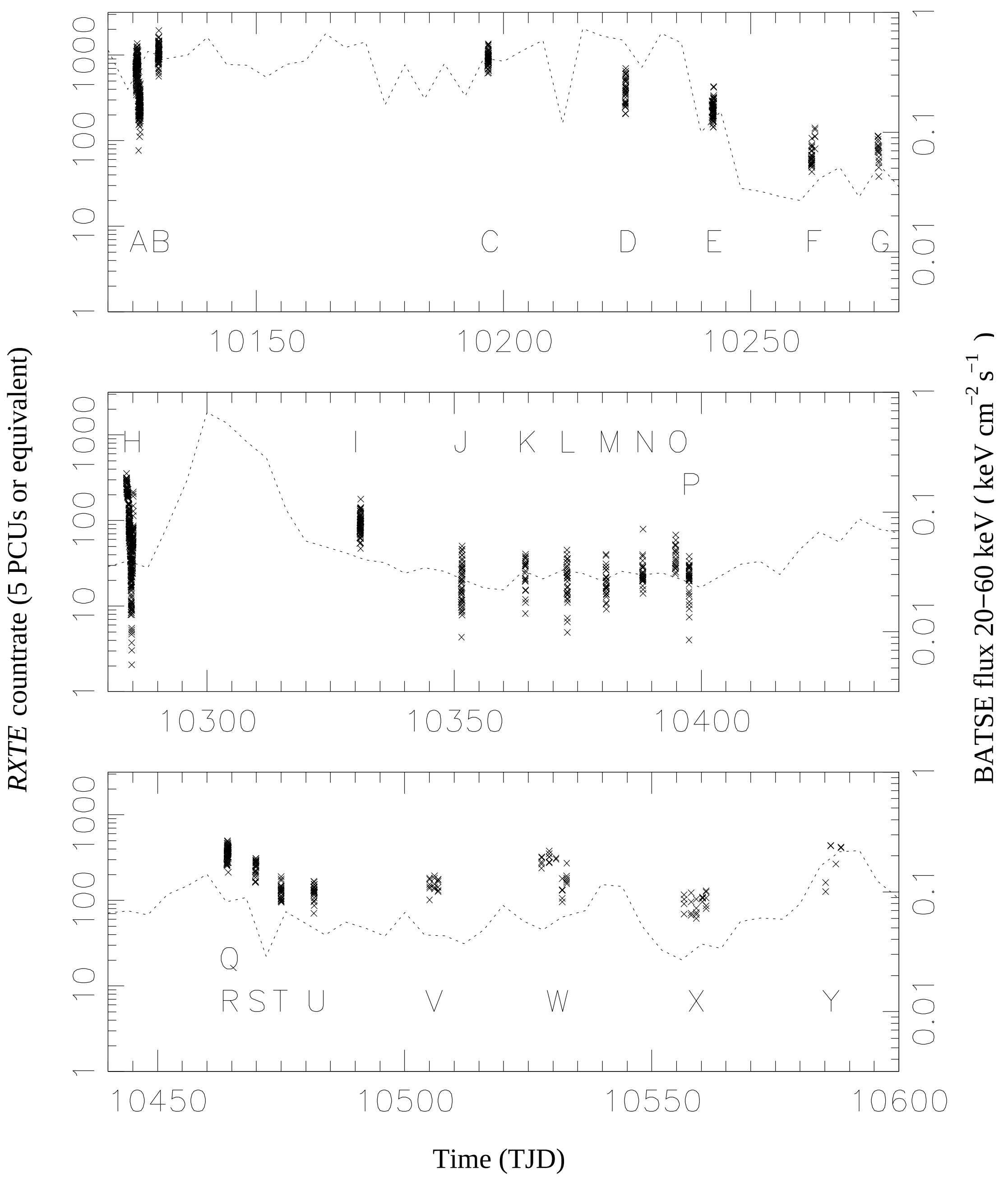

Figure 3.1 *RXTE* and BATSE observations of GX 1+4 between Feburary 1996 and May 1997. Phase-averaged background-subtracted count rate from pointed observations using the PCA aboard *RXTE* are plotted as crosses (left hand scale in each panel). The observations are labelled A...Y; see Table 3.1. The pulse period for the averaging has been determined by phase folding or interpolation of BATSE period measurements; see section 4.1. The dotted line represents the 20–60 keV pulsed flux as measured by BATSE (right hand scale).

3.1.1 A — 12–13 February 1996

The first *RXTE* observation of GX 1+4 was made around six weeks following the launch of the satellite, and found the source to be in a moderately bright state (Figure 3.2). After screening the observation consists of fifteen ≈ 1 h intervals over almost 24 h, with interruptions as a result of solar conjunctions. Initially the phase-averaged count rate was ≈ 600 count s^{-1}. The count rate rose steadily over a period of 6 h to ≈ 1400 count s^{-1} (with the 1 s binned rate reaching ≈ 2500 count s^{-1}) before decreasing over approximately the same timescale to around 150 count s^{-1}. It remained around this level for the last ≈ 10 h of the observation. Superimposed on the broad-scale variations were significant sub-hourly excursions of the phase-averaged count rate, with amplitudes which depend roughly on the hourly mean. The large-amplitude pulsations observed at the neutron star rotation period resulted in the wide scatter of the 1 s rates about the phase-averaged line.

The pulse profile changed subtly over the course of the observation (Figure 3.2, lower panel). Initially the profile was smooth, slightly asymmetrical, with a broad triangular dip which becomes steeper closer to the minimum. In the second half of the observation the profile asymmetry was enhanced, with a 'shoulder' appearing immediately after the dip. A configuration error for this observation resulted in only one-half of the GoodXenon telemetry being obtained, which alone is useless. Since no complete high time resolution modes were available for this observation it was not possible to obtain detailed pulse profiles on more than one energy band, but the profiles from 16 s Standard-2 mode data on 2–7, 7–20 and > 20 keV bands exhibit similar shapes.

Initial spectral analysis focussed on mean spectra from the first and second halves of the observation. Model fits were attempted using a range of continuum models including power law, power law and blackbody, power law modified by a high energy exponential cutoff and a two-valued 'broken' powerlaw. Although each of these models had been used to fit spectra from previous observations of this and other sources, it was not possible to obtain adequate fits in this case. The analytic Comptonization approximation of Titarchuk (1994), when combined with a Gaussian representing iron line emission and the standard low-energy absorption and galactic ridge component (see section 2.1.2) unambiguously offered the best fit in terms of χ^2_ν of all the models tested. While the spectrum from the first half of the observation gave a reasonable fit with $\chi^2_\nu = 1.62$, the results for the second half were distinctly worse ($\chi^2_\nu = 4.5$). A large value of χ^2_ν may indicate a poor choice of spectral model or significant spectral variation over the integration time for the spectrum. In order to test for the latter effect, spectra were extracted for each of the 15 separate ≈ 1 h intervals (see Figure 3.2) and analysed independently.

The resulting spectral fits offered greatly improved χ^2_ν values compared to the mean spectra, and the fit parameters confirm that spectral variations ontributed significantly to the poor fits initially (Table 3.2). Parameters are given for the mean spectra over the first half of the observation (which exhibited little spectral variation), referred to as A1. Subsequent spectra are from each ~ 1 h separate

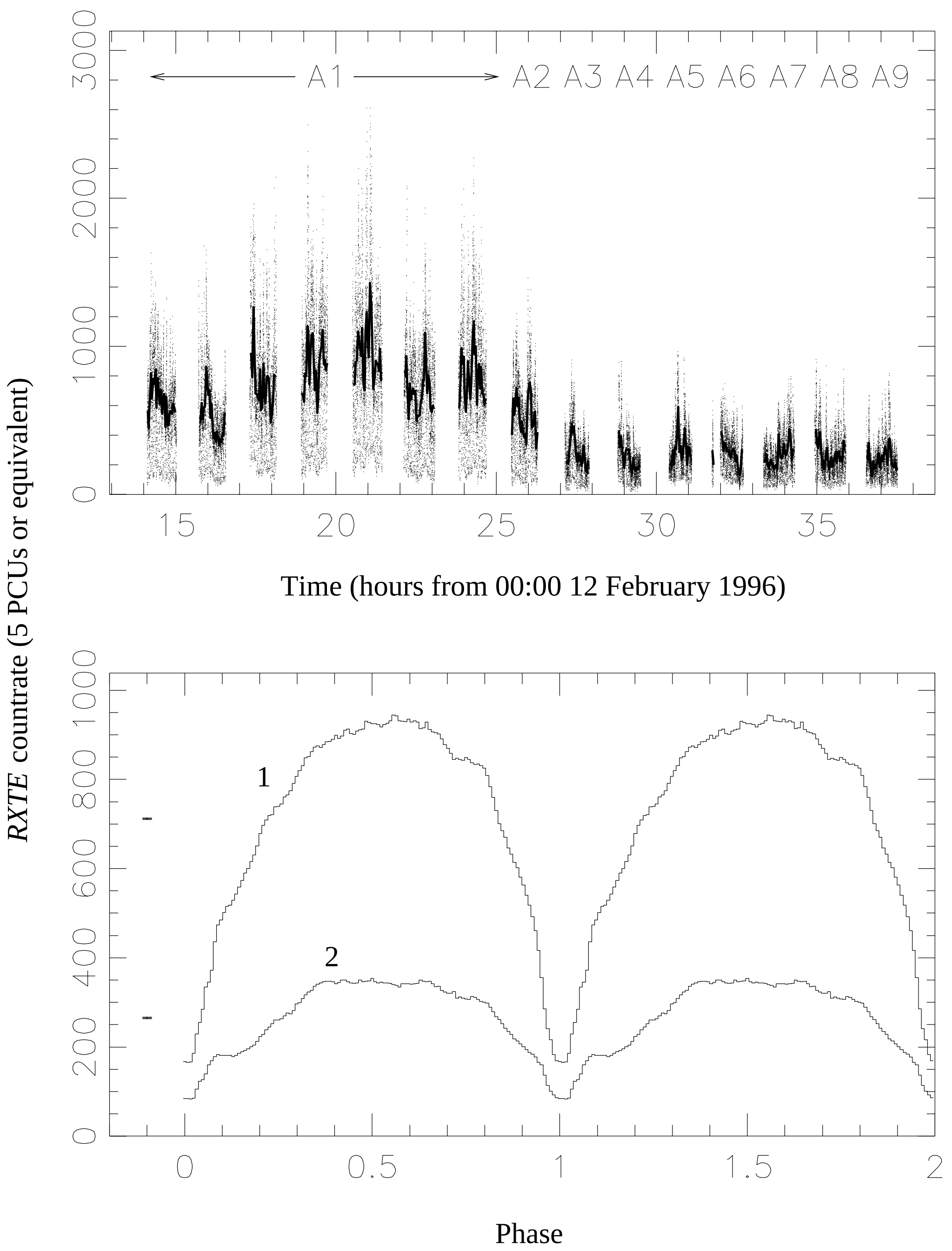

Figure 3.2 *RXTE* observation of GX 1+4, 12-13 February 1996 (TJD 10126.08). The top panel shows the variation of count rate in the full PCA energy range with time, with points corresponding to counts accumulated over 1 s bins and the count rate averaged over the pulse period 123.61548(6) $\pm$ 0.00003(9) s (see section 4.1) as a thick line. The bottom panel shows the mean pulse profiles calculated from the same 1 s lightcurve. The profile labelled '1' is from the first half of the observation, to $\approx$02:30 h 13 February 1996, while the second profile is from the remaining portion of the observation. Representative 1σ error bars for each profile are shown at the left. Two full cycles are plotted for clarity.

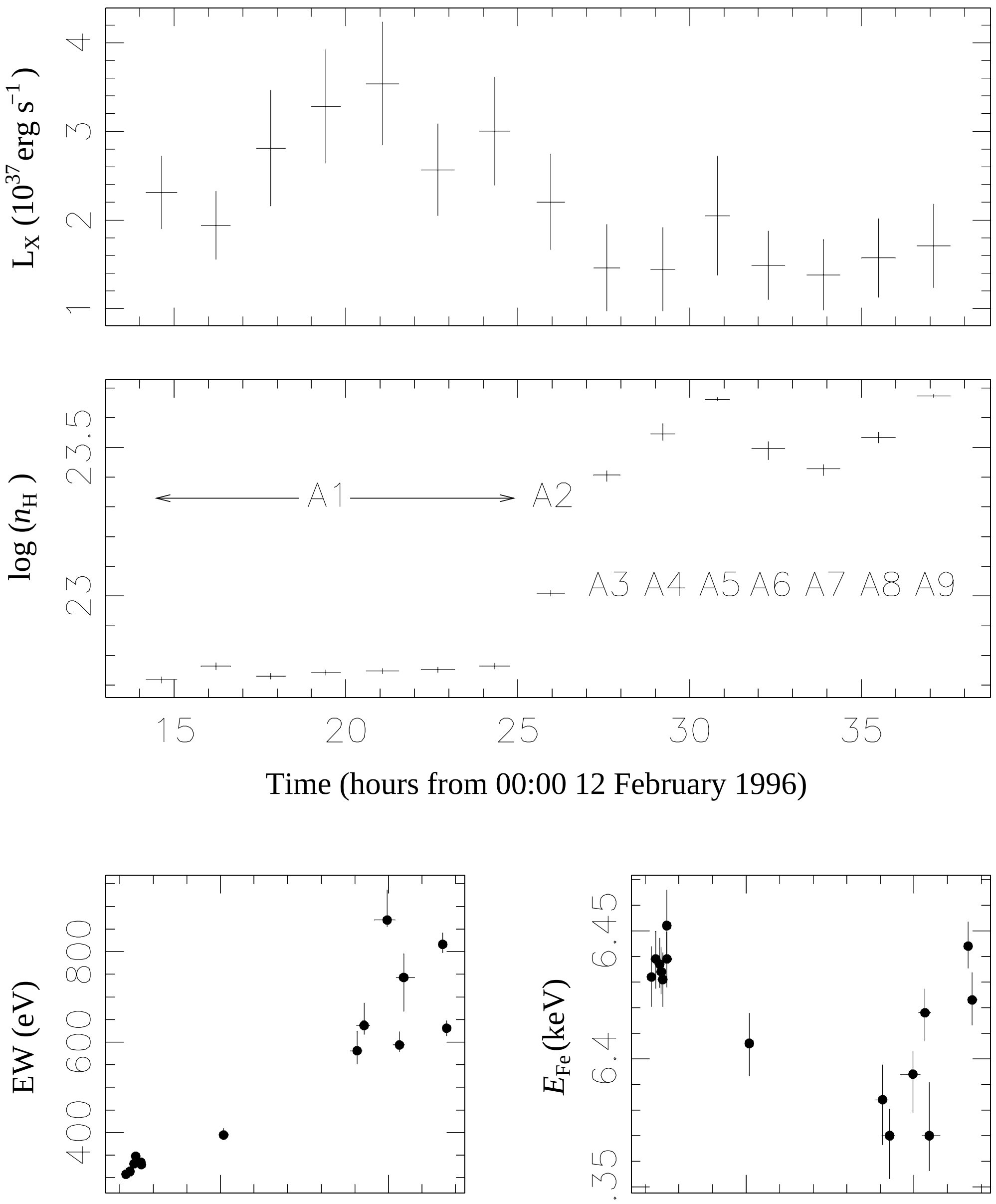

Figure 3.3 Variation of selected spectral fit parameters from the 12-13 February 1996 *RXTE* observation of GX 1+4. The top panel shows the time evolution of the unabsorbed 2–20 keV luminosity (assuming a source distance of 10 kpc) The uncertainty was calculated from the variance of the phase-averaged count rate in each interval. The middle panel shows the fitted column depth $n_{\rm H}$. The bottom left panel plots the equivalent width of the Gaussian component (representing fluorescent Fe emission) versus $n_{\rm H}$, while the bottom right panel shows the centre energy of the line component versus $n_{\rm H}$. The error bars show confidence intervals of 1σ.

Table 3.2 Spectral fit parameters using the Comptonization continuum component from the 12-13 February 1996 *RXTE* observation of GX 1+4. Fit parameters are the absorption column density $n_{\rm H}$ (in units of 10^{22} cm^{-2}), source spectrum temperature T_0, plasma temperature $T_{\rm e}$ and optical depth τ, Comptonization component normalisation $A_{\rm C}$ (in units of 10^{-2} photons cm^{-2} s^{-1} keV^{-1}), Gaussian component center energy $E_{\rm Fe}$, width σ, normalisation $A_{\rm Fe}$ (in units of 10^{-3} photons cm^{-2} s^{-1} keV^{-1}) and equivalent width EW, and finally the 2–20 keV luminosity $L_{\rm X}$ in units of 10^{37} erg s^{-1} (assuming a distance of 10 kpc). Energy range for fitting is typically 2.8–35 keV; confidence intervals are at the 1σ level.

Parameter	A1	A2	A3	A4	A5
$n_{\rm H}$	$5.57_{5.52}^{5.62}$	$10.22_{9.98}^{10.47}$	$25.51_{24.29}^{26.45}$	$35.13_{33.35}^{37.92}$	$45.88_{45.34}^{46.58}$
T_0 (keV)	$1.274_{1.270}^{1.278}$	$1.170_{1.152}^{1.189}$	$1.184_{1.143}^{1.242}$	$1.223_{1.114}^{1.293}$	$0.429_{0.001}^{0.557}$
$T_{\rm e}$ (keV)	$8.16_{8.12}^{8.20}$	$6.65_{6.57}^{6.72}$	$6.04_{5.98}^{6.11}$	$6.01_{5.93}^{6.06}$	$6.75_{6.60}^{6.85}$
τ	$4.96_{4.94}^{4.98}$	$5.54_{5.48}^{5.60}$	$5.87_{5.83}^{5.93}$	$6.18_{6.12}^{6.30}$	$6.17_{6.04}^{6.33}$
$A_{\rm C}$	$3.44_{3.42}^{3.45}$	$3.28_{3.23}^{3.32}$	$2.33_{2.25}^{2.40}$	$2.24_{2.15}^{2.41}$	$3.94_{3.55}^{5.16}$
$E_{\rm Fe}$ (keV)	$6.437_{6.433}^{6.441}$	$6.406_{6.393}^{6.418}$	$6.384_{6.366}^{6.398}$	$6.370_{6.356}^{6.391}$	$6.444_{6.435}^{6.454}$
σ	$0.331_{0.322}^{0.340}$	$0.356_{0.330}^{0.382}$	$0.342_{0.313}^{0.374}$	$0.364_{0.325}^{0.391}$	$0.287_{0.265}^{0.310}$
$A_{\rm Fe}$	$4.82_{4.77}^{4.87}$	$4.63_{4.50}^{4.78}$	$4.51_{4.36}^{4.70}$	$5.46_{5.20}^{5.65}$	$7.49_{7.32}^{7.69}$
EW (eV)	329_{326}^{333}	395_{383}^{410}	581_{551}^{623}	743_{668}^{795}	816_{797}^{842}
$L_{\rm X}$	2.78 ± 0.78	2.20 ± 0.54	1.46 ± 0.49	1.45 ± 0.47	2.05 ± 0.67
χ^2_ν	1.62	1.02	1.09	0.99	1.40

Parameter	A6	A7	A8	A9
$n_{\rm H}$	$31.38_{28.74}^{33.08}$	$26.77_{25.36}^{27.75}$	$34.11_{32.67}^{35.42}$	$47.15_{46.51}^{47.81}$
T_0 (keV)	$1.267_{1.191}^{1.388}$	$1.287_{1.238}^{1.352}$	$1.143_{1.073}^{1.208}$	$0.288_{0.001}^{0.511}$
$T_{\rm e}$ (keV)	$6.47_{6.38}^{6.55}$	$6.69_{6.57}^{6.75}$	$7.02_{6.97}^{7.11}$	$7.51_{7.35}^{7.69}$
τ	$6.55_{6.47}^{6.77}$	$5.50_{5.46}^{5.62}$	$5.51_{5.45}^{5.57}$	$4.79_{4.68}^{4.92}$
$A_{\rm C}$	$2.09_{1.97}^{2.17}$	$1.97_{1.90}^{2.03}$	$2.20_{2.12}^{2.30}$	$4.41_{3.25}^{5.71}$
$E_{\rm Fe}$ (keV)	$6.394_{6.379}^{6.403}$	$6.370_{6.353}^{6.380}$	$6.418_{6.407}^{6.427}$	$6.423_{6.413}^{6.434}$
σ	$0.334_{0.314}^{0.366}$	$0.376_{0.357}^{0.407}$	$0.236_{0.212}^{0.261}$	$0.286_{0.260}^{0.310}$
$A_{\rm Fe}$	$6.02_{5.89}^{6.21}$	$4.61_{4.49}^{4.81}$	$4.79_{4.68}^{4.91}$	$5.33_{5.19}^{5.48}$
EW (eV)	870_{855}^{937}	637_{617}^{687}	594_{579}^{624}	631_{614}^{648}
$L_{\rm X}$	1.49 ± 0.39	1.38 ± 0.40	1.57 ± 0.44	1.71 ± 0.47
χ^2_ν	1.39	1.01	1.50	1.26

interval in the second half (see Figure 3.2), labelled A2. . . 9. The decrease in flux following the first half of the observation coincided with a substantial increase in $n_{\rm H}$ (Figure 3.3). Both these effects contributed to the dramatic decrease in count rate observed at this time. For most of the observation the blackbody temperature of the source spectrum $T_0 \approx 1.2$ keV, however during the second half of the observation it fell below 0.5 keV during intervals A5 and A9 (although with a large error). The low values of T_0 measured during these intervals may contribute to a slight (spurious) increase in the measured $n_{\rm H}$; compare the values for A5,9 to those for the other intervals following A2 in Figure 3.3. The Gaussian (Fe) component also exhibited significant variation over the course of the observation. The equivalent width (EW) increased proportionately with $n_{\rm H}$. The line centre energies were generally lower at higher measured $n_{\rm H}$ (corresponding to the second half of the observation) but showed much greater variability. The electron temperature $T_{\rm e}$ and optical depth τ were reasonably consistent over the course of the observation at 6–8 keV and 4.5–6.5 respectively, typical values for spectra from the source at fluxes of $\gtrsim 1.35 \times 10^{37}\ {\rm erg\,s^{-1}}$ (see section 3.2).

3.1.2 R — 16 January 1997

GX 1+4 was again observed by *RXTE* between 03:00 h and 08:00 h UT on 16 January 1997. After screening the observation consists of three ≈ 1 h and one final ≈ 0.2 h intervals, separated by ≈ 0.7 h. All 5 PCUs were on during the observation except during the second interval when #4 was switched off, leaving 4. The phase-averaged count rate was $\approx 400\ {\rm count\,s^{-1}}$ initially, dropping to $\approx 300\ {\rm count\,s^{-1}}$ during the second interval (equivalent rate for 5 PCUs on) before recovering towards the end (Figure 3.4). Variations in the phase-averaged count rate of $\approx 100\ {\rm count\,s^{-1}}$ on timescales of a few minutes were observed in the first two intervals, increasing to $\approx 200\ {\rm count\,s^{-1}}$ during the third interval. No significant pulse profile variations were observed over the course of the observation. The full-range profile was rather flat topped, mildly asymmetric with a very sharp dip feature. The dips from individual pulsations were noticeable also in the 1 s lightcurve.

A spectra was extracted for the interval during which only 4 PCUs were on (R2), and since this divides the first and last parts of the observation separate spectra were extracted for those intervals also (R1 and R3 respectively). Fitting results using the Comptonization continuum component (which gives the best χ^2_ν of the models tested; see section 3.2) are shown in Table 3.3. The fit parameters were generally consistent across the three intervals. The absorption column density was significantly lower than for the 12-13 February 1996 observation at $\approx 1.3\times10^{22}\ {\rm cm^{-2}}$. Also different were the scattering plasma parameters, with $T_{\rm e} \approx 10$ keV and $\tau \approx 3$. This variation may have been related to the flux, which was marginally decreased compared to the February 1996 results. The source spectrum temperature T_0 was quite consistent with the fit values for spectra from the first half of the earlier observation at ≈ 1.3 keV. The Fe line energy was somewhat greater at 6.47–6.53 keV.

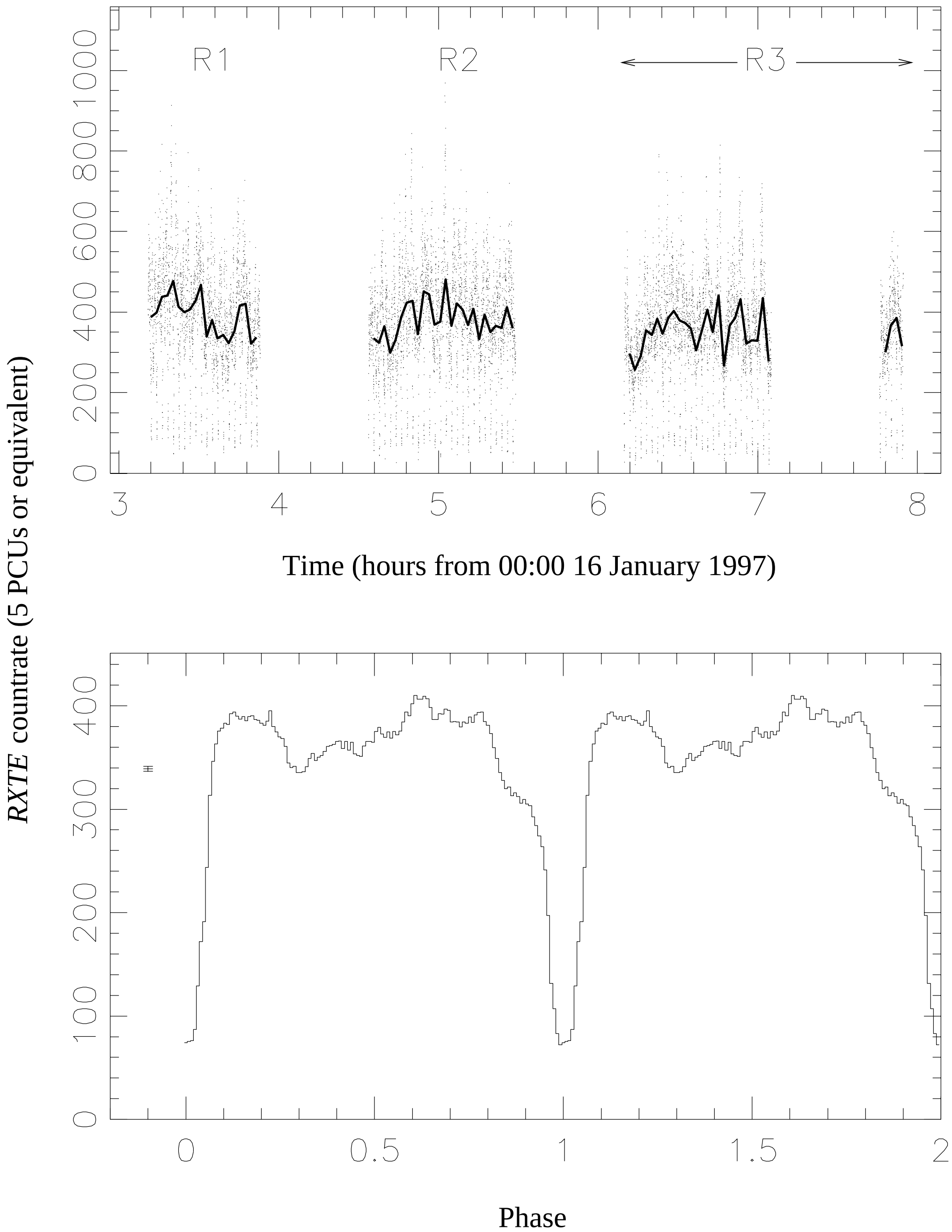

Figure 3.4 *RXTE* observation of GX 1+4, 16 January 1997 (TJD 10464.25). The top panel shows the count rate for 5 PCUs on, scaled appropriately when less than 5 are operating. The points represent counts accumulated over 1 s bins, while the thick line shows the count rate averaged over the pulse period $125.4551(6) \pm 0.0003(0)$ s (see section 4.1). The bottom panel shows the mean pulse profile over the full PCA energy range. A representative 1σ error bar is shown at the left. Two full cycles are plotted for clarity.

Table 3.3 Spectral fit parameters using the Comptonization continuum component from the 16 January 1997 *RXTE* observation of GX 1+4. Fit parameters and units are as for Table 3.2. Energy band for fitting is typically 2.5–35 keV.

Parameter	R1	R2	R3
$n_{\rm H}$	$1.20_{0.85}^{1.54}$	$1.72_{1.43}^{2.00}$	$1.30_{0.96}^{1.65}$
T_0 (keV)	$1.361_{1.343}^{1.381}$	$1.337_{1.321}^{1.345}$	$1.333_{1.314}^{1.352}$
$T_{\rm e}$ (keV)	$10.81_{9.99}^{11.96}$	$10.38_{9.72}^{11.25}$	$9.25_{8.74}^{9.59}$
τ	$3.15_{2.95}^{3.32}$	$3.15_{3.00}^{3.30}$	$3.43_{3.28}^{3.51}$
$A_{\rm C}$	$1.29_{1.16}^{1.39}$	$1.27_{1.17}^{1.36}$	$1.39_{1.30}^{1.48}$
$E_{\rm Fe}$ (keV)	$6.468_{6.446}^{6.480}$	$6.531_{6.523}^{6.548}$	$6.498_{6.474}^{6.510}$
σ	$0.292_{0.245}^{0.336}$	$0.075_{0.000}^{0.149}$	$0.337_{0.290}^{0.380}$
$A_{\rm Fe}$	$1.72_{1.63}^{1.83}$	$1.29_{1.24}^{1.36}$	$1.60_{1.51}^{1.70}$
EW (keV)	210_{197}^{224}	167_{159}^{176}	212_{198}^{226}
$L_{\rm X}$	1.32 ± 0.16	1.24 ± 0.19	1.22 ± 0.18
χ_ν^2	0.79	1.39	0.91

3.1.3 V–Y — 26 February – 20 May 1997

In the first half of 1997 GX 1+4 was observed in four groups of observations each spanning several days, and separated by just under one month. The phase-averged count rate ranged from ≈20–600 count s^{-1} (Figure 3.5). The spacing of the observations clearly shows the variability in the source on timescales of minutes, days, and months. During February (observation V) the count rate was reasonably steady at between 100 and 200 count s^{-1}. During March (W) the source was both brighter and more variable, with the mean count rate ranging from ≈100–600 count s^{-1} and the 1 s rates peaking at almost 1000 count s^{-1}. The April observation (X) showed the source to be faint once more, with typical phase-averaged rates of ≈ 100 count s^{-1}, while May (Y) saw a return to the greater variability of March. The observations were divided into subintervals based on the count rate. Observation W was subdivided into two intervals with W1 covering the first three pointings between TJD 10527 and 10532, and W2 the remaining 2. Observation Y was divided into a subinterval for each pointing, numbered Y1. . .5. No background spectrum could be extracted for the final pointing in observation Y due to problems with the extent of the filter file, and so the background spectrum for the previous days' observation was used instead.

Spectral fits with the Comptonization continuum component showed significant

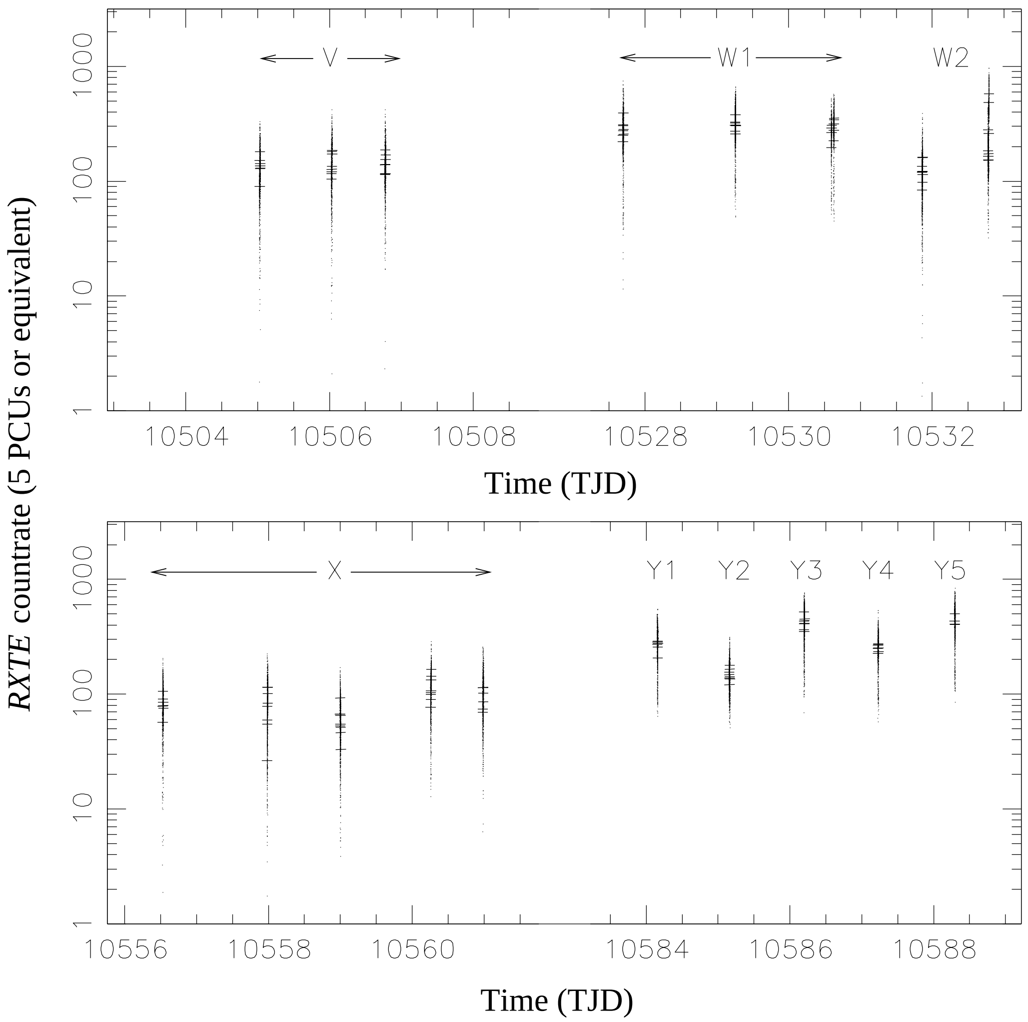

Figure 3.5 *RXTE* observations of GX 1+4, 26 February – 16 May 1997. Each panel shows the count rate for all 5 PCUs, with points showing counts accumulated over 1 s bins. The integration times are much shorter than the span of each observation, making the short-term variation in the 1 s binned rate difficult to see. The horizontal markers show the count rate averaged over the pulse period (see section 4.1).

variability in several parameters (Table 3.4). The column density n_{H} was initially 5×10^{21} cm^{-2} but increased during observation W to around 2.2×10^{22} cm^{-2} (25 March). Observation X (18–22 April) exhibited a slightly higher value again. Between 16–20 May however, n_{H} was around an order of magnitude higher than previous observations and exhibited variability on timescales of a few days (observation Y). The scattering plasma temperature T_{e}, when it could be measured reliably, was between 6–8 keV. For the fainter observations V and W1 the fit value was closer to 10 keV, but no confidence limits could be determined; for observations X and Y1 no fit value could be determined, and so this parameter was frozen at the calculated mean for the low-L_{X} observations (see section 3.2). The optical depth τ increased significantly between April and May from ≈ 3.5 to 4.78 by May 20, with the notable exception of observation Y2 when it jumped to around 20. The equivalent width of the Fe line steadily increased between February and May, also with a dramatic jump during observation Y2. These variations occured as the luminosity varied between ~ 0.3–2×10^{37} erg s^{-1}. The ${\chi^2}_\nu$ fit statistic values indicate good fits in all but observation Y2.

The spectrum extracted during this pointing was quite remarkable (Figure 3.8). The spectrum did not resemble any of the other ≈ 50 spectra extracted over the course of the *RXTE* observations, and featured unusually strong Fe line emission with EW≈ 1.7 keV (see also Figure 3.11c). The peak in the count rate spectrum (neglecting the Fe line) occurs at > 10 keV, although the slope of the high-energy tail is roughly similar to that of observation B. The spectrum strongly suggests an order-of-magnitude increase in the optical depth with respect to scattering compared to the other spectra. The fitted T_0 value was much larger than was consistent than for the other spectra and so was fixed at 1.3 keV. The resulting fit statistic $\chi^2_\nu = 2.75$ was higher than for several of the alternative continuum models considered, but the otherwise excellent agreement of GX 1+4 spectra with the `compTT` model makes a case for further examination of the resulting fit parameters. The fits suggest an optical depth around 5 times more than for other spectra close to this time. Both τ and the strength of the iron line places this spectrum in a region of parameter space far from all the others (Figures 3.10, 3.11c). It is somewhat reassuring that the other spectra from these observations also appear to be unusual, in that they feature values of T_0 (e.g. X and Y1) and τ (W2, Y1, Y3 and Y4) which are atypically large compared to those measured for other spectra at comparable luminosity levels. The values of τ measured during May in particular place all of these spectra between the two main groupings in Figure 3.10b, and at an appropriately intermediate luminosity of $\approx 1.4 \times 10^{37}$ erg s^{-1}.

The lightcurve during observation Y2 was also unusual (Figure 3.6). Generally, the sharp dips in the mean pulse profiles (see Chapter 4) were clearly observed once every pulse period in the lightcurves (provided the time resolution was sufficient). The 1 s lightcurves for observations Y1 and Y3–5 clearly exhibited these dips. In the first part of the lightcurve for Y2, however, the location of the dips could not be determined accurately, and the minima were broader and more irregular. The dips appeared to make a partial return in the latter half of the observation. The absence

Table 3.4 Spectral fit parameters using the Comptonization continuum component for the February-May 1997 *RXTE* observations of GX 1+4. Fit parameters and units are as for Table 3.2.

Parameter	V	W1	W2	X
$n_{\rm H}$	$0.56_{0.34}^{0.75}$	$0.89_{0.75}^{1.03}$	$2.23_{1.99}^{2.47}$	$3.06_{2.79}^{3.40}$
T_0 (keV)	$1.296_{1.277}^{1.315}$	$1.293_{1.281}^{1.305}$	$1.267_{1.240}^{1.293}$	$1.356_{1.330}^{1.374}$
$T_{\rm e}$ (keV)	9.15 (fixed)	10.59 (fixed)	$8.27_{7.61}^{9.21}$	9.00 (fixed)
τ	$3.43_{3.40}^{3.46}$	$3.19_{3.18}^{3.21}$	$3.75_{3.49}^{3.99}$	$3.40_{3.37}^{3.44}$
$A_{\rm C}$	$0.54_{0.53}^{0.54}$	$0.97_{0.96}^{0.98}$	$0.91_{0.82}^{0.99}$	$0.36_{0.36}^{0.37}$
$E_{\rm Fe}$ (keV)	$6.528_{6.490}^{6.566}$	$6.482_{6.461}^{6.504}$	$6.500_{6.471}^{6.530}$	$6.461_{6.438}^{6.498}$
σ	$0.127_{0.000}^{0.245}$	$0.135_{0.000}^{0.206}$	$0.313_{0.247}^{0.370}$	$0.265_{0.224}^{0.311}$
$A_{\rm Fe}$	$0.47_{0.43}^{0.52}$	$1.12_{1.07}^{1.19}$	$1.04_{0.97}^{1.13}$	$0.55_{0.51}^{0.59}$
EW (eV)	165_{150}^{181}	188_{178}^{199}	240_{222}^{259}	282_{259}^{299}
$L_{\rm X}$	0.46 ± 0.20	0.96 ± 0.78	0.71 ± 0.42	0.314 ± 0.053
χ^2_ν	1.00	0.90	0.97	0.87

Parameter	Y1	Y2	Y3	Y4	Y5
$n_{\rm H}$	$18.46_{16.73}^{20.15}$	$12.12_{11.34}^{12.86}$	$18.85_{17.80}^{19.81}$	$27.40_{25.21}^{29.62}$	$21.61_{20.54}^{22.70}$
T_0 (keV)	$1.473_{1.393}^{1.560}$	1.3 (fixed)	$1.369_{1.322}^{1.422}$	$1.395_{1.304}^{1.494}$	$1.293_{1.243}^{1.345}$
$T_{\rm e}$ (keV)	9.00 (fixed)	$6.42_{6.35}^{6.47}$	$8.71_{8.19}^{9.35}$	$7.66_{7.18}^{8.26}$	$7.33_{7.06}^{7.65}$
τ	$4.24_{4.18}^{4.30}$	$20.85_{20.21}^{21.55}$	$4.24_{4.04}^{4.43}$	$4.57_{4.29}^{4.83}$	$4.78_{4.61}^{4.95}$
$A_{\rm C}$	$1.28_{1.23}^{1.34}$	$0.72_{0.71}^{0.72}$	$2.24_{2.08}^{2.38}$	$1.72_{1.58}^{1.80}$	$2.79_{2.66}^{2.85}$
$E_{\rm Fe}$ (keV)	$6.458_{6.420}^{6.496}$	$6.463_{6.444}^{6.478}$	$6.462_{6.431}^{6.491}$	$6.476_{6.442}^{6.511}$	$6.489_{6.463}^{6.515}$
σ	$0.355_{0.283}^{0.424}$	$0.197_{0.162}^{0.229}$	$0.372_{0.316}^{0.428}$	$0.306_{0.236}^{0.369}$	$0.325_{0.276}^{0.370}$
$A_{\rm Fe}$	$2.79_{2.52}^{3.09}$	$2.36_{2.30}^{2.42}$	$3.97_{3.67}^{4.32}$	$3.33_{3.03}^{3.65}$	$4.50_{4.20}^{4.80}$
EW (eV)	440_{384}^{507}	1730_{1680}^{1770}	368_{334}^{408}	451_{392}^{517}	398_{366}^{435}
$L_{\rm X}$	1.17 ± 0.28	0.614 ± 0.056	1.93 ± 0.36	1.341 ± 0.098	2.048 ± 0.080
χ^2_ν	1.11	2.75	0.99	0.89	1.76

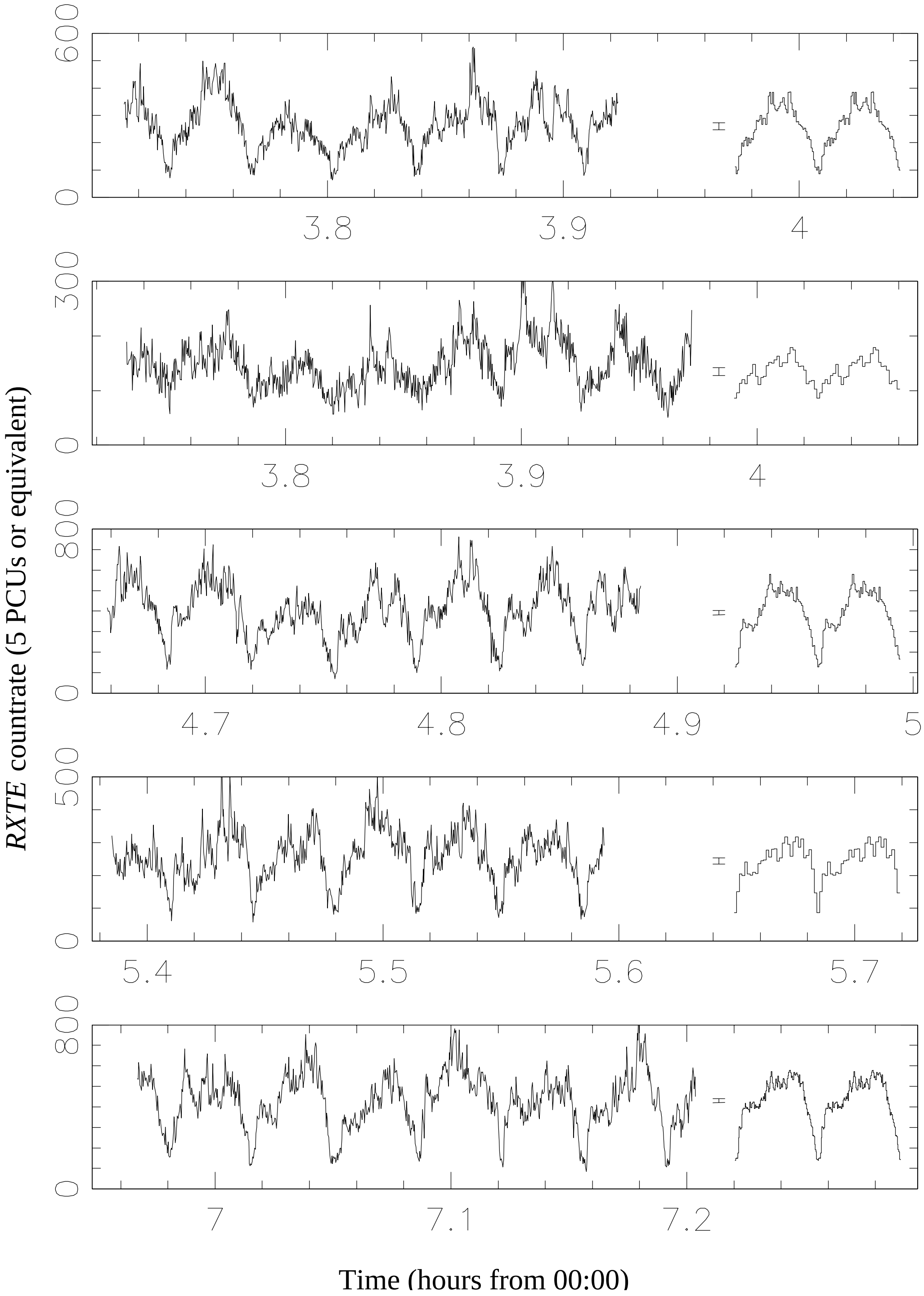

Figure 3.6 *RXTE* observations of GX 1+4, 16–20 May 1997. Each panel shows the count rate on 1 s bins for all 5 PCUs for the short observations on 16, 17, 18, 19 and 20 May from top to bottom respectively. Shown at the right are the corresponding mean pulse profiles (over two full cycles) with a representative error bar. The profiles are calculated by folding the 1 s lightcurves on the pulse period $126.4319(0) \pm 0.0005(5)$ s estimated from regular BATSE monitoring of the source. Note the change in scale on the y-axis between the panels

of the dips was reflected by the unusually low pulse fraction ≈ 0.5 (see Chapter 4).

The data from each of the observations V–Y were divided into 10 phase bins based on the pulse period $P = 126.4319(0) \pm 0.0005(5)$ s estimated from regular BATSE monitoring of the source. The ephemeris for each day was chosen arbitrarily so that the first phase bin was centered on the primary minimum, defined as phase 0.0. Each of the resulting phase-selected spectra were fitted with the usual spectral model with at most $T_{\rm e}$, τ and the `compTT` and Gaussian component normalisations free to vary. The other parameters were fixed at the fit values for the phase-averaged spectrum on the same day. For the May 16 and 19 observations $T_{\rm e}$ was also fixed at the same value as for the phase-averaged spectrum (see Table 3.4). Variation of $T_{\rm e}$ and τ with phase is small except close to the primary minimum. The fitted τ around phase 0.0 on May 16 and 18–20 was significantly greater than the value for the phase-averaged spectrum, by 20–60 per cent. This is typical for GX 1+4; see Chapter 5. For the May 17 observation however, at the much shallower primary minimum τ is instead marginally lower than the phase-averaged fit values, while $T_{\rm e}$ is somewhat higher (Figure 3.7).

3.2 Mean X-ray spectra

The observations which have been described in detail so far illustrate several aspects of spectral variability in GX 1+4. The column density $n_{\rm H}$ was particularly variable on timescales as short as hours. When the 2–20 keV unabsorbed luminosity was below $\approx 1.4 \times 10^{37}\ {\rm erg\,s^{-1}}$ the scattering plasma parameters were typically $T_{\rm e} \gtrsim 9$ keV and $\tau \approx 3$. At higher luminosities all fit parameters could be measured more precisely and generally $T_{\rm e} \approx 7.5$ and $\tau \approx 5$. Spectral analysis over many more observations would be necessary to determine whether this variation of fit parameters with luminosity is a general feature of the source. Fortunately, an extensive archive of *RXTE* observations of GX 1+4 and other sources is now available courtesy of the High Energy Astrophysics Science Archive Research Center (HEASARC) at the WWW address `http://heasarc.gsfc.nasa.gov`.

In this section I combine the spectral fitting results from the previous sections with results from previously published *RXTE* data obtained through the HEASARC archive. As before, Standard-2 mode spectra were extracted from each individual observation; examples are shown in Figure 3.8. Where significant count rate variations were seen within the observation (e.g. observation A, section 3.1.1) or the number of PCUs functioning varied, the observation was subdivided into two or more separate intervals and a spectrum extracted from each. As the spectral fit parameters (particularly the column density $n_{\rm H}$) tended to vary on hourly timescales it was necessary in some cases to further subdivide intervals to obtain adequate fits. A summary of the results from the spectral fitting is shown in Table 3.5.

For any spectral model, the fit statistic χ^2_ν depends strongly on the count rate during the observation. When the count rate (and hence the source-to-background ratio) is low, error bars on the spectral bins will be large, and typically more than

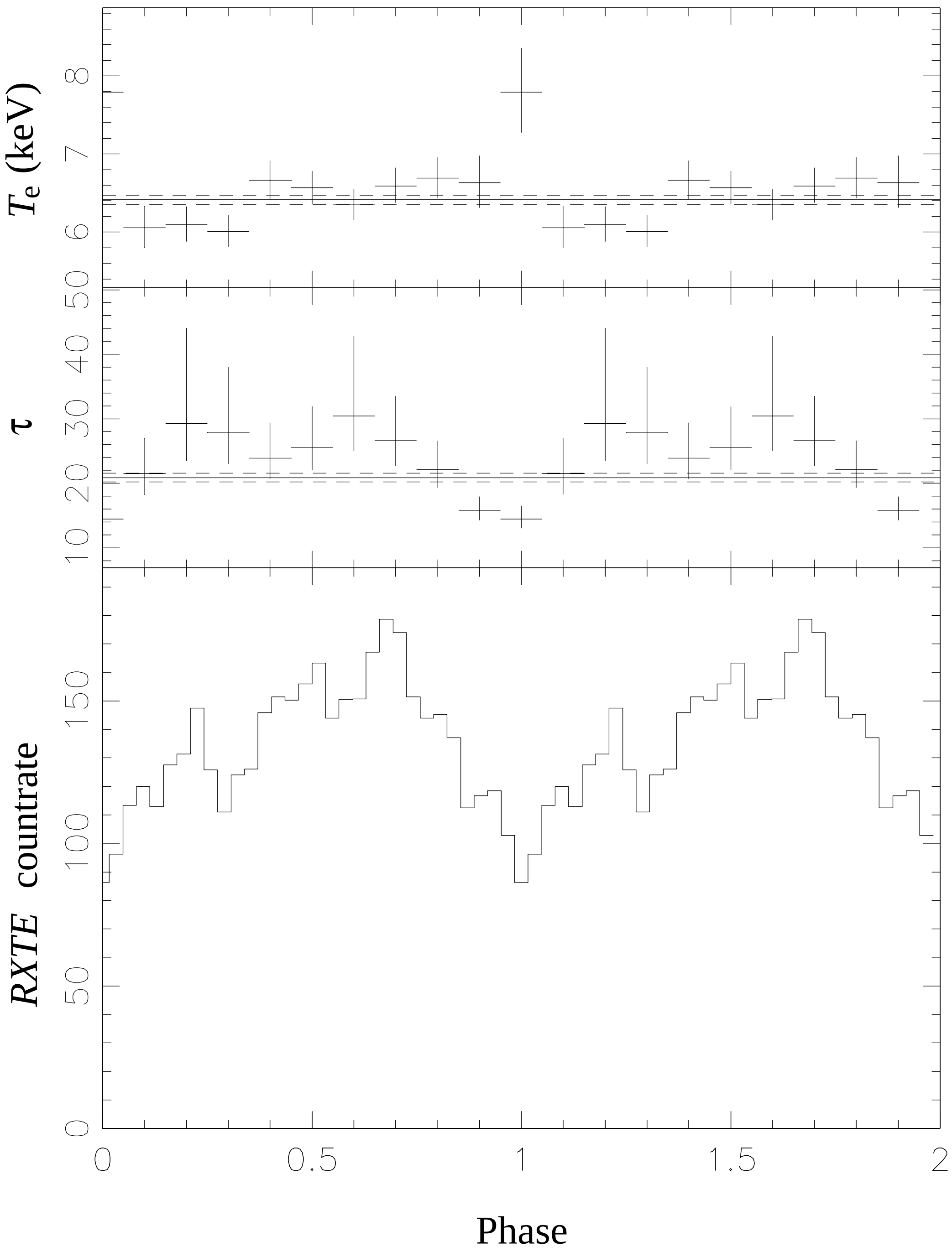

Figure 3.7 Pulse-phase spectroscopy of data from the *RXTE* observation of GX 1+4 on 1997 May 17 (Y2). The top and middle panels show the variation in fitted T_e and τ respectively with phase. The solid and dotted lines show the fitted values and 1σ uncertainty limits for the phase-averaged spectrum. Error bars represent 1σ uncertainty limits. The bottom panel shows the pulse profile over the full PCA energy range (as shown in Figure 3.6).

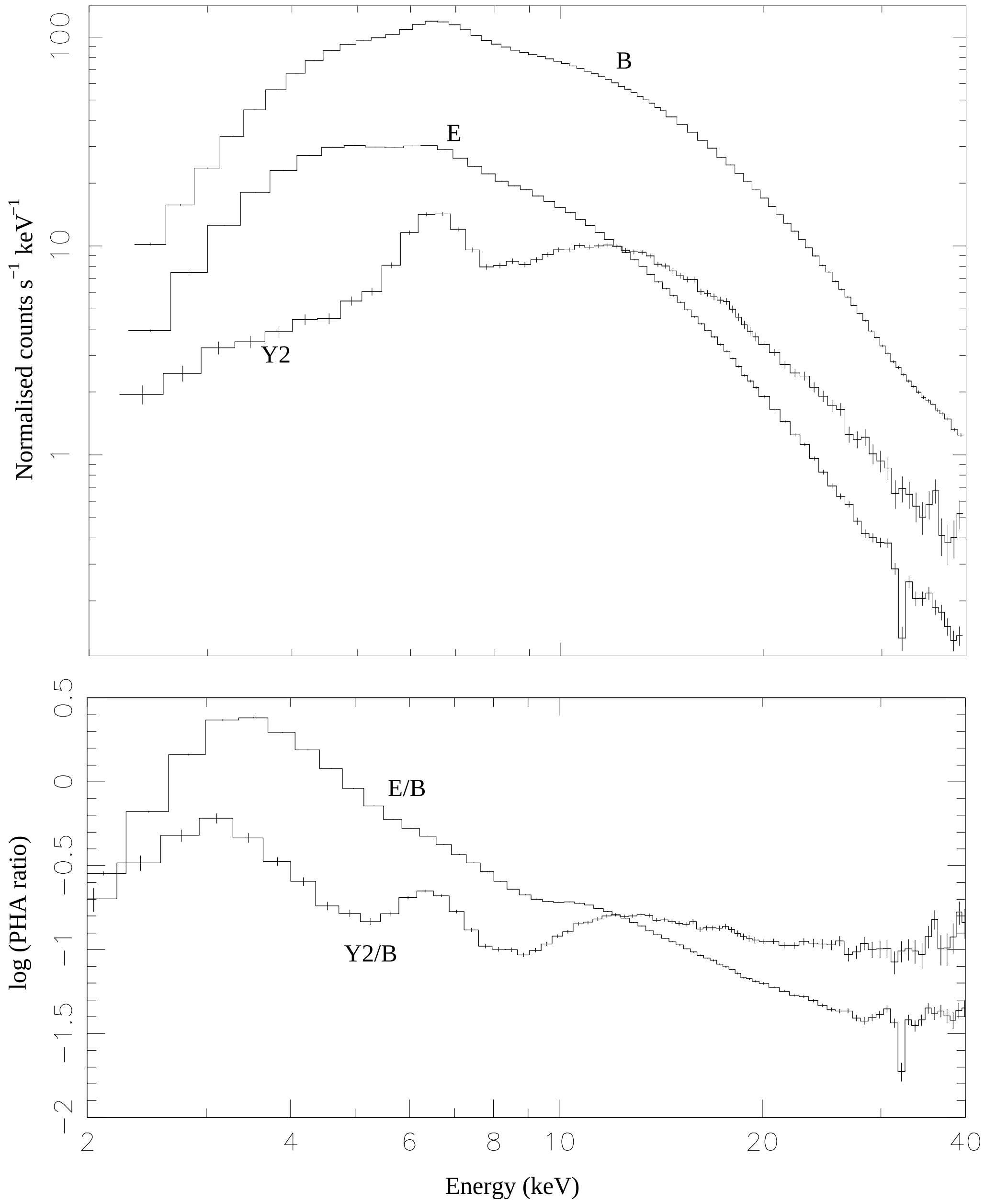

Figure 3.8 Sample raw *RXTE* spectra from GX 1+4. The top panel plots mean spectra from observations B (17 February 1996), E (8 June 1996) and Y2 (17 May 1997). The bottom panel shows the PHA ratio calculated by dividing the count rate in each spectral bin for spectra from observations E and Y2 by the spectrum from observation B.

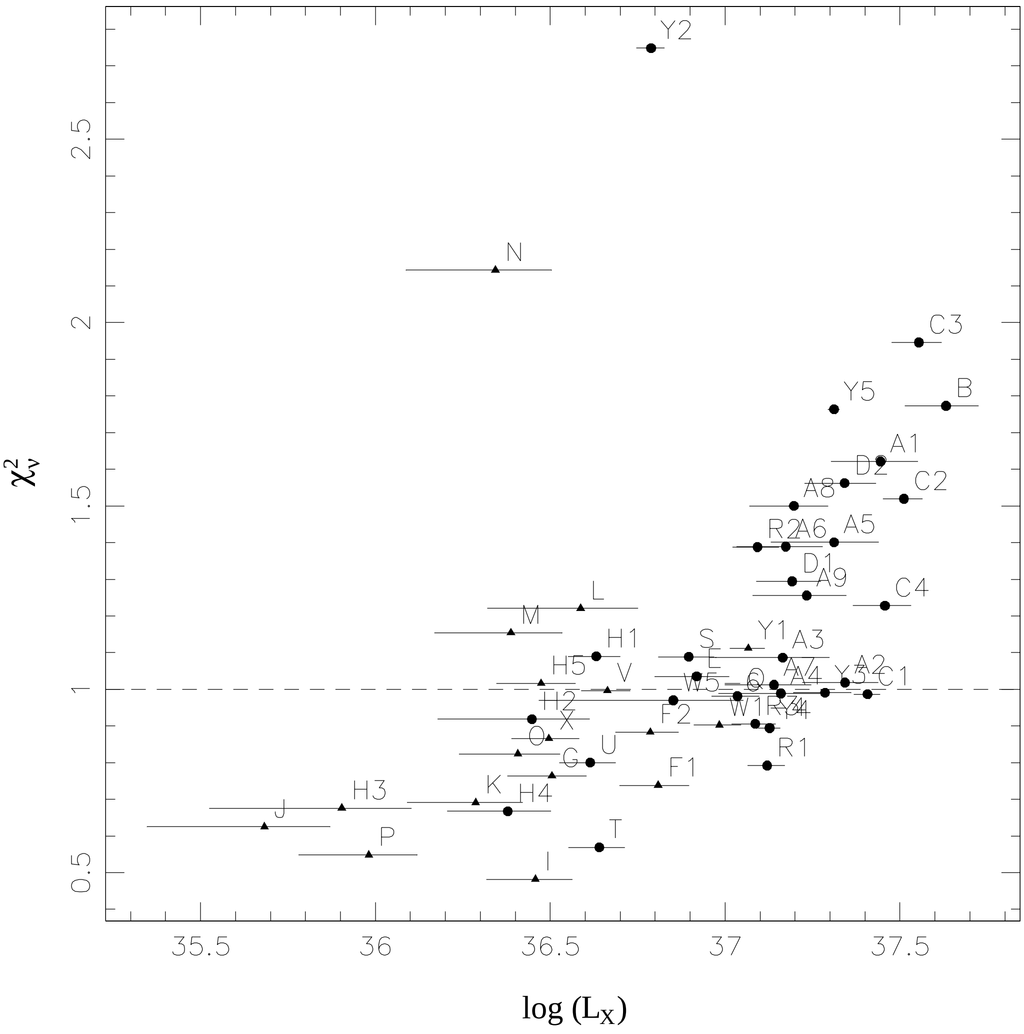

Figure 3.9 Reduced-χ^2 for fits to *RXTE* spectra from GX 1+4 using an analytic Comptonization continuum component (`compTT` in XSPEC) as a function of 2–20 keV luminosity (assuming a source distance of 10 kpc). Spectral range for fitting is typically 2.5–35 keV. Circles indicate those fits where all the spectral parameters are free to vary, while for observations marked by triangles at least one parameter (usually T_e) is fixed in order to obtain error limits on the other parameters. The markers are labelled with the letter corresponding to the observation, in some cases also with a number where the observation has been divided into separate intervals for spectral analysis. Error bars show 1σ limits calculated from the variance in the phase-averaged count rate over each observation (see Figure 3.1).

one (if not all) of the models will give a statistically acceptable spectral fit. The comparison between the models for those observations at the highest available count rates (e.g. A...E, Q...U) provided a much more stringent test. For the powerlaw continuum during these intervals χ^2_ν varied between $\approx$ 2–150, typically ≈ 5. A powerlaw modified by an exponential high-energy cutoff provided some improvement, with typical values $\approx$ 1.5–6, as did a broken power law (with two spectral indexes above and below some 'break' energy) giving $\chi^2_\nu \approx$ 1.5–4. A combination powerlaw and blackbody was acceptable for most of the observations with typical values ≈ 1.3, but can be as high as e.g. $\chi^2_\nu \approx 25$ for observation A1. Only the Comptonization continuum (see section 2.1.2) gave $\chi^2_\nu \lesssim 2.5$ for each of the spectra tested. Spectral fitting results using this model for the remaining *RXTE* observations are listed in Table A.1, Appendix A.

The expected correlation between χ^2_ν and source flux is readily apparent although there was also substantial scatter (Figure 3.9). Significant variations in χ^2_ν were seen even between immediately adjacent observations (e.g. R1/R2/R3). While it was necessary to subdivide certain intervals (most noticeably the second half of observation A; see section 3.1.1) to obtain reasonable values of χ^2_ν, the Comptonization model still unambiguously offered the best fit over the shorter integration times which resulted.

The fitted values of the source spectrum temperature T_0 were seen to cluster strongly around the weighted mean of 1.28 ± 0.05 keV[1] over a wide range of luminosity (Figure 3.10a). Below $\approx 3 \times 10^{36}\ \mathrm{erg\,s^{-1}}$ (2–20 keV, assuming a source distance of 10 kpc) the fit values were subject to large uncertainties but were yet consistent with the mean. The fit parameter ranges are limited at the lower boundary by the minimum allowed by the `compTT` implementation in XSPEC of 0.001. Several previously noted spectra suggest much lower values of T_0, with observations

[1] The quoted error for each set of spectral fit parameter values $\{x_i\}$ with associated errors $\{\sigma_i\}$ is

$$\sigma_{\mathrm{w}} = \sqrt{\frac{\Sigma(x_i - \bar{x})^2/\sigma_i^2}{\Sigma(1/\sigma_i)^2}} \tag{3.1}$$

where $\bar{x} = \Sigma(x_i/\sigma_i^2)/\Sigma(1/\sigma_i^2)$ is the conventional weighted mean. An added complication arising from the XSPEC parameter ranges is that they are often asymmetric about the best fit value. If $x_i > \bar{x}$, the lower 1σ uncertainty range σ_{i-} is used, while if $x_i < \bar{x}$ the upper range σ_{i-} is used instead. Since $\bar{x}$ must be calculated in the same manner, both $\bar{x}$ and σ_{w} are determined simultaneously using an iterative procedure where the initial value of $\bar{x}$ is the unweighted mean.

While the formal statistical properties of σ_{w} have not been established (to my knowledge), it is an obvious extension of the usual definition of the standard deviation, appropriate for data with heteroscedastic errors. Note that just as the weighted mean $\bar{x}$ reduces to the normal definition of the mean when $\sigma_i = \sigma$ for all i, so does σ_{w} to the usual definition of the standard deviation. Furthermore, σ_{w} is clearly a better descriptive parameter than the other alternative, the standard error in the mean $\sigma_{\bar{x}} = \Sigma(1/\sigma_i^2)$ since this does not take into account the spread of the x_i values. (The calculation of $\sigma_{\bar{x}}$ implicitly assumes that each measurement x_i is drawn from the same parent population, with the same mean and standard deviation; clearly this is not necessarily true for the spectral parameter values, where there may also be intrinsic scatter due to genuine spectral variation).

A5, A9 and also F1 resulting in values of $T_0 < 0.5$ keV (although at rather low significance).

Parameter	$L_X < 1.4 \times 10^{37}$ erg s^{-1}	$L_X > 1.4 \times 10^{37}$ erg s^{-1}
T_0 (keV)	1.28 ± 0.05	
T_e (keV)	7.4 ± 0.9	
τ	3.1 ± 0.3	5.2 ± 0.5
y	0.78 ± 0.09	1.7 ± 0.2
E_{Fe} (keV)	6.52 ± 0.04	6.43 ± 0.03
σ	0.30 ± 0.07	
χ^2_ν	1.12 ± 0.44	

Table 3.5 Weighted mean and standard deviation σ_w (equation 3.1) of spectral parameters for GX 1+4 as a function of the 2–20 keV luminosity. Shown are the `compTT` component source spectrum temperature T_0, scattering plasma temperature T_e and optical depth τ, Compton y-parameter (calculated according to equation 1.7), Fe line component center energy E_{Fe} and Gaussian width σ, and the mean reduced-χ^2. Note that the calculation of the mean τ and y in the low-luminosity class excludes the results for observations P and Y2 (see section 3.1.3).

The fitted optical depth τ varied between 2–6 over the measured luminosity range of $10^{35.5}$–$10^{37.5}$ erg s^{-1} (Figure 3.10b). Note that this figure omits the value for observation Y2, which was by far the highest measured at around $\tau = 20.9^{21.6}_{20.2}$ (see section 3.1.3). When the luminosity was $\lesssim 1.4 \times 10^{37}$ erg s^{-1} the τ values clustered around 3, whereas above that a range of 4-6 was more typical. While the mean values disagree at the 3σ level only (Table 3.5), the calculated T-statistic for the two groups is 10.4, indicating a significantly different mean at a confidence level of 8σ ($P = 1.69 \times 10^{-13}$; however this does not take into account the varying errors on each parameter). The variance was somewhat greater at high luminosity.

The observed variation may instead be interpreted as a rough correlation between τ and L_X. To test the significance of the relationship I used the BCES(Y—X) estimator of Akritas and Bershady (1996). Ordinary weighted least squares methods are not strictly appropriate for fitting data with heteroscedastic (varying) errors in both parameters, and where there are thought to be *systematic* errors in addition to measurement errors in the parameters. The resulting gradient for a linear fit confirms a significant (6σ) relationship, with gradient $b = 0.851 \pm 0.141$ (curved line in Figure 3.10b). The straight line represents a logarithmic fit with a slope of 2.02 ± 0.38, significantly different from zero at a similar level (5σ). However, note

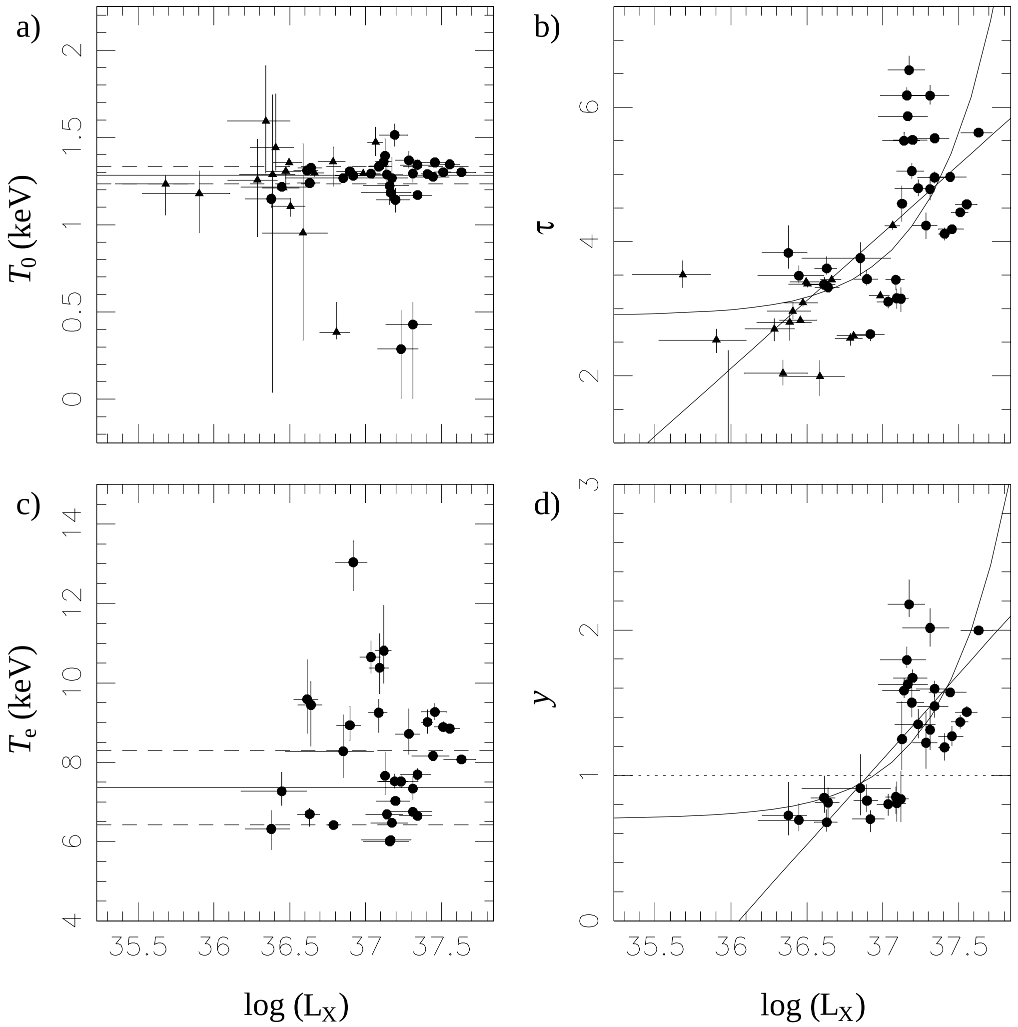

Figure 3.10 Fit values for the Comptonization continuum component ('compTT' in XSPEC) parameters for spectral fits to *RXTE* observations of GX 1+4 versus unabsorbed 2–20 keV luminosity (assuming a source distance of 10 kpc). a) Source spectrum temperature T_0; b) optical depth for scattering τ; c) plasma temperature $T_{\rm e}$; and d) Compton y-parameter (calculated from the fitted τ and $T_{\rm e}$ values). The weighted mean and $1\sigma_{\rm w}$ (see equation 3.1) ranges for T_0 and $T_{\rm e}$ are shown by solid and dashed lines respectively. Linear and logarithmic fits to τ and y versus $L_{\rm X}$ are plotted as solid lines. Error bars show 1σ confidence limits from XSPEC. Other details are as for Figure 3.9.

that separate fits to the data above and below $L_X = 1.4 \times 10^{37}$ erg s^{-1} tell a different story, with (linear) gradients $b = -0.63 \pm 0.49$ and 0.62 ± 0.30 respectively.

It is possible that the variation of fitted τ values was due to aliasing by some dependence of the fitting algorithm on the varying count rate. This can be tested by (for example) selecting a spectral model with parameters from one of the higher flux observations, generating a simulated spectra with much lower flux, and comparing the resulting spectral fitting results. In general the spectral parameters were found to depend only weakly on flux for simulated observations. There was certainly no abrupt drop to lower τ values as the simulated flux was decreased. Visual inspection of representative spectra from the high- and low-τ groups further supports the significant differences between the two (Figure 3.8). Fits to mean spectra from observations B and E gave similar column densities of $n_H = 5.35^{5.56}_{5.14}$ and $4.35^{4.87}_{3.83}$ respectively. However, the peak in the spectra clearly occurred at different energies. The PHA ratio between the two demonstrates that the high-energy slopes are different, as is the turnover energy (where the slope changes around 10 keV; note the 'kink' in the PHA ratio around that energy).

The corresponding plot for T_e shows much more evenly distributed fit values, with no significant variation observed with luminosity. The mean value was $T_e = 7.4 \pm 0.9$ keV. With low count rates it was much more difficult to determine T_e precisely, and in fact for approximately half the spectra which fell into the lower half of the luminosity range ($< 1.4 \times 10^{37}$ erg s^{-1}) the value could not be determined at all (note the smaller number of points in Figure 3.10c compared to a,b). For these spectra I fixed the value at 9 keV, consistent with the mean for this group.

The Compton y-parameter was calculated for each spectra from the fitted τ, T_e. Since $kT_e \ll m_e c^2$ the nonrelativistic form is more appropriate (equation 1.7). The plot of y as a function of source luminosity exhibits similar clustering to the corresponding plot with τ (Figure 3.10d). The two groups fall neatly on either side of the line $y = 1$, normally considered the limiting value between spectra which are weakly modified ($y \ll 1$) and spectra strongly modified ($y \gg 1$) by Comptonization. The mean values for the low- and high-luminosity groups were 0.78 ± 0.9 and 1.6 ± 0.2 which differ at the 3.6σ level. Linear or logarithmic fits (solid lines) again resulted in slopes which are significantly different from zero at the 6σ level (0.338 ± 0.056 and 1.17 ± 0.19 respectively).

The mean center energy of the Gaussian component, representing fluorescent Fe Kα emission, was 6.45 ± 0.05 keV. Least squares fits to the center energy versus L_X suggest systematic variation at a significance level of at least 4σ, with higher center energies measured at lower flux (although with correspondingly larger error bars; Figure 3.11a). The equivalent width (EW) on the other hand, did not appear to depend systematically on the luminosity (Figure 3.11b), but was roughly correlated with the absorption column density n_H, as has been found in previous observations (Kotani et al., 1999 Figure 3.11c). The correlation has significant scatter, with the results from 11-21 July 1996 (G,H) in particular populating a distinctly different area of the graph than the majority of measurements. The column density n_H varied by more than two orders of magnitude over the course of the observations, often on

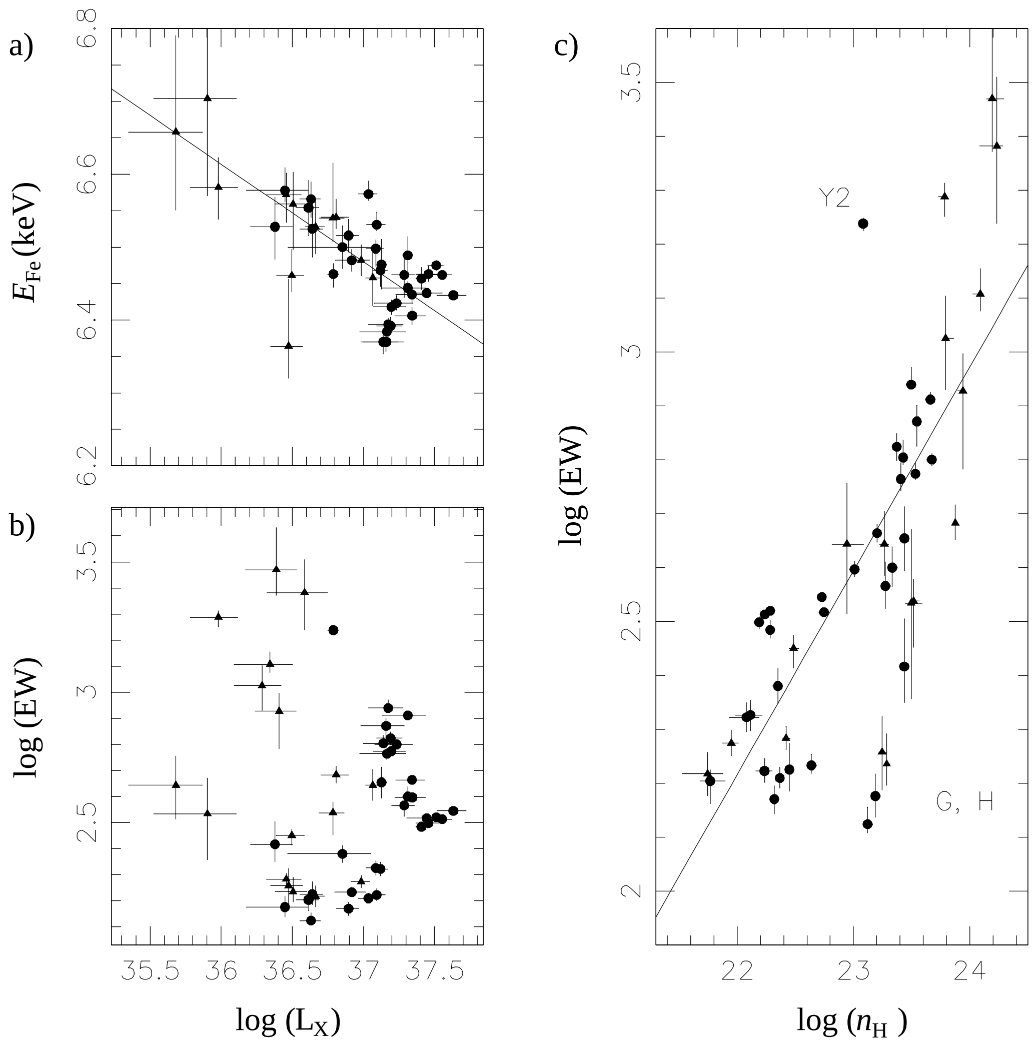

Figure 3.11 Measurements of the strong Fe fluorescence line in GX 1+4. a) Line center energy and b) equivalent width (EW) as a function of the 2–20 keV luminosity (assuming a distance of 10 kpc). c) EW plotted as a function of the absorption column density n_H. Solid lines show the lines of best fit; error bars represent the 1σ uncertainties. Other details are as for Figure 3.9.

short timescales. In particular, the ≈ 1 d observation in February 1996 (observation A, section 3.1.1) featured a dramatic rise in scattering column density $n_{\rm H}$ over just a few hours. Also notably different was the measurement for observation Y2, with $n_{\rm H} \approx 10^{23}$ cm^{-2} but EW≈ 1.8 keV.

3.3 Discussion

The archival data accumulated through *RXTE* observations of GX 1+4 cover a wide range of source conditions for this enigmatic pulsar. Particularly clear is the degree of variability of the source on all timescales, from seconds to years.

Analysis of the previously unpublished observations have provided some important new results. During February 1996 the source was close to the brightest level seen by *RXTE* between 1996 and mid-1997, and the ~ 1 d observation at that time featured a dramatic rise in scattering column density $n_{\rm H}$ over just a few hours. This event was very similar to that observed during the July 1996 observation ('H'; Galloway et al., 2000). Such events are clearly relatively common and may occur at both high and low luminosities. This strongly suggests $n_{\rm H}$ variations are a significant source of observed count rate modulation on hourly (and longer) timescales. The sensitivity limit of *RXTE* does not provide a high enough count rate to resolve spectral variations on smaller timescales, but $n_{\rm H}$ variations may have a significant influence there too.

The extremely unusual spectra observed during May 1997 (Y2) provides evidence for source conditions which do not appear to have been repeated in any of the other *RXTE* observations, and which has perhaps been observed just once or twice before. (The observation during which GX 1+4 was discovered found the source to be pulsing strongly during the first pointing, but not the second, which occurred only a short time later; Lewin et al. 1971). An even lower 20–100 keV pulse fraction $\approx 35\%$ was obtained from balloon-borne instruments on 11 December 1993 (Rao et al., 1994). Then also the spectrum was found to be unusually hard with power law energy index 0.54 ± 0.18. Power law fits to 20–40 keV *RXTE* spectra during observation Y2 were even more extreme with power law *photon* index $1.16_{1.04}^{1.29}$. BATSE flux measurements indicate that following the December 1993 observation the source entered a hard X-ray low state with $L_{\rm X} \lesssim 0.1\ {\rm keV\,cm^{-2}\,s^{-1}}$ (20–60 keV) which persisted (with brief interruptions) for the next ≈ 250 d. In contrast, observation Y was made during a flare lasting ≈ 20 d where the flux peaked at $0.2\ {\rm keV\,cm^{-2}\,s^{-1}}$.

The interpretation of these results are quite problematic. If the spectral fit parameters are reliable the source has apparently switched briefly to a completely different accretion regime. As I discuss in Chapters 4 and 5, the dip normally observed in the 1 s light curves and mean pulse profiles is probably related to enhanced Compton scattering due to the closest passage of the accretion column axis to the line of sight. Its disappearance suggests that the accretion column has been disrupted, or perhaps that the column has moved sufficiently that the column axis no longer passes close to the line of sight each rotation period. The pulse-phase spectral variation was also different to that normally observed in the source. Typically τ is significantly greater than the mean value around the primary minimum (see Chapter 5); this is the case for the other observations in 1997 May, Y1 and Y3–5. For observation Y2 τ was instead somewhat *less* than the phase-averaged value around the primary minimum. These results point to a substantially different distribution of matter close to the source.

That the optical depth has increased fivefold compared to values obtained before and after suggests that the source has been 'smothered' by hot accreting material, which presumably also contributes to the unusually strong Fe line emission. The increase in the equivalent width was not accompanied by the usual increase in the neutral column density $n_{\rm H}$, further indicating varying conditions close to the star rather than the outer circumstellar matter. That material can enter the magnetosphere of the star apparently without being channeled along the field lines suggests either that the magnetic field strength is in fact low, or that some global magnetohydrodynamic instability is operating which can significantly disrupt the flow. The other spectra from observation Y give fitted τ values at intermediate levels between the two groups suggested by Figure 3.8b. Both Y2 and the earlier observation with similar spectra (Rao et al., 1994) were made coincident with moderately significant variations in the 20–60 keV flux measured by BATSE. It seems possible that observation Y2 was made at a time of transition between the two mean spectral states (see below).

The iron line energy and the observed relationship between equivalent width and $n_{\rm H}$ are roughly consistent with the spherical distribution of matter inferred by Kotani et al. (1999). However the minimum timescale of $n_{\rm H}$ variations ≈ 2 h is much too rapid to be attributable to the negative feedback effect which those authors suggest regulates mass transfer to the neutron star in the long term. The variation may instead be an indication of significant inhomogeneities in the stellar wind from the companion on spatial scales of

$$\delta s \sim 7 \times 10^9 \left(\frac{v_{\rm w}}{10\ {\rm km\,s^{-1}}} \right)\ {\rm cm} \tag{3.2}$$

along the line of sight to the neutron star. Infrared observations suggest that $v_{\rm w}$ may be as much as 250 km s^{-1} (Chakrabarty et al., 1998), but since the line of sight may intercept the system at varying distances form the companion (depending upon the orbital phase) the local wind speed may also vary due to deceleration. The suggestion of an increase in $E_{\rm Fe}$ at lower $L_{\rm X}$ is contrary to what might be expected if the ionisation balance of the circumstellar material depends solely on the X-ray emission from the pulsar. Clearly, the situation is much more complex than that, and future observations with high-resolution instrument such as *Chandra* may be the only way to improve our understanding of the wind dynamics in this source.

The inclusion of all the archival *RXTE* data in the spectral analysis has confirmed the general applicability of the Comptonization model of Titarchuk (1994) ('`compTT`' in XSPEC) to GX 1+4 spectra. Similar models have been used to fit spectra for this source in previous analyses (e.g. Staubert et al., 1995, Galloway et al., 2000);

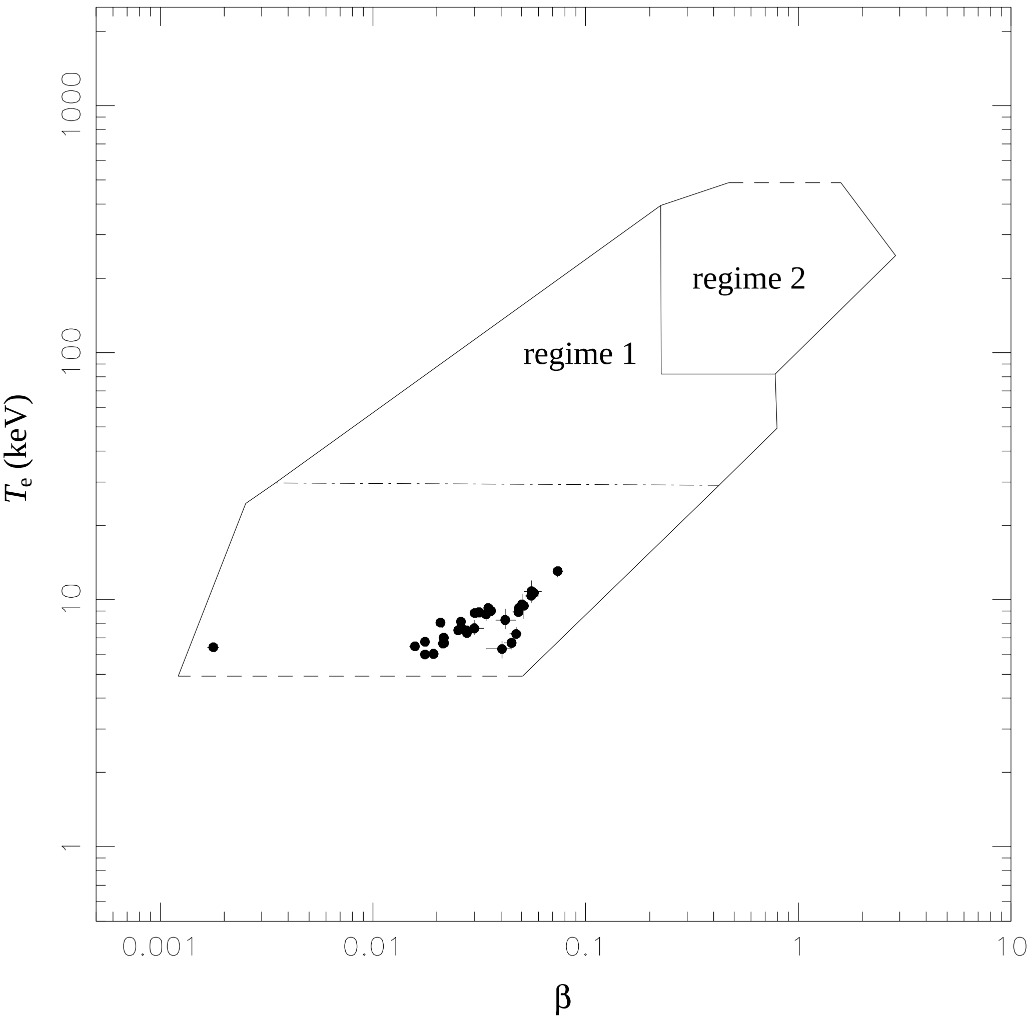

Figure 3.12 Scattering plasma temperature T_{e} versus Titarchuk β-parameter appropriate for disc geometries (equation 3.3). The enclosed regions are those plotted in Figure 7 of Hua and Titarchuk (1995), and delineate the range of parameters over which the analytical model of Titarchuk (1994) is consistent with equivalent Monte Carlo calculations. Error bars show 1σ confidence limits.

however it has only been possible to eliminate all other candidate models on the basis of the χ^2 fit parameter using data from *RXTE*. To assess the reliability of the model over the range of parameters obtained for GX 1+4, I calculated the β-parameter appropriate for disc geometries:

$$\beta = \frac{\pi^2}{12(\tau+2/3)^2}(1-e^{-1.35\tau}) + 0.45e^{-3.7\tau}\ln\left(\frac{10}{3\tau}\right) \tag{3.3}$$

(Hua and Titarchuk, 1995). For the range of τ and $T_{\rm e}$ appropriate for GX 1+4, the analytic model has been shown to yield results consistent with Monte-Carlo simulations (Figure 3.12; Hua and Titarchuk, 1995) and thus should provide reasonable results. The model simulates Comptonization in an unmagnetised plasma, and since the available evidence points towards a strong magnetic field in GX 1+4 (although this awaits confirmation by more direct measurements such as a cyclotron resonance line) the model fit parameters may not be an accurate measure of the source conditions. It is likely that the principal effect of the magnetic field will be to make the spectral parameters dependent on the emission angle. Hence the model fit parameters obtained from the mean spectra are expected to be an approximate measure of the actual physical conditions in the source (L. Titarchuk, pers. comm.).

The source spectrum presumably originates from the polar cap itself, or perhaps a slab-shaped post-shock region of the column. Assuming that the majority of the X-ray emission originates from a blackbody at most the size of the neutron star ($R_* \approx 10$ km) the calculated temperature is $T_0 \gtrsim 0.5$ keV. The model fit values for the input spectrum temperature $T_0 \approx 1.3$ keV was consistent with this calculation. The fit values for T_0 were remarkably consistent for the majority of spectra. The observation of a much lower value during subintervals of observation A was the exception but the errors were quite large. Since there was a suggestion of reduced pulse fraction at times during this observation, it is possible the latter measurements were related to a spectrum similar to that from observation Y2. The polar cap temperature is presumably maintained by the supply of energy from residual thermal and kinetic motion of the accreting plasma in competition with cooling by radiation and conduction through the neutron star crust. That the temperature varies little over the range of source luminosities points to extremely efficient cooling mechanisms.

Estimating the physical dimensions of the scattering region from the measured τ values is complicated by the degree of inhomogeneity likely to exist in both density and velocity of the accretion column plasma (e.g. Becker, 1998, Klein et al., 1996). The accretion luminosity (which is equal to the X-ray luminosity $L_{\rm X}$ to within the uncertainty of the source distance) is $L_{\rm acc} \approx GM_*\dot{M}/R_*$ and thus

$$\begin{aligned}\dot{M} &\approx \frac{R_*}{GM_*}L_{\rm acc} \\ &= 5.0\times10^{16}\,L_{37}\ {\rm g\,s^{-1}}\end{aligned} \tag{3.4}$$

where $L_{\rm acc} = L_{37}\times10^{37}\ {\rm erg\,s^{-1}}$. The cross-sectional area of the base of the accretion column is some fraction of the surface area of the neutron star, i.e. $A = f\,4\pi R_*^2$.

The value of f is thought to depend on the magnetic field strength and also the inner disc radius, since this determines which magnetic field lines form the accretion column between the inner disc edge and the polar cap. It is usually estimated that $f \sim 10^{-4}$–10^{-1} (e.g Frank et al., 1992) with smaller values appropriate for higher magnetic field systems. Increased $\dot{M}$ is thought to push the disc to smaller radii (Ghosh and Lamb, 1979a,b), resulting in an increase in the extent of the accretion column since the field lines which delineate the accretion column will be pushed to lower magnetic latitudes, i.e. a greater distance from the magnetic pole itself.

The optical depth for each photon trajectory will be different due to the temporal and spatial variations of the plasma density and velocity within the column. However, because each spectrum is comprised of many photons each following different trajectories, we may adopt an effective mean bulk velocity $\tilde{v}$ and density $\tilde{N}_{\rm e}$ over the scattering region. Assuming (for arguments' sake) that the column is laterally homogeneous, essentially all the accreting mass will pass through the scattering region in which case

$$\tilde{N}_{\rm e} = \frac{\dot{M}}{A\tilde{v}m_{\rm p}}\ {\rm cm}^{-3} \tag{3.5}$$

where $m_{\rm p}$ is the proton mass. Thus the optical depth for a photon moving perpendicular to the column axis may be approximated by

$$\begin{aligned} \tau &\sim \sqrt{A}\,\tilde{\sigma}\tilde{N}_{\rm e}(r) \\ &= \frac{k}{0.5}\left(\frac{f}{0.01}\right)^{-1/2}\left(\frac{\tilde{v}}{c}\right)^{-1} L_{37} \\ &\approx 2-6 \quad \text{(measured)} \end{aligned} \tag{3.6}$$

where $\tilde{\sigma} = k\sigma_{\rm T}$ is the effective cross section for Compton scattering. In actual fact the cross section depends upon both the photon energy and the angle between the photon propagation direction and the local magnetic field vector (e.g. Daugherty and Harding, 1986). However, since the cyclotron energy in GX 1+4 is $\gtrsim 200$ keV (given the estimated surface magnetic field strength), the variation with energy over the (relatively small) energy band of interest will also be small. And since each spectrum is averaged over all neutron star phases, we also average over a range of viewing angles with respect to the magnetic axis, which is unlikely to change significantly with $\dot{M}$. From examination of Fig. 3 in Daugherty and Harding (1986), for GX 1+4 a range of $k = 0.1$–0.5 is probably reasonable, depending upon the source aspect.

Equation 3.6 illustrates the broad-scale relationships governing the (laterally homogeneous) column structure: firstly, if the cross-sectional area f of the column increases with the other free parameters held constant, the mean density (and hence τ) must decrease; and secondly, if the mean velocity should decrease, τ must increase. With $L_{\rm X}$ varying by more than two orders of magnitude over the *RXTE* observations of GX 1+4, either f or $\tilde{v}$ must also vary to a comparable degree in order to be consistent with the small observed range of τ. And since $\tilde{v}$ is expected to be *inversely* proportional to $L_{\rm X}$ (due to the increasingly important effects of radiative deceleration of the flow), equation 3.6 implies that the cross-sectional area of the accretion column must increase appreciably with L_X. In fact, f must vary by a factor of at least 10^3 over the observed range of L_X, more if $\tilde{v}$ decreases significantly with L_X. Given reasonable estimates for f at low luminosity, such an increase in area would indicate the accretion column growing to cover the entire surface of the neutron star over the range of L_X spanned by the *RXTE* observations. This does not seem feasible given the estimated high magnetic field of the source and also the fact that strong pulsations are observed at the highest measured L_X. Measurements of the width of the dip which forms the primary minimum in the pulse profile suggest a much more modest variation of the column dimensions with L_X (see Chapter 4).

It appears that the initial assumption is incorrect, and there probably is a significant lateral density gradient within the accretion column. An optically thick (perhaps shock-heated) core region may be surrounded by a less dense region through which X-ray photons are emitted, from optical depths corresponding in the mean to the measured value. In that case the mass flow rate through the scattering region would be only a small fraction of the total $\dot{M}$, and similarly the cross-sectional area of the scattering region is only a fraction of the total column area. In that case equation 3.5 is no longer valid, and the observational properties of the accretion column are instead dominated by the lateral density gradients present within it.

The suggested correlation between τ and $L_X$may partially arise from grouping of the fit values around different mean values above and below $L_X \approx 1.5 \times 10^{37}$ erg s^{-1}, since the correlation does not seem to be present in the both the high- and low-luminosity observations fitted separately. This implies two distinct spectral states for the source, which appears to be borne out by the clustering of τ values for high- and low-luminosity spectra around significantly different mean values. A possible explanation for the distinction is the presence of a radiative shock in the higher luminosity observations. The T_e parameter is a measure of the temperature of the plasma within the scattering region; the generally lower T_e at higher luminosities is the opposite of what might be expected if shock heating is present. However, in the low L_X case the kinetic energy of the plasma from the infall velocity may be comparable to the thermal energy, in which case the spectral shape may owe more to the bulk fluid properties than T_e. Note the significant variations in the fitted T_e as a function of pulse phase in phase-selected spectra from both GX 1+4 (Chapter 5) and RX J0812.4−3114 (Chapter 6). For spherical inflow, neglecting shock deceleration of the flow close to the surface of the neutron star, bulk Comptonization will give rise to a turnover at energies > 100 keV (Titarchuk et al., 1996), far higher than the ~ 10 keV typically seen in the spectra from GX 1+4 (Table 3.5). However, the velocity structure in the accretion column is substantially more complex, and it is not clear how this may interact with the thermal properties of the plasma to give rise to the observed cutoff energy.

There was significant overlap in luminosity between the two groups, even neglecting the uncertainties which were also present in the luminosity estimations. This was particularly true for observation A, when the latter half of the observation found the luminosity decreasing to below 1.4×10^{37} erg s^{-1} (2–20 keV), but with a fitted $\tau \gtrsim 5$. The implication is that the shock, once formed, may be present at lower luminosities than it first arose, indicating a hysteresis between the shock formation and the luminosity. (On the other hand, bolometric corrections to the flux for the two different classes of spectra may eliminate the overlap). The combined variation of τ and $T_{\rm e}$ result in the calculated Compton y-values forming two groups which are separated by the line $y = 1$. It is compelling to suggest that the switch is due to a change from a situation when Comptonization is relatively unimportant to one where it is the dominant effect in spectral formation, but such distinctions are really only appropriate for the asymptotic cases $y \ll 1$ and $y \gg 1$ respectively. Additionally there is no way to estimate the systematic errors on any of the parameters involved (recall that the measured τ is only a relative measure of the optical depth in the column, as noted in section 2.1.2), and so the fact that the y-values cross the $y = 1$ line as $L_{\rm X}$ increases was perhaps merely a coincidence.

Chapter 4

Luminosity dependence of pulse profiles from GX 1+4

4.1 Pulse period determination

Pulse periods for each of the observations listed in Table 3.1 were determined as described in section 2.1.3 (Table 4.1). When an observation spans several days (with the long gaps this entails) peaks in the χ^2-P plot were rather poorly defined, and it was then necessary to separate the observation into two or more distinct intervals. These are denoted in the table with a letter and number $1 \ldots n$ (observation F). Ideally in such a case the two separate measurements might be combined to give a better overall estimate of the pulse period, but the discrepancy between the errors on the measurements for interval F1 and the much shorter F2 makes this somewhat pointless. (Note that the disagreement between the two period values is only at the 2σ level and thus not significant). For some observations (in particular V–Y) it was not possible to determine a period at all using phase folding. Instead the period interpolated from BATSE measurements was used; these values are also shown in Table 4.1.

From February 1996 to May 1997 GX 1+4 experienced steady spin-down at a mean rate of $\approx 7 \times 10^{-8}\ \mathrm{s\,s^{-1}}$ ($\approx 1.8\%\ \mathrm{yr^{-1}}$; Figure 4.1, top panel). Between TJD 10120 and 10320 the mean rate was somewhat lower, $\approx 5.0 \times 10^{-8}\ \mathrm{s\,s^{-1}}$ ($1.2\%\ \mathrm{yr^{-1}}$); following the low flux period between TJD 10350 and 10400 the rate more than doubled to $\approx 1.0 \times 10^{-7}\ \mathrm{s\,s^{-1}}$ (2.6% per year). During the intervals of low flux (e.g. TJD 10260–80, TJD 10320–420) the BATSE-measured period exhibited frequent excursions above and below the line of best fit of the order of 0.5 s. Transitions from spin-down to spin-up, as might be suggested by these excursions, are rather rare in this source and have only been definitely observed a few times over the ~ 30 yr of observations (Chakrabarty et al., 1997). Despite the large variation, the quoted errors in frequency are still of the order of 0.01% and it seems more likely that the error is grossly underestimated. A more detailed re-analysis of the BATSE measurements during the *RXTE* observation on 19-21 July 1996 (TJD 10283–5) did however confirm a suspected short-lived torque reversal (Giles et al., 2000). In comparison the $P_{\rm fit}$ values from *RXTE* observations generally increase monotonically through the low-flux interval.

The discrepancy between the two methods is clearer from the plot of $P_{\rm fit}$ against $P_{\rm BATSE}$ (Figure 4.1, middle and bottom panels). The significant scatter of points about the line of equality between 124 and 125 s is probably due to errors in the BATSE period estimations from the low-flux interval (as discussed above). Otherwise the agreement is quite good, to the order of 0.1 s. One additional source of disagreement is the choice of energy range for the lightcurve to fold. The BATSE data used was from channel 1 of the DISCLA mode (20–50 keV), while the PCA typically is most sensitive between 2–20 keV. As a test, the pulse period for observation C was estimated by folding *RXTE* lightcurves in the 2–7, 7–20 and > 20 keV bands. The resulting periods were 123.9399, 123.9541 and 123.9625 s respectively, a variation several orders of magnitude greater than the estimated error on the full range lightcurve determination (Table 4.1).

ID	TJD_{mean}	ΔTJD	Period (s) P_{fit}	P_{BATSE}
A	10126.07861	0.97500	$123.61548(6) \pm 0.00003(9)$	$123.6177(2) \pm 0.0004(0)$
B	10130.23760	0.20818	$123.6368(1) \pm 0.0003(8)$	$123.6425(0) \pm 0.0003(0)$
C	10196.89689	0.19378	$123.9475(9) \pm 0.0004(3)$	$123.9392(8) \pm 0.0002(0)$
D	10224.70640	0.09837	$124.105(4) \pm 0.002(0)$	$124.0917(2) \pm 0.0004(1)$
E	10242.34997	0.29820	$124.1677(0) \pm 0.0005(6)$	$124.1701(4) \pm 0.0008(6)$
F1	10262.32518	0.09334	$124.248(4) \pm 0.007(9)$	$124.238(5) \pm 0.001(2)$
F2	10262.97675	0.01260	$124.4(8) \pm 0.1(2)$	$124.251(2) \pm 0.001(1)$
G	10275.84449	0.15640	$124.309(2) \pm 0.006(2)$	$124.327(3) \pm 0.001(4)$
H	10284.40497	1.41095	$124.3662(2) \pm 0.0001(6)$	$124.282(3) \pm 0.001(0)$
I	10331.03424	0.18848	$124.506(5) \pm 0.001(5)$	$124.346(3) \pm 0.001(0)$
J	10351.55255	0.17140	$124.575(0) \pm 0.006(9)$	$124.8718(1) \pm 0.0001(3)$
K	10364.42440	0.03834	$124.64(3) \pm 0.01(5)$	$124.604(5) \pm 0.001(3)$
L	10372.86800	0.19066	$124.67(0) \pm 0.01(4)$	$124.8183(8) \pm 0.0008(8)$
M	10380.76740	0.12000	$124.70(7) \pm 0.06(3)$	$124.609(7) \pm 0.001(0)$
N	10388.19080	0.08234	$124.78(7) \pm 0.01(9)$	$124.974(6) \pm 0.001(0)$
O	10394.80903	0.08194	$124.81(8) \pm 0.01(2)$	$124.6711(0) \pm 0.0009(6)$
P	10397.55185	0.08108	$124.87(6) \pm 0.02(6)$	$124.806(7) \pm 0.001(1)$
Q	10464.05946	0.08116	$125.445(9) \pm 0.002(1)$	$125.451(3) \pm 0.001(5)$
R	10464.23565	0.19825	$125.4551(6) \pm 0.0003(0)$	$125.452(9) \pm 0.001(4)$
S	10469.84944	0.09630	$125.508(2) \pm 0.001(3)$	$125.4679(6) \pm 0.0009(3)$
T	10474.99699	0.08138	$125.544(1) \pm 0.002(8)$	$125.533(8) \pm 0.001(4)$
U	10481.65460	0.09364	$125.622(7) \pm 0.002(5)$	$125.6853(4) \pm 0.0006(7)$
V	10505.90618	1.75505	-	$125.798(2) \pm 0.001(3)$
W	10530.24134	5.09516	-	$125.991(8) \pm 0.001(4)$
X	10558.75678	4.46567	-	$126.197(4) \pm 0.001(5)$
Y	10586.22225	4.14524	-	$126.4319(0) \pm 0.0005(5)$

Table 4.1 Calculated pulse periods for GX 1+4. P_{fit} is calculated from Gaussian fitting to χ^2 versus trial period curves, with 1σ errors estimated from period determinations of simulated lightcurves including Poisson noise appropriate for the combined source and background rate. P_{BATSE} is interpolated from BATSE archival pulse-period measurements over the equivalent time period.

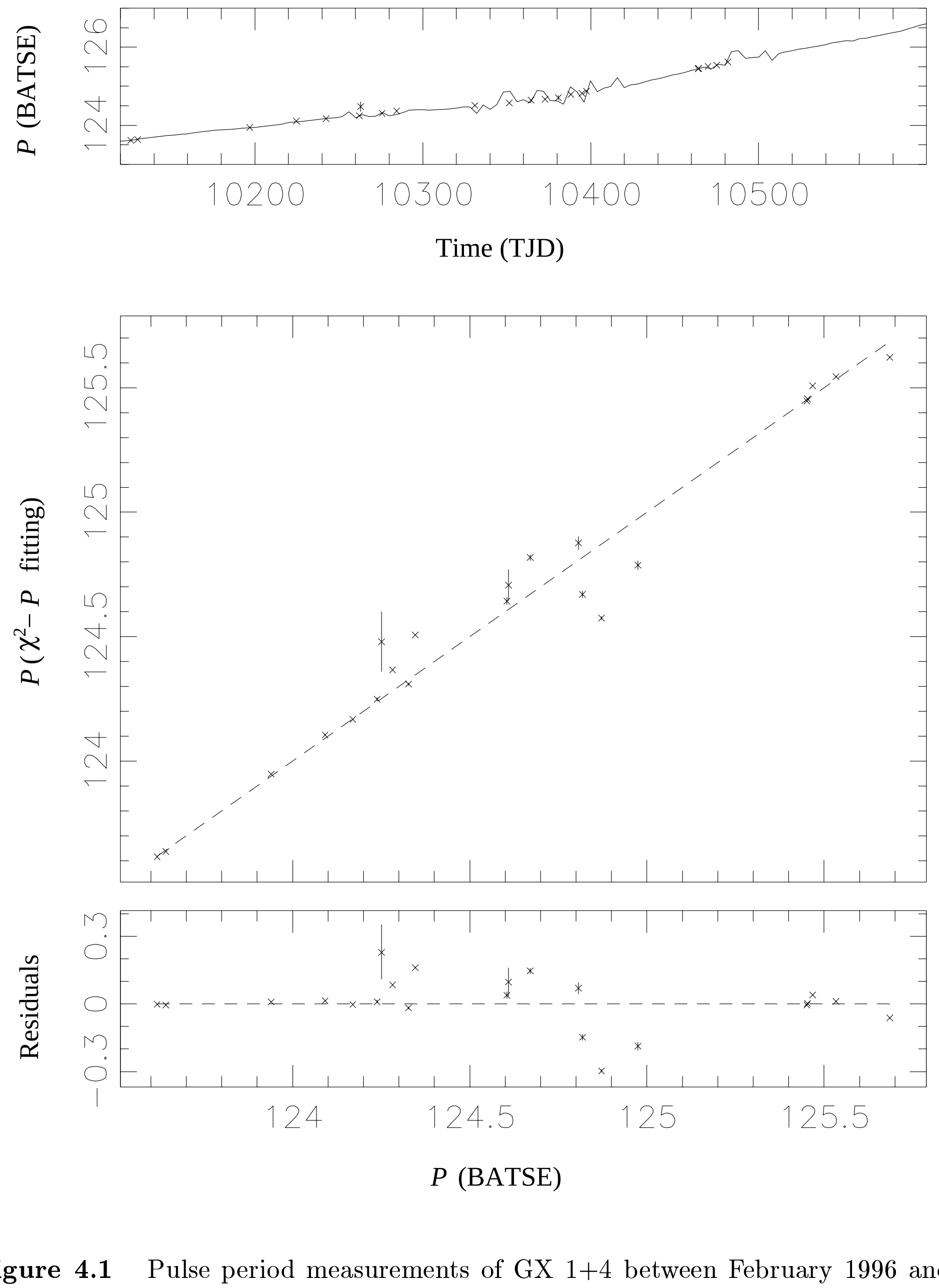

Figure 4.1 Pulse period measurements of GX 1+4 between February 1996 and May 1997. The top panel shows the pulse period determined from BATSE monitoring of the source $P_{\rm BATSE}$; typical 1σ errors are 10^{-3} s. The period calculated from trial period folding of *RXTE* data ($P_{\rm fit}$) is plotted for comparison as crosses. The middle panel plots $P_{\rm fit}$ against $P_{\rm BATSE}$ interpolated over the duration of the appropriate *RXTE* observation. The bottom panel shows the residuals once the $P_{\rm fit} = P_{\rm BATSE}$ line is subtracted out. Errors, where shown, represent 1σ confidence limits.

4.2 *RXTE* pulse profiles

The pulse profile $F(\phi)$, $\phi \in [0.0, 1.0)$ for each of the *RXTE* observations listed in Table 4.1 was calculated from lightcurves with 1 s resolution folded on the best-fit pulse period from *RXTE* data where available, or from interpolated BATSE measurements otherwise (e.g. observations V–Y). Standard-1 data were used to calculate the profiles over the full PCA energy range, while the greater flexibility of GoodXenon, generic Event or generic Bin mode data allowed extraction of lightcurves and calculation of pulse profiles over restricted energy ranges. When changes in the profile occurred on timescales shorter than the span of the observation it was broken into two or more intervals and separate profiles calculated for each. The ephemeris was defined so that the primary minimum fell at phase $\phi = 0.0$. The resulting pulse profiles exhibited a wide range of shapes, so much so that it is somewhat difficult to make any generalisations at all (Figure 4.2). The profiles are all rather smooth with a single minimum, which may be quite sharp. When the flux was high the profiles approached a symmetric $\sin^2 \phi$-type profile with one maximum, while at low fluxes the profile was generally flatter (accentuating the sharpness of the primary minimum) and sometimes with more than one local maxima, at varying phases. At times the profile varied significantly on timescales of $\lesssim 1$ d (e.g. observation H). In general the profiles showed little variation within the energy range of the PCA.

The pulse fraction is calculated from the maximum and minimum count rate over the phase range and is defined as

$$f_{\rm p} = \frac{F_{\rm max} - F_{\rm min}}{F_{\rm max}} \qquad \text{where} \qquad (4.1)$$
$$F_{\rm min} < F(\phi) < F_{\rm max} \quad \forall\ \phi \in [0.0, 1.0)$$

For the *RXTE* pulse profiles $f_{\rm p}$ varied significantly with luminosity (Figure 4.4). At low luminosities the primary minimum typically reached zero and the corresponding pulse fraction was ≈ 1. In fact, the profile count rate in the dip dropped below zero in some cases, presumably due to systematic errors in the background estimation. At higher luminosities the minimum generally did not reach zero and the pulse fraction was somewhat lower, typically around 0.8. Linear fits to the pulse fraction versus the log of the luminosity indicate a systematic variation at the 3–4σ level, depending upon the energy range for the profile calculation. There was no significant overall variation in the pulse fraction from profiles in different energy bands. The mean for the full-range profiles was 0.831 ± 0.086, compared to 0.83 ± 0.11, 0.829 ± 0.086 and 0.91 ± 0.14 in the 2–7, 7–20 and > 20 keV energy bands respectively. One notable observation which has been discussed previously was Y2 (labelled in Figure 4.4), when the sharp dip all but disappeared and the pulse fraction became ≈ 0.5. The period interpolated from BATSE data was used to fold the lightcurve for this observation, and errors noted in these period estimations (Figure 4.1) may have contributed to a reduction of the calculated pulse fraction compared to the true value. However, the dip was clearly defined in the other profiles from observations

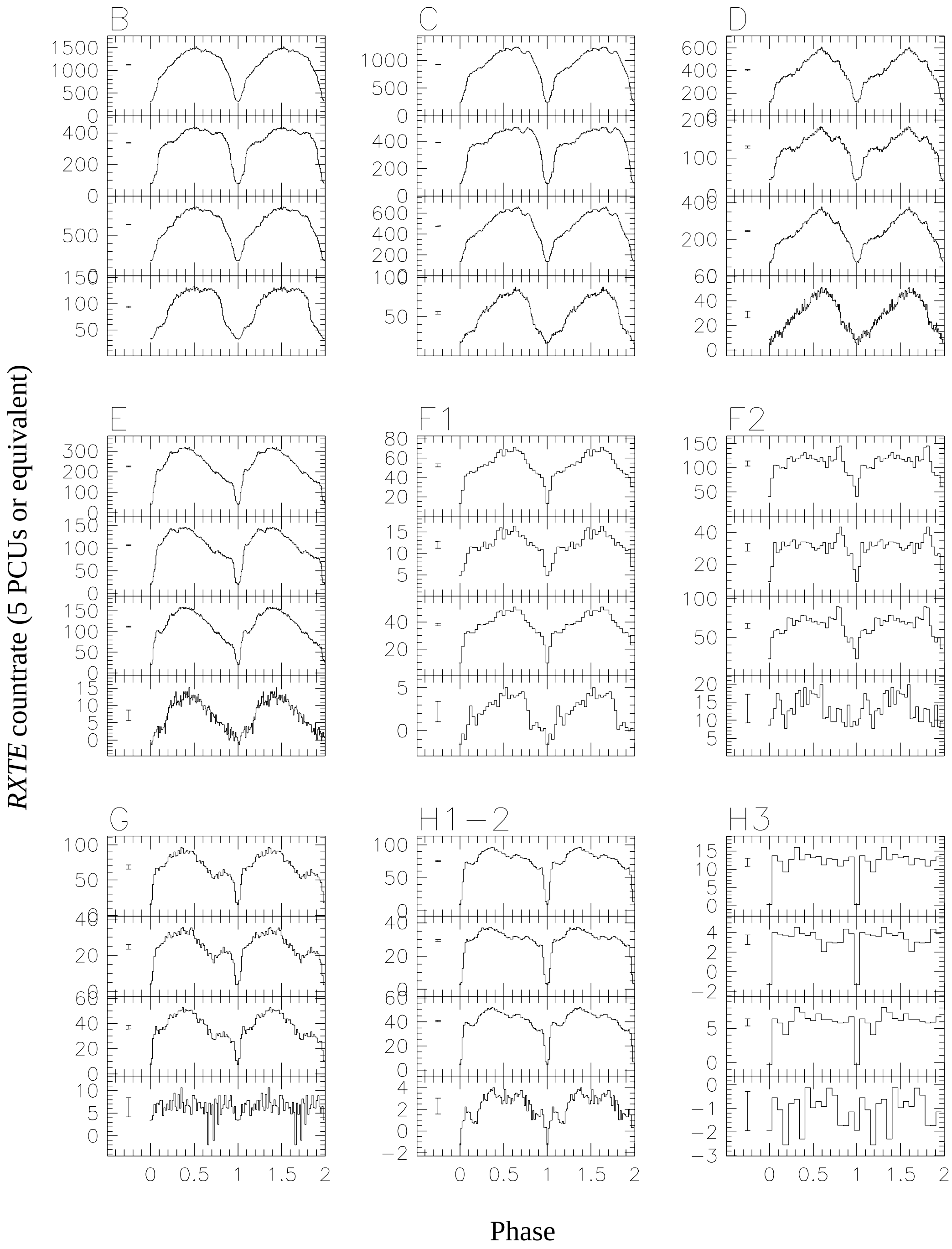

Figure 4.2 Pulse profiles from *RXTE* observations of GX 1+4 between February 1996 and May 1997 (Table 3.1) calculated from folding 1 s lightcurves on $P_{\rm fit}$ (see Table 4.1). The four profiles in each panel represent profiles in the full PCA energy range 2–60 keV and subranges 2–7, 7–20 and > 20 keV from top to bottom respectively. Typical 1σ error bars are shown at the left of each profile.

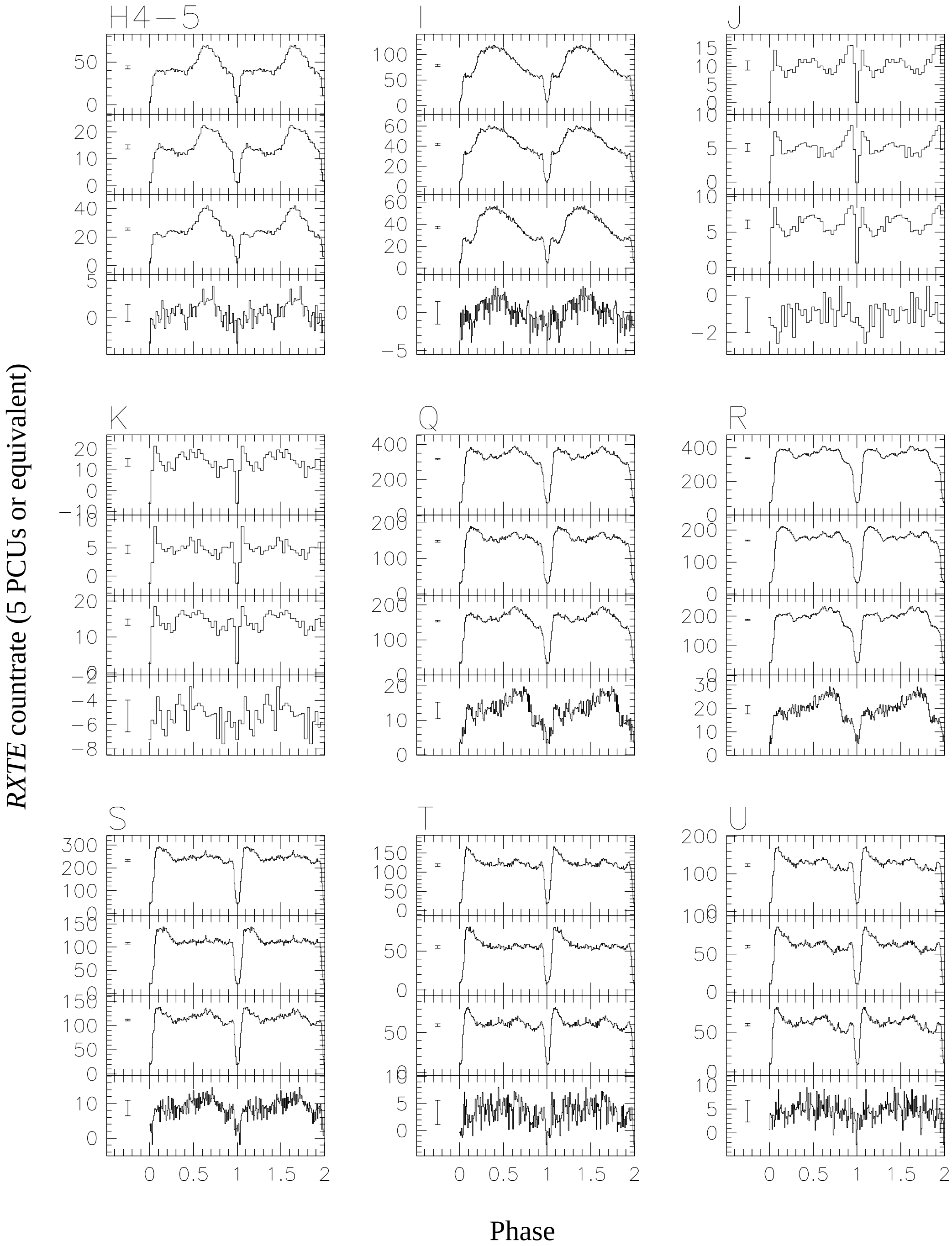

Figure 4.2 continued

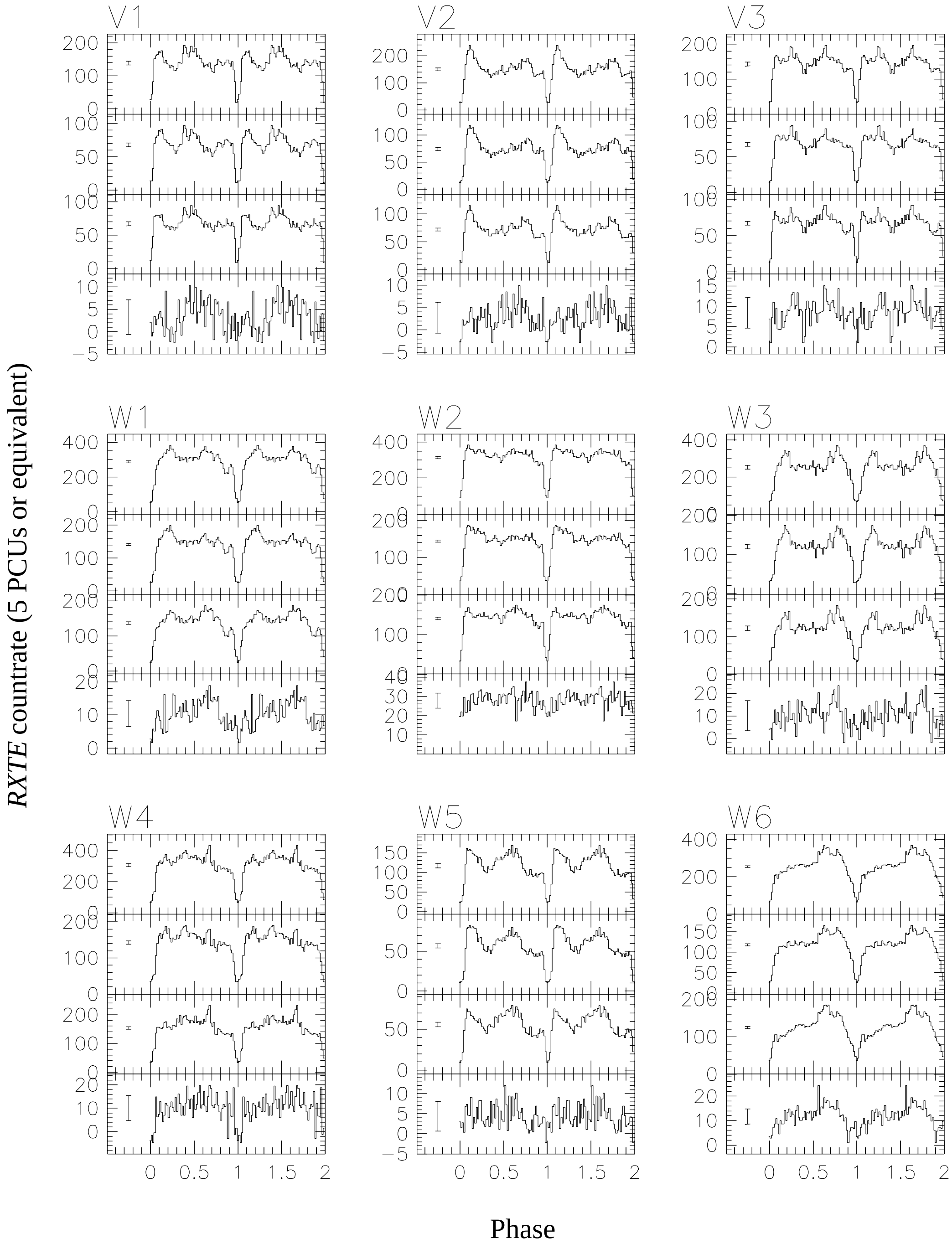

Figure 4.2 continued

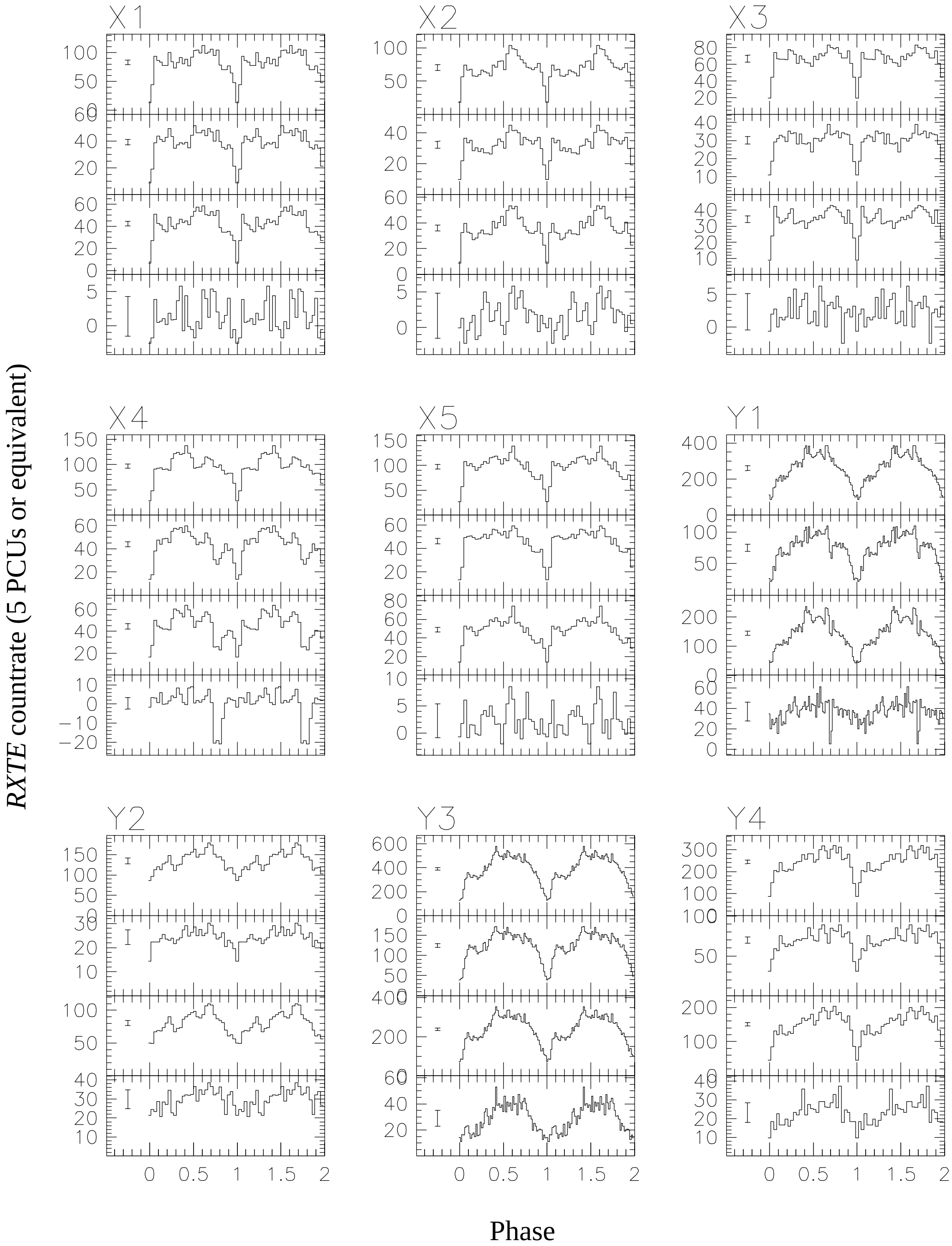

Figure 4.2 continued

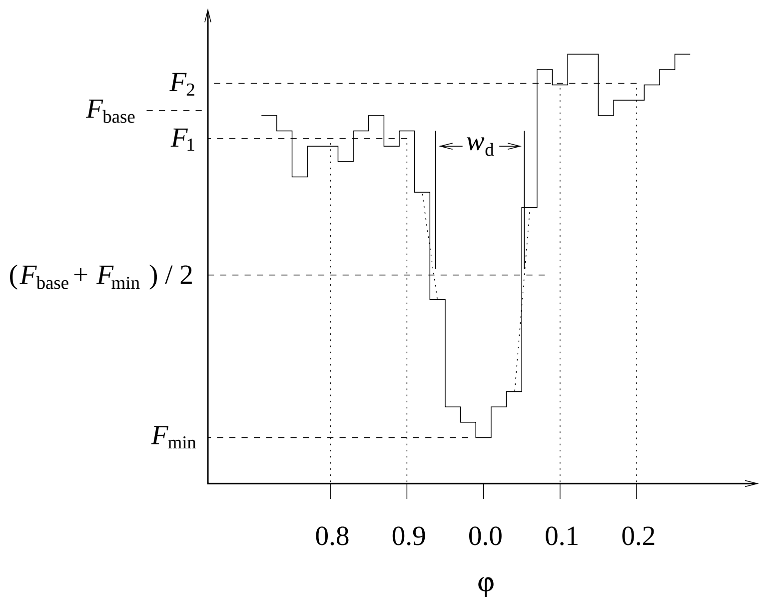

Figure 4.3 Schematic showing the dip width $w_{\rm d}$ calculated for an example pulse profile.

V–Y, and also the lightcurves (see Figure 3.6). Observation Y2 was unusual in other ways (see section 3.1.3).

The profiles exhibited the greatest variation with energy close to the primary minimum. When the flux was moderately high (e.g. observations C, D), the minimum appeared in the low energy profiles as a sharp drop from close to the mean level extending $\Delta\phi \lesssim 0.2$ in phase. At higher energies the count rate immediately before and after the dip tended to decrease relative to the mean, and in the highest energy profiles the sharp dip almost disappeared altogether, replaced by a much broader dip with $\Delta\phi \sim 0.4$. This decrease in count rate surrounding the dip also occurred at low flux, but the dip instead appeared to get significantly narrower with increasing energy (e.g. H, I). The narrowing of the dip in some cases was accompanied by the appearance of local maxima immediately before and after the dip, which were typically more prominent at higher energies (e.g. J, T–U). As a measure of the dip width I define

$$\begin{aligned} w_{\rm d} &= \phi_+ - \phi_- \qquad \text{where} \\ F(\phi_\pm) &= \frac{F_{\rm base} + F_{\rm min}}{2} \\ F_{\rm base} &= 0.2^{-1}\left(\int_{0.8}^{0.9} F(\phi)\,{\rm d}\phi + \int_{0.1}^{0.2} F(\phi)\,{\rm d}\phi\right) \end{aligned} \tag{4.2}$$

where the integrals are approximated by summing the count rate in the phase bins within the limits of integration. With the finite resolution of the pulse profiles the $\phi_\pm$ are determined by interpolating between successive bins with count rates falling above and below $(F_{\rm base}+F_{\rm min})/2$ (Figure 4.3). The error in phase is then determined

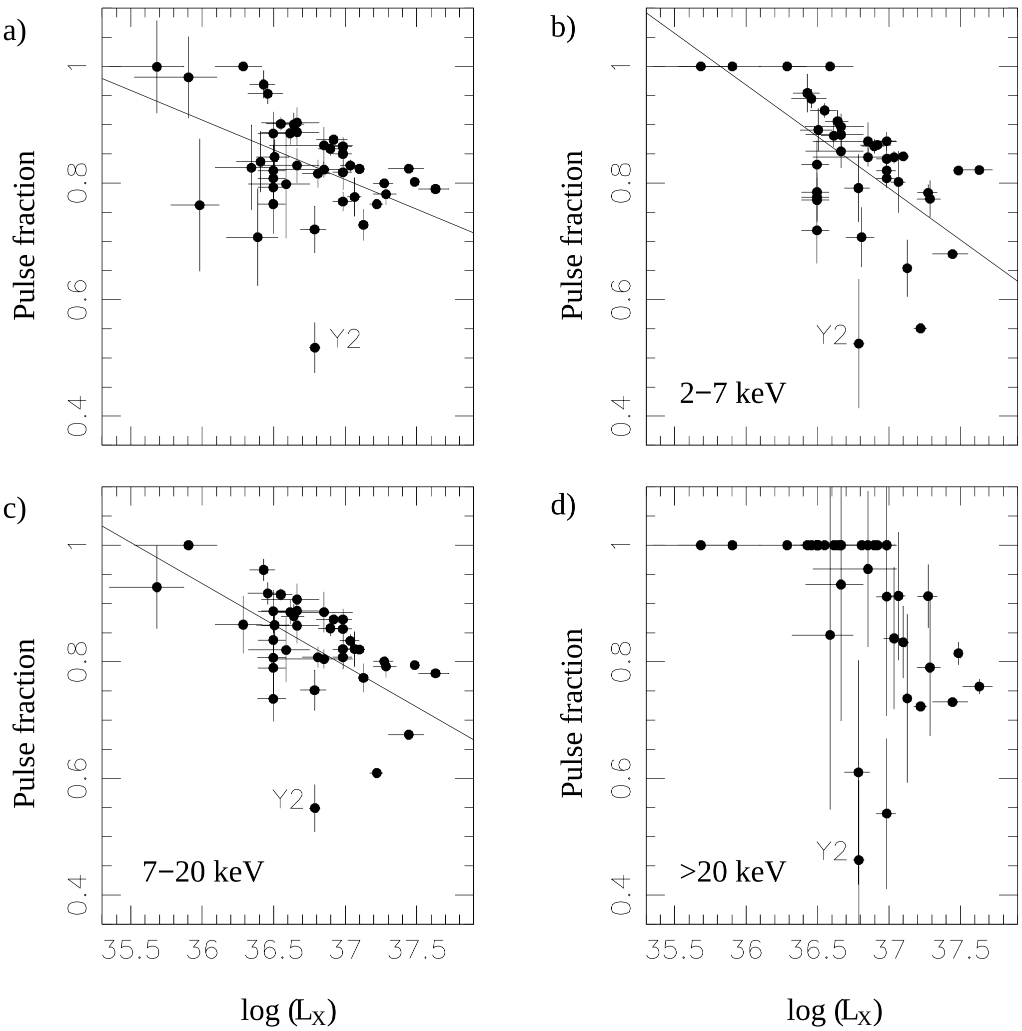

Figure 4.4 Pulse fraction f_{p} (equation 4.1) from *RXTE* pulse profiles of GX 1+4 plotted against the unabsorbed source luminosity in the range 2–20 keV (assuming a distance of 10 kpc). Error bars show the 1σ confidence limits. Solid lines, where plotted, show the line of best fit. The errors on the luminosity are calculated from the variance in the phase averaged count rate over the observation. The four panels plot f_{p} versus flux in different energy ranges: a) Full PCA energy range, b) 2–7 keV, c) 7–20 keV and d) $>$ 20 keV.

according to the calculated slope $\mathrm{d}F/\mathrm{d}\phi$ between the two bins and the errors in $F_{\rm base}$ and $F_{\rm min}$. Since the count rate on either side of the dip generally varied significantly with phase, and was also quite different on average before and after, the definition of $F_{\rm base}$ is problematic. However the dip ingress and egress are usually so steep that the error due to this parameter is likely to be small.

The increase of $w_{\rm d}$ with luminosity is shown conclusively in Figure 4.5. When $L_{\rm X} \sim 10^{36}\ \mathrm{erg\,s^{-1}}$ the dip in the full range profiles was $\Delta\phi \approx 0.03$, whereas as the flux increased it reached $\Delta\phi \approx 0.14$. Linear fits to the data result in slopes which are distinct from zero at the 5–7σ significance level, depending upon the energy band in which the profile is calculated. Similar relations were seen for profiles in each energy band, although the scatter was much greater for the > 20 keV measurements because of the generally low count rates and the difficulty of unambiguously locating $\phi_\pm$. Additionally there was some suggestion of a narrowing of the dip in higher energy bands, which was more noticeable at lower luminosities. It may be argued that the correlation between $w_{\rm d}$ and $L_{\rm X}$ is partially or wholly an artefact of the definition of $w_{\rm d}$. However the correlation is obvious even on visual inspection of the profiles (Figure 4.2), and is also found using an alternative definition of $w_{\rm d}$ where I instead calculate $\phi_\pm$ by solving $F(\phi_\pm) = 2F_{\rm min}$ about $\phi = 0.0$. (Clearly this definition will only work well when the luminosity is relatively high and the count rate in the dip does not reach zero).

4.3 Pulse profile asymmetry

4.3.1 *RXTE* profiles

The profiles measured by *RXTE* were typically asymmetric, with the maximum leading the primary minimum by $\Delta\phi > 0.5$ (e.g. E; these profiles are termed 'leading-edge bright') or by $\Delta\phi < 0.5$ (e.g. F; 'trailing-edge bright'). The highest flux observations (e.g. A…D, Y1…4) generally featured profiles with very slight asymmetry tending to trailing edge bright, whilst the asymmetry wasmuch more variable at lower fluxes. The sense of asymmetry in some cases changed dramatically on timescales $\lesssim 1$ d. It is possible to qualitatively measure the asymmetry using a number of methods, including the second moment, but I choose instead the α-parameter of Greenhill et al. (1998):

$$\alpha = \frac{\int_{0.5}^{0.75} F(\phi)\,\mathrm{d}\phi}{\int_{0.25}^{0.5} F(\phi)\,\mathrm{d}\phi} \tag{4.3}$$

with the primary minimum defined as phase 0.0 (Figure 4.6).

For trailing-edge bright profiles, with the maximum following the primary minimum in phase by $\Delta\phi > 0.5$, $\alpha > 1$ whereas for leading-edge bright profiles $\alpha < 1$. This measure has the advantage that it does not depend strongly on the precise location of the primary minimum, which is not a problem for the *RXTE* profiles

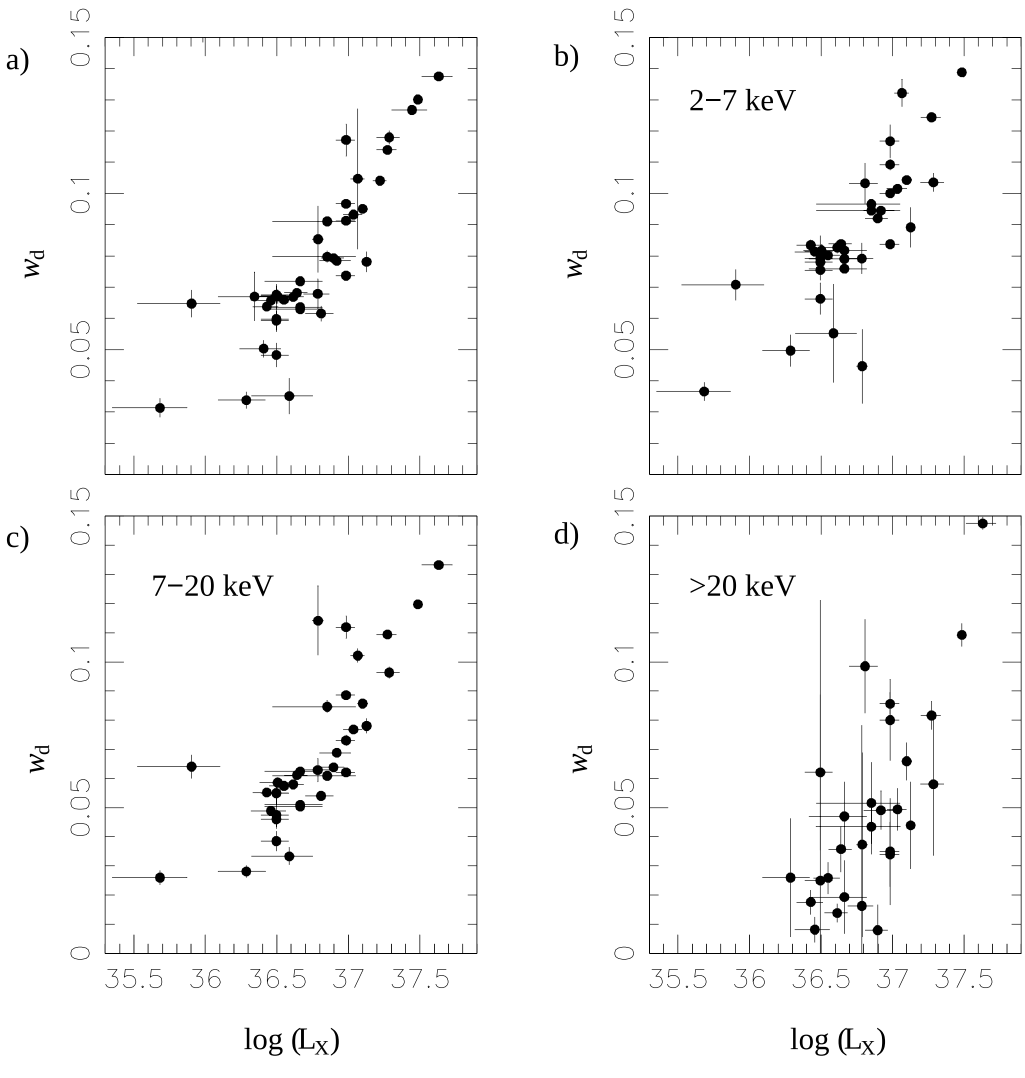

Figure 4.5 Dip width $w_{\rm d}$ (equation 4.2) in units of phase from *RXTE* pulse profiles of GX 1+4 plotted against the unabsorbed source luminosity in the range 2–20 keV (assuming a distance of 10 kpc). Error bars show the 1σ confidence limits. The four panels plot $w_{\rm d}$ versus luminosity in different energy ranges: a) Full PCA energy range, b) 2–7 keV, c) 7–20 keV and d) > 20 keV.

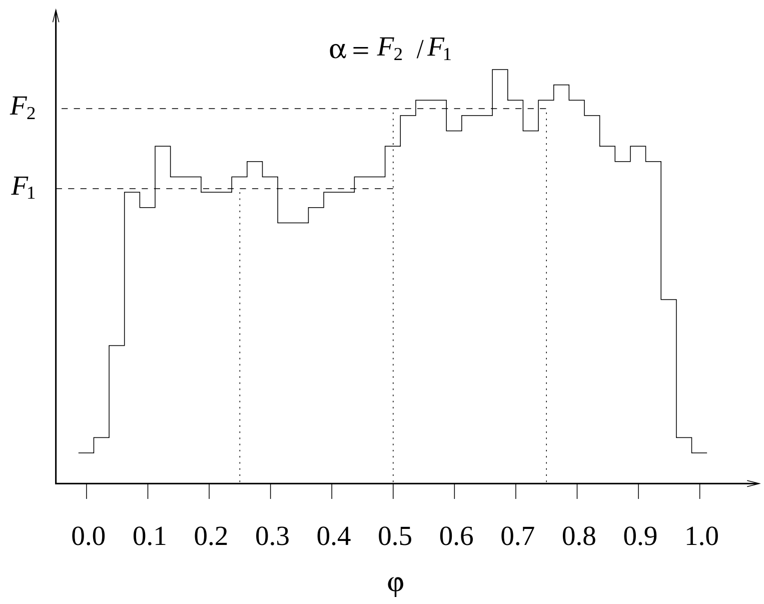

Figure 4.6 Schematic showing the asymmetry α-parameter calculated for an example pulse profile.

but is more difficult for low time resolution profiles from previously published observations. The α-parameter for each of the observations or sub-intervals listed in Table 4.1 is shown in Figure 4.7.

For most profiles $\alpha \gtrsim 1$, indicating that they are trailing edge bright, although typically the degree of asymmetry was modest $\alpha \lesssim 1.3$. The scatter of α with $L_{\rm X}$ was significant, and (as suggested from the pulse profiles) seemed to be greatest at moderate luminosities $L_{\rm X} \approx 10^{36.8}\ {\rm erg\,s^{-1}}$. That the pulse profile variation seen during observation H was unusual (Galloway et al., 2000) is confirmed by the atypically high value of α measured during the second half of this observation, at 1.6–1.7. The distribution of points as a function of the luminosity was similar between the 2–7 and 7–20 keV profiles, whilst in the > 20 keV profiles the errors were again very large due to the low count rate in this energy band. Each plot suggests a marginal correlation between α and $L_{\rm X}$, which can again be tested using the BCES(Y—X) estimator of Akritas and Bershady (1996). In each band a linear relationship was found with slope different from zero at less than the 2σ confidence level. The Spearman rank-order correlation coefficient and Kendall's τ indicate that there is a relationship between the luminosity and asymmetry parameters to a maximum confidence level of just over 3σ (Table 4.2).

4.3.2 BATSE profiles

The number of *RXTE* pulse profiles available for analysis was limited by the small number of observations. A potentially more useful set of profiles can be calculated from the public BATSE data obtained from regular monitoring of the source

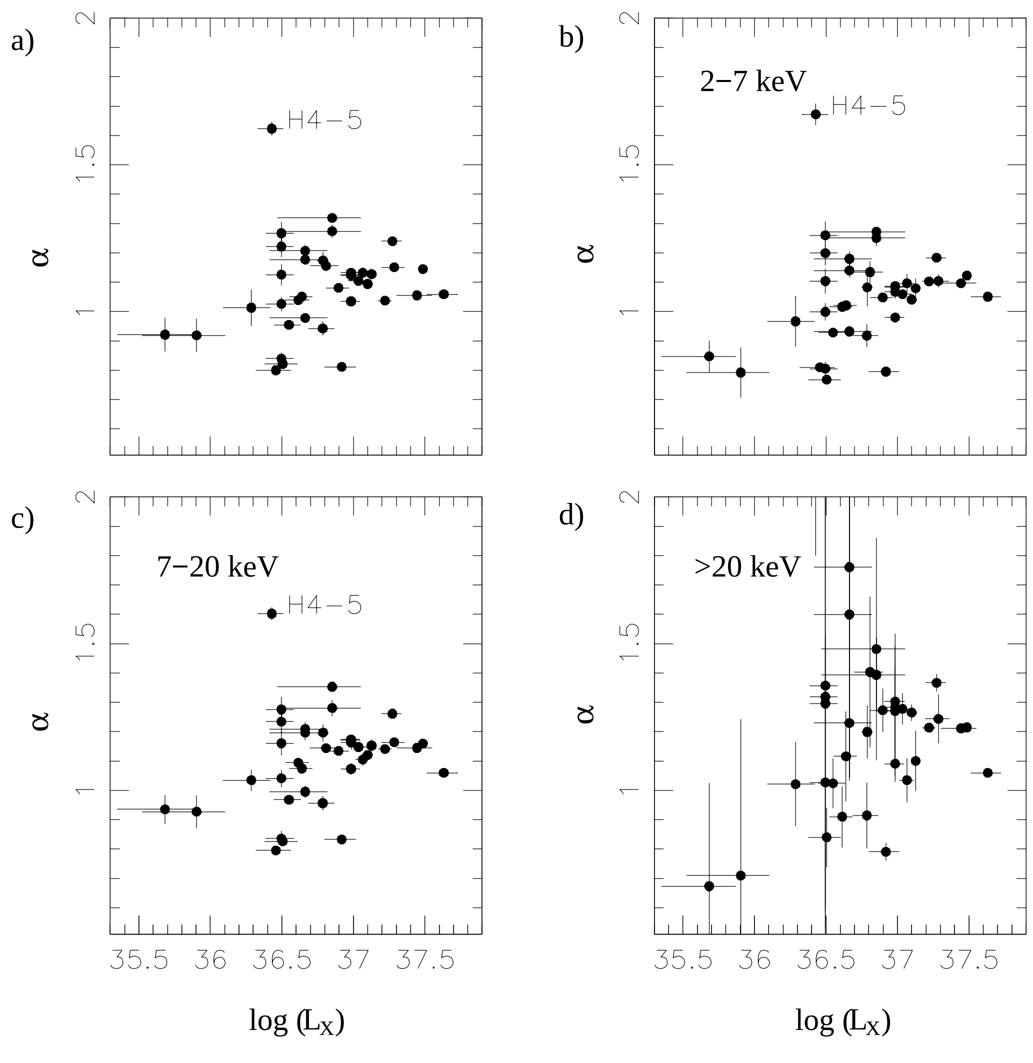

Figure 4.7 Asymmetry in *RXTE* pulse profiles of GX 1+4 measured by the α-parameter (equation 4.3) plotted against the unabsorbed source luminosity in the range 2–20 keV (assuming a distance of 10 kpc). The errors on the luminosity are calculated from the variance in the phase averaged count rate over the observation. The four panels plot α versus luminosity in different energy ranges: a) Full PCA energy range, b) 2–7 keV, c) 7–20 keV and d) $>$ 20 keV.

Energy band	r_s	$P(>r_s)$	τ_k	$P(>\tau_k)$
full PCA range	0.449	0.00253	0.294	0.00548
2–7 keV	0.465	0.00168	0.334	0.00157
7–20 keV	0.442	0.00302	0.287	0.00665
20–60 keV	0.424	0.00462	0.260	0.0140

Table 4.2 Rank correlation coefficients between the asymmetry parameter α (calculated from pulse profiles in various bands) and the unabsorbed 2–20 keV luminosity L_X (assuming a distance of 10 kpc). The first column gives Spearman's rank-order correlation coefficent r_s, with the calculated significance (the probability that r_s could exceed the calculated value through chance alone) in the second column. The third and fourth columns contain Kendall's τ and corresponding significance, respectively.

throughout the lifetime of that satellite. Whilst these profiles were determined from much more frequent (and long-running) observations, they too suffer from limitations. The apparent lack of precision of period determination during the low-flux intervals (Figure 4.1) implies that the calculated coefficients will not describe the 'true' pulse profile, resulting in an underestimation of the pulse fraction and hence the asymmetry parameter. Indeed, comparing the BATSE and *RXTE* pulse profiles in similar energy bands confirms that agreement between the two instruments was worst when the source flux was low (observation H; Figure 4.8). Furthermore, the Fourier coefficients were normally determined from pulse profiles averaged over ~ 1 d intervals, whilst the *RXTE* observations demonstrated that significant profile evolution may take place on timescales as short as ≈ 6 h (Figure 4.2 and Giles et al., 2000). Profile variations on these timescales will clearly not be resolved by the BATSE data and the profiles calculated from the Fourier coefficients will not always accurately reflect the source variation with pulse phase.

For each set of Fourier coefficients I generated a pulse profile on 100 phase bins, shifted the profile in phase to ensure the primary minimum fell at $\phi = 0.0$ and calculated the asymmetry parameter alpha (equation 4.3). The most noticeable feature of the variation of α with the pulsed BATSE flux is the large scatter (Figure 4.9, top panel). As is clear from the comparison with *RXTE* profiles, erroneous determination of the Fourier components may have contributed to this scatter at low flux, but at higher flux there was still significant variation between observations at comparable levels. While there is a suggestion that the mean asymmetry parameter was greater in the highest flux bin (Figure 4.9, lower panel), clearly there was no systematic variation in asymmetry with flux. It is worthwhile recalling that the flux in Figure 4.9 is pulsed flux only. The addition of a non-zero offset to the profile, representing the unpulsed flux from the source, will tend to decrease α and thus the calculated values represent an upper limit only. Results from *RXTE* suggest the pulse fraction may fall to ≈ 0.8 in the > 20 keV energy band for observations at the highest luminosity. The neglect of this component is sufficient to overestimate α by 5–10% in the highest L_X band, which will contribute to the increase observed

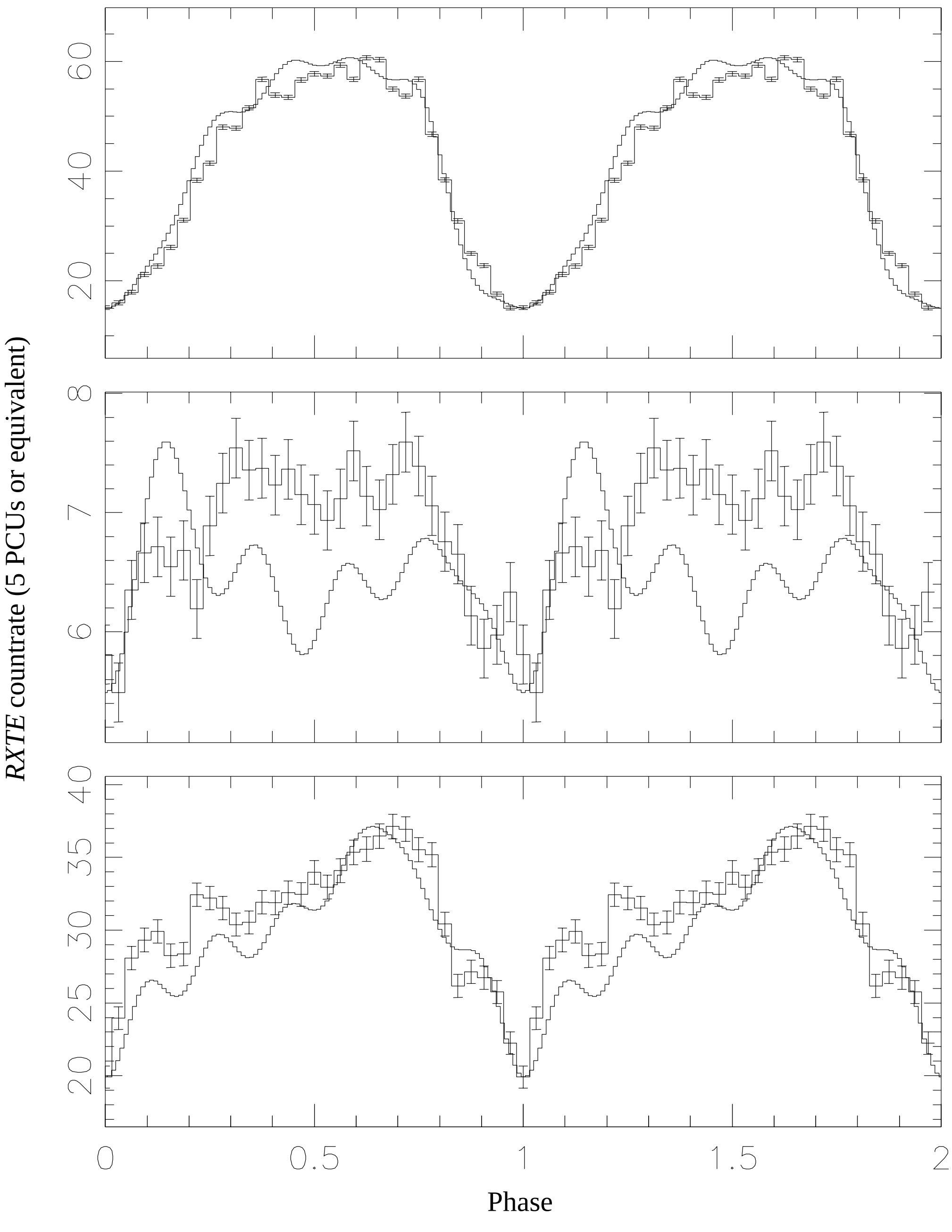

Figure 4.8 Comparison of GX 1+4 pulse profiles measured by the PCA onboard *RXTE* (histogram with error bars) and calculated from Fourier decompositions from BATSE observations for observations A (top), H (middle) and R (bottom) (see Figure 3.1). The energy range for the PCA data is 20–60 keV. The BATSE profile is constructed on phases $\phi_k = k/100$, $k = \{0 \ldots 100\}$ as described in section 2.2. Two pulse periods are shown for clarity.

in the mean.

Additionally, the flux measured by BATSE is calculated assuming a constant spectral model for GX 1+4, an optically thin thermal bremsstrahlung with temperature $T = 28.4$ keV. The mean spectral variation with luminosity seen in the *RXTE* observations (Chapter 3) means that this assumption may introduce systematic luminosity-dependent errors in the calculated flux from BATSE. *RXTE* spectra from observations B and E (Table 3.1) were chosen as representatives for the two spectral regimes and fit with thermal bremsstrahlung components above 20 keV. The resulting plasma temperatures were $55.3^{56.4}_{53.8}$ and $45.8^{50.1}_{42.0}$ keV respectively. That both these fit values are distinctly different from the BATSE value may be due to the contribution of the unpulsed flux in the *RXTE* spectra. Despite this discrepancy, the fit values do indeed disagree significantly, indicating that a constant spectral model for GX 1+4 at all flux levels is inappropriate.

4.3.3 Previously published profiles

Finally, it is instructive to compare the more recent BATSE and *RXTE* pulse profiles with those from the literature, which in some cases have been obtained when the source flux was much higher than during the period covered by these satellites. During the 1970s observations found the source to be in a bright state with flux levels which have not been matched over the last 20 yr. Pulse profiles at times exhibited complex dependence with energy (White et al., 1995), which is not observed (over the PCA energy range at least) for the *RXTE* observations. In general the profiles from this era exhibit trailing-edge bright asymmetry, i.e. $\alpha > 1$. In some cases the sharp primary minimum is not observed, which may be a function of limited temporal resolution. For those high-energy observations where the primary minimum can be reliably located the asymmetry parameter α is calculated as before (equation 4.3). The plot of α against source flux exhibits strong evidence for a correlation (Figure 4.10). The calculated slope using the BCES(Y—X) estimator confirms the relationship, with $b = 0.178 \pm 0.0408$. The range of intensity observed by *RXTE* throughout 1996–7 however is substantially lower than for these earlier observations. For observation B, when the source was at its brightest over that period, the intensity at 20 keV was only $2.9 \times 10^{-4}\ \mathrm{cm^{-2}\,s^{-1}\,keV^{-1}}$. Thus even the weakest observation plotted in Figure 4.10 is almost 3 times the intensity as seen by RXTE.

4.4 Discussion

The spin period and pulse profile evolution of GX 1+4 is enigmatic. Whilst the observations to date have suggested that the source exhibits long-term periods of almost constant spin-up or spin-down, closer analysis of the recent BATSE observations seems to suggest more complex behaviour, with spin-down rate perhaps 'quantised' to some degree. This is in stark contrast to the predictions of the widely-cited Ghosh and Lamb (1979a,b) model, which includes a correlation between $\dot{M}$ (and

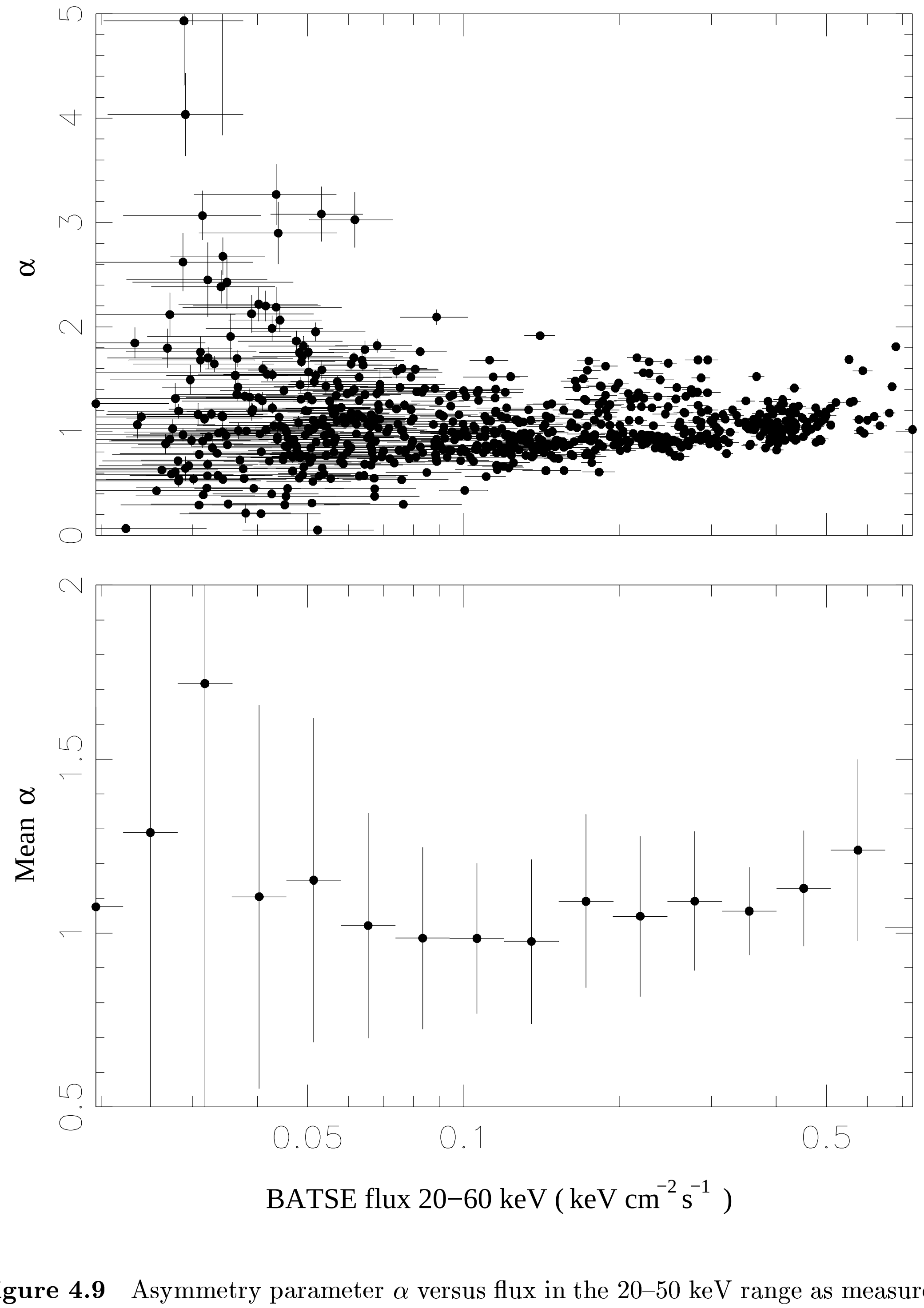

Figure 4.9 Asymmetry parameter α versus flux in the 20–50 keV range as measured by BATSE. The top panel shows α calculated for individual monitoring observations, while the bottom panel shows the mean α calculated over regularly spaced flux bins. The errors are 1σ based on the variance of the α calculated for the individual observations.

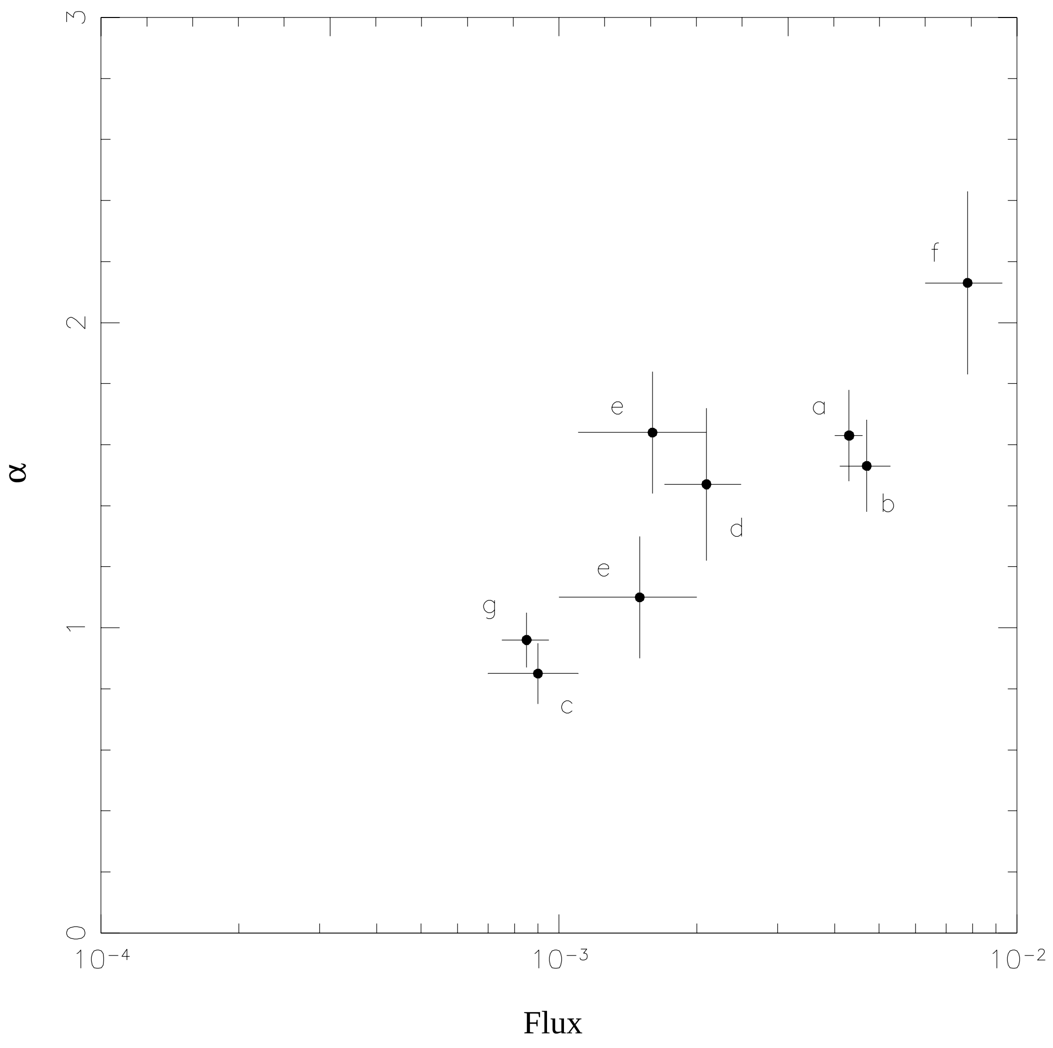

Figure 4.10 Asymmetry parameter α vs. 20 keV intensity ($\mathrm{cm}^{-2}\,\mathrm{s}^{-1}\,\mathrm{keV}^{-1}$) for published hard X-ray (> 20 keV) measurements. a) White et al. (1983), b) Doty et al. (1981), c) Greenhill et al. (1993), d) Kendziorra and Staubert (1982), e) Laurent et al. (1993), f) Maurer et al. (1982), g) Mony et al. (1991). Reproduced from Greenhill et al. (1998).

hence L_X) and the spin-up or spin-down rate. A number of theorists have attempted to refine this picture to include the possibility of 'torque reversals' between intervals of almost constant spin-up or spin-down at approximately the same magnitude (e.g. Lovelace et al., 1995, Li and Wickramasinghe, 1998, Torkelsson, 1998). However none of these models attempt to explain torque 'switches' between intervals with the same sign, and in fact no model to date offers any explanation for the *regulation* of torque despite significant changes in luminosity. I suggest that this may be the most important feature of pulse period evolution in this (and perhaps other) X-ray pulsars, and deserves future attention.

The *RXTE* and BATSE pulse profiles described here are an important addition to the already large set of observations of the source. The BATSE data offer a long-term timeseries of moderate quality, high-energy profiles which is unprecedented in scope. Complementing this is the *RXTE* data which have provided excellent sensitivity over intervals when the source has been fainter than ever before. The quality and quantity of data now available make it even more frustrating that the understanding of pulse profile formation is lacking in so many respects. Past modeling has made use of geometric models featuring opposed (or offset) disk (or annular) emission regions on the surface of neutron stars, with idealised beam patterns (e.g. Leahy, 1991). While such models are successful in explaining broad features of pulse profiles from a range of sources, they offer no explanation as to the variation of profiles. The observed variation in pulse profile shapes measured by *RXTE*, which may take place on timescales $\lesssim 1$ d, suggests that profile formation is a consequence of a much less permanent feature of the neutron star.

The sharp dip generally observed in GX 1+4 profiles may be associated with the passage of the magnetic axis close to the line of sight (see Chapter 5). The variation of fitted optical depth for Compton scattering τ observed in the mean spectra (which provides constraints on the variation of the extent of the accretion column with luminosity; see Chapter 3) is in contrast with the measured variation of dip width with luminosity. If the magnetic axis (and hence the accretion column axis) passes directly through the line of sight, the column radius (assuming a circular cross section) is related to the dip width w_d (see equation 4.2) by

$$R_C \approx \pi w_d R_* \tag{4.4}$$

suggesting that the column radius is varying between 0.09 and $0.4R_*$, or 900 to 4000 m as L_X increases over two orders of magnitude. This represents a lower limit to the column radius, since if the magnetic axis does not pass directly through the line of sight w_d will measure the column radius off-axis and hence underestimate it. The inferred increase in R_C is insufficient to maintain a relatively constant τ (in turn a function of the accretion column plasma density) as L_X increases. However the cross-sectional area of the column may increase without an increase in the overall extent. For example, if at low luminosities an accretion 'curtain' is formed (e.g. Miller, 1996) the column cross-section will be an annulus which is not completely closed. The total cross sectional area can then increase by accreting material closing the annulus and filling the central cavity, without increasing the outer radius of the annulus. It is important to note that the definition of $w_{\rm d}$ was somewhat arbitrary, and it is in no way suggested that this measure represents a firm boundary to the accretion column. On the contrary, as the luminosity increases the dip ingress and egress become more gradual, and it seems likely that the density profile across the column may become progressively more smooth at higher accretion rates. Significant accretion 'outside' the column will allow lower densities overall and help to maintain an approximately constant τ. An additional caveat is that variations in the phase of primary minimum may serve to enhance the apparent width of the dip in the mean profiles. This effect is explored in more detail in Chapter 5.

The pulse profile asymmetry observed in GX 1+4 and other X-ray pulsars is generally ascribed to non-dipolar magnetic field components near the surface. The influence of inherent asymmetries in the beam pattern about each polar cap is thought to be small, partly due to the effect of light bending resulting from the compactness of the neutron star. Both the *RXTE* and BATSE results confirm that the asymmetry varies significantly over the entire observed range of $L_{\rm X}$, with no systematic trend. This is in contrast to the subset of previously published profiles examined, which show a very significant variation with $L_{\rm X}$, although there is no overlap in source intensity between the two groups of observations. With only a small number of observations during the high-flux 1970s it is not possible to discount selection effects as giving rise to the observed variation. The rapid timescale of variations of the asymmetry $\lesssim 1$ d as measured by *RXTE* suggests a more dynamic cause of asymmetry, perhaps related to accretion variability. Field lines approaching a neutron star with significant multipole components may reach a cusp where neighboring field lines diverge and meet the neutron star surface at widely separated points. Slight variations in the initial location of the accretion column may result in the matter falling on completely different parts of the star, and producing variations in the beam pattern also on timescales of $\lesssim P$. Whether such an effect can then be translated into a net variation in profile asymmetry is unknown, but note that in general the variations between profiles are much greater than would be expected from counting noise alone.

Chapter 5

Accretion column eclipses in GX 1+4

5.1 Pulse-phase spectroscopy

The GoodXenon mode data from selected *RXTE* observations of GX 1+4 (see Table 3.1) were divided into 10 equal phase bins, and a spectrum obtained for each phase range as described in section 2.1.4. Observations B (17 February 1996) and E (8 June 1996) were chosen in particular for their high count rate and similar fitted values of $n_{\rm H}$ (see Appendix A). Furthermore, they represent examples of the two distinct groups of GX 1+4 spectra; the high-$L_{\rm X}$, high τ and low $T_{\rm e}$, and moderate-$L_{\rm X}$, low τ and high $T_{\rm e}$ respectively (see Chapter 3). The pulse periods used were calculated from Gaussian fitting to peaks in the χ^2_ν-$P_{\rm trial}$ plot and are listed in Table 4.1. The ephemeris was chosen so that the primary minimum fell at phase 0.0, with the first bin centred there. Each of the 10 spectra were then fitted with a model identical to that used for the phase averaged spectra, with a Comptonization component ('`compTT`' in XSPEC) and a Gaussian component (representing Fe line emission) both attenuated by neutral interstellar material (see sections 2.1.2 and 3.2).

All fit parameters (barring those of the galactic ridge component) were left free to vary. The greatest spectral variation with phase was observed close to the primary minimum (Figure 5.1). The source spectrum temperature T_0 was generally quite consistent with the phase-averaged value, except at phase $\phi = 0.0$ where it fell to ≈ 0.8 keV. The scattering plasma temperature also decreased significantly at $\phi = 0.0$ as well as in the two adjacent bins, by at most $\approx 20\%$. The optical depth τ exhibited a highly significant increase at the phase of primary minimum, from around 5.6 for the phase-averaged spectrum to 10. The `compTT` normalisation exhibited the greatest variation of all the parameters, and traced the pulse profile quite well. The error limits on all the parameters were generally small except at $\phi = 0.0$. The spectral variation and the pulse profiles were both quite symmetric about the primary minimum.

Since τ and $T_{\rm e}$ are typically strongly anticorrelated in `compTT` component fits, it is important to also examine the corresponding two-dimensional parameter space and the error limits therein. These can be determined by fixing both parameters on a grid of values, performing a fit (with the remaining model parameters free to vary), and determining the $\Delta\chi^2$ values at each point. Confidence intervals for a given level of significance are then plotted as contours, with $\Delta\chi^2$ values appropriate for 2 degrees of freedom. The confidence contours for the phase-selected spectra from observation B confirm the highly significant variation in both parameters (Figure 5.2). The correlation between the two parameters is evident from the elongated shape of the confidence contours.

The column density $n_{\rm H}$ also varied significantly with phase (Figure 5.3). At $\phi = 0.0$ the measured value of $n_{\rm H}$ was around 60% greater than the phase-averaged value, at a significance of more than 5σ. Some variation in the Fe line component was also measured, particularly the width σ and the normalisation $A_{\rm Fe}$. While the peak deviation from the phase-averaged value of the former parameter was only significant at around the 2σ level, $A_{\rm Fe}$ reached a minimum between $\phi = 0.3$–0.4 distinct from

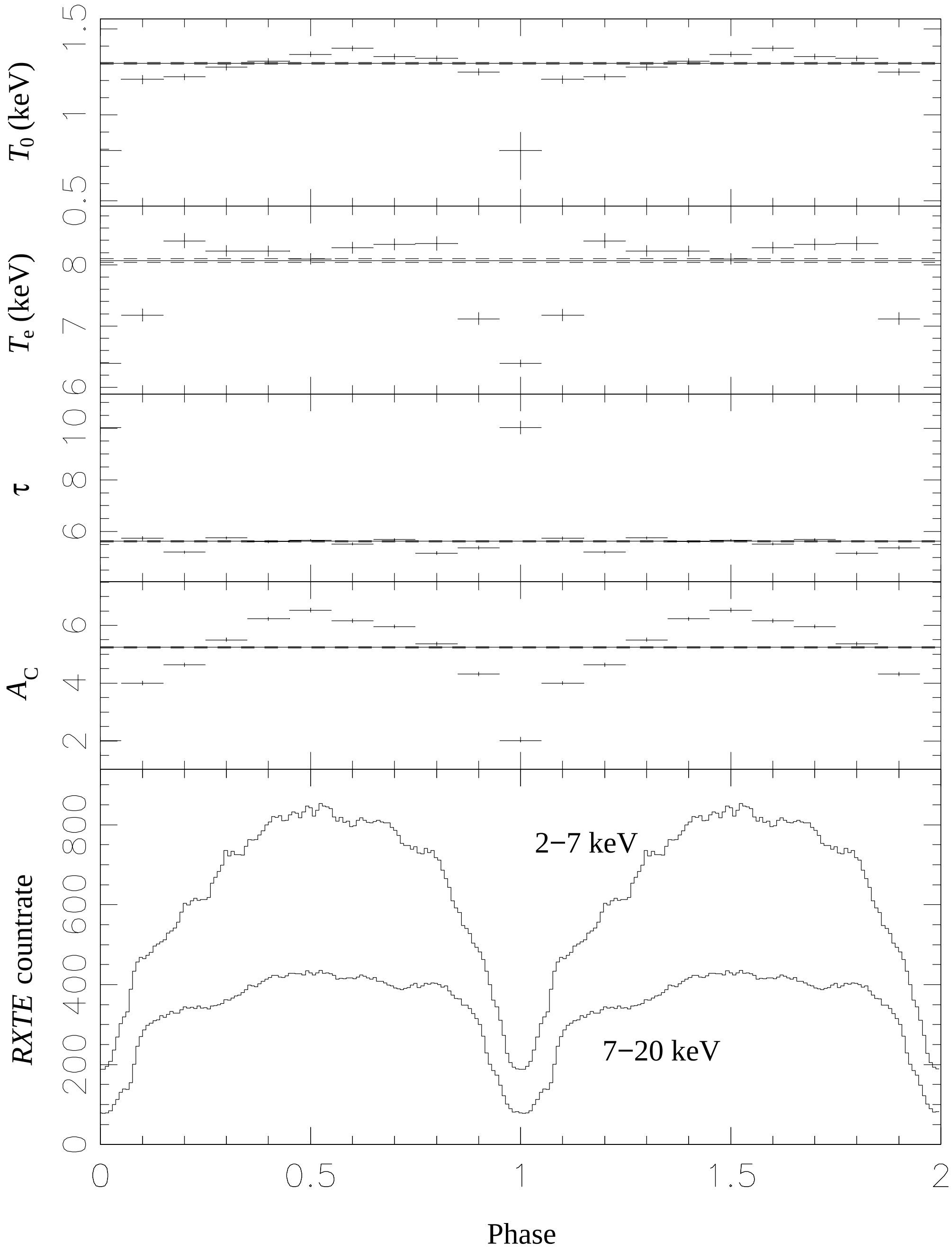

Figure 5.1 Comptonization component fit parameters versus pulse phase for the 17 February 1996 *RXTE* observation of GX 1+4 (B). From top to bottom, the panels shows the source spectrum temperature T_0, scattering plasma temperature T_e and optical depth τ, normalisation A_C (units of photons $cm^{-2}\,s^{-1}\,keV^{-1}$) and the pulse profile in 2–7 and 7–20 keV energy bands respectively. Fitted parameter values for the phase-averaged spectra covering the same interval are shown by the solid lines; error bars and the dotted lines show the 1σ confidence intervals. Two full pulse periods are shown for clarity.

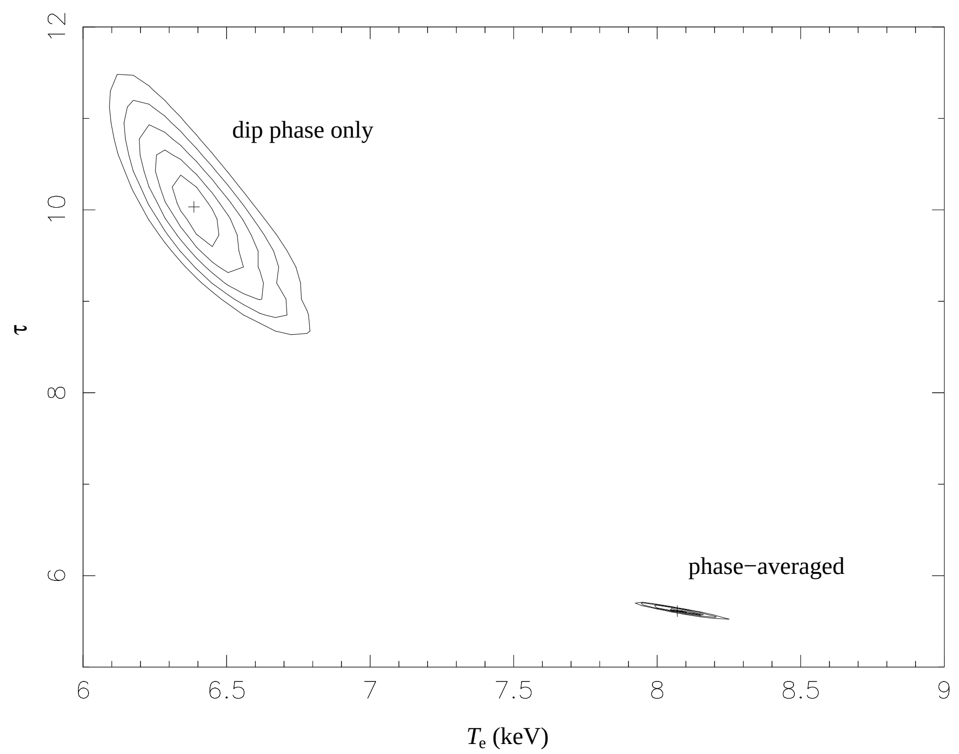

Figure 5.2 Comparison of confidence contours in T_e-τ parameter space between the phase-averaged spectrum (lower right corner) for observation B and the spectrum extracted from the dip phases only ($\phi \in -0.05, 0.05$). The best-fit parameter combinations for the two spectra are shown by a cross. Contours are plotted at $\Delta\chi^2$ values of 2.296, 6.180, 11.83, 19.34 and 28.77 corresponding to confidence levels of 1, 2, 3, 4 and 5-σ respectively for two degrees of freedom.

the mean value at more than 4σ. Additionally, these two parameters appeared to be somewhat out of phase with the Comptonization component parameters.

The results from observation E were somewhat more complex (Figure 5.4). That the phase-averaged spectra were substantially different is clear from comparing the pulse profiles for the two observations. The 2–7 keV profile for observation B was typically twice that for 7–20 keV, whereas for observation E they are almost identical. The variation of spectral parameters with phase is also different; for observation E there is now evidence for significant asymmetry about the primary minimum. In contrast with the observation B results, no significant variation was observed in the column density n_H or the Gaussian Fe line component parameters. Thus these parameters were fixed at the values obtained for the phase-averaged spectrum (following the approach of Galloway et al., 2000).The source temperature T_0 was again quite consistent with the phase-averaged value, except around the primary minimum. In the bin immediately before $\phi = 0.0$ T_0 decreased significantly ($> 4\sigma$), while within the phase bin including the minimum T_0 increased instead by $\approx 20\%$ (at lower significance however). For several of the phase-selected observation E spectra,

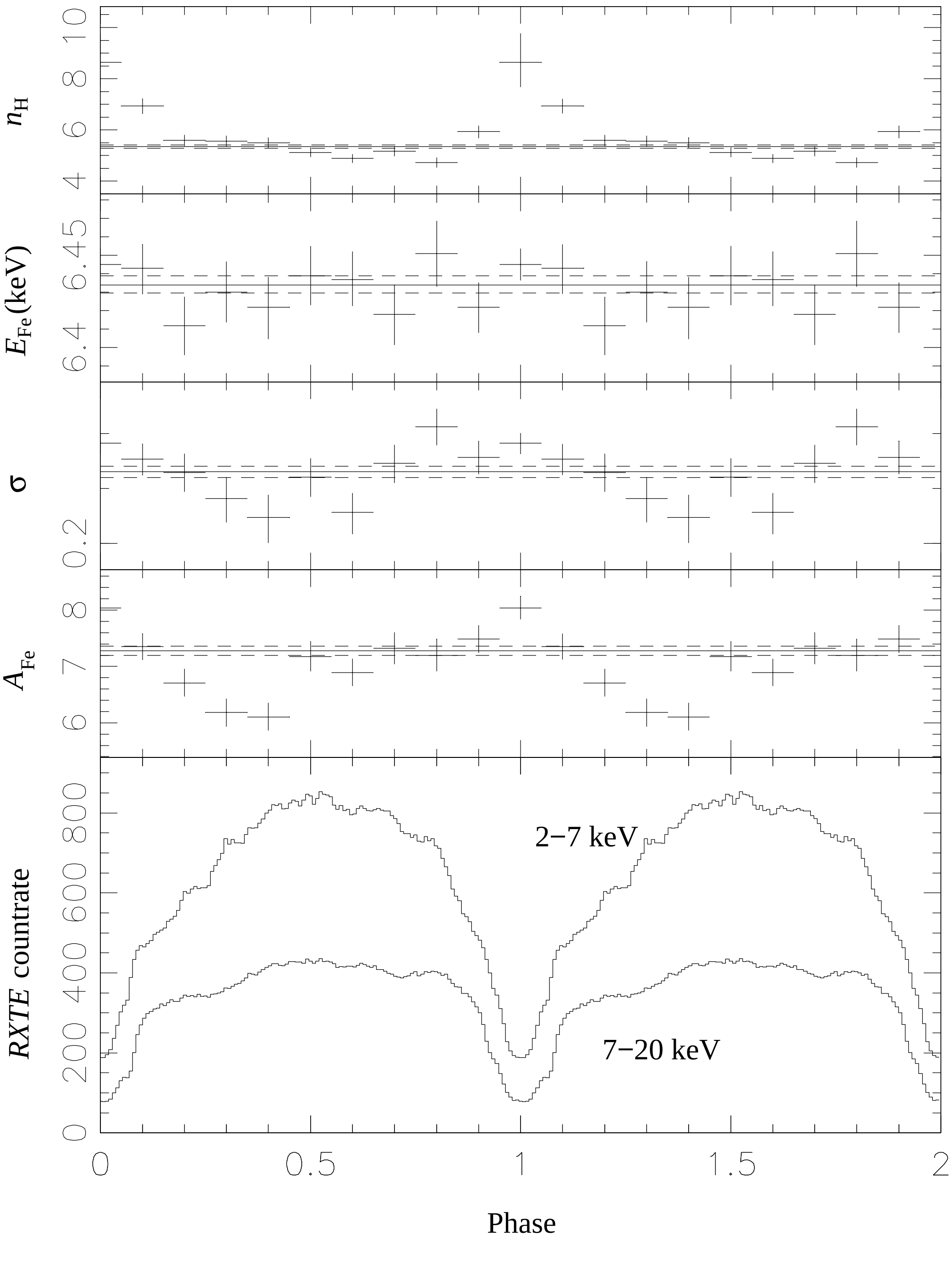

Figure 5.3 Additional spectral model fit parameters versus pulse phase for the 17 February 1996 *RXTE* observation of GX 1+4 (B). From top to bottom, the panels shows the neutral column density n_H (in units of 10^{22} cm^{-2}), Fe line component centre energy E_{Fe}, width σ and normalisation A_{Fe} (units of photons cm^{-2} s^{-1} keV^{-1}) and the pulse profiles in the 2–7 and 7–20 keV energy bands. Other details are as for Figure 5.1.

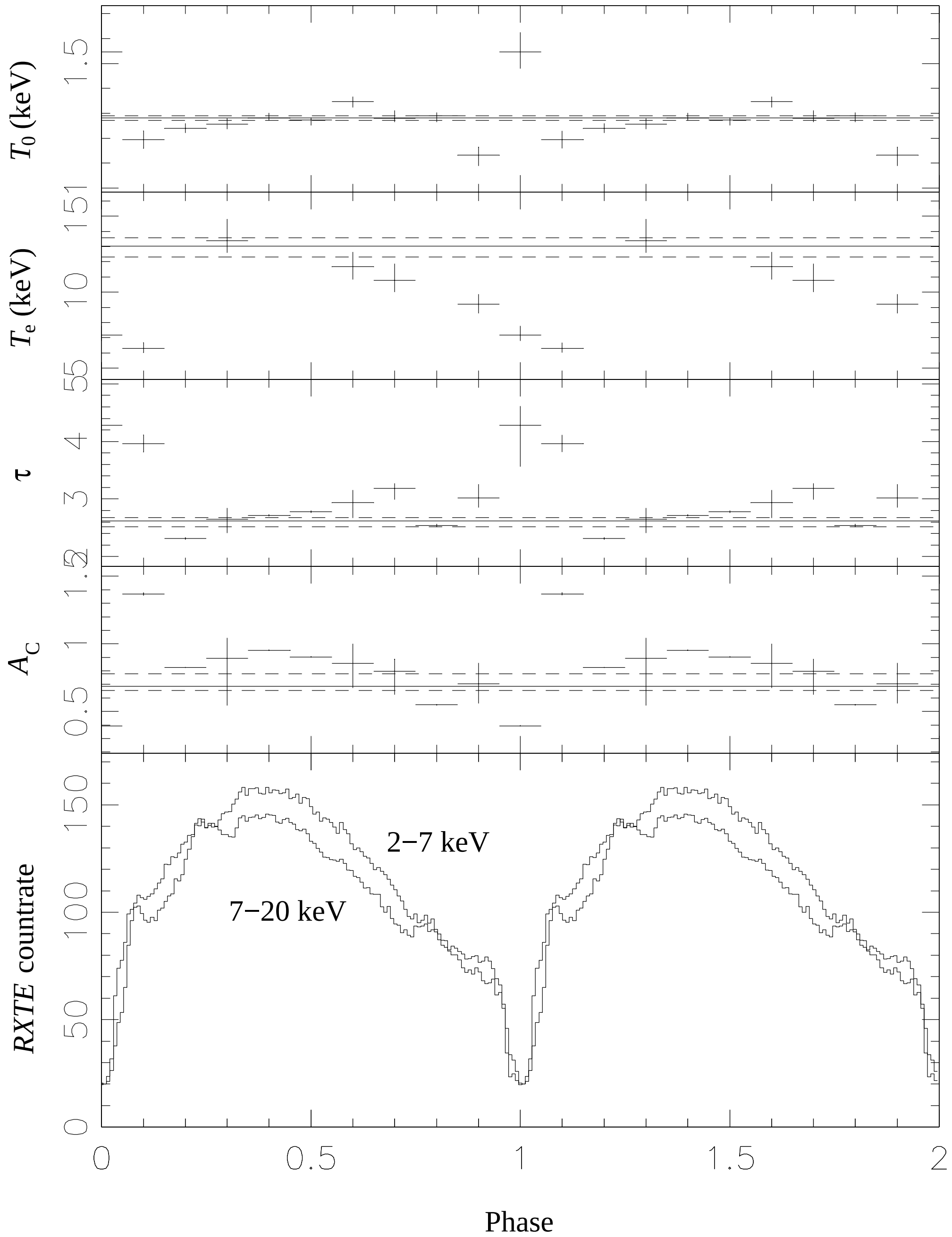

Figure 5.4 Spectral model fit parameters versus pulse phase for the 8 June 1996 *RXTE* observation of GX 1+4 (E). The plot variables are identical to Figure 5.1; the pulse profiles in 2–7 and 7–20 keV energy bands are shown in the bottom panel. At phases where the scattering plasma temperature $T_{\rm e}$ was fixed ('frozen') at the phase averaged value no point is plotted (second panel from top).

the scattering plasma temperature T_e was not constrained or confidence limits could not be determined. In those cases the parameter was fixed at the value appropriate for the observation-averaged spectrum. For those phase bins for which T_e could be determined it appeared to decrease systematically with phase, with maximum deviation from the phase-averaged value at $\phi = 0.1$, significant at $> 8\sigma$.

The increase in τ at $\phi = 0.0$ was not as large (or as significant) as for observation B, which may have been due to the decreased dip phase width. If the phase bin includes data from the dip ingress and egress, the contribution to the spectrum of these intervals may be disproportionate compared to their duration because of the substantially larger count rate. The most significant increase in τ was observed at $\phi = 0.1$, at $> 8\sigma$. It is interesting to note that the τ values for phases 0.0–0.1 are consistent with an elevated level compared to the mean (of $\approx 50\%$), but a decrease in emission is only observed within the phase range -0.05–0.05 (the dip). At $\phi = 0.1$, in order to fit for the much higher flux compared to that measured over the dip, A_C is increased by a factor > 3 relative to the previous bin. In contrast with the results for T_e, the measured τ appeared to systematically increase with phase (up to the maximum at $\phi = 0.1$). Finally the normalisation A_C did not trace the pulse profile as well as for observation B, with marked deviations in particular at $\phi = 0.1$ when it is increased by almost a factor of two.

As with the results for observation B, it is instructive to compare the confidence contours in T_e-τ parameter space for the dip phase $\phi = 0.0$, the phase-averaged spectrum and also the bin following the dip $\phi = 0.1$. The contours confirm that the deviations in the $\phi = 0.1$ phase bin from the phase-averaged spectrum are significant at much greater than 5σ. However, the 5σ contour for the $\phi = 0.0$ bin includes the best-fit value for the phase averaged spectrum. The 3σ confidence region extends beyond the limits of the plot, to $T_e > 15$ keV.

5.2 Dip timing

At moderate count rates the individual dips forming the primary minimum were usually well defined in the 1 s lightcurves (e.g. Figure 3.6). These features seemed to be ideal for determining the pulse period, as described in section 2.1.3. The algorithm was applied to 1 s barycentre-corrected lightcurves from the observations listed in Table 3.1, with several exceptions. For observations F, J–P and the latter part of observation H, the count rate was so low that individual eclipses were impossible to reliably identify in the lightcurves. For observations V–Y, the span of each observation was such that a constant period solution did not provide accurate enough predictions of arrival times to enable a fit to be made. For the remaining observations, the period was adjusted to give a least-squares line of best fit with gradient $\lesssim 10^{-6}\,\mathrm{s\,cycle}^{-1}$. However, in general the pulse period determined using this method did not agree exactly with the value calculated from χ^2-P fitting or interpolation of the BATSE data. The likely reason was that the individual dip arrival times showed significant scatter with respect to the predicted arrival time

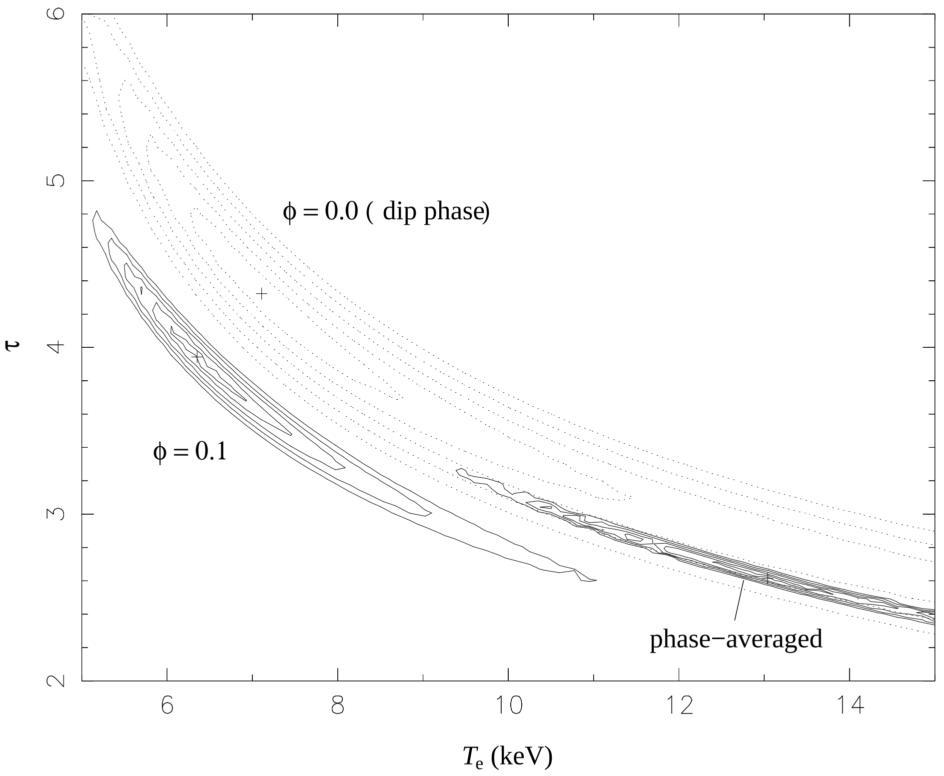

Figure 5.5 Comparison of confidence contours in T_e-τ parameter space between the phase-averaged spectrum (lower right corner) for observation E, the spectrum extracted from the dip phase bin ($\phi \in -0.05, 0.05$) and the bin immediately following ($\phi \in 0.05, 0.15$). The best-fit parameter combinations for the two spectra are shown by a cross. Contours are plotted at $\Delta\chi^2$ values of 2.296, 6.180, 11.83, 19.34 and 28.77 corresponding to confidence levels of 1, 2, 3, 4 and 5-σ respectively for two degrees of freedom.

based on the period estimate (Figure 5.6).

Typical values of Δt_d were $\sim \pm 2$ and $\sim \pm 1$ s for observations B and E respectively. Clearly, such systematic errors on the dip arrival times combined with the generally rather short observation durations (a few hundred cycles) will significantly influence the period required to give a zero-slope line of best fit. Indeed, the results which agreed best with periods from the other methods described were for the longest observations, A and H. Visual inspection of the individual fits confirms that the arrival time errors were genuine and not simply an artefact of counting noise between adjacent bins (for example). The residuals did not appear to exhibit any periodic or quasiperiodic variation with cycle number (time). A search for periodic signals using the Lomb-Scargle periodgram (Press et al., 1996) over all residuals for each of the observations on which the analysis was performed did not result in any significant detections. The most significant peaks were found for low frequency signals in the longest observations, but these detections were most likely

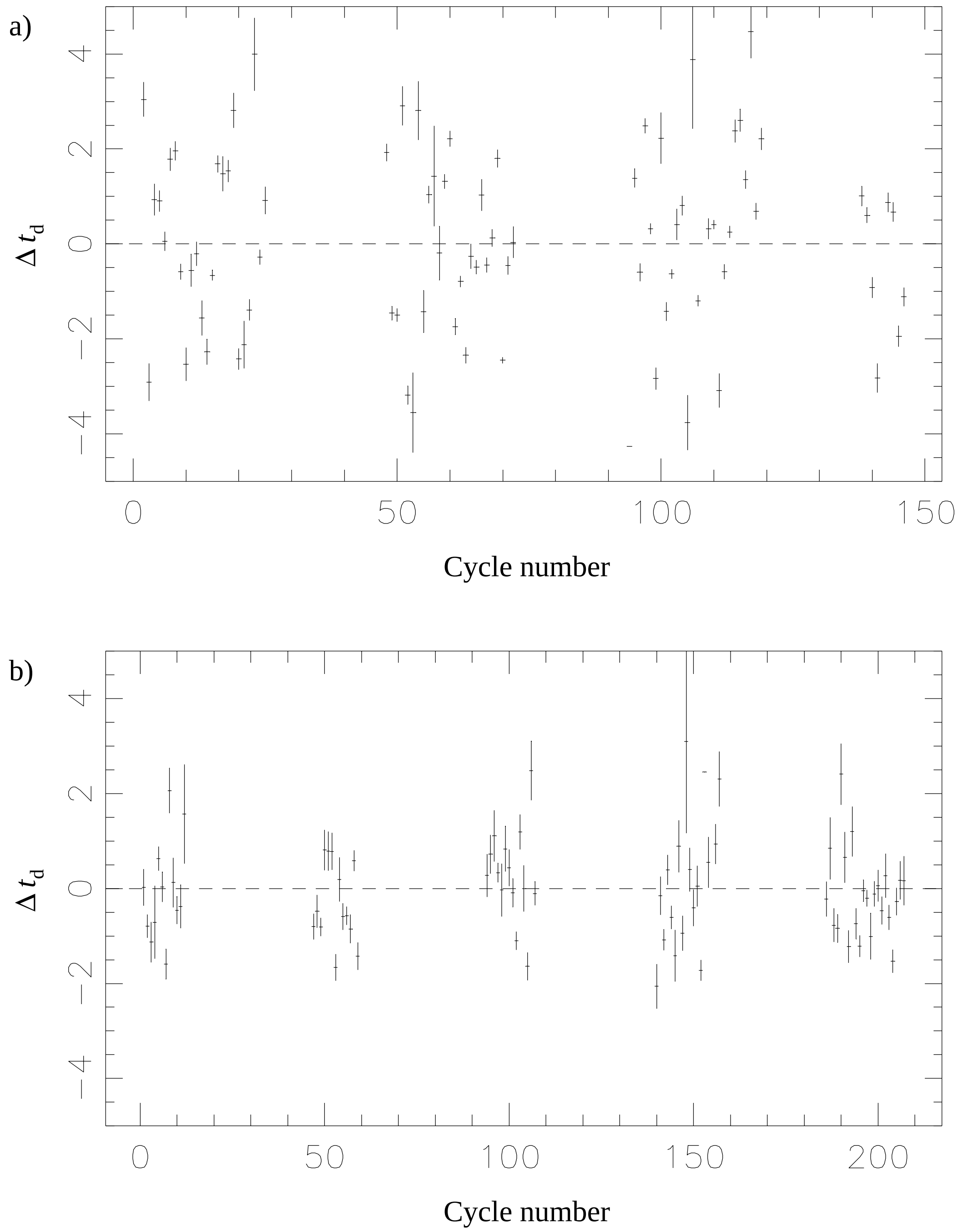

Figure 5.6 Dip arrival time residuals plotted against cycle number for *RXTE* observations of GX 1+4. The difference between the expected dip arrival time and the measured time (based on parabolic fitting of the lightcurve in a 16 s window) is $\Delta t_{\rm d}$ (seconds). The plots show representative results from observations a) B and b) E (see Table 3.1).

due to aliasing related to regular interruptions to the data as a result of screening.

Comparison of the residuals for observations B and E suggest that the variance may depend on the source luminosity, since the source was significantly brighter in observation B than E. The standard deviation of the dip residuals $\sigma(\Delta t_{\rm d})$ plotted against the luminosity for each of the analysed observations confirms this relationship (Figure 5.7). Above $10^{37}\,{\rm erg\,s^{-1}}$ $\sigma(\Delta t_{\rm d})$ traced the luminosity well, but below that level the degree of variation varied between 0.6–1.3 for observations at comparable luminosities.

The fitted parameter $w_{\rm q}$ (see equation 2.2) represents a measure of the width of individual dips. However, it is not quite as straightforward as $w_{\rm d}$ defined in Chapter 4 (equation 4.2) which is instead measured from the mean pulse profiles. From examination of equation 2.2, it is clear that $w_{\rm q}$ will depend on the count rate as well as the sharpness of the dip. To compare values between fits at different count rates it is first necessary to normalise $w_{\rm q}$ by the mean count rate over the fitting window. A larger value is then indicative of a narrower dip. On averaging the appropriately normalised $w_{\rm q}$ over all the dips in each observation I find that individual dips were wider at higher source luminosity, although the uncertainties were substantial (Figure 5.7, lower panel). The points with the largest error correspond to observation G and the first half of observation H. This scatter cannot be attributed solely to the low count rate, since the error for observations with comparable (or lower) luminosity were much smaller.

More qualitatively, the dip phase width at a given count rate can be determined using equation 2.2 and solving for Δt. I choose a level corresponding to half the mean (over the fitting window) above the baseline rate. This should give a reasonable approximation of $w_{\rm d}$ as follows:

$$\begin{aligned} w_{\rm q}\Delta t^2 &= 0.5F_{\rm mean} \qquad \text{or} \\ \frac{2\Delta t}{P} &= \frac{2}{P}\left(\frac{F_{\rm mean}}{2w_{\rm q}}\right)^{1/2} \approx w_{\rm d} \end{aligned} \tag{5.1}$$

The dip width estimated in this manner corresponds quite closely with that measured from the mean profiles, although the luminosity range is significantly more limited (Figure 5.8). The two estimates deviated somewhat at the highest energies, with the width measured from the mean profile significantly greater than that estimated from the fits.

5.3 Discussion

The pulse phase spectroscopy results show that each of the Comptonization component parameters are significantly modulated at the pulsar rotation period. As suggested in Chapter 3, these parameters represent a measure of conditions in the accretion column and on the neutron star poles. Variation in the spectral fit parameters with pulse phase may in turn provide clues to the distribution of matter in the

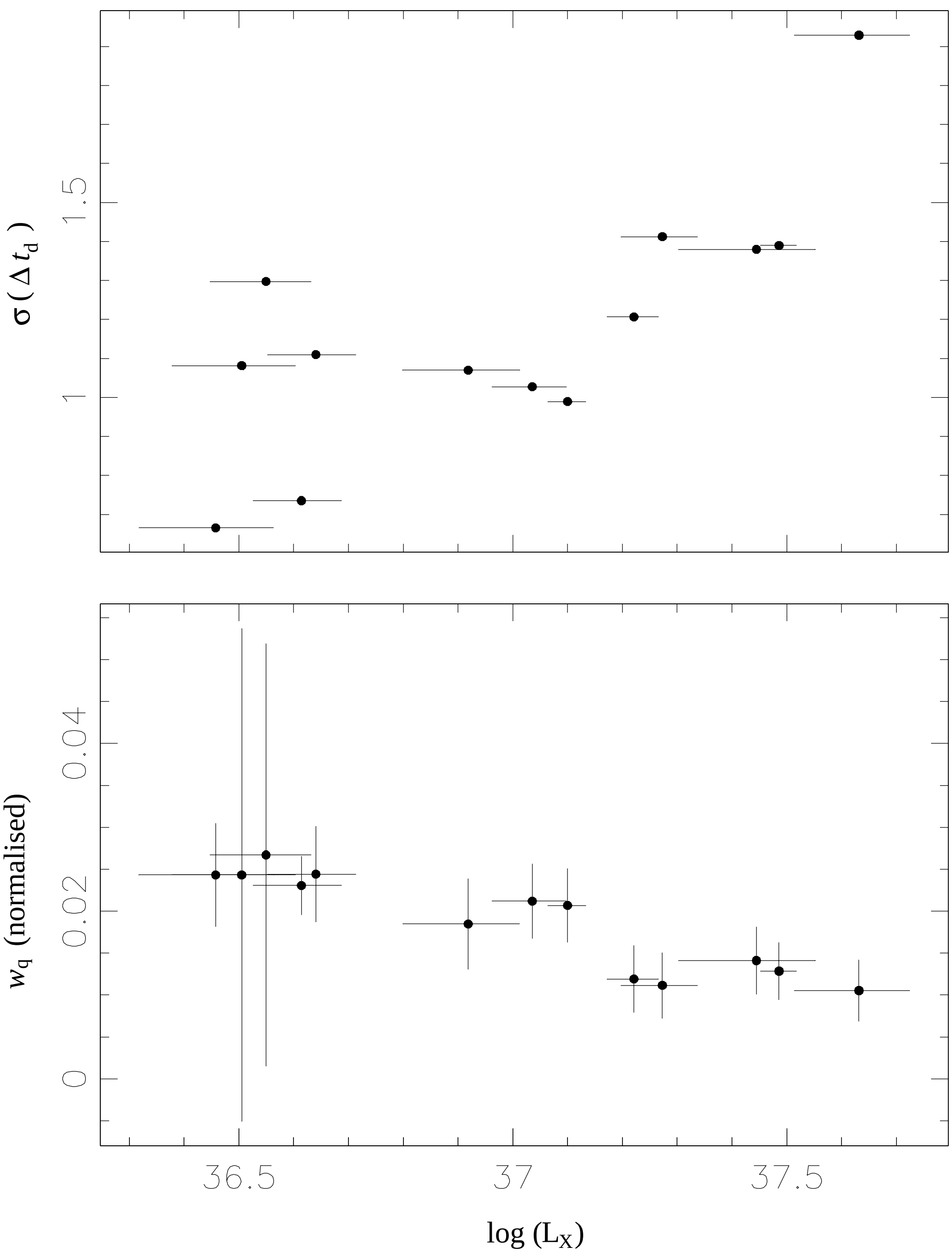

Figure 5.7 Analysis of dip arrival times for *RXTE* observations of GX 1+4. The top panel plots the standard deviation of dip arrival time errors $\sigma = (\sum \Delta t_{\rm d}/n)^{0.5}$ versus 2–20 keV X-ray luminosity (assuming a source distance of 10 kpc) for each separate observation. The bottom panel plots the fitted $w_{\rm q}$, normalised by the mean count rate over the fitting window and averaged over all dips in each observation versus luminosity. Error bars are 1σ.

accretion column. In addition, depending upon the luminosity, significant variations in n_{H} and the normalisation of the Gaussian component A_{Fe} were found.

The sharp dip in the pulse profiles is clearly associated with a significant increase in the scattering optical depth τ both for GX 1+4 (at distinctly different luminosities and phase-averaged spectral conditions) and also for RX J0812.4−3114 (Chapter 6). Such an effect may be observed if the accretion column moves into the observers line of sight of the emission region — a partial 'eclipse' of the neutron star pole by the accretion column (see Figure 1.1). Accretion column eclipses have not before been convincingly shown to occur in any X-ray pulsar, and this result opens exciting new possibilities for understanding the dynamics of the accretion column in these sources. Narrow absorption dips in the orbital lightcurves of some polars (e.g RX J1802.1+1804; Greiner et al., 1998) have previously been associated with just such an effect. The spectral variation in the latter source during the eclipse suggests a warm absorber, in good agreement with the results described here.

An eclipse of the neutron star by the accretion column requires that the inclination angle i is greater than or equal to β, the magnetic colatitude. If $i \approx \beta$, the column axis passes close to the line of sight once every pulse period resulting in a 'near-field' eclipse, as opposed to a 'far-field' eclipse taking place well above the surface of the star. It might be expected that systems with $i > \beta$ are rather common, perhaps making up $\approx 50\%$ of all pulsars (neglecting any observational selection effects). That sharp dips are found in the pulse profiles of only 3 X-ray pulsars — GX 1+4, RX J0812.4−3114 and A 0535+262 (Čemeljić and Bulik, 1998) — of ~ 50 known sources seems to be more consistent with the dips being caused by near-field eclipses, given the relative unlikelihood of the necessary alignment. Furthermore, the accretion column will be less tightly constrained the further from the neutron star the interaction takes place, and the decrease in flux for far-field eclipses may be spread out over such a wide range of phases as to be essentially unnoticeable. Monte Carlo modelling based on Comptonization as the source of high-energy photons supports this as a possible mechanism (see Chapter 7).

That the plasma temperature T_{e} is also low around the phase of primary minimum may be related to the bulk motion of the column plasma, since the relative velocity of the plasma in the observer's frame will depend on orientation (and hence pulse phase). The velocity of bulk motion is likely to be many orders of magnitude above the thermal velocity in the plasma rest frame. Photons emerging from the polar cap will be preferentially scattered in the direction of motion of the plasma, and thus the spectrum observed in the opposite direction will be made up of a disproportionately large number of unscattered photons compared to the phase-averaged spectrum. Model fits should give a significantly lower T_{e} at this phase (corresponding to a softer spectrum) than at other phases. Results from Monte-Carlo simulations suggest the measured T_{e} may be somewhat lower than the mean even without this effect (Chapter 7).

The asymmetry of the spectral parameter variation with respect to the primary minimum in the lower luminosity observation E (and the March 1999 observation of RX J0812.4−3114, Chapter 6) points to asymmetry of emission on the 'leading' and 'trailing' side of the pole. Particularly interesting is the fact that the τ values for these observations are enhanced relative to the mean both in the dip phase and the one following, with a dramatic difference between the continuum normalisation A_C measured within the two bins accounting for the count rate variations between them. It is compelling to speculate that the increase in A_C within the phase bin following the dip results from the decrease in the scattering cross section which is experienced by photons propagating directly along the field lines (Daugherty and Harding, 1986) — i.e. that in these two cases it is actually the $\phi = 0.1$ phase bin which corresponds to the closest approach of the local magnetic field direction to the line of sight, not the dip phase. If that is the case the amount of material along the line of sight in the $\phi = 0.1$ bin may actually be substantially more than for the dip phase to give rise to the same optical depth, and thus it is actually this phase in which the closest alignment of the accretion column and the line of sight occurs (which is of course consistent with the picture of the accretion column as being delineated by the field lines). Why this effect — and the asymmetry of accretion it implies — should be apparent in GX 1+4 only at lower luminosity levels (and not in e.g. observation B) is unknown.

Count rates in pulse profiles from GX 1+4 immediately before and after the dip are frequently significantly different (see Chapter 4), which may be interpreted as further evidence for longitudinal asymmetry. Such asymmetry may originate in the boundary region where the disc plasma becomes entrained into the accretion column (e.g Wang and Welter, 1981). Any longitudinal density inhomogeneities which develop in the boundary region may persist to the neutron star surface due to the lack of motion (and hence mixing) of the plasma perpendicular to the field lines. This is one possible source of pulse profile asymmetry in X-ray pulsars which may be variable on short timescales, as are the observed profiles. However, if the asymmetry is the same relative to the sense of rotation of the neutron star in both poles, the variation in emission will tend to cancel out courtesy of light bending. This effect probably cannot generate profile asymmetry as is typically observed without additonal anisotropic emission effects (e.g. magnetic) or significant brightness variation between the two poles (see Chapter 7).

The observation of significant eclipse arrival time residuals with respect to the ephemeris is an important result. Typical timing errors observed over the range of luminosities in the *RXTE* observations imply that the region of maximum density in the column is wandering stochastically in longitude by 2–6° (depending upon the source flux) on timescales of $\lesssim P$. Although the plasma in the accretion column is fixed to the field lines from the neutron star, this does not necessarily imply that the field itself is moving relative to the star. The accretion column is roughly defined by the 'bundle' of field lines along which significant plasma flows. If conditions in the boundary region between the disk and magnetosphere are such that this set of field lines can vary with time, the accretion column will appear to change position relative to the star (and the corotating magnetic field). The conditions within the boundary region are poorly understood, and since hydromagnetic instabilities are thought to play an important role the uptake of plasma to the field lines is likely to

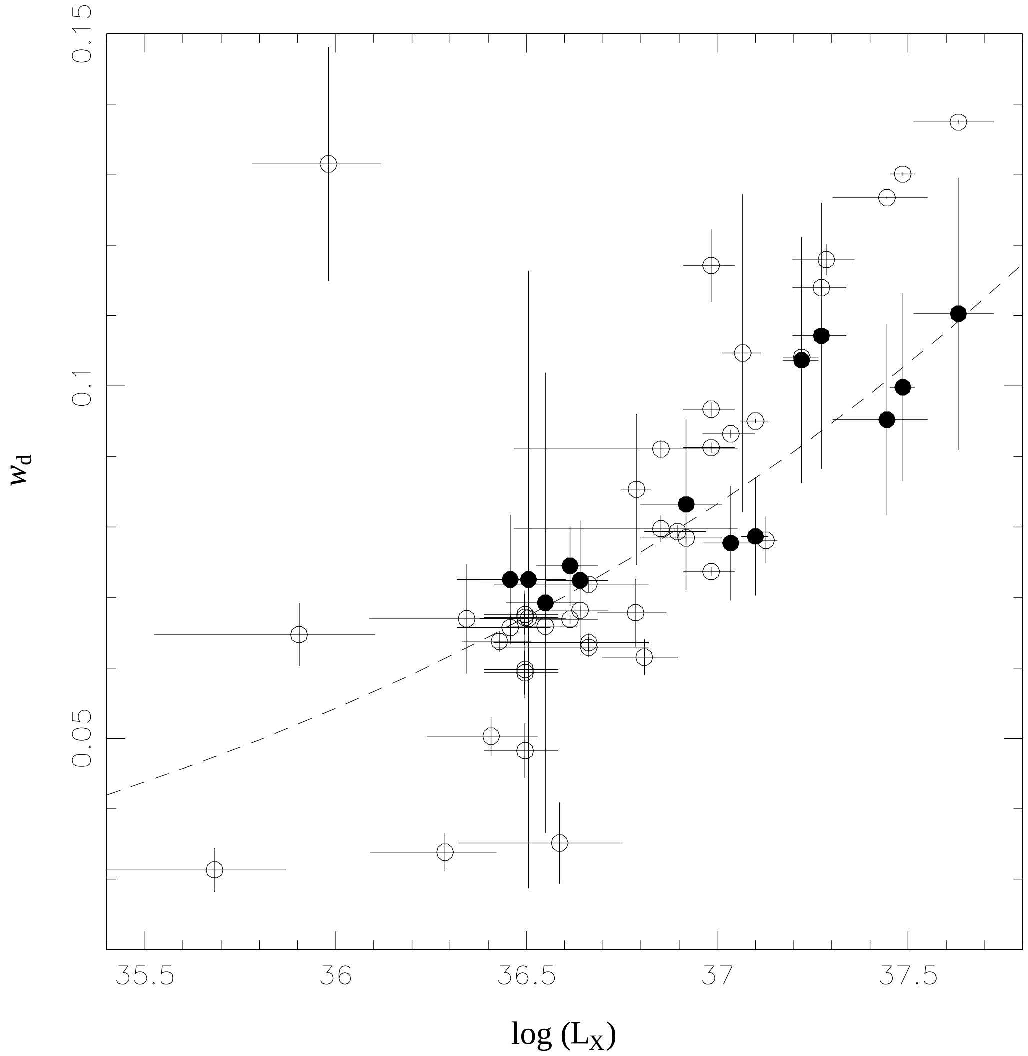

Figure 5.8 Combined analysis of dip arrival times for *RXTE* observations of GX 1+4 and comparison with theoretical estimates. Both the dip width w_d (equation 4.2) calculated from mean pulse profiles (open circles), and w_d estimated from the mean normalised w_q (equation 2.2) for the available observations (filled circles) are plotted against the 2–20 keV luminosity (assuming a distance to the source of 10 kpc). The dotted line represents the theoretical calculation (equation 5.2). Error bars represent the 1σ uncertainties.

be unpredictable and time-varying. The flow of denser 'blobs' of plasma (which are threaded more slowly by the neutron stars magnetic field) into the threading region can also significantly alter the position and size of the accretion column (Warner, 1995 page 314).

Finally, the dip fitting results have quantified the role of dip arrival time errors in the width measurements from mean pulse profiles (Chapter 4). As $L_{\rm X}$ increases the individual dips do appear to become significantly wider on average. The dip arrival time residuals appear to contribute to the proportionality in Figure 4.5, but only to exaggerate the underlying relationship. Variance in the widths for each observation appear to be more or less constant over the luminosity range investigated, however the variance is very large for two of the observations: G and the first part of observation H. In the latter case the significant variation of flux over the observation may be responsible for the large variation, but this does not seem to be the case for the former.

The dynamics of the boundary layer between the accretion disc and the magnetosphere may be responsible for the increasing dip width with luminosity, as follows. At higher $L_{\rm X}$ (and consequently higher $\dot{M}$) the Alfvén radius $r_{\rm A}$ decreases (see equation 1.3), and the inner disk edge moves closer to the neutron star. As a consequence, the radial velocity of the disk plasma just outside the boundary layer will increase. Recall that in the absence of significant magnetic pressure the disk rotates at approximately the Keplerian velocity $v_{\rm K}$ (equation 1.2). A necessary condition for X-ray pulsations to be observed is that the magnetic field axis is misaligned with the spin axis, i.e. $\beta > 0$. In this case the area of the boundary region on the inner disc edge where significant uptake of plasma to the accretion column occurs will probably span a limited phase range (giving rise to an accretion 'curtain' at the neutron star surface). Assuming there exists some characteristic timescale $\Delta t_{\rm e}$ for the plasma to become entrained onto the field lines (which is roughly constant), the time required for all the plasma flowing into the uptake region to move into the accretion column will also be roughly constant. At higher $\dot{M}$, and hence higher Keplerian velocities in the uptake region, entrainment will clearly take place over a wider range of phases with respect to the neutron star rotation. The result will be an accretion column which is wider at the boundary region, and hence will be wider also at the neutron star surface and produce a broader dip. Combining equations 1.1, 1.2 and 1.3, it is straightforward to show that in this case

$$\begin{aligned} w_{\rm d} &\approx \frac{v_{\rm K}\Delta t_{\rm e}}{\pi r_{\rm A}} \qquad \text{or} \\ w_{\rm d} &\propto L_{\rm X}^{3/7} \end{aligned} \tag{5.2}$$

The comparison of this relation (with arbitrary normalisation due to the free parameters) with the dip width measurements from the curve fitting is very good, although the uncertainties are significant (Figure 5.8). Dip width measurements at even higher luminosities, as well as analysis over shorter timescales to resolve possible flux variations, may improve the measurements and allow a better assessment of consistency with this model.

Chapter 6

X-ray observations of RX J0812.4−3114

6.1 Observations

RX J0812.4−3114 was observed by *RXTE* during two intervals in February 1998 and one in March 1999 (Table 6.1). The source count rate was found to be $\approx 20\,\mathrm{count\,s^{-1}}$ (3–30 keV) on 1 February 1998, increasing to $\approx 40\,\mathrm{count\,s^{-1}}$ on 3 February and undergoing a modest flare to $\approx 80\,\mathrm{count\,s^{-1}}$ over ≈ 2 h in the latter part of the observation (Reig and Roche, 1999). The 25 March 1999 observation was scheduled at the expected time for an outburst, which have occurred regularly on an ≈ 81 d period since 1998 (Corbet and Peele, 2000).

ID	Start	End	On-source (sec)	Ref.
A	01/02/1998 11:28:47	01/02/1998 16:24:47	10128	[1]
B	03/02/1998 09:53:51	03/02/1998 14:01:51	8912	
C	25/03/1999 07:55:11	25/03/1999 13:42:07	13584	[2]

Table 6.1 *RXTE* observations of RX J0812.4−3114. Start and end times and on-source durations are calculated from Standard-2 spectra taking into account screening (see section 2.1.1). Times are terrestrial time (TT). Publications quoting observations are 1. Reig and Roche (1999) and 2. Corbet and Peele (2000)

PCU #1 was not functioning during the 25 March 1999 observation, so the count rates were scaled appropriately to represent expected rates for 5 PCUs. The results indicate that this was the brightest yet seen by *RXTE*, with full-range PCA count rate consistently $\approx 80\,\mathrm{count\,s^{-1}}$ over ≈ 6 h (Figure 6.1). The phase-averaged count rate varied by $\approx 20\,\mathrm{count\,s^{-1}}$ on timescales of ≈ 1 min. No evidence of spectral variation (as indicated from the count rate hardness ratio in 2–7 and 7–20 keV PCA energy bands) was observed over the course of the observation. The pulse profiles were very similar to those observed in the February 1998 observation, with strong trailing-edge asymmetry, a sharp dip forming the primary minimum, and a small local maximum around phase 0.3 relative to the dip. As before the profiles exhibited little variation with energy, although the dip appeared to become shallower at higher energy bands.

The pulse period was determined through Gaussian fitting of the peak in χ^2-$P_{\rm trial}$, with errors determined from equivalent analysis on 100 simulated lightcurves. The calculated solar system barycentre-corrected period was $P = 31.885623(9) \pm 0.000007(5)$ s, in excellent agreement with the value $P = 31.8856 \pm 0.0001$ s obtained by Corbet and Peele (2000) for the same observation. This value is somewhat greater than found for the February 1998 observations, providing marginal evidence for spin-down at a mean rate of $(1.5 \pm 1.1) \times 10^{-11}\,\mathrm{s\,s^{-1}}$ (or $\approx 0.0014\%\ \mathrm{yr^{-1}}$).

Previous spectral analyses primarily used a power-law model with an exponential cutoff (Reig and Roche, 1999, Corbet and Peele, 2000). Using the recently updated

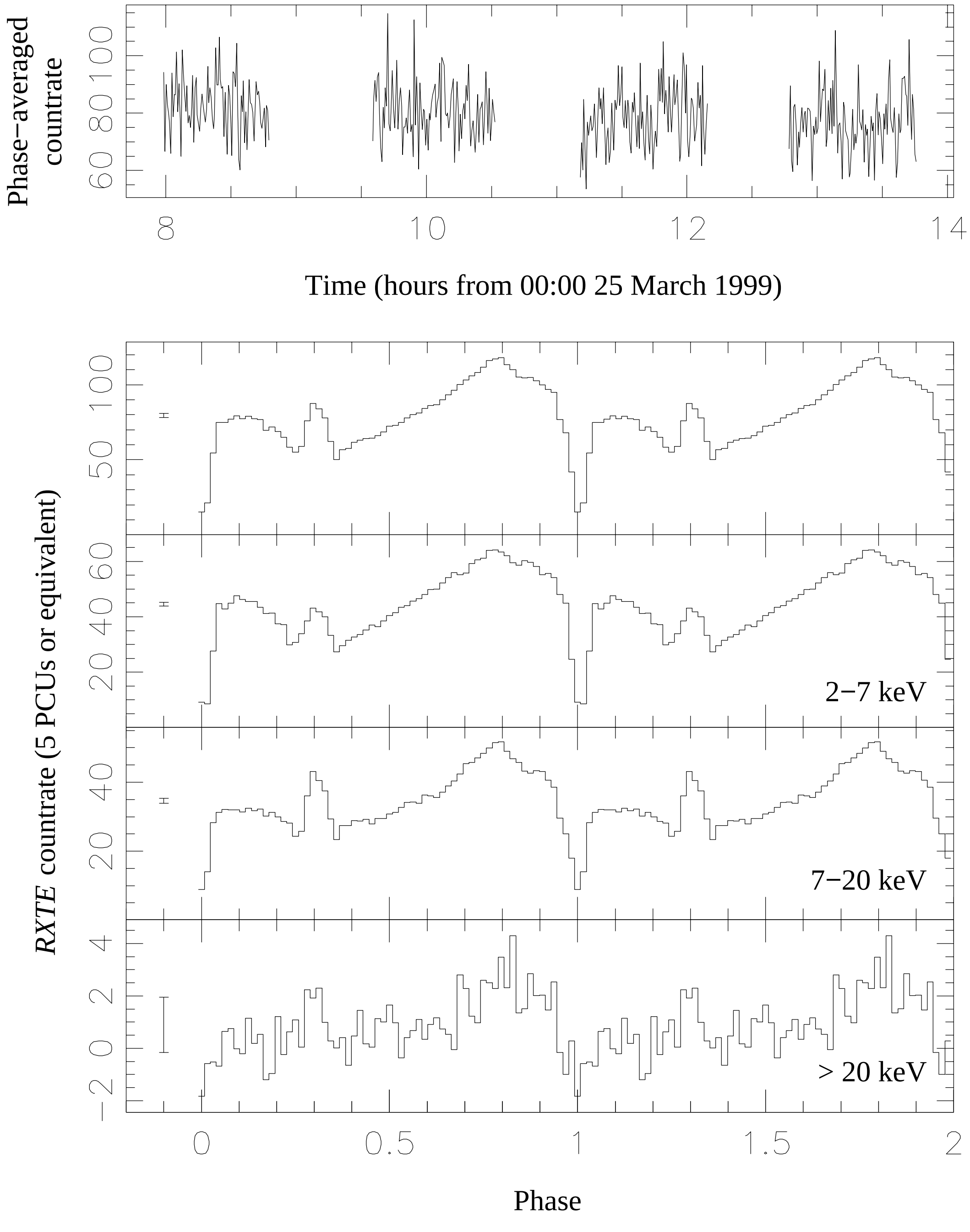

Figure 6.1 *RXTE* observation of RX J0812.4−3114 on 25 March 1999. The top panel plots the count rate averaged over the pulse period 31.885623(9) s, while the panels below plot the pulse profile over the full PCA range and subranges 2–7, 7–20, and > 20 keV from top to bottom respectively. Typical error bars are shown to the left of each profiles; two full periods are plotted for clarity. Count rates are scaled to 5 PCU equivalent.

response matrices and faint background models, the cutoff power law model results in generally unacceptable fits, as do power law, power law and blackbody, and broken (two index) power law. Instead the best fitting spectral model was the Comptonization continuum component of Titarchuk (1994), implemented in XSPEC as '`compTT`' with a maximum $\chi^2_\nu = 1.52$ for the 25 March 1999 observation. Resulting spectral fit parameters for each of the *RXTE* observations are shown in Table 6.2. Note that at the beginning of the 1 February 1998 observation only four PCUs were on for $\approx$ 2900 s; data from this interval were extracted and analysed separately (A1). The remaining portion of the 1 February observation is termed A2. During the 1 February observation the count rate was at the lowest seen by *RXTE*, and it was not possible to determine error limits for the fitted $T_{\rm e}$. Instead, this parameter was fixed ('frozen') at the fitted value for the 3 February 1998 spectrum (B).

Table 6.2 Fit parameters for *RXTE* PCA spectra of RX J0182.4−3114 using a model based on Comptonization of soft photons by hot plasma. T_0 is the temperature of the thermal input spectrum, $T_{\rm e}$ and τ are the temperature and optical depth respectively of the scattering plasma, and $A_{\rm C}$ is the normalisation parameter for the Comptonized model component in units of 10^{-3} photons cm^{-2} s^{-1} keV^{-1}. The model spectra is attenuated by photoelectric absorption by cold matter along the line of sight, with column density $n_{\rm H}$. The luminosity $L_{\rm X}$ is integrated over 2–20 keV assuming a source distance of 9 kpc, with errors calculated from the variance of the phase-averaged PCA count rate. Data used is from PCA mode Standard-2. Confidence intervals are 1σ; fit statistic is reduced-χ^2 (χ^2_ν).

Parameter	A1	A2	B	C
$n_{\rm H}$ ($\times 10^{22}$ cm^{-2})	< 1.21	$0.34^{1.14}_{0.0}$	< 0.068	$0.71^{1.1}_{0.31}$
T_0 (keV)	$0.998^{1.04}_{0.895}$	$0.966^{1.01}_{0.897}$	$1.15^{1.16}_{1.13}$	$1.19^{1.22}_{1.16}$
$T_{\rm e}$ (keV)	6.39 (fixed)	6.39 (fixed)	$6.39^{6.70}_{5.79}$	$5.18^{5.39}_{5.01}$
τ	$3.77^{3.91}_{3.64}$	$3.79^{3.87}_{3.72}$	$4.13^{4.46}_{4.03}$	$4.57^{4.71}_{4.40}$
$A_{\rm C}$	$1.10^{1.22}_{1.06}$	$1.21^{1.30}_{1.17}$	$3.20^{3.54}_{3.04}$	$5.93^{6.20}_{5.61}$
$L_{\rm X}$ ($\times 10^{36}$ erg s^{-1})	0.45 ± 0.20	0.48 ± 0.21	1.45 ± 0.55	2.08 ± 0.26
χ^2_ν	0.643	0.873	1.21	1.52

With the measured increase in unabsorbed source flux (2–20 keV) from $\lesssim 10^{36}$ erg s^{-1} to $\approx 2 \times 10^{36}$ erg s^{-1} between February 1998 and March 1999, the most significant variation in any spectral parameter was in the optical depth for scattering τ (Table 6.2). During observation A $\tau \approx 3.8$, however during B and C $\tau \approx 4.1$–4.4. The τ confidence limits for observations A2 and C indicate an increase at $> 4\sigma$ significance level. A less significant increase was seen in the source spectrum temperature T_0.

Initially $T_0 \approx 1$ keV, increasing during observations B and C to ≈ 1.15 keV. The confidence limits for observations A2 and C indicate an increase at almost 3σ significance. The neutral column density was consistent with zero during the February 1998 observations but increased to around 7×10^{21} cm^{-2} by March 1999. Despite the different continuum spectral model, the measured flux and $n_{\rm H}$ variation is roughly consistent with that measured by Corbet and Peele (2000).

The sharp primary minimum has been attributed to interactions between the emitting region and the accretion flow, although previous pulse phase spectroscopy offered no support to this idea (Reig and Roche, 1999). Given the new mean spectral models, I divided the GoodXenon data from the 25 March 1999 observation into 10 equal phase bins (with the first bin centred on the primary minimum) and extracted a spectrum from each. Initial fitting of the mean spectral model to the phase-selected spectra resulted in poorly constrained fit values of $n_{\rm H}$ and T_0 which offered no significant evidence for spectral variation with phase. Following the approach of Galloway et al. (2000), I fixed these two parameters at the values determined for the phase-averaged spectra and re-fit the phase-selected spectra. The remaining parameter fit values do show evidence for significant variation with phase (Figure 6.2). The phase bin covering the dip and following it both show evidence for reduced $T_{\rm e}$ and increased τ. The most significant deviation from the mean τ is in the $\phi = 0.1$ phase bin, with an increase of $\approx 20\%$ at a significance of $> 4\sigma$. The preceding bin, which covers the dip itself, exhibits a slightly smaller enhancement significant at only the 2σ level. Variations in the Comptonization component normalisation are significant, and $A_{\rm C}$ reaches a maximum also in the bin following the dip. Throughout almost all of the phase range $T_{\rm e}$ increases with increasing phase, while τ decreases. This behaviour is in curious contrast to the results for observation E of GX 1+4 (see Chapter 5), which exhibits a general decrease in $T_{\rm e}$ and increase in τ with increasing phase. It is interesting to note that the sense of asymmetry in the pulse profiles is opposite between these two observations (compare Figures 6.2 and 5.4), with the peak emission for observation E of GX 1+4 closer to the leading edge of the pulse, while for the March 1999 observation of RX J0812.4-3114 the peak emission is almost immediately before the dip.

As previously noted, it is inadequate to simply compare the confidence intervals obtained for each parameter individually when two or more of those parameters are strongly correlated (or anticorrelated). Instead, the joint confidence regions for $T_{\rm e}$ and τ are determined adopting $\Delta\chi^2$ values appropriate for two degrees of freedom, as was done for the analysis of the pulse-phase spectra from GX 1+4 (see Chapter 5). For the March 1999 observation of RX J0812.4−3114 the confidence contours show that $T_{\rm e}$ and τ values for the $\phi = 0.1$ phase bin are in fact different from the mean at much greater than 5σ significance (Figure 6.3). In contrast, the 5-σ contour for the $\phi = 0.0$ phase bin almost completely encompasses the corresponding region for the phase-averaged spectrum, with the best fit-value for the latter spectrum distinct from the former at between 3–4σ. Note that the phase range for the bin which encompasses the dip ($\phi = -0.05$–0.05) also includes some of the much stronger emission on the ingress and egress. Clearly, the significantly larger confidence regions

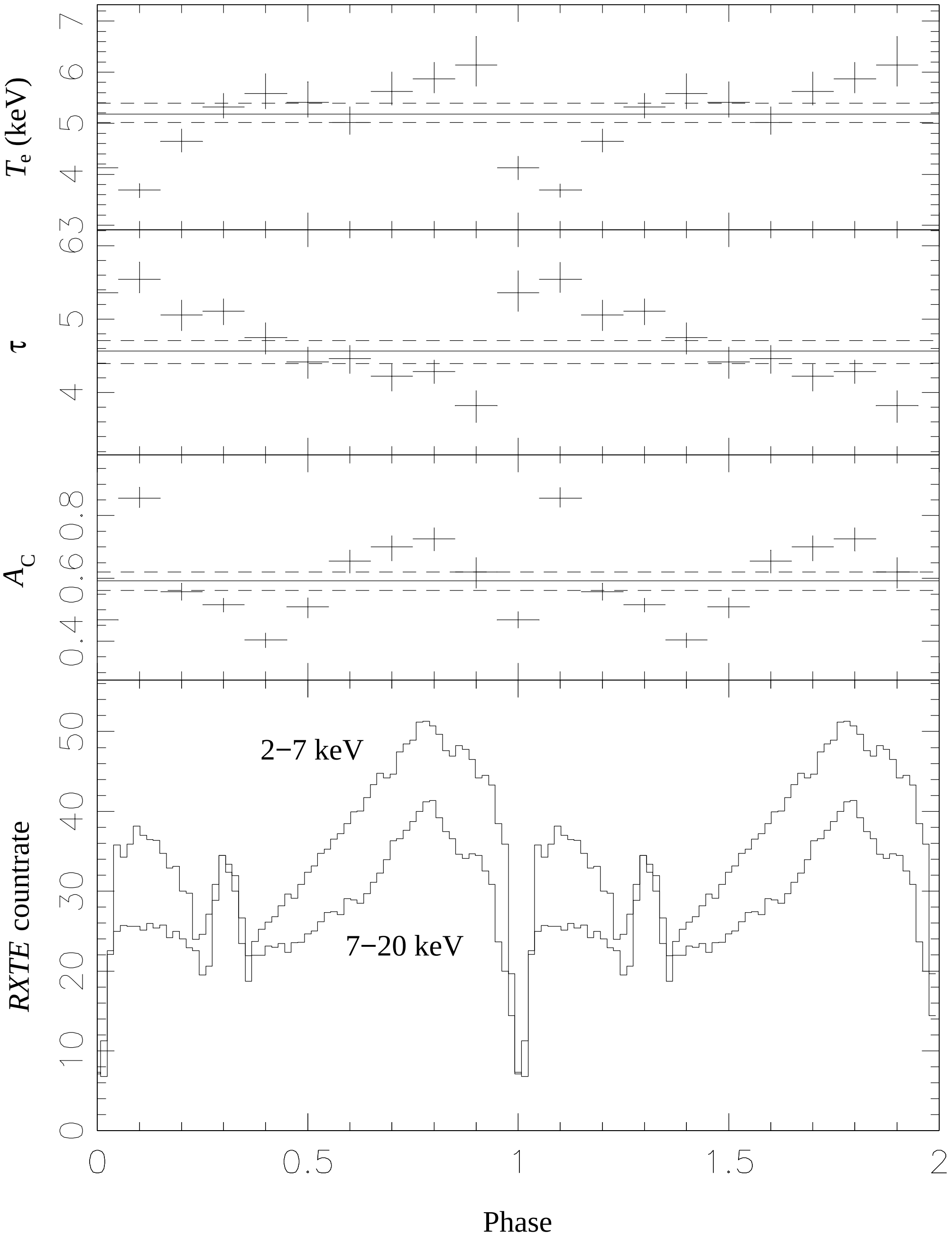

Figure 6.2 Spectral model fitting parameters versus pulse phase for the 25 March 1999 *RXTE* observation of RX J0812.4−3114. From top to bottom, the panels shows the scattering plasma temperature $T_{\rm e}$, optical depth for scattering τ, normalisation $A_{\rm C}$ and the pulse profile in 2–7 and 7–20 keV energy bands respectively. Fitted parameter values for the phase-averaged spectra covering the same interval are shown by the solid lines; error bars and the dotted lines show the 1σ confidence intervals. Two full pulse periods are shown for clarity.

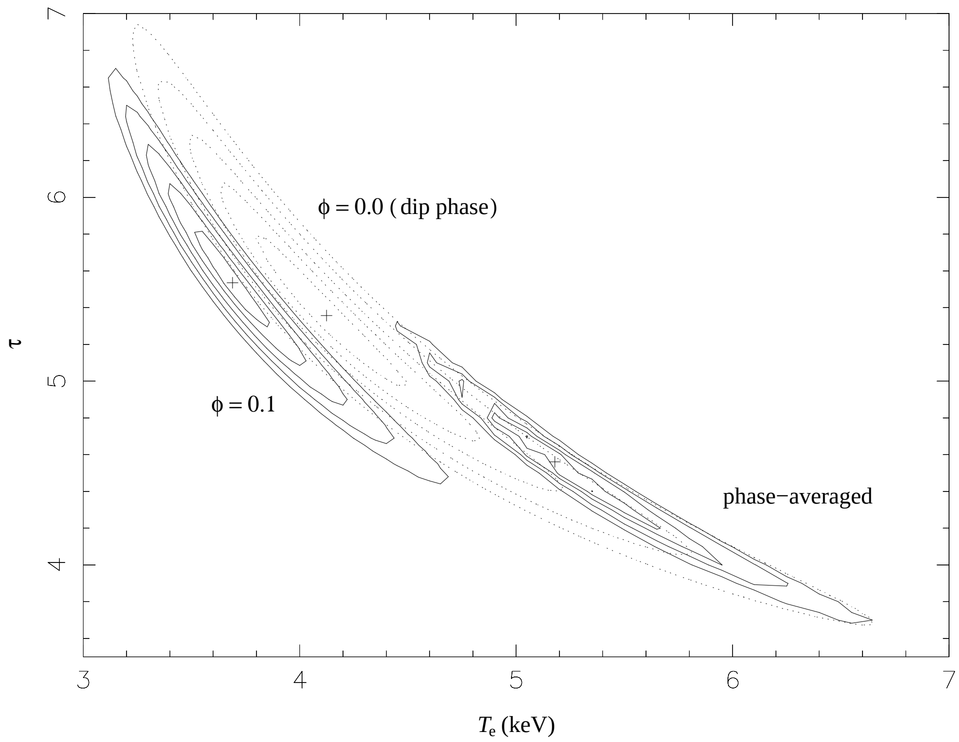

Figure 6.3 Comparison of confidence contours in T_e-τ parameter space between spectra extracted from the March 1999 observation of RX J0812.4−3114. Solid contours represent the confidence regions for the phase-averaged spectrum (lower right) and the $\phi = 0.1$ phase bin (upper left). Contours for the $\phi = 0.0$ bin (which covers the dip) are shown as dotted lines. The best-fit parameter combinations for each spectra are shown by a cross. Contours are at $\Delta\chi^2$ values of 2.296, 6.180, 11.83, 19.34 and 28.77, corresponding to confidence intervals of 1, 2, 3, 4 and 5σ respectively for two degrees of freedom.

for this phase range are to some extent a consequence of the rapidly varying spectra around the dip phase (note the difference in spectral parameters between the $\phi = 0.9$ and $\phi = 0.1$ phase bins).

6.2 Discussion

RX J0812.4−3114 provides a second example of an X-ray pulsar whose mean spectra are consistent with a Comptonization continuum component. In contrast to GX 1+4 (Chapter 3), this source is probably very typical, since Be/X-ray binaries make up a significant proportion of all known X-ray pulsars. This lends strong support to the picture of spectral formation as originiating with approximately blackbody spectra emitted from the polar cap, and undergoing Compton scattering within the accretion column. The phase-averaged spectral fit parameters fall within the ranges expected for neutron star accretors, as previously discussed for GX 1+4. The measurement of a disproportionate increase in τ as L_X increases fourfold again suggests that the accretion column increases substantially in cross-sectional area as $\dot{M}$ increases, maintaining a relatively constant column density. Note however that the spectral fitting results for GX 1+4 indicate that such an effect cannot account for the small variation in τ over the full range of luminosity seen in *RXTE* observations of that source (Chapter 3). In any case Comptonization continuum components are excellent candidates for fits to spectra from these sources.

In contrast to GX 1+4, no Gaussian model component is required for spectral fits, suggesting that the system is relatively free from cold matter surrounding the neutron star. The increase in $n_{\rm H}$ observed in the March 1999 observation as compared to February 1998 does however suggest variations in the circumstellar region, possibly related to an episodic mass ejection of the companion star or, more likely, regular variations related to an eccentric orbit. The earlier observations were made at a phase of 0.9 relative to the calculated ephemeris based on the regular outbursts observed by the *RXTE* ASM, whilst the most recent observation was coincident with a flare ($\phi_{\rm orb} \approx 0.0$; Corbet and Peele, 2000). It is likely that the flares coincide with the periastron passage of the neutron star in a mildly eccentric orbit, which is common in Be/X-ray binaries (e.g. Stella et al., 1986). The increase in both $L_{\rm X}$ and $n_{\rm H}$ arise from the increased wind density (and hence mass capture rate for the neutron star) closer to the massive companion.

Pulse profiles from the source appear to be quite stable on yearly timescales. Pulse phase spectral analysis of the most recent *RXTE* data support interactions with the accretion column as the dip origin. Both the phase bin coincident with the dip and the one immediately following exhibit spectra with enhanced τ compared with the phase-averaged spectra. This is to be expected if at this phase the column axis is aligned or almost aligned with the line of sight, providing greater optical depth due to the accretion columns extension above the polar cap (see also Chapter 5). Although the increase is relatively modest, particularly in the phase bin including the dip, note that that phase interval also covers the dip ingress and egress. The spectrum will tend to be dominated by emission at these phases due to the higher count rate. It is possible that a spectrum taken over the phases covering only the bottom of the dip may exhibit a much higher τ, although the current observations do not provide sufficient count rate to confirm this.

The results bear a striking similarity to the analysis of *RXTE* observations of GX 1+4 at comparable count rates, despite the distinctly different pulse profile (observation E, Chapter 5; and Galloway et al., 2000). Note in particular that the arguments for the closest approach of the accretion column to the line of sight occurring within the $\phi = 0.1$ phase bin apply equally well here. While the dip may indeed be caused by an increase in optical depth due to partial alignment of the column and the line of sight, the recovery of the count rate in the following bin may be attributed to a decrease in the scattering cross section indicative of closer alignment of the line of sight with the local magnetic field direction within the scattering region. If that is the case then the approximately equal values of τ for the $\phi = 0.0$, 0.1 phase bins will not accurately reflect the discrepancy in the path length for photons to escape the column, which will actually be much greater in the later phase bin.

Chapter 7

Monte-Carlo simulation of the pulsar emission region

In this chapter I investigate the model described in section 2.3. For a first estimate of appropriate physical conditions for the model, parameters roughly corresponding to the spectral fitting results from Chapter 3 are chosen: $T_{0,\mathrm{input}} = 1$ keV, $T_{\mathrm{e,input}} = 8$ keV and $\tau_{\mathrm{input}} = 3$. The column radius R_{C} is more difficult to estimate; I set $R_{\mathrm{C}} = 1$ km corresponding to $f = R_{\mathrm{C}}/R_* = 0.1$, roughly consistent with theoretical estimates (e.g. Frank et al., 1992) and the measurements from mean GX 1+4 pulse profiles (Chapter 4).

7.1 Comptonization in a spherically symmetric cloud

As a preliminary test of the agreement of the Monte-Carlo model with `compTT` I first simulate the spectra originating from Comptonization of a point source of blackbody photons at the centre of a homogeneous, spherical cloud. Input parameter values are as above except for the input spectrum temperature, which takes the values $T_0 = 1$, 0.5, and 0.1 keV. The ratio of each of the Monte-Carlo simulation results to the `compTT` spectrum with the same input parameters over the range 2–90 keV demonstrates the clear differences between the two models (Figure 7.1).

With $\tau = 3$, the corresponding Titarchuk β-parameter (calculated assuming a 'disc' geometry; equation 3.3) is 0.06 (Titarchuk, 1994), placing this set of parameters well inside the region of the β–T_{e} diagram where agreement is good (see Figure 3.12 and Hua and Titarchuk, 1995). Despite this, the agreement is rather poor for spectra with $T_0 = 0.5$, 1 keV. As T_0 is reduced, the agreement improves, and the spectral ratio approaches a constant over all energy bands, indicating a much improved agreement. The contribution from numerical noise, particularly at high energies and for low input spectrum temperatures, is apparent.

7.2 Comptonization in an accretion column

It is not obvious that the differences found between the two simulations in the spherical situation will translate directly to the spectra originating from an accretion column (Figure 2.1). With the source photons emitted evenly across the polar cap, those from near the edge will experience a smaller effective optical depth than those near the centre. The resulting spectra will thus be characterised by an *average* optical depth which will depend not only upon the plasma density but the geometry. Furthermore, a significant proportion of photons will be scattered directly back on to the neutron star surface. The physics at this detailed level are poorly understood, and for computational convenience these photons are removed from the simulation. These two effects are likely to have significant impacts on the shape of the emitted spectrum.

To quantitatively assess the influence of the input parameters on the simulation, mean spectra originating from a single accretion column with are generated over

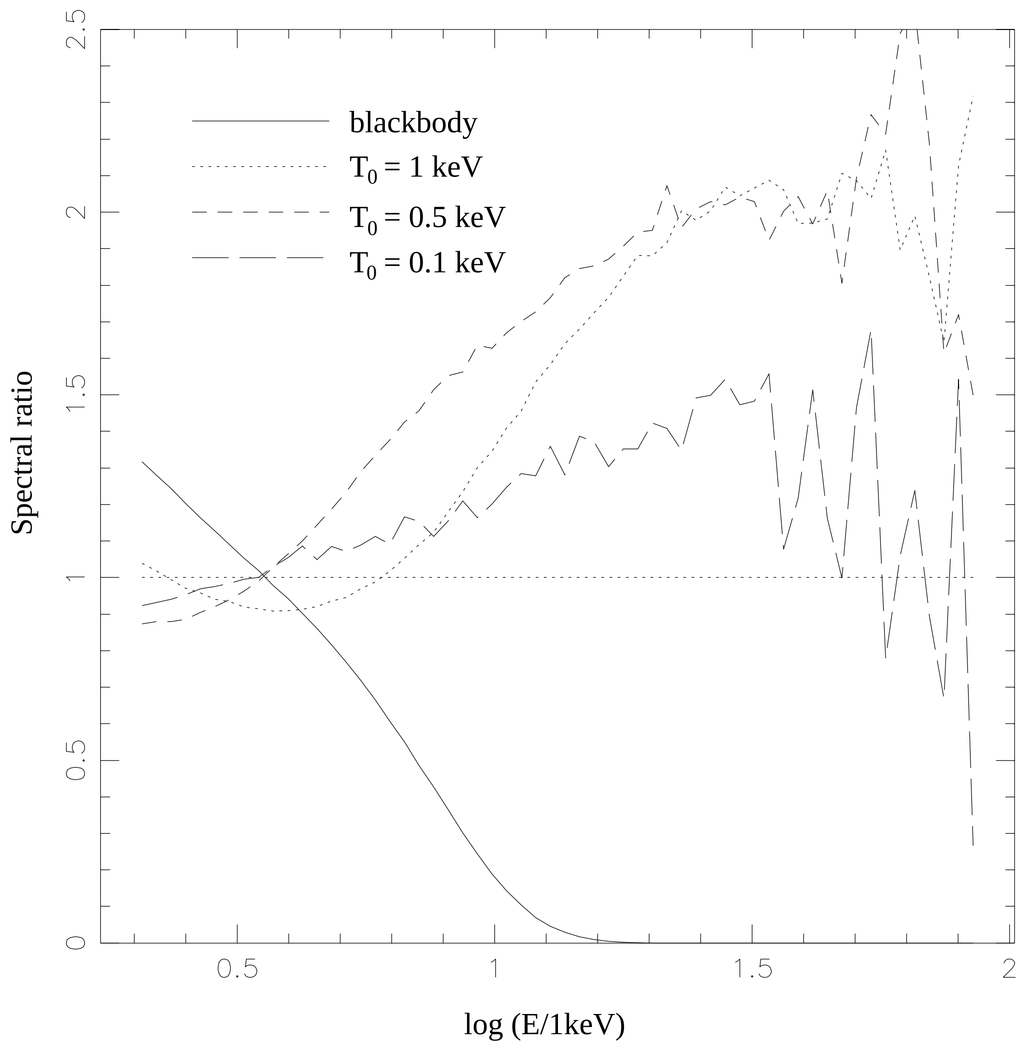

Figure 7.1 Spectral ratios calculated by dividing Monte-Carlo simulation spectra by simulated `compTT` spectra for equivalent input parameters $T_e = 8$ keV, $\tau = 3$, and $T_0 = 1$, 0.5, and 0.1 keV. Corresponding spectral ratio for a 1 keV blackbody is also shown. The normalisation is arbitrary.

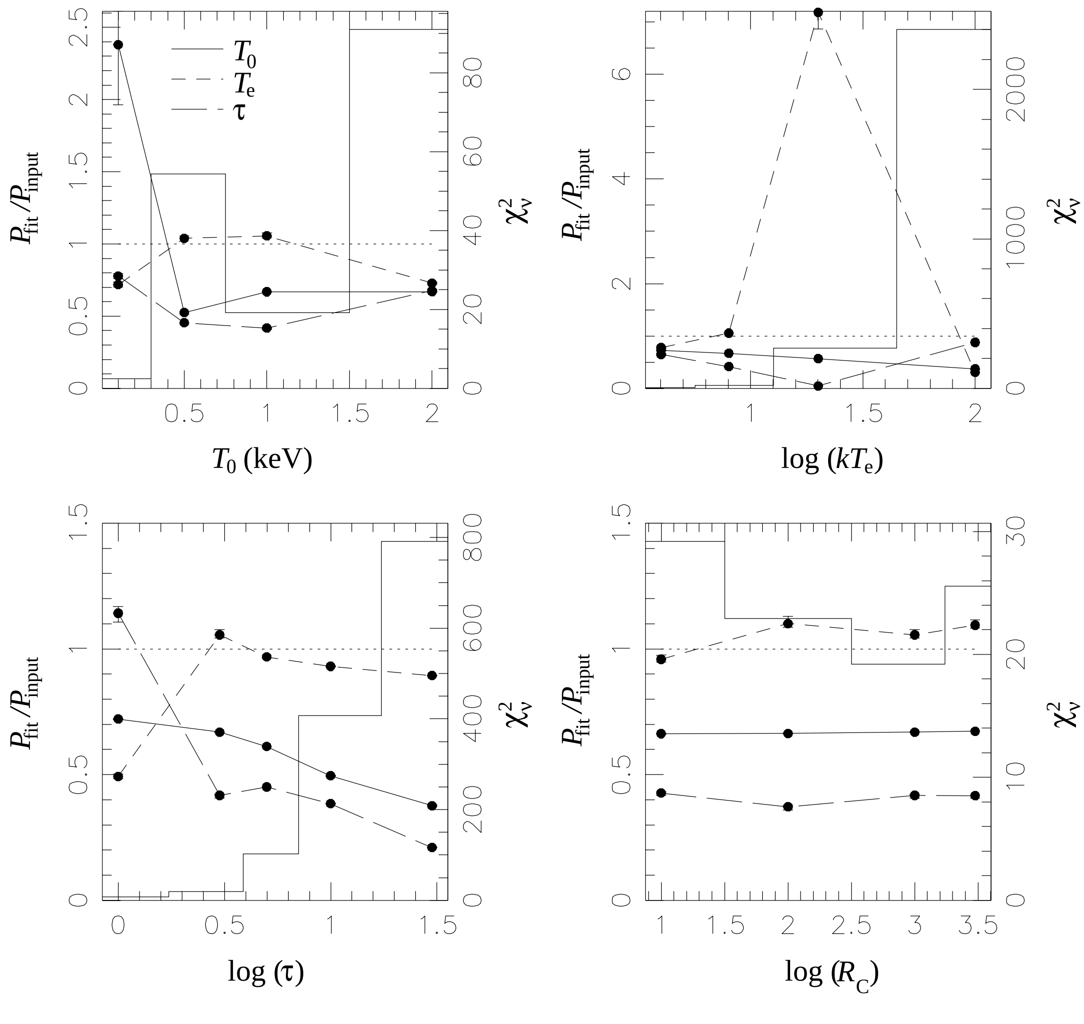

Figure 7.2 Model fit results from Monte-Carlo simulations of Comptonization of a circular source of blackbody photons on the surface of a nonreflective neutron star. Nominal model parameters are $T_{0,\mathrm{input}} = 1$ keV, $T_{\mathrm{e,input}} = 8$ keV, $\tau_{\mathrm{input}} = 3$ and $R_{\mathrm{C}} = 1$ km. Each panel describes the effects of varying one of the input parameters with the other three kept constant. Clockwise from top left, the varied parameters are T_0, T_{e}, R_{C} and τ. Within each panel the fit parameter P_{fit} from the `compTT` model divided by the input value P_{input} is plotted, with 90% error bars from the fit. Each line represents one of the three fit parameters; only one input parameter is varied for each panel. The histogram and the right-hand y-axis shows the reduced chi-squared χ^2_ν value for each fit. Maximum energy range for fitting is 2–90 keV.

a range of input parameters. Since a proportion of input photons will be lost at the neutron star surface, the number of input photons for each simulation is set so that there are 10^6 photons in total contributing to each output spectrum. These spectra are then fit with the `compTT` model from XSPEC; fit parameters and χ^2_ν are shown in Figure 7.2. Although model spectra are generated over the energy range 2–90 keV the influence of numerical noise in the highest energy range means that the useful energy range for fitting is typically 2–50 keV. The geometry parameter for the `compTT` model component was set to 1.0, in accordance with the spectral fitting for the observational data (see Chapter 3).

Within the explored region of parameter space it is generally observed that $T_{0,\mathrm{fit}} \approx (0.5 - 0.7)\, T_{0,\mathrm{input}}$, $T_{\mathrm{e,fit}} \approx (0.7 - 1.2)\, T_{\mathrm{e,input}}$ and $\tau_{\mathrm{fit}} \approx (0.3 - 0.8)\, \tau_{\mathrm{input}}$. Input T_0 values are almost always underestimated by the fits. When $T_{0,\mathrm{input}}$ is well below the minimum energy of the spectrum the fitted value is $\approx 2.5 T_{0,\mathrm{input}}$ with large uncertainties. The curves are otherwise quite featureless. The plot versus τ shows $T_{0,\mathrm{fit}}$ decreasing monotonically with τ_{input}. As the number of photons lost (after being reflected back into the neutron star's surface following collisions with plasma electrons) will increase with increasing plasma density (i.e. τ), the contribution to the output spectrum of photons from the edge of the polar cap will increase, and the fitted input temperature will decrease. The fits exhibit a rather complex relationship between $T_{0,\mathrm{input}}$ and χ^2_ν. The most outstanding feature is the large values of the χ^2_ν for the worst fits (see below). In general as $T_{0,\mathrm{input}}$ is increased, χ^2_ν also increases. This may be related to the observation that for the spherical case the agreement between the two models is best for the very low T_0 case. However the relationship is not monotonic and from increasing $T_{0,\mathrm{input}}$ from 0.5 to 1.0 χ^2_ν decreases significantly, possibly related to the slight improvement in accuracy of the fitted T_0.

The fitted T_e depends significantly on variations in the other input parameters, and in general does not trace $T_{\mathrm{e,input}}$. The principal observational signature of the plasma temperature is the 'break' in the spectrum at $\approx 3kT_\mathrm{e}$ (Pozdnyakov et al., 1983) which can presumably be located reasonably accurately by the fitting algorithm so long as the break energy is within the energy range of the fit and the optical depth is > 1. If the optical depth is $\ll 1$ the `compTT` model becomes very insensitive to the T_e parameter and a reliable, stable fit in XSPEC is impossible. The apparent anticorrelation of the fitted T_e and τ ratios is clear in almost all the panels. This effect is also seen when fitting the observational data (see Chapter 3).

Fitted τ values vary somewhat erratically with variations in the other input parameters, in part due to the anticorrelation generally observed with $T_{\mathrm{e,fit}}$. As τ_{input} is increased, τ_{fit} increases disproportionately (lower left panel), substantially underestimating the input value for the highest optical depth. This effect, combined with the dramatic increase in χ^2_ν as τ_{input} increases, is further evidence for the superposition of the highly Comptonized spectrum from photons originating near the pole and the relatively unscattered photons from the edge in the output spectrum. Finally note that the effect of the column radius R_C is relatively minor.

The values of χ^2_ν for the simulation fits are much greater than 1, which generally indicates a statistically unacceptable fit. The main reason for this is the generally low optical depth and the form of the input spectrum for the Monte-Carlo simulation, as illustrated in the previous section. Another reason is that the expectation of $\chi^2_\nu \approx 1$ depends on the specific assumption that the errors are Poisson distributed (e.g. Press et al., 1996). For the Monte-Carlo simulation there is a contribution due to numerical noise which cannot be neglected given a finite number of input photons. This contribution is illustrated in Figure 7.3. When the number of simulation photons is small, so is χ^2_ν; however the fit parameters exhibit large uncertainties and vary significantly with N. As N increases, the fit parameters approach a asymptotic values with decreasing uncertainties, but above $N \approx 10^6$ the χ^2_ν begins to increase dramatically with N (particularly for the `compTT` only fits, top panel). The `compTT` model is an analytic approximation to a Comptonized spectrum assuming a particular geometry and simplified form of the input spectrum, and it is at this point the numerical errors are small enough that the discrepancy between this and the Monte-Carlo simulation becomes significant.

It is worthwhile pointing out that a formally unacceptable value of χ^2_ν does not necessarily mean a bad fit in qualitative terms. Plotting the two models for the column geometry with $N = 10^6$ on logarithmic and linear scales demonstrates that the fit is actually quite good, despite the large $\chi^2_\nu = 18.96$ (Figure 7.4). Despite any reservations, the χ^2_ν value remains a useful fit statistic in a relative sense.

Given the problems encountered in fitting the simulated spectra with the `compTT` model (primarily resulting from the form of the input spectrum), it may be instructive to add a blackbody component to the model and re-fit. Conceptually this corresponds to a spectrum formed from a blackbody input and a hard tail from Comptonization of an arbitrarily low-energy input spectrum. This should improve the χ^2_ν and potentially also improve the agreement of input and fit parameters. Results from fits of the `comptt+bbody` fit in XSPEC over the range 2–90 keV are shown in Figure 7.5.

As expected, the χ^2_ν values are dramatically lower in every case. For the fitted `compTT` parameter values using the composite model, $T_{0,\text{fit}} \approx (1-1.3)\, T_{0,\text{input}}$, $T_{\text{e,fit}} \approx (0.6 - 0.8)\, T_{\text{e,input}}$ and $\tau_{\text{fit}} \approx (0.5 - 1.0)\, \tau_{\text{input}}$ in general. $T_{0,\text{fit}}$ now typically slightly overestimates the input value. As with the `compTT` only fit the accuracy is worst when the input value is below the energy range of the spectrum. A correlation between $T_{0,\text{fit}}$ and $T_{\text{e,input}}$ is found on varying the latter input parameter (top right panel). Apart from this and the dramatic drop in $T_{0,\text{fit}}$ at the maximum $\tau_{i\text{input}}$ the curves are encouragingly flat and featureless, and in general the input T_0 is measured to an accuracy of $\approx 20\%$. Similar to the previous set of results, χ^2_ν tends to be higher for extreme values of input T_0.

The situation with the fitted T_e values has improved dramatically from the `compTT` only case. The input value is consistently underestimated by $\approx 30\%$, but the variation with the input parameter values is small as are the uncertainties. The fitted value is no less accurate even when the input T_e is outside the spectral energy range (top right panel), although note that χ^2_ν increases in general with input T_e.

The τ_{fit} values show significantly less variation with varying input parameters. In general the τ_{fit} underestimates the input value by $\approx 30\%$. Particularly problematic is

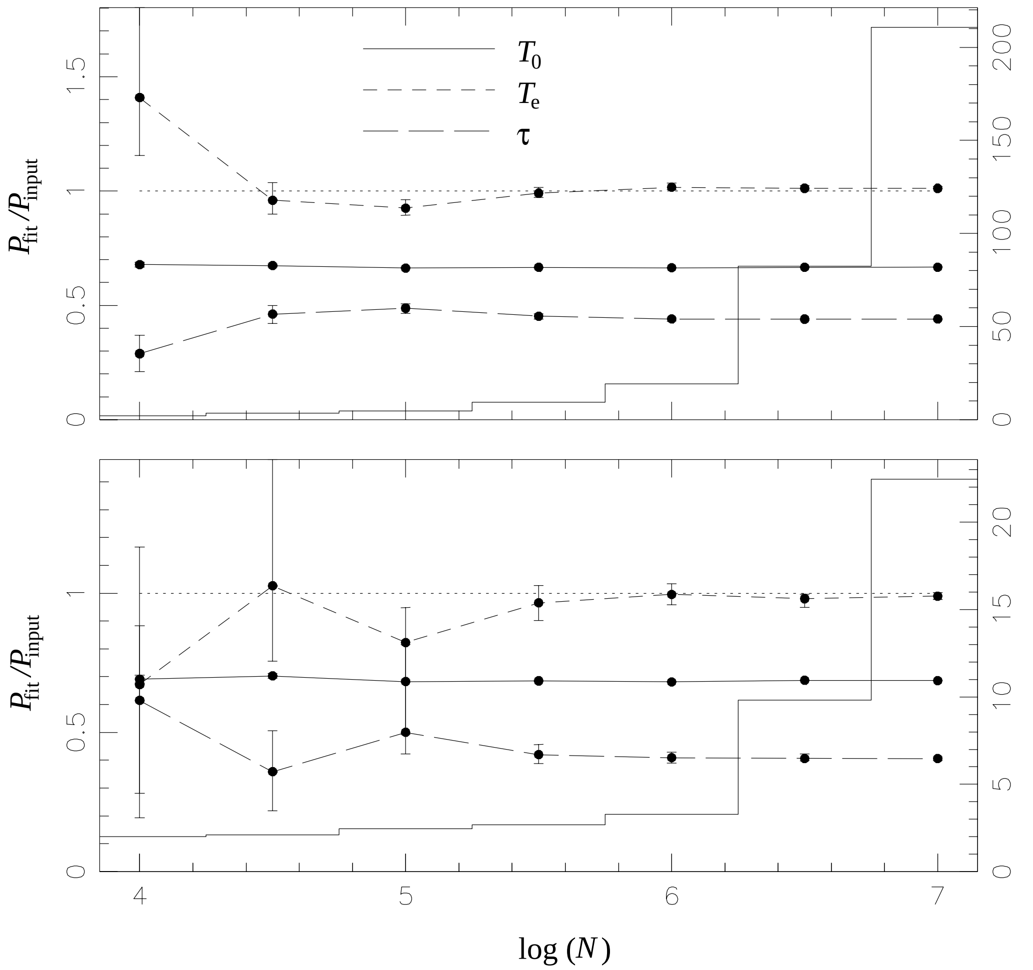

Figure 7.3 Model fit results from simulations of Comptonization in an accretion column, with input parameters $T_0 = 1$ keV, $T_e = 8$ keV and $\tau = 3$. As with Figure 7.2, fit parameters divided by input parameters are plotted as points with error bars showing the 90% confidence intervals; χ^2_ν values for each fit are plotted as a histogram with the scale on the right-hand y-axis. The top panel shows the effect of varying number of input photons N on fits using the `compTT` model in XSPEC. The bottom panel shows results using the `compTT+bbody` composite model. The energy range used in each case is (at most) 2–90 keV.

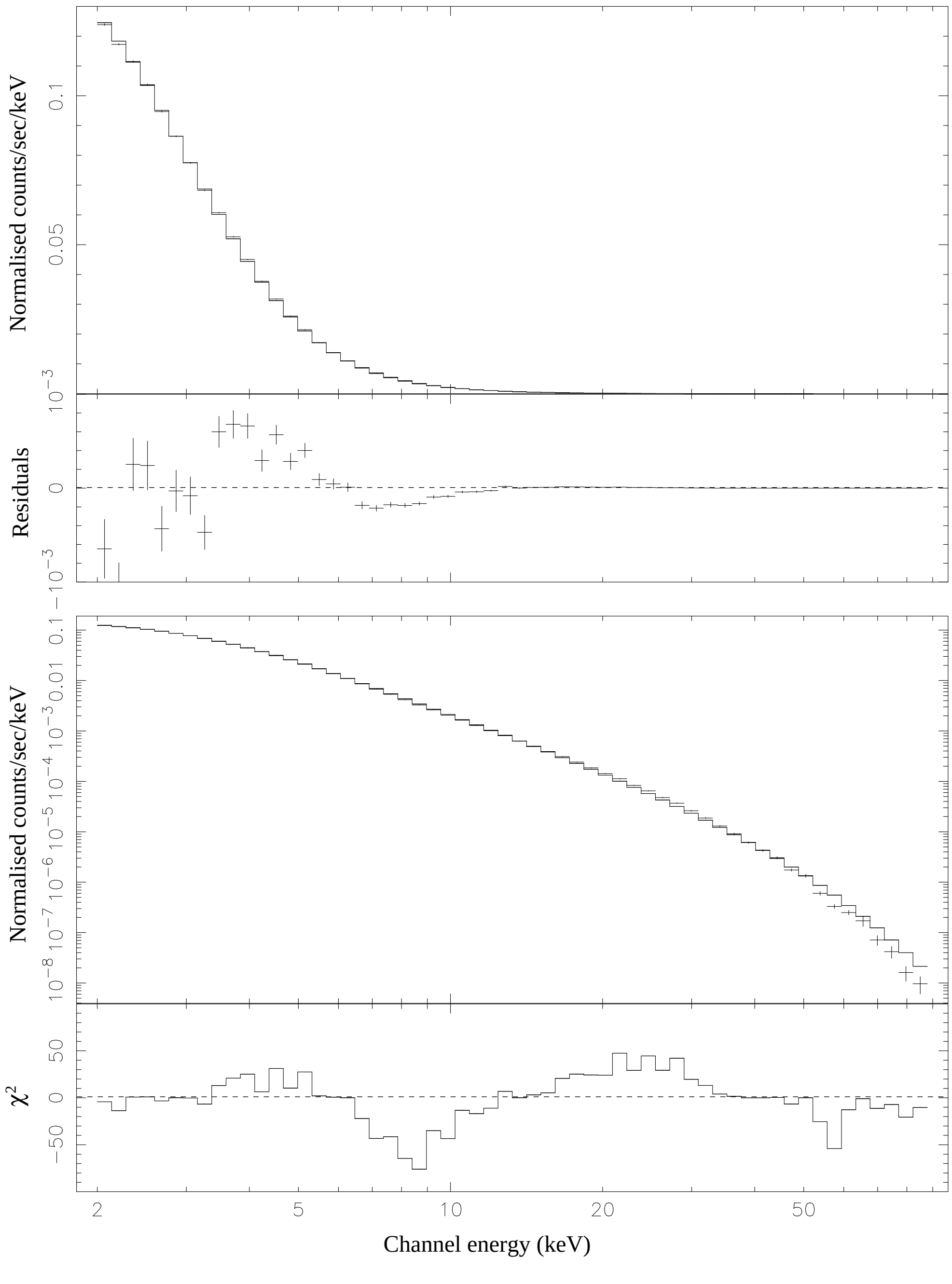

Figure 7.4 Monte-Carlo simulation of the spectrum originating from an accretion column and the corresponding `compTT` model fit, with model conditions as for Figure 7.3 and the number of input photons $N = 10^6$. The top panel plots the simulation (crosses) and `compTT` model fit (histogram) on a log-linear scale, and residuals on a linear scale. The lower panel plots the models on a log-log scale, and also shows the contribution to χ^2 in each energy bin.

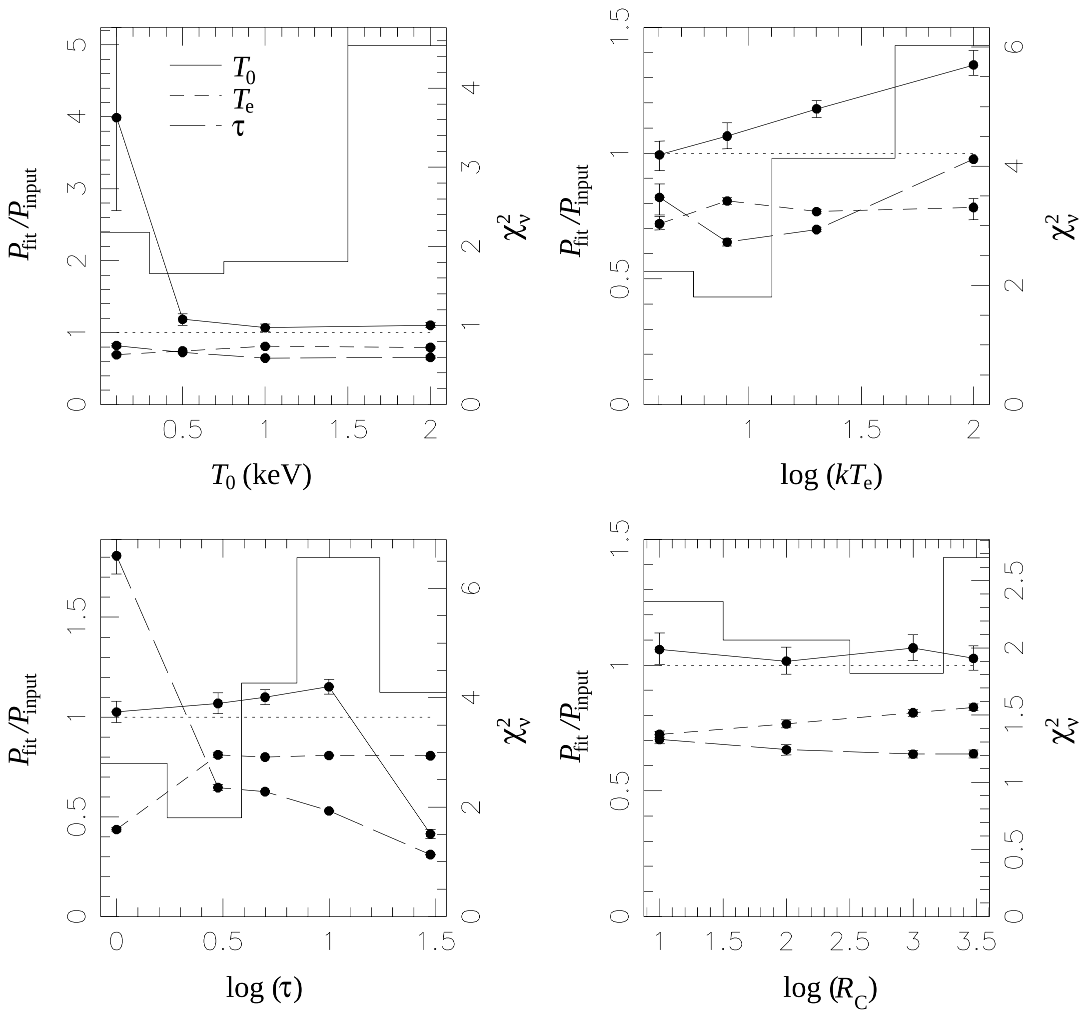

Figure 7.5 Model fit results from simulations of Comptonization in an accretion column. The spectra are identical to those used in Figure 7.2, but the fitted model includes a blackbody component (`bbody` in XSPEC). All the model parameters for the blackbody component are free to vary independently to those of the `compTT` component.

the $\tau_{\rm fit}/\tau_{\rm input}$ curve versus the input $T_{\rm e}$ which is no longer monotonic. Such behaviour would make it difficult to unambiguously estimate source conditions from observed spectra. As the input τ increases, note that $\tau_{\rm fit}/\tau_{\rm input}$ decreases as with the `compTT` only fits, so that at low τ the input value is substantially overestimated while at large τ it is underestimated. The behaviour of χ^2_ν is somewhat complicated, reaching a maximum for the $\tau_{\rm input} = 10$ case and dropping at higher τ. The drop in this case is accompanied by a dramatic decrease in the $T_{0,\rm fit}$, as previously noted.

As before, note that the effect of the accretion column diameter $R_{\rm C}$ on the fit values and χ^2_ν is relatively minor. The best fit is found for $R_{\rm C} = 1$ km.

7.3 Influence of the source aspect

Examination of the mean spectra originating from the accretion column model is instructive, but is not strictly speaking representative of what is expected in the observational situation. In that case the combination of the source aspect (inclination angle i, magnetic colatitude β) and the anisotropy of the X-ray emission from the star means that the phase-averaged spectra will be an average over a limited range of emission angles with respect to the accretion column axis. This may introduce systematic variations in pulsar profiles which are dependent only upon the system aspect.

A typical example of the angular dependence of X-ray flux (the 'beam pattern') for the Monte-Carlo simulation resembles what is conventionally referred to as a 'fan' shape (Figure 7.6). The decrease of emission at small angles is caused by the increased optical depth (due to the column geometry) for photons propagating along trajectories close to the column axis. The beam pattern generated by the simulation will be a fan beam unless $\tau \lesssim 0.01$. Maximum emission from the column at < 7 keV occurs at an angle of $\approx 135°$ with respect to the column axis. This is a direct consequence of the gravitational light bending; the amount of deviation also depends on the size of the column $R_{\rm C}$. Note the localised peak in emission at $\theta = \pi/2$ relative to the column axis, particularly evident in the 7–20 keV contour. This peak is dependent upon the extent of the polar cap, and is analogous to a caustic amplification event in stellar microlensing.

It is straightforward to determine the phase-averaged spectra of pulsars with the beam pattern in Figure 7.6 over a grid of source aspects. Fit parameters obtained by fitting these spectra with the `compTT` model on the range 2–90 keV are shown in Figure 7.7. It is firstly worth noting that the plotted surfaces are all moderately symmetric about the line $i = \beta$. This is to be expected since the set of emission angles observed if i and β are exchanged are essentially the same. Any discrepancy between the cases is likely to be mainly due to numerical noise.

As with the mean column spectra, the fitted T_0 values consistenly underestimate $T_{0,\rm input}$ (top panel). Variation over the entire grid is $\approx 10\%$, with the maximum fitted value measured close to $i \approx \beta \approx 0°$. This corresponds to the case in which the column is viewed essentially along the axis at all phases, and very little emission

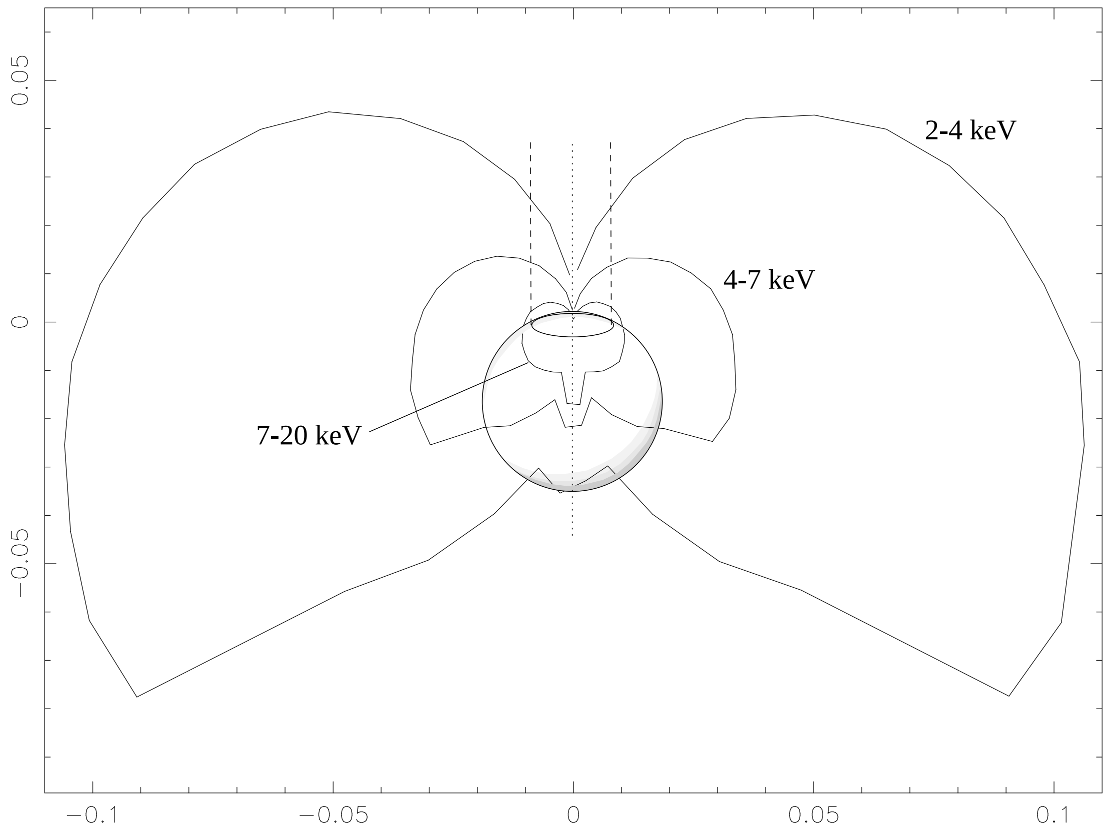

Figure 7.6 The X-ray beam pattern originating from a neutron star accretion column with $R_* = 10$ km, $T_0 = 1$ keV, and column plasma $T_e = 8$ keV, $\tau = 3$ and $R_C = 1$ km. The beam pattern is symmetric about the y-axis, which also represents the column axis; the origin is the intersection of the column axis and the neutron star surface. Contours represent beam shapes for varying energy ranges; from outermost to innermost 2–4 keV, 4–7 keV and 7–20 keV. Normalisation (and hence scale) is arbitrary.

is seen from the sides. In this case a large fitted optical depth is expected since photons must propagate through a significant part of the length of the column to escape. Variations in the fitted T_e values are more dramatic; $\approx 50\%$. The fitted value is at a minimum at $i \approx \beta \approx 0°$, and increases with both i and β. When $i + \beta < 60°$ the fitted value generally underestimates the input value, while above $60°$ it is overestimated. Fitted τ values generally underestimate $\tau_{\rm input}$ by $\approx 50\%$. The maximum value is found at $i \approx \beta \approx 0°$ as expected. As i and β increase, the fitted τ decreases, primarily due to the column being viewed at greater angles with respect to the axis and thus a generally smaller optical depth experienced by the photons in their path to the observer. The χ^2_ν (not shown) varies between 3–7, lowest at $i = \beta = 0°$ and increasing with both i and β. Due to the nature of the algorithm, different numbers of photons are accumulated for each particular choice of i, β and thus the contribution of numerical noise to χ^2_ν varies. Thus it is not generally possible to compare the values between different source aspect cases.

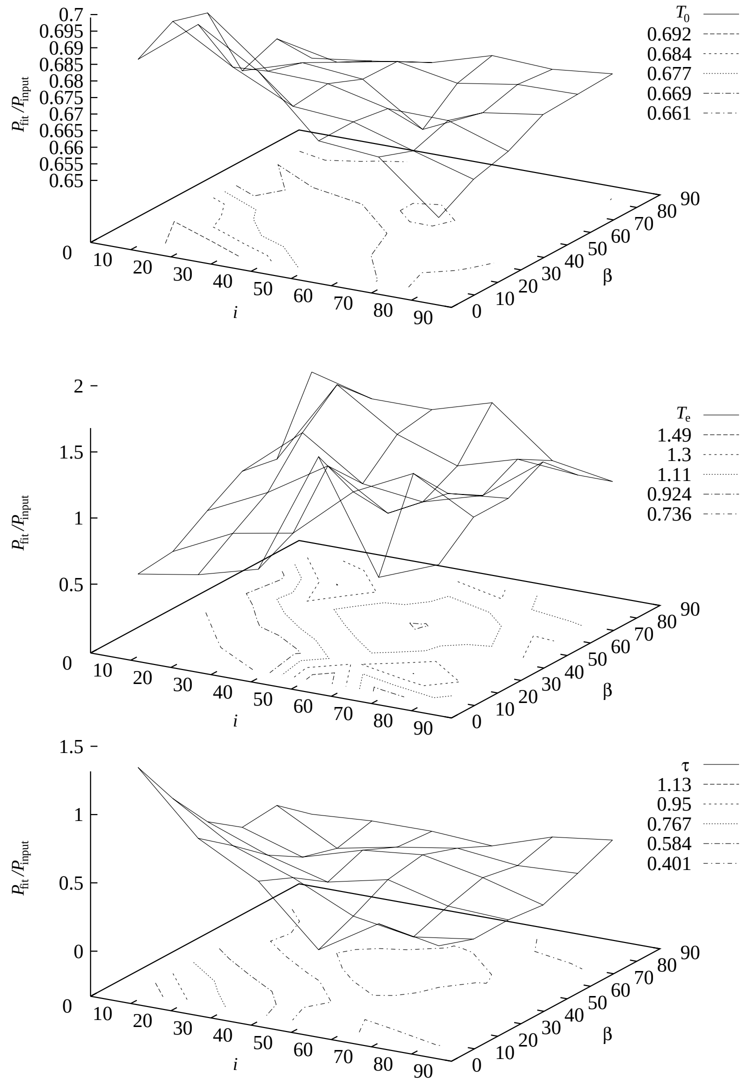

Figure 7.7 Fit parameters divided by input parameters ($P_{\rm fit}/P_{\rm input}$) for Comptonization component fits to phase-averaged spectra as a function of inclination angle i and magnetic colatitude β. Spectra are generated with i, β taking the values $= 7.5°, 22.5°, 37.5°...$). Model conditions are as for Figure 7.6. From top to bottom, the three panels show T_0, $T_{\rm e}$, and τ.

As with the mean column spectral fits, an improvement is achieved by adding a `bbody` component to the fit. The resulting fitted parameters versus geometry are shown in Figure 7.8. The χ^2_ν values are now ≈ 2.5–3, indicating significantly better fits than for the `compTT` only model. In contrast to the previous set of results, fitted T_0 values for the composite model show little systematic variation but a larger overall range of $\approx 50\%$. The fitted T_e and τ distributions are roughly similar to the `compTT` only case, but also exhibit some larger variations. The increased scatter in the fit parameters is due to the fit parameter variations of the additional fit component.

7.4 Pulse profiles

Typical pulse profiles for the model are shown in Figures 7.9 and 7.10 for energy ranges 2–7 keV and 7–20 keV respectively. The pulse profile varies significantly as a function of the source aspect. When $|i - \beta| \lesssim 45°$ a strong modulation in the 2–7 keV flux is observed, with the primary minimum corresponding to the closest passage of the line of sight with one of the magnetic polar axes. These minima can be rather narrow ($\Delta\phi \approx 0.3$) for certain choices of geometry. When $i \approx \beta \approx 90°$, a secondary minimum is observed due to the passage of the opposite column axis through the line of sight. Pulse profile shapes range from roughly sinusoidal, through triangular to the more typical flat-topped type. In the higher energy band a strong modulation is seen when $|i - \beta| \lesssim 30°$ (Figure 7.10), although the pulse fraction is not as large. Pulse profiles are generally similar to those in the lower energy band, with some notable exceptions. When $i \approx \beta \lesssim 45°$ a local maximum centred on phase 0.0 appears, at the centre of the primary minimum. At the minimum i, β, this maximum may even dominate the usual maximum at phase 0.5. This maximum is caused by the peak in emission at $\theta = \pi/2$ as seen in the beam pattern (Figure 7.6), and is indeed much more prominent in the high energy profiles. The appearance of this maximum is strongly dependent upon the column size, and disappears in all but the $i = \beta = 7.5°$ case when $R_\mathrm{C} < 0.5$ km.

The pulse fraction (defined as for the observational pulse profiles, equation 4.1) is essentially a function of $|i - \beta|$, and is only weakly dependent upon the optical depth (Figure 7.11). In the case of $\tau = 1$, the overall increase in pulse fraction in the 7–20 keV band compared to the cases with $\tau = 3, 10$ can be partially attributed to numerical noise due to the low numbers of counts. It is interesting to note that the energy dependence of pulse fraction appears to be primarily a consequence of light bending, as the results with no bending exhibit virtually identical pulse fraction between the two energy bands. The column diameter R_C is clearly also an important influence, particularly in the higher energy band.

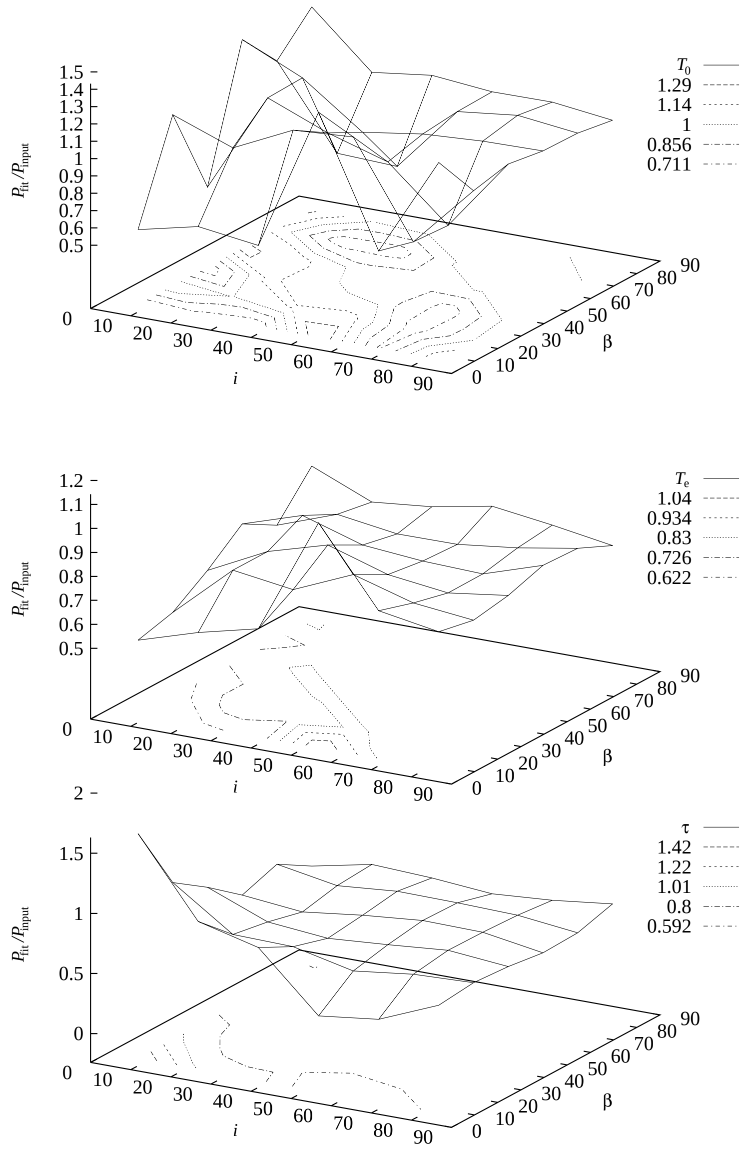

Figure 7.8 Fit parameters divided by input parameters ($P_{\rm fit}/P_{\rm input}$) for the Comptonization component in model fits (including a blackbody component) to phase-averaged spectra as a function of inclination angle i and magnetic colatitude β. Conditions are otherwise identical as for Figure 7.7.

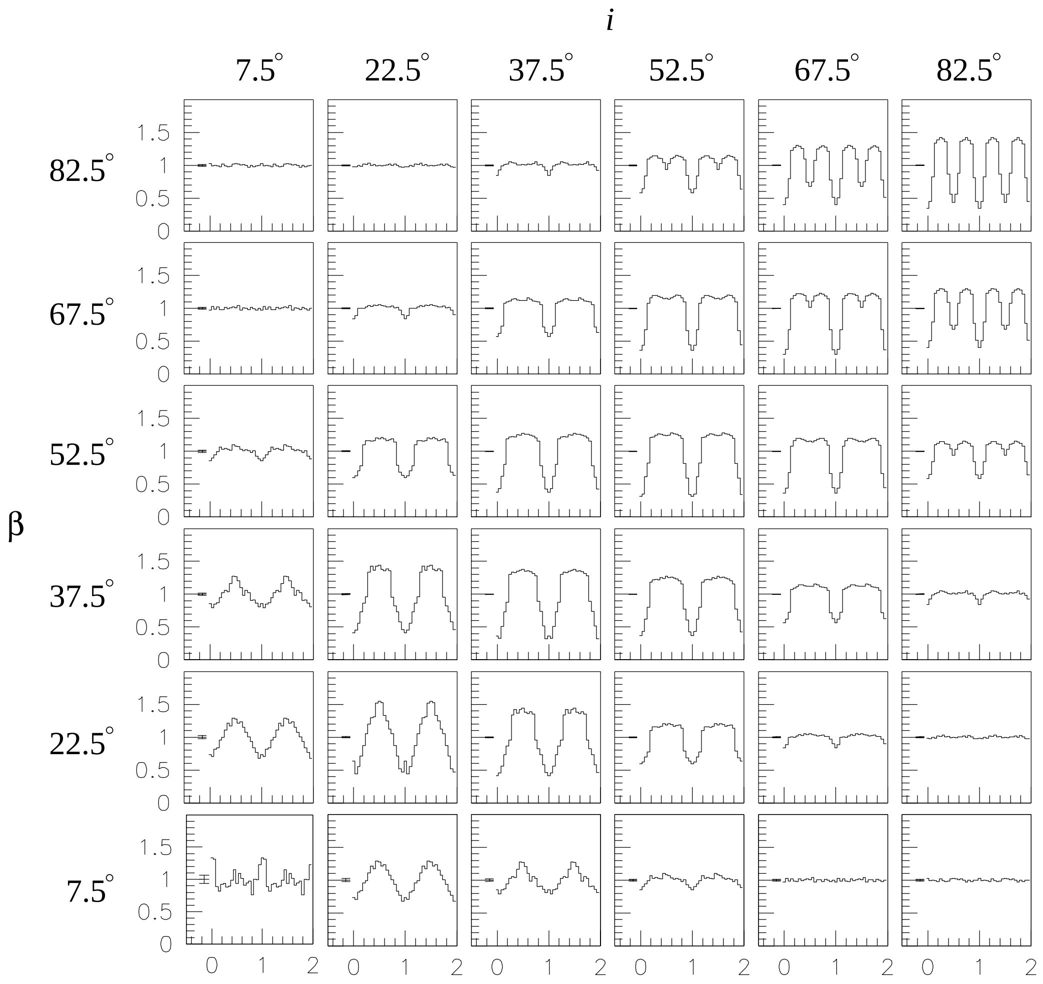

Figure 7.9 Pulse profiles in the energy range 2–7 keV versus inclination angle i, and magnetic colatitude β (which take the same values as for Figure 7.7). Model conditions are as for Figure 7.6. Each profile is independently normalised; typical error bars are plotted on the left. Two full cycles are shown for clarity.

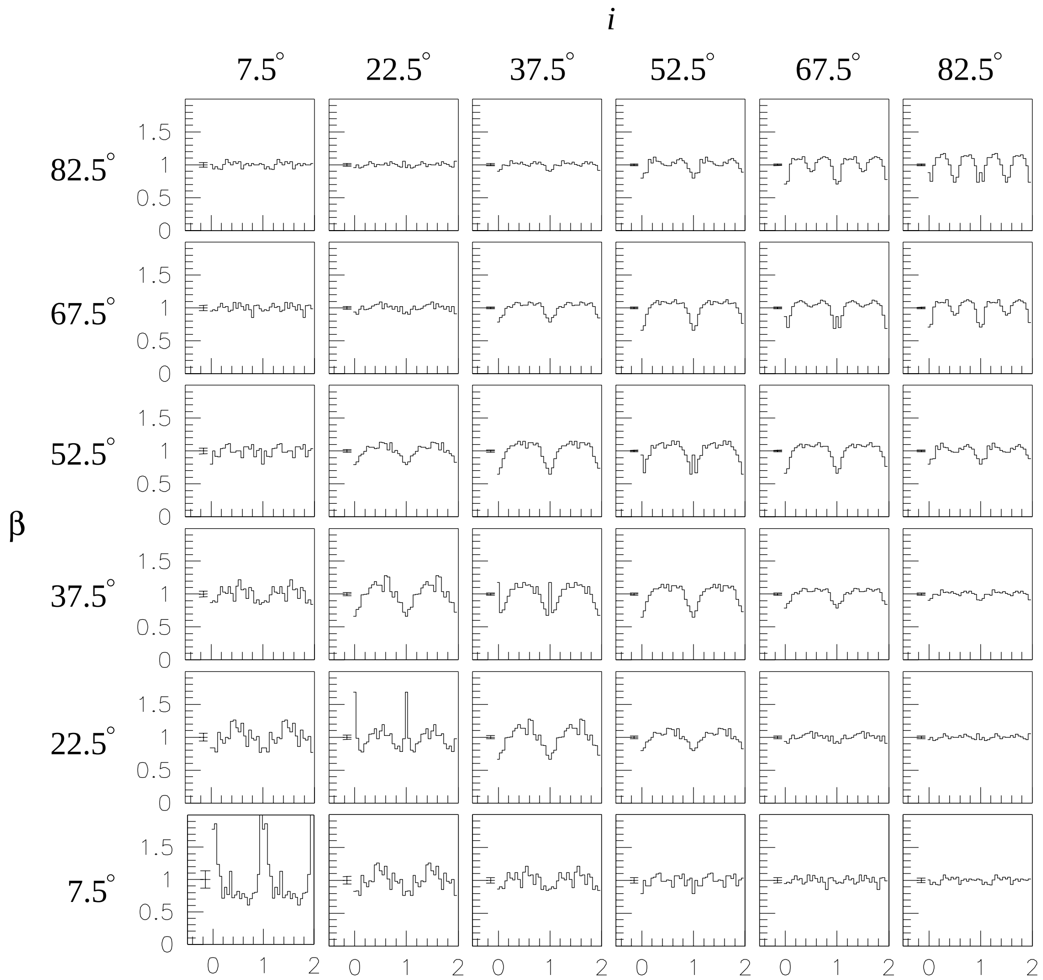

Figure 7.10 As for Figure 7.9, with energy range 7–20 keV.

7.5 Pulse phase spectroscopy

Since the emission angle varies significantly with phase (depending upon the aspect), so too may the spectral fit parameters. For any significant spectral variation clearly it is important to sample a wide range of emission angles. For the case $i = \beta = 67.5°$, the column is viewed over the range $\theta = 0$–$135°$ throughout each neutron star rotation period. Spectral fit parameters using the `compTT` model with 20 phase-selected spectra are plotted with phase in Figure 7.12.

The most significant deviations from the mean spectral fit parameters occurs around phase 0.0, which corresponds to the passage of the magnetic axis through the line of sight. The fitted value of T_0 is increased by around 10%, while T_e appears to be somewhat decreased. The optical depth τ and the normalisation A_C

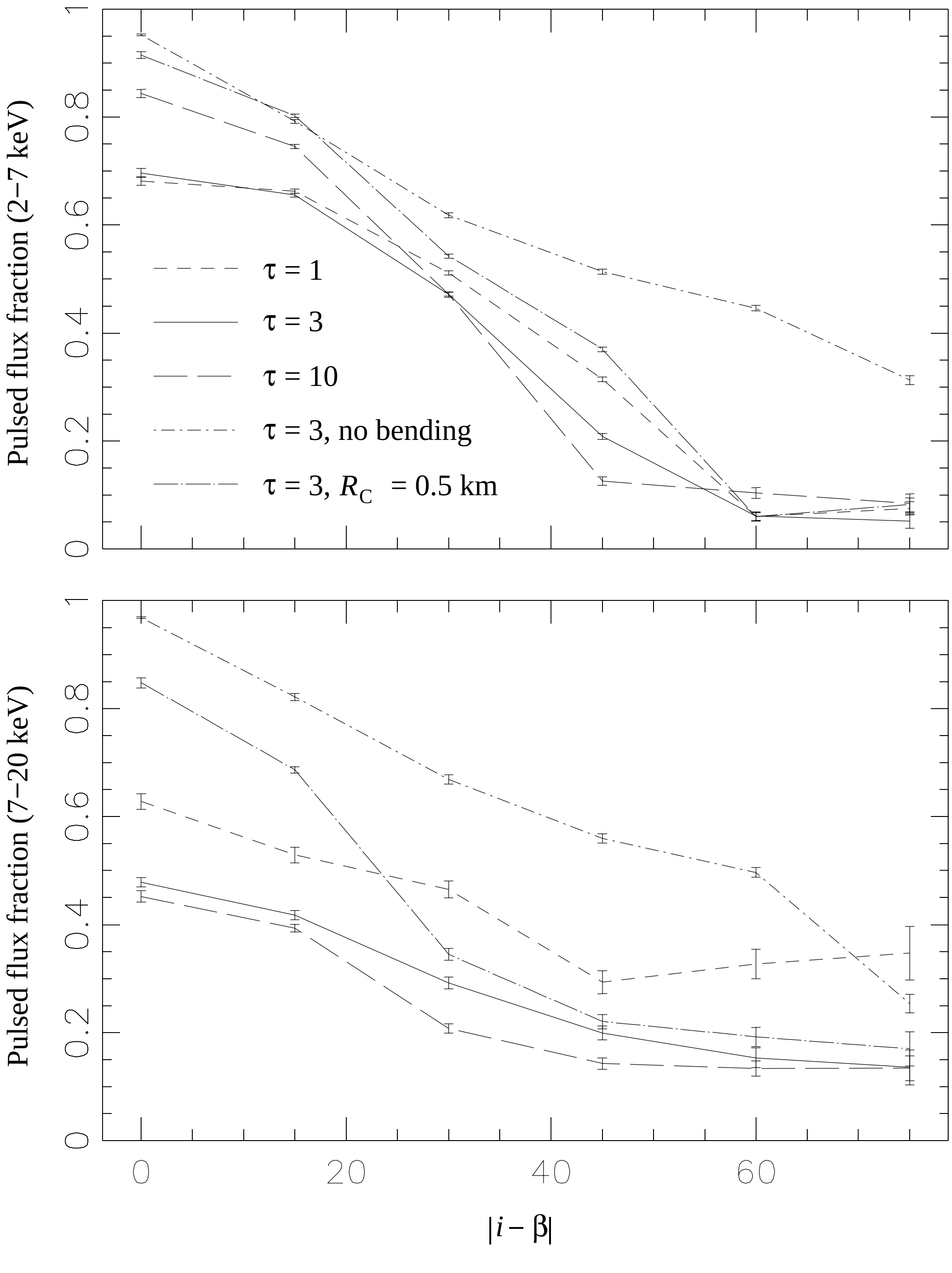

Figure 7.11 Pulse fraction f_p (see equation 4.1) versus $|i - \beta|$ for a range of model conditions. Unless otherwise specified, model conditions are as those for Figure 7.9. The top panel plots the pulsed fraction in the 2–7 keV band while the bottom panel shows the 7–20 keV band. Error bars show 1σ uncertainties.

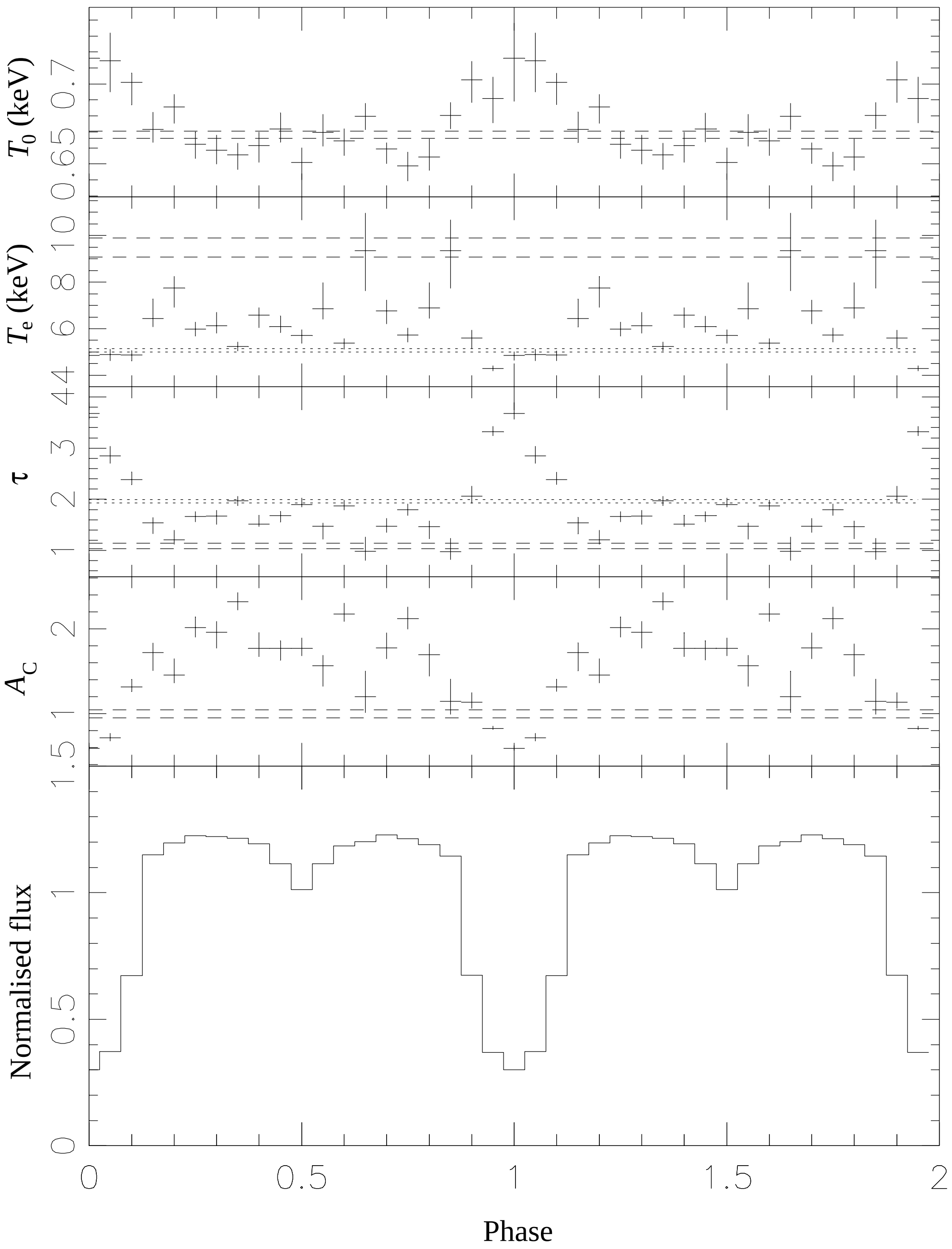

Figure 7.12 Parameter values and 90% confidence ranges for spectral fits to pulse-phase selected data using the `compTT` model in XSPEC. Model aspect is $i = \beta = 67.5°$. The top four panels show T_0, T_e, τ and A_C (`compTT` normalisation) from top to bottom respectively. The 90% confidence intervals for the same fit to the phase-averaged spectra are shown by the dashed lines. The dotted lines show the 90% confidence intervals for the fit parameter averaged over phase (where different from the phase-averaged spectral fit parameter). The bottom panel shows the corresponding normalised pulse profile in the energy range 2–7 keV. Two full cycles are plotted for clarity.

exhibit the most significant deviations, with dramatic increase in particular for τ of around 100%. For the fitted T_0 and $A_{\rm C}$ the fit parameter for the phase-averaged spectrum corresponds closely to the mean calculated from the individual phase-selected fits. For $T_{\rm e}$ and τ however, there is a significant discrepancy. This is not entirely surprising, since in general the phase-averaged spectrum may not be strictly representative of the 'typical' phase-selected spectra; that both parameters exhibit an opposite bias is related to their previously noted anticorrelation.

7.6 Pulse profile asymmetry

Profile asymmetry, frequently observed in X-ray pulsars, can be attributed to a variety of causes. One possibility is a longitudinal density differential across the column, from 'east' to 'west'. Such a density differential could potentially develop in the region where the disc plasma becomes entrained onto the magnetic field lines. Closer to the star plasma flow across the field lines is increasingly limited as the local magnetic field strength rises, and thus an asymmetry within the entrainment region could persist to the footpoint of the accretion column on the neutron star. Pulse profile asymmetry will then depend on the column asymmetry in both the accretion columns. Symmetry suggests that the sense of the differential will be identical for each column, i.e. both will be denser on the 'leading' or 'trailing' side. Since both poles are visible over a wide range of angles courtesy of gravitational light bending, the emission asymmetry in one pole will generally cancel the asymmetry in the other pole. Thus to obtain any appreciable asymmetry it is also neccesary to introduce a brightness differential between the two accretion columns.

I measure profile asymmetry using the α-parameter of Greenhill et al. (1998), as with the observational pulse profiles (see equation 4.3). Note that since α does not depend on the count rate around $\phi = 0.0$, the local maximum sometimes observed at phase 0.0 will have no effect. Model results with different plasma density in either half of the accretion column (i.e. $\tau_1 \neq \tau_2$ in Figure 2.1) indicate that the asymmetry depends only weakly on system aspect, and confirm that the profiles are indeed quite symmetric unless one pole is brighter than the other (Figure 7.13). For a density differential factor of 2 ($\tau_1 = 3$, $\tau_2 = 6$) the maximum α is around 1.8, while for a factor of 10 ($\tau_1 = 3$, $\tau_2 = 30$) it is ≈ 4.5. In general the asymmetry is slightly greater in the 7–20 keV energy band.

Previously I discussed the contribution to the total spectrum of photons originating near the edge of the polar cap, which may experience a negligible optical depth for scattering compared to those originating closer to the centre. With $T_0 = 1$ keV these photons will contribute primarily to the 2–7 keV profiles, and since they will not be as affected by the column plasma density differential the profile asymmetry in that band should be less. To test this conjecture I generate spectra with $\tau = 3/6$ as before but with the emission region on the neutron star only half the radius of the accretion column. Every photon will now experience a minimum optical depth and the contribution of unscattered photons to the final spectrum will

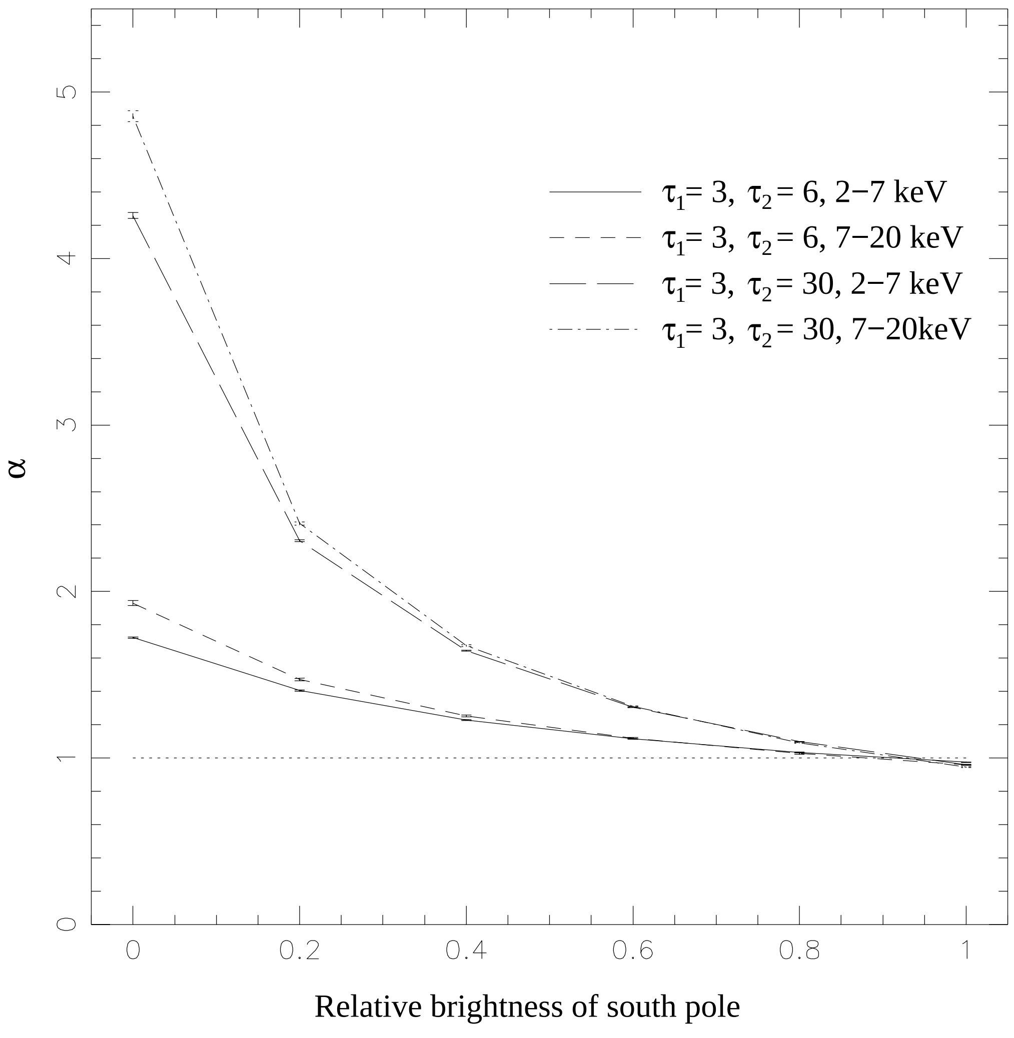

Figure 7.13 Asymmetry parameter α (see equation 4.3) versus south pole brightness fraction. α is calculated from pulse profiles in two energy bands 2–7 keV and 7–20 keV from model runs with a varying longitudinal density asymmetry, $\tau_1 = 3$, $\tau_2 = 6$ and $\tau_1 = 3$, $\tau_2 = 30$. Error bars show the 1σ confidence limits.

be decreased. The resulting α in each band is significantly greater compared to the previous result. As expected there is better agreement between the energy bands, with $\alpha_{\rm max} = 2.158 \pm 0.008/2.019 \pm 0.014$ in the 2–7 and 7–20 keV bands respectively.

7.7 Observational effects

To qualitatively assess the influence of observational influences on the model spectral fitting I select a mean spectrum from the Monte-Carlo simulation with $i = \beta = 67.5°$ (see section 7.3). Pulse profiles from the model with these parameters correspond approximately to those observed in GX 1+4 (see Chapter 4). A simulated observation by *RXTE* is generated as described in section 2.3. For the column density choose $n_{\rm H} = 10^{23}\,{\rm cm}^{-2}$; the exposure time for the example is 24 ks and the resulting net count rate is 144.3 count $\rm s^{-1}$. Comparison fit parameters and statistic are shown in Table 7.1.

In stark contrast to the fits of the raw model data, the $T_{\rm e}$ parameter for the simulated observational spectra (with emission over the entire polar cap as usual) appears to be effectively unconstrained. As a result of this, the optical depth τ falls almost to the minimum allowed by the `compTT` model, 0.01. This is not due to the inclusion of an absorption component since an equivalent unabsorbed spectrum exhibits the same large fit values of $T_{\rm e}$. It is not obvious why there should be such a discrepancy between the raw model fits and the simulated observation. A possibility is that once more the contribution from essentially unscattered photons emitted near the edge of the polar cap is driving the spectral fits to erroneously large values of $T_{\rm e}$. Columns 3 and 4 of Table 7.1 list corresponding results for the modified simulation described in section 7.6, with photon emission from only half the polar cap. `compTT` model fit parameters to the mean spectrum for $i = \beta = 67.5°$ are listed in column 3 while the simulated observational fit (using the same data) is shown in column 4. The agreement between the model fit and the simulated observation is much improved. Note that the model fit parameters for the half-cap model feature a significantly lower $T_{\rm e}$ and higher τ than for the full-cap model.

7.8 Discussion

As discussed in section 2.3, the Monte-Carlo simulation may be expected to qualitatively reproduce the emission characteristics of X-ray pulsars at low accretion rates. The broad-scale physical description of an accreting neutron star adopted for this simulation is widely accepted. The presence of a polar hot spot and scattering atmosphere within the accretion column are both robust predictions of basic accretion theory. Input parameters used in the model correspond closely both to values determined from spectral fitting of selected pulsars and order-of-magnitude estimates from theoretical calculations (see Chapter 3). The physics of Compton scattering in relativistic plasmas is well understood, as are the general relativistic

Table 7.1 Spectral fit parameters for the phase-averaged spectrum originating from the Monte-Carlo model with $i = \beta = 67.5°$. The first column is the parameter values from `compTT` model fits to the Monte-Carlo model spectrum as converted to fits format using `flx2xsp`. Energy range is 2–90 keV. The fits for the second column use the same data converted to a simulated *RXTE* observation using appropriate background and response matrices, with a neutral absorption column density of $n_\mathrm{H} = 10^{23}\,\mathrm{cm}^{-2}$. The model fit includes a component to account for the neutral column absorption; the energy range for fitting is 2.2–40 keV. The third and fourth columns present equivalent results for a model where photons are emitted from a region only half the radius of the accretion column. The symbols have their usual meanings; A_C is the normalisation of the `compTT` model component in units of 10^{-2} photons $\mathrm{cm}^{-2}\,\mathrm{s}^{-1}\,\mathrm{keV}^{-1}$.

	Full cap emission		Half cap emission	
Parameter	Model fit	Simulation	Model fit	Simulation
n_H ($\times 10^{23}\,\mathrm{cm}^{-2}$)	-	$1.061_{1.055}^{1.067}$	-	$0.926_{0.907}^{0.946}$
T_0 (keV)	$0.668_{0.666}^{0.671}$	$0.645_{0.637}^{0.652}$	$0.715_{0.712}^{0.717}$	$0.787_{0.781}^{0.798}$
T_e (keV)	$9.41_{9.07}^{9.89}$	155_{153}^{171}	$5.57_{5.50}^{5.64}$	$6.05_{5.56}^{6.65}$
τ	$1.10_{1.03}^{1.15}$	$0.0128_{0.01}^{0.0293}$	$2.45_{2.42}^{2.48}$	$2.25_{2.06}^{2.43}$
A_C	$2.01_{1.90}^{2.09}$	$0.126_{0.123}^{0.129}$	$2.59_{2.55}^{2.62}$	$2.04_{1.82}^{2.28}$
χ^2_ν	8.59	1.57	4.60	1.19

effects of photon propagation within the strong gravitational field of an object as compact as a neutron star.

The results suggest that phase-averaged spectra from X-ray pulsars will typically be consistent with Comptonization spectra, with possible additional components as described. Analytic model fit parameters correspond roughly to the physical conditions but may vary significantly as a function of source aspect. This effect may contribute to the range of spectral conditions measured from the presently known source catalogue. The discrepancy between the analytic Comptonization model and the simulation is a strong function of the source spectrum temperature, and is presumably due to the different input spectra. The disagreement is exacerbated by the contribution by photons emitted near the edge of the polar cap, which experience a much lower than average optical depth. At the most extreme, $\approx 50\%$ of photons emitted from the very edge of the cap will leave the column having experienced no scattering whatsoever. Observationally these photons will contribute significantly to the spectrum, requiring addition of a blackbody component for the best fit. That the pulsar spectral model fits undertaken in this thesis do not require such additional components (Chapter 3) suggests the polar cap does not extend to the edge of the column. Analysis of the phase-averaged spectrum in a simulated observation by

RXTE supports this hypothesis, with accurate fits essentially impossible for full polar cap emission.

A fan-type beam is observed for typical values of the column optical depth $\tau \approx 3$. The plasma infall velocity in the absence of deceleration is estimated to be close to the free-fall velocity for spherical infall $v_{\rm ff} \approx 0.5c$. The mass accretion rate $\dot{M}$ is then related to the optical depth for scattering by the relation

$$\begin{aligned} \dot{M} &\approx \frac{\pi R_{\rm C} v_{\rm ff} \tau}{\sigma_{\rm T} N_{\rm A}} \\ &= 2.35 \times 10^7 \left(\frac{R_{\rm C}}{R_*}\right) \left(\frac{v_{\rm ff}}{c}\right) \tau \, {\rm g\,s^{-1}} \end{aligned} \tag{7.1}$$

where $N_{\rm A} = 6.022 \times 10^{23}\,{\rm mol^{-1}}$ is the Avogadro constant. The lower limit of $\tau \gtrsim 0.01$ for the observation of a fan beam for the model corresponds to an accretion rate limit of $\dot{M} \gtrsim 1.18 \times 10^{14}\,{\rm g\,s^{-1}}$. This finding corresponds approximately with the conventional picture that the emission switches to a 'pencil' type beam at low accretion rates (White et al., 1995), but in this case because of the low τ, the smoothing effect of gravitational light bending and the isotropy of the source photons the resulting beam pattern will also be quite isotropic.

The combination of the beam pattern and the source aspect can give rise to a wide range of pulse profile shapes. These profiles are qualitatively similar to those observed for X-ray pulsars (e.g. White et al., 1995), although are generally rather smooth and featureless as a consequence of the simple geometry and gravitational light bending. The sharper features generally observed in pulsar profiles may be a consequence of more complex accretion column geometries possibly including additional scattering material outside the column (Sturner and Dermer, 1994). The primary minimum is coincident with the closest passage of one of the magnetic axes to the line of sight; at high inclination angles a secondary minimum from passage of the opposite pole may also be observed. For some source aspects the primary minimum is rather narrow, but still ≈ 3 times as wide as that found in typical observations of GX 1+4 and RX J0812.4−3114 for example (see Chapters 3 and 6). Pulse-phase spectroscopy of simulation spectra indicate that the primary minimum is associated with an increase in the model fitted τ, as well as a decrease in both the $T_{\rm e}$ and `compTT` component normalisation. This variation is in excellent agreement with results from the observational data (Chapter 3) and provides perhaps the most convincing validation of the model so far.

At the phase of primary minimum (when the viewing angle is closest to the magnetic axis) magnetic effects are most likely to be important. The magnetic cross section reaches a minimum for photons propagating along the magnetic field, and thus emission will be enhanced along the accretion column. This effect will compete with the increase in column depth due to the geometry for moderate τ. (When $\tau \lesssim 0.01$ this may give rise to the 'pencil' type beam as opposed to the more isotropic emission resulting in the non-magnetic case). Again, the effects are somewhat difficult to predict, but note that for $B = 0.1B_{\rm cr}$ (where $B_{\rm cr} = 4.413 \times 10^{13}$ G is the magnetic field strength at which the cyclotron energy corresponds to the rest mass energy of the electron) the magnetic cross section reaches a minimum of $0.01\sigma_{\rm T}$ for photons with $\nu = 0$ propagating exactly along the magnetic field (see e.g. Figure 3d in Daugherty and Harding, 1986). The *increase* in column depth due to the geometry is limited instead only by the minimum angle between the line of sight and the accretion column axis, and the curvature and radius of the column. For certain choices of the system geometry it may still be possible for the increase in column depth from geometrical effects to more than counteract the increase in transmission due to decrease in scattering cross section along the column. In this case a dip should still be observed, but the dip may be narrower, shallower, or both. Note that the dips observed in GX 1+4 and RX J0812.4−3114 are significantly narrower than those predicted by the model (Chapters 3 and 6), and that for GX 1+4 on either side of the dip are 'shoulders', local maxima which may be a signature of the magnetic cross section effects

When $i = \beta$ a local maximum is observed centred on the phase of primary minimum. Appearance of this maximum is strongly dependent on the column radius $R_{\rm C}$, and is no longer observed for any source aspect if $R_{\rm C} \lessapprox 0.5$ km. This 'spike' is strongly reminiscent of that observed in *Ginga* data from GX 1+4 during March 1987 (Dotani et al., 1989) and results from photons emitted towards the star from the accretion column above the pole pointing *away* from the observer, which reach the observer due to significant deviation of their trajectories by general relativistic effects. This can be seen in the small increase of emission at $\theta = 180°$ relative to the column axis in Figure 7.6. In contrast to the *Ginga* results, the simulation gives rise to a maximum which is strongly energy dependent; the reason being that only photons from relatively high in the accretion column (which have likely undergone several scatterings to enhance their energy) may be observed in this way. That the maximum observed in GX 1+4 is essentially energy independent suggests that the emitted spectrum during the 1987 observation is much less dependent on the height above the star, and perhaps that an extended, optically thick column is present. This is not simply a function of the accretion rate since the *RXTE* observations span up to an order of magnitude greater luminosity without any comparable observations of local maxima centred on the primary minimum.

Profile asymmetry, which is frequently observed in X-ray pulsars, can be generated in the simulation by a combination of lateral density differentials in the accretion column and unequal brightness of the two neutron star poles. That a density differential is strictly required is suggested by profiles from both GX 1+4 and RX J0812.4−3114, which exhibit significantly different levels of X-ray emission on either side of the primary minimum (Chapter 3). As demonstrated, a density differential alone cannot provide sufficient asymmetry to match that observed in X-ray pulsars, since asymmetry in the two columns tends to cancel courtesy of light bending. An additional asymmetry in accretion rate to the two poles is necessary. Unequal accretion rates to the two poles is possible in particular if the magnetic field deviates from a pure dipole, or if the dipole is not centred within the star. This effect further suggests a mechanism for the rapid changes in profile asymmetry observed in GX 1+4 (Giles et al., 2000); that is, the relative brightness of the poles and possibly also the sense of asymmetry in the column changes, and consequently so does the pulse profile.

Despite its simplicity, the Monte-Carlo code described offers a promising framework for future investigations. Simulation of more complicated accretion column geometries, which are relatively straightforward to implement in the code, may refine the generation of profile asymmetry from the model. Addition of magnetic effects in the Compton scattering cross section could improve predictions of the dip measurements, particularly the narrow width from observations. This would also make the model applicable to sources with cyclotron resonance spectral features. Finally, the addition of radiation pressure to the model would extend applicability to the high $\dot{M}$ regime.

Appendix A

Spectral fitting results from GX 1+4

Table A.1 Results for spectral fits to *RXTE* spectra of GX 1+4, observations B to Q and S to U (see Table 3.1). Parameter values and units are as for Table 3.2.

Parameter	B	C1	C2	C3	C4
$n_{\rm H}$	$5.35_{5.28}^{5.42}$	$1.92_{1.76}^{2.08}$	$1.93_{1.84}^{2.01}$	$1.73_{1.66}^{1.80}$	$1.54_{1.43}^{1.65}$
T_0 (keV)	$1.300_{1.294}^{1.306}$	$1.291_{1.275}^{1.307}$	$1.301_{1.292}^{1.309}$	$1.346_{1.338}^{1.354}$	$1.357_{1.346}^{1.368}$
$T_{\rm e}$ (keV)	$8.07_{8.04}^{8.10}$	$9.01_{8.73}^{9.33}$	$8.89_{8.76}^{9.02}$	$8.85_{8.75}^{8.95}$	$9.27_{9.06}^{9.49}$
τ	$5.62_{5.60}^{5.64}$	$4.11_{4.02}^{4.21}$	$4.43_{4.39}^{4.48}$	$4.55_{4.52}^{4.59}$	$4.18_{4.12}^{4.25}$
$A_{\rm C}$	$5.24_{5.22}^{5.26}$	$2.93_{2.83}^{3.03}$	$3.74_{3.68}^{3.79}$	$4.10_{4.09}^{4.10}$	$3.16_{3.08}^{3.23}$
$E_{\rm Fe}$ (keV)	$6.434_{6.430}^{6.439}$	$6.457_{6.442}^{6.473}$	$6.475_{6.468}^{6.482}$	$6.462_{6.456}^{6.469}$	$6.463_{6.453}^{6.474}$
σ	$0.330_{0.319}^{0.340}$	$0.267_{0.232}^{0.300}$	$0.266_{0.249}^{0.283}$	$0.231_{0.216}^{0.245}$	$0.239_{0.213}^{0.265}$
$A_{\rm Fe}$	$7.28_{7.20}^{7.36}$	$4.43_{4.28}^{4.60}$	$5.85_{5.74}^{5.95}$	$6.25_{6.15}^{6.35}$	$5.01_{4.89}^{5.14}$
EW (eV)	351_{346}^{355}	305_{294}^{318}	331_{325}^{337}	326_{320}^{331}	315_{306}^{323}
$L_{\rm X}$	4.3 ± 1.0	2.56 ± 0.23	3.25 ± 0.42	3.58 ± 0.59	2.87 ± 0.54
χ^2_ν	1.77	0.99	1.52	1.95	1.23

Parameter	D1	D2	E	F1	F2
$n_{\rm H}$	$23.60_{22.35}^{24.90}$	$15.97_{15.39}^{16.52}$	$4.35_{4.19}^{4.53}$	$75.26_{74.22}^{76.13}$	$32.91_{30.45}^{37.05}$
T_0 (keV)	$1.514_{1.450}^{1.580}$	$1.342_{1.312}^{1.373}$	$1.281_{1.272}^{1.291}$	$0.384_{0.344}^{0.558}$	$1.361_{1.218}^{1.444}$
$T_{\rm e}$ (keV)	$7.52_{7.34}^{7.71}$	$7.69_{7.54}^{7.85}$	$13.04_{12.31}^{13.58}$	12.32 (fixed)	14.35 (fixed)
τ	$5.05_{4.94}^{5.16}$	$4.95_{4.87}^{5.04}$	$2.62_{2.52}^{2.67}$	$2.60_{2.54}^{2.66}$	$2.56_{2.45}^{2.64}$
$A_{\rm C}$	$1.95_{1.88}^{2.03}$	$2.80_{2.74}^{2.87}$	$0.69_{0.65}^{0.78}$	$1.20_{0.73}^{19.43}$	$0.45_{0.42}^{0.50}$
$E_{\rm Fe}$ (keV)	$6.392_{6.381}^{6.404}$	$6.435_{6.424}^{6.445}$	$6.482_{6.466}^{6.497}$	$6.541_{6.525}^{6.566}$	$6.540_{6.507}^{6.616}$
σ	$0.306_{0.281}^{0.330}$	$0.271_{0.248}^{0.294}$	$0.197_{0.158}^{0.236}$	$0.240_{0.168}^{0.310}$	$0.199_{0.100}^{0.268}$
$A_{\rm Fe}$	$5.30_{5.12}^{5.47}$	$5.36_{5.21}^{5.53}$	$0.91_{0.88}^{0.95}$	$1.60_{1.47}^{1.76}$	$1.30_{1.10}^{1.41}$
EW (eV)	667_{627}^{707}	461_{443}^{480}	171_{165}^{179}	482_{448}^{521}	345_{283}^{379}
$L_{\rm X}$	1.56 ± 0.33	2.20 ± 0.51	0.83 ± 0.20	0.64 ± 0.15	0.61 ± 0.13
χ^2_ν	1.29	1.56	1.04	0.74	0.88

Table A.1 Continued

Parameter	G	H1	H2	H3	H4
$n_{\rm H}$	$19.36_{18.31}^{20.74}$	$13.25_{12.89}^{13.53}$	$15.45_{15.21}^{15.62}$	$31.39_{27.76}^{39.07}$	$27.37_{25.47}^{29.25}$
T_0 (keV)	$1.106_{1.047}^{1.154}$	$1.239_{1.229}^{1.258}$	$1.217_{1.205}^{1.241}$	$1.179_{0.951}^{1.311}$	$1.148_{1.096}^{1.180}$
$T_{\rm e}$ (keV)	9.00 (fixed)	$6.69_{6.38}^{6.85}$	$7.27_{6.91}^{7.76}$	8.40 (fixed)	$6.32_{5.79}^{6.79}$
τ	$3.37_{3.32}^{3.42}$	$3.60_{3.51}^{3.78}$	$3.49_{3.38}^{3.64}$	$2.53_{2.34}^{2.70}$	$3.83_{3.60}^{4.24}$
$A_{\rm C}$	$0.40_{0.38}^{0.43}$	$0.72_{0.69}^{0.77}$	$0.43_{0.39}^{0.47}$	$0.11_{0.09}^{0.16}$	$0.44_{0.41}^{0.51}$
$E_{\rm Fe}$ (keV)	$6.559_{6.497}^{6.603}$	$6.566_{6.540}^{6.590}$	$6.578_{6.562}^{6.610}$	$6.704_{6.570}^{6.939}$	$6.528_{6.483}^{6.569}$
σ	< 0.211	< 0.112	$0.241_{0.168}^{0.304}$	$0.478_{0.266}^{0.679}$	$0.312_{0.233}^{0.399}$
$A_{\rm Fe}$	$0.34_{0.31}^{0.38}$	$0.38_{0.37}^{0.41}$	$0.28_{0.25}^{0.30}$	$0.18_{0.13}^{0.25}$	$0.41_{0.36}^{0.49}$
EW (eV)	172_{157}^{196}	133_{128}^{143}	150_{137}^{165}	342_{227}^{470}	261_{224}^{320}
$L_{\rm X}$	0.320 ± 0.082	0.428 ± 0.073	0.28 ± 0.13	0.080 ± 0.047	0.239 ± 0.079
χ^2_ν	0.76	1.09	0.92	0.68	0.67
Parameter	H5	I	J	K	L
$n_{\rm H}$	$17.61_{16.41}^{19.27}$	$2.63_{2.46}^{2.86}$	$8.78_{6.50}^{12.33}$	$61.99_{58.70}^{73.21}$	$171.30_{121.80}^{194.30}$
T_0 (keV)	$1.306_{1.209}^{1.332}$	$1.211_{1.198}^{1.217}$	$1.234_{1.054}^{1.281}$	$1.256_{0.932}^{1.490}$	$0.953_{0.339}^{1.463}$
$T_{\rm e}$ (keV)	9.00 (fixed)	9.91 (fixed)	7.24 (fixed)	9.00 (fixed)	9.00 (fixed)
τ	$3.09_{3.03}^{3.16}$	$2.83_{2.81}^{2.84}$	$3.51_{3.31}^{3.72}$	$2.70_{2.52}^{2.85}$	$1.99_{1.70}^{2.23}$
$A_{\rm C}$	$0.36_{0.35}^{0.40}$	$0.32_{0.32}^{0.33}$	$0.07_{0.07}^{0.08}$	$0.23_{0.19}^{0.37}$	$0.56_{0.25}^{28.58}$
$E_{\rm Fe}$ (keV)	$6.364_{6.320}^{6.456}$	$6.572_{6.533}^{6.602}$	$6.658_{6.550}^{6.791}$	6.4 (fixed)	6.4 (fixed)
σ	< 0.263	$0.251_{0.201}^{0.297}$	$0.419_{0.315}^{0.530}$	$1.293_{1.140}^{1.437}$	$1.101_{0.923}^{1.211}$
$A_{\rm Fe}$	$0.37_{0.31}^{0.43}$	$0.36_{0.34}^{0.38}$	$0.13_{0.10}^{0.17}$	$1.38_{1.10}^{1.78}$	$6.03_{3.57}^{11.06}$
EW (eV)	181_{154}^{211}	192_{183}^{202}	440_{326}^{571}	1060_{851}^{1270}	2410_{1730}^{3240}
$L_{\rm X}$	0.298 ± 0.076	0.287 ± 0.079	0.048 ± 0.026	0.194 ± 0.071	0.39 ± 0.18
χ^2_ν	1.02	0.48	0.63	0.69	1.22

Table A.1 Continued

Parameter	M	N	O	P
$n_{\rm H}$	$156.40^{197.85}_{139.05}$	$123.40^{132.91}_{106.25}$	$87.55^{91.01}_{78.90}$	$60.97^{64.58}_{53.86}$
T_0 (keV)	$1.288^{1.747}_{0.039}$	$1.594^{1.909}_{1.294}$	$1.443^{1.752}_{1.309}$	$4.324^{4.451}_{3.772}$
$T_{\rm e}$ (keV)	9.00 (fixed)	13.39 (fixed)	9.00 (fixed)	8.40 (fixed)
τ	$2.80^{2.94}_{2.52}$	$2.04^{2.24}_{1.86}$	$2.96^{3.10}_{2.84}$	$0.01^{2.38}_{0.01}$
$A_{\rm C}$	$0.25^{34.27}_{0.16}$	$0.15^{0.21}_{0.12}$	$0.29^{0.32}_{0.27}$	$0.09^{0.10}_{0.09}$
$E_{\rm Fe}$ (keV)	6.4 (fixed)	6.4 (fixed)	6.4 (fixed)	$6.582^{6.623}_{6.538}$
σ	$0.800^{1.055}_{0.675}$	$0.345^{0.445}_{0.260}$	$0.648^{0.773}_{0.520}$	$0.280^{0.344}_{0.213}$
$A_{\rm Fe}$	$4.19^{11.59}_{3.23}$	$1.81^{2.27}_{1.48}$	$1.44^{1.78}_{1.16}$	$0.66^{0.74}_{0.61}$
EW (eV)	2950^{4290}_{2350}	1280^{1430}_{1190}	847^{995}_{606}	1940^{2060}_{1780}
$L_{\rm X}$	0.244 ± 0.097	0.221 ± 0.098	0.256 ± 0.082	0.096 ± 0.036
χ^2_ν	1.15	2.14	0.82	0.55

Parameter	Q	S	T	U
$n_{\rm H}$	$2.33^{2.44}_{2.22}$	$2.08^{2.21}_{1.95}$	$2.81^{3.06}_{2.60}$	$0.58^{0.79}_{0.48}$
T_0 (keV)	$1.292^{1.303}_{1.281}$	$1.305^{1.318}_{1.293}$	$1.326^{1.344}_{1.299}$	$1.310^{1.330}_{1.285}$
$T_{\rm e}$ (keV)	$10.65^{11.07}_{10.24}$	$8.93^{9.41}_{8.55}$	$9.44^{10.02}_{8.40}$	$9.58^{10.60}_{8.72}$
τ	$3.10^{3.18}_{3.00}$	$3.44^{3.57}_{3.35}$	$3.32^{3.42}_{3.26}$	$3.36^{3.46}_{3.30}$
$A_{\rm C}$	$1.09^{1.13}_{1.06}$	$0.94^{0.97}_{0.91}$	$0.49^{0.56}_{0.45}$	$0.46^{0.52}_{0.40}$
$E_{\rm Fe}$ (keV)	$6.573^{6.591}_{6.564}$	$6.516^{6.538}_{6.493}$	$6.525^{6.564}_{6.486}$	$6.554^{6.591}_{6.516}$
σ	$0.146^{0.192}_{0.081}$	$0.153^{0.211}_{0.085}$	$0.282^{0.360}_{0.197}$	$0.217^{0.302}_{0.098}$
$A_{\rm Fe}$	$1.08^{1.14}_{1.04}$	$0.73^{0.78}_{0.69}$	$0.46^{0.51}_{0.42}$	$0.40^{0.43}_{0.37}$
EW (eV)	162^{170}_{155}	148^{157}_{139}	168^{188}_{153}	160^{168}_{145}
$L_{\rm X}$	1.09 ± 0.17	0.79 ± 0.14	0.437 ± 0.081	0.411 ± 0.076
χ^2_ν	0.98	1.09	0.57	0.80

Appendix B

Publications and presentations

The research presented in this thesis has already been the subject of several publications: Greenhill et al. (1998), Greenhill et al. (1999), Galloway et al. (2000), Galloway (2000), Giles et al. (2000) and Galloway et al. (2001). Some of the results were also presented at conferences as listed below.

D. K. Galloway, A. B. Giles, J. G. Greenhill and M. C. Storey. Order from chaos—A coherent picture of GX 1+4 pulse profiles. Poster presentation at the *Astronomical Society of Australia Annual Scientific Meeting*, University of NSW, 7–10 July 1997.

D. K. Galloway, A. B. Giles, J. G. Greenhill. Spectral characteristics of GX 1+4 throughout a low flux state. *Astrophysical Theory Centre Workshop on Magnetic Fields and Accretion*, Australian National University, 12–13 November 1998.

D. K. Galloway, A. B. Giles, J. G. Greenhill and M. C. Storey. GX 1+4: High field neutron star system. *Research Centre for Theoretical Astrophysics Workshop on Supernova Remnants, Pulsars and the ISM*, University of Sydney, 18–19 March 1999.

D. K. Galloway, A. B. Giles, J. G. Greenhill, M. C. Storey and J. Swank. A serendipitous *RXTE* observation of the strong field X-ray pulsar GX 1+4. *AAS High Energy Astrophysics Division Meeting*, 12–15 April 1999, Charleston SC. Also presented at the *ASA Annual Scientific Meeting*, University of Western Sydney Nepean, 9–13 July 1999.

D. K. Galloway and K. Wu. X-ray beaming in the high magnetic field pulsar GX 1+4. Poster presentation at the *ASA Annual Scientific Meeting*, University of Western Sydney Nepean, 9–13 July 1999.

D. K. Galloway and K. Wu. Beaming due to Comptonization in X-ray Pulsars. *Proceedings, IAU Colloquium 177: Pulsar Astronomy — 2000 and Beyond*, Bonn, Germany, 30 August – 3 September, 1999.

D. K. Galloway and K. Wu. X-ray beaming in the high magnetic field pulsar GX 1+4. *Proceedings, X-ray Astronomy '99: Stellar Endpoints, AGN, and the Diffuse Background*, Bologna, Italy, 6–10 September 1999.

D. K. Galloway, A. B. Giles, K. Wu and J. G. Greenhill. Accretion column eclipses in the X-ray pulsars GX 1+4 and RX J0812.4−3114. Poster presentation at the *AAS High Energy Astrophysics Division Meeting*, 6–9 November 2000, Honolulu, HI.

Bibliography

M. G. Akritas and M. A. Bershady. Linear regression for astronomical data with measurement errors and intrinsic scatter. Astrophysical Journal, 470:706–714, 1996.

K. A. Arnaud. XSPEC: The first ten years. In G. Jacoby and J. Barnes, editors, *Astronomical Data Analysis Software and Systems V*, page 17, San Fransisco, 1996. ASP Conf. Ser. 101.

G.J. Babu and E.D. Feigelson. *Astrostatistics*. Chapman & Hall, London, 1st edition, 1996.

M. M. Basko and R. A. Sunyaev. Radiative transfer in a strong magnetic field and accreting X-ray pulsars. Astronomy and Astrophysics, 42:311–321, 1975.

P. A. Becker. Dynamical structure of radiation-dominated pulsar accretion shocks. Astrophysical Journal, 498:790–801, 1998.

R. H. Becker, E. A. Boldt, S. S. Holt, S. H. Pravdo, R. E. Rothschild, P. J. Serlemitsos, and J. H. Swank. Spectral variability in the X-ray pulsar GX 1+4. Astrophysical Journal Letters, 207:L167–L169, 1976.

K. Belczyński, J. Mikołajewska, U. Munari, R. J. Ivison, and M. Friedjung. A catalogue of symbiotic stars. Astronomy and Astrophysics Supplements, 146: 407–435, 2000.

K. Beurle, A. Bewick, P.K.S. Harper, J.J. Quenby, N.J.C. Spooner, A.G. Fenton, K.B. Fenton, A.B. Giles, J.G. Greenhill, and D.M. Warren. Balloon altitude studies of southern hemisphere hard X-ray sources by the Imperial College-University of Tasmania-INPE collaboration. Advances in Space Research, 3(10–12):43–46, 1984.

L. Bildsten, D. Chakrabarty, J. Chiu, M. H. Finger, D. T. Koh, R. W. Nelson, T. A. Prince, B. C. Rubin, D. M. Scott, M. Stollberg, B. A. Vaughan, C. A. Wilson, and R. B. Wilson. Observations of accreting pulsars. Astrophysical Journal Supplements, 113:367–408, 1997.

T. M. Braje, R. W. Romani, and K. P. Rauch. Light curves of rapidly rotating neutron stars. Astrophysical Journal, 531:447–452, 2000.

D. J. Burnard, J. Arons, and R. I. Klein. Accretion powered pulsars - continuum spectra and light curves of settling accretion mounds. Astrophysical Journal, 367: 575–592, 1991.

M. Čemeljić and T. Bulik. The influence of reprocessing in the column on the light curves of accretion powered neutron stars. Acta Astronomica, 48:65–75, 1998.

D. Chakrabarty, L. Bildsten, M. H. Finger, J. M. Grunsfeld, D. T. Koh, R. W. Nelson, T. A. Prince, B. A. Vaughan, and R. B. Wilson. On the correlation of torque and luminosity in GX 1+4. Astrophysical Journal Letters, 481:L101–L105, 1997.

D. Chakrabarty and P. Roche. The symbiotic neutron star binary GX 1+4/V2116 Ophiuchi. Astrophysical Journal, 489:254–271, 1997.

D. Chakrabarty, M. H. van Kerkwijk, and J. E. Larkin. Infrared spectroscopy of GX 1+4/V2116 Ophiuchi: Evidence for a fast red giant wind? Astrophysical Journal Letters, 497:L39–L42, 1998.

R. H. D. Corbet. The three types of high-mass X-ray pulsator. Monthly Notices of the Royal Astronomical Society, 220:1047–1056, 1986.

R. H. D. Corbet and A. G. Peele. The orbital period of the Be/neutron star binary RX J0812.4-3114. Astrophysical Journal Letters, 530:L33–L36, 2000.

W. Cui. Evidence for 'propeller' effects in X-ray pulsars GX 1+4 and GRO J1744-28. Astrophysical Journal Letters, 482:L163–L166, 1997.

E. P. Cutler, B. R. Dennis, and J. F. Dolan. An elliptical binary orbit model of GX 1+4. Astrophysical Journal, 300:551–556, 1986.

J. K. Daugherty and A. K. Harding. Compton scattering in strong magnetic fields. Astrophysical Journal, 309:362–371, 1986.

A. Davidsen, R. Malina, and S. Bowyer. The optical counterpart of GX 1+4 — a symbiotic star. Astrophysical Journal, 211:866–871, 1977.

K. Davidson and J. P. Ostriker. Neutron-star accretion in a stellar wind: Model for a pulsed X-ray source. Astrophysical Journal, 179:585–598, 1973.

T. Dotani, T. Kii, F. Nagase, K. Makishima, T. Ohashi, T. Sakao, K. Koyama, and I. R. Tuohy. Peculiar pulse profile of GX 1+4 observed in the spin-down phase. Publications of the Astronomical Society of Japan, 41:427–440, 1989.

J. P. Doty, W. H. G. Lewin, and J. A. Hoffman. *SAS 3* observations of GX 1+4. Astrophysical Journal, 243:257–262, 1981.

R.P. Fender and M.A. Hendry. The radio luminosity of persistent X-ray binaries. Monthly Notices of the Royal Astronomical Society, 317 (1):1–8, 2000.

J. Frank, A. R. King, and D. J. Raine. *Accretion power in astrophysics*. Cambridge University Press, Cambridge, England; New York, NY, USA, 2nd edition, 1992.

G. Fritz, R.C. Henry, J.F. Meekins, T.A. Chubb, and H. Friedman. X-ray pulsar in the Crab nebula. Science, 164:709, 1969.

F. Frontera and D. Dalfiume. The high-energy properties of X-ray pulsars. In *Two Topics in X-ray Astronomy Volume 1: X-ray Binaries*, pages 57–69, 1989.

D. K. Galloway. Accretion column disruption in GX 1+4. Astrophysical Journal Letters, 543:L137–L140, 2000.

D. K. Galloway, A. B. Giles, J. G. Greenhill, and M. C. Storey. Spectral variation in the X-ray pulsar GX 1+4 during a low-flux episode. Monthly Notices of the Royal Astronomical Society, 311:755–761, 2000.

D. K. Galloway, A. B. Giles, K. Wu, and J. G. Greenhill. Accretion column eclipses in the X-ray pulsars GX 1+4 and RX J0812.4−3114. Monthly Notices of the Royal Astronomical Society, 325 (1):419, 2001.

P. Ghosh and F. K. Lamb. Accretion by rotating magnetic neutron stars. II - Radial and vertical structure of the transition zone in disk accretion. Astrophysical Journal, 232:259–276, 1979a.

P. Ghosh and F. K. Lamb. Accretion by rotating magnetic neutron stars. III - Accretion torques and period changes in pulsating X-ray sources. Astrophysical Journal, 234:296–316, 1979b.

R. Giacconi, H. Gursky, F.R. Paolini, and B. Rossi. Evidence for X-rays from sources outside the solar system. Physical Review Letters, 9:439–443, 1962.

A. B. Giles, D. K. Galloway, J. G. Greenhill, M. C. Storey, and C. A. Wilson. Pulse profiles, accretion column eclipses and a flare in GX 1+4 during a faint state. Astrophysical Journal, 529:447–452, 2000.

A. B. Giles, K. Jahoda, J. H. Swank, and W. Zhang. Prospects for coordinated observations with *XTE*. Publications of the Astronomical Society of Australia, 12:219–226, 1995.

J. G. Greenhill, D. K. Galloway, and J. R. Murray. Angular momentum transfer in the binary X-ray pulsar GX 1+4. Publications of the Astronomical Society of Australia, 16:240–246, 1999.

J. G. Greenhill, D. K. Galloway, and M. C. Storey. Luminosity dependent changes of pulse profiles in the X-ray binary GX 1+4. Publications of the Astronomical Society of Australia, 15:254–258, 1998.

J. G. Greenhill, D. P. Sharma, S. W. B. Dieters, R. K. Sood, L. Waldron, and M. C. Storey. Observations and modelling of the hard X-ray emission from GX 1+4. Monthly Notices of the Royal Astronomical Society, 260:21–27, 1993.

J. Greiner, R. A. Remillard, and C. Motch. The X-ray stream-eclipsing polar RX J1802.1+1804. Astronomy and Astrophysics, 336:191–199, 1998.

W.A. Heindl, W. Coburn, D.E. Gruber, M. Pelling, Rothschild. R.E., P. Kretchmar, I. Kreykenbohm, J. Wilms, K. Pottschmidt, and R. Staubert. *RXTE* studies of cyclotron lines in accreting pulsars. In *Proceedings of the 5th Compton Symposium*, 2000.

R.F. Hirsh. *Glimpsing and invisible universe: the emergence of X-ray astronomy.* University Press, Cambridge, 1983.

X-M. Hua. Monte Carlo simulation of Comptonization in inhomogeneous media. Computers in Physics, 11(6):660–668, 1997.

X-M. Hua and L Titarchuk. Comptonization models and spectroscopy of X-ray and gamma-ray sources: a combined study by Monte Carlo and analytical methods. Astrophysical Journal, 449:188–203, 1995.

F. A. Jansen and R. Laine. The *XMM* observatory, a technical and scientific overview. In *Proceedings of the American Astronomical Society Meeting #191, Washington DC*, pages 9601–, 1998.

J. G. Jernigan, R. I. Klein, and J. Arons. Discovery of kilohertz fluctuations in Centaurus X-3: Evidence for photon bubble oscillations (PBO) and turbulence in a high-mass X-ray binary pulsar. Astrophysical Journal, 530:875–889, 2000.

P. Jetzer, M. Straššle, and N. Straumann. On the variation of pulsar periods in close binary systems. New Astronomy, 3/8:619–630, 1998.

E. Kendziorra and R. Staubert. The pulsating X-ray source GX 1+4 (4U 1728−24). In P.W. Sanford, P. Laskarides, and J. Salton, editors, *Galactic X-ray Sources*, pages 205–216. John Wiley & Sons, Chichester, 1982.

J.G. Kirk. The formation of the continuum spectrum in X-ray pulsars. Astronomy and Astrophysics, 158:305–309, 1986.

R. I. Klein, J. Arons, G. Jernigan, and J. J. . Hsu. Photon bubble oscillations in accretion-powered pulsars. Astrophysical Journal Letters, 457:L85–+, 1996.

A.S. Kompaneets. The establishment of thermal equilibrium between quanta and electrons. Soviet Physics, JETP, 4:730, 1957.

T. Kotani, T. Dotani, F. Nagase, J. G. Greenhill, S. H. Pravdo, and L. Angelini. *ASCA* and *Ginga* observations of GX 1+4. Astrophysical Journal, 510:369–378, 1999.

M. Lampton, B. Margon, and S. Bowyer. Parameter estimation in X-ray astronomy. Astrophysical Journal, 208:177–190, 1976.

P. Laurent, L. Salotti, J. Paul, F. Lebrun, M. Denis, D. Barret, E. Jourdain, J. P. Roques, E. Churazov, M. Gilfanov, R. Sunyaev, A. Dyachkov, N. Khavenson, B. Novikov, I. Chulkov, and A. Kuznetzov. Photon spectrum and period evolution of GX 1+4 as observed at hard X-ray energies by SIGMA. Astronomy and Astrophysics, 278:444–448, 1993.

D. A. Leahy. Modelling observed X-ray pulsar profiles. Monthly Notices of the Royal Astronomical Society, 251:203–212, 1991.

W. H. G. Lewin, G. R. Ricker, and J. E. McClintock. X-rays from a new variable source GX 1+4. Astrophysical Journal Letters, 169:L17–L21, 1971.

W. H. G. Lewin, J. van Paradijs, and E. P. J. van den Heuvel, editors. *X-ray Binaries*. Cambridge University Press, Cambridge, 1995.

J. Li and D. T. Wickramasinghe. On spin-up/spin-down torque reversals in disc accreting pulsars. Monthly Notices of the Royal Astronomical Society, 300:1015–1022, 1998.

R. V. E. Lovelace, M. M. Romanova, and G. S. Bisnovatyi-Kogan. Spin-up/spin-down of magnetized stars with accretion discs and outflows. Monthly Notices of the Royal Astronomical Society, 275:244–254, 1995.

M. Matsumoto and T. Nishimura. Mersenne Twister: A 623-dimensionally equidistributed uniform pseudorandom number generator. ACM Transmissions on Modeling and Computer Simulation, 8(1):3–30, 1998.

G.S. Maurer, W.N. Johnson, J.D. Kurfess, and M.S. Strickman. Balloon observations of galactic high-energy X-ray sources. Astrophysical Journal, 254:271–278, 1982.

P. Mészáros and W. Nagel. X-ray pulsar models. I — Angle-dependent cyclotron line formation and comptonization. Astrophysical Journal, 298:147–160, 1985a.

P. Mészáros and W. Nagel. X-ray pulsar models. II — Comptonized spectra and pulse shapes. Astrophysical Journal, 299:138–153, 1985b.

G.S. Miller. The accretion curtain and pulse phase variations of the bursting X-ray pulsar GRO J1744-28. Astrophysical Journal Letters, 468:L29–L32, 1996.

B. Mony, E. Kendziorra, M. Maisack, R. Staubert, J. Englhauser, S. Dobereiner, W. Pietsch, C. Reppin, J. Trumpler, E. M. Churazov, M. R. Gilfanov, and R. Sunyaev. Hard X-ray observations of GX 1+4. Astronomy and Astrophysics, 247: 405–409, 1991.

C. Motch, F. Haberl, K. Dennerl, M. Pakull, and E. Janot-Pacheco. New massive X-ray binary candidates from the *ROSAT* galactic plane survey. I. Results from a cross-correlation with OB star catalogues. Astronomy and Astrophysics, 323: 853–875, 1997.

F. Nagase. Iron lines in X-ray pulsators. In A. Treves, G. C. Perola, and L. Stella, editors, *Iron Line Diagnostics in X-ray Sources, Varenna, Como, Italy, 9-12, October, 1990*, pages 111–121, Heiderberg, 1991. Springer-Verlag.

I. Negueruela. On the nature of Be/X-ray binaries. Astronomy and Astrophysics, 338:505–510, 1998.

I. Negueruela, P. Reig, M.H. Finger, and P. Roche. Detection of X-ray puslations from the Be/X-ray transient A 0535+26 during a disc loss phase of the primary. Astronomy and Astrophysics, 356:1003–1009, 2000.

M. G. Pereira, J. Braga, and F. Jablonski. The orbital period of the accreting pulsar GX 1+4. Astrophysical Journal Letters, 526:L105–L109, 1999.

L. A. Pozdnyakov, I. M. Sobel, and R. A. Syunyaev. Comptonization and the shaping of X-ray source spectra — Monte Carlo calculations. Astrophysics and Space Physics Research, 2:189–331, 1983.

W. H. Press, S. A. Teukolsky, W. T. Vetterling, and B. P. Flannery. *Numerical Recipes in Fortran 77: The Art of Scientific Computing*. Cambridge University Press, Cambridge, New York, Melbourne, 2nd edition, 1996.

J. E. Pringle and M. J. Rees. Accretion disc models for compact X-ray sources. Astronomy and Astrophysics, 21:1–9, 1972.

A. R. Rao, B. Paul, V. R. Chitnis, P. C. Agrawal, and R. K. Manchanda. Detection of a very low hard X-ray pulse fraction in the bright state of GX 1+4. Astronomy and Astrophysics, 289:L43–L46, 1994.

P. Reig and P. Roche. Discovery of X-ray pulsations in the Be/X-ray binary LS 992/RX J0812.4−3114. Monthly Notices of the Royal Astronomical Society, 306:95–99, 1999.

A. P. Reynolds, A. N. Parmar, M. T. Stollberg, F. Verbunt, P. Roche, R. B. Wilson, and M. H. Finger. Accretion torques in the transient X-ray pulsar EXO 2030+375. Astronomy and Astrophysics, 312:872–878, 1996.

H. Riffert and P. Meszaros. Gravitational light bending near neutron stars. I - Emission from columns and hot spots. Astrophysical Journal, 325:207–217, 1988.

R. E. Rutledge, L. Bildsten, E. F. Brown, G. G. Pavlov, and V. E. Zavlin. The thermal X-ray spectra of Centaurus X-4, Aquila X-1, and 4U 1608-522 in quiescence. Astrophysical Journal, 514:945–951, 1999.

G.B. Rybicki and A.P. Lightman. *Radiative processes in astrophysics.* John Wiley & Sons, New York, 1979.

A. Sandage, P. Osmer, R. Giacconi, P. Gorenstein, H. Gursky, J. Waters, H. Bradt, G. Garmire, B.V. Sreekantan, M. Oda, K. Osawa, and J. Jugaku. On the optical identification of Scorpius X-1. Astrophysical Journal, 146:316–322, 1966.

A. Santangelo, A. Segreto, S. Giarrusso, D. dal Fiume, M. Orlandini, A. N. Parmar, T. Oosterbroek, T. Bulik, T. Mihara, S. Campana, G. L. Israel, and L. Stella. A *BeppoSAX* study of the pulsating transient X0115+63: The first X-ray spectrum with four cyclotron harmonic features. Astrophysical Journal Letters, 523:L85–L88, 1999.

E. Schreier, R. Levinson, H. Gursky, E. Kellogg, H. Tananbaum, and R. Giacconi. Evidence for the binary nature of Centaurus X-3 from *Uhuru* X-ray observations. Astrophysical Journal, 172:L79–L89, 1972.

N. I. Shakura and R. A. Sunyaev. Black holes in binary systems. Observational appearance. Astronomy and Astrophysics, 24:337–355, 1973.

R. Staubert, M. Maisack, E. Kendziorra, T. Draxler, M. H. Finger, G. J. Fishman, M. S. Strickman, and C. H. Starr. Observations of a large flare in GX 1+4 with the Compton Gamma Ray Observatory. Advances in Space Research, 15:119–122, 1995.

L. Stella, N. E. White, and R. Rosner. Intermittent stellar wind accretion and the long-term activity of Population I binary systems containing an X-ray pulsar. Astrophysical Journal, 308:669–679, 1986.

S. J. Sturner and C. D. Dermer. Energy-dependent effects of scattering atmospheres on X-ray pulsar pulse profiles. Astronomy and Astrophysics, 284:161–173, 1994.

J.H. Swank. Observations of type I bursts from neutron stars. In S.S. Holt and W.W. Zhang, editors, *Cosmic Explosions, the 10th Annual October Astrophysics Conference, Maryland, October 11–13 1999, AIP Conf. 522*, Woodbury NY, 2000. AIP.

L. Titarchuk. Generalized Comptonization models and application to the recent high-energy observations. Astrophysical Journal, 434:570–586, 1994.

L. Titarchuk, A. Mastichiadis, and N. D. Kylafis. Spherical accretion onto neutron stars and black holes. Astronomy and Astrophysics Supplements, 120:171–174, 1996.

U. Torkelsson. Magnetic torques between accretion discs and stars. Monthly Notices of the Royal Astronomical Society, 298:L55–L59, 1998.

A. Valinia and F. E. Marshall. *RXTE* measurement of the diffuse X-ray emission from the galactic ridge: Implications for the energetics of the interstellar medium. Astrophysical Journal, 505:134–147, 1998.

M. van der Klis. Millisecond oscillations in X-ray binaries. Annual Reviews of Astronomy & Astrophysics, 38:717–760, 2000.

Y. M. Wang and G. L. Welter. An analysis of the pulse profiles of the binary X-ray pulsars. Astronomy and Astrophysics, 102:97–108, 1981.

B. Warner. *Cataclysmic Variable Stars*. Cambridge University Press, Cambridge, 1st edition, 1995.

M. C. Weisskopf. The Chandra X-ray Observatory (CXO). In *Proceedings, NATO Advanced Study Institute, Crete, Greece, 7-18 June*, 1999.

N. E. White, F. Nagase, and A. N. Parmar. The properties of X-ray binaries. In Lewin et al. (1995), pages 1–57.

N. E. White, J. H. Swank, and S. S. Holt. Accretion powered X-ray pulsars. Astrophysical Journal, 270:711–734, 1983.

S. N. Zhang, B. A. Harmon, G. J. Fishman, and W. S. Paciesas. Hard X-ray all-sky imaging with BATSE/*CGRO*. Experimental Astronomy, 6:57–62, 1995.